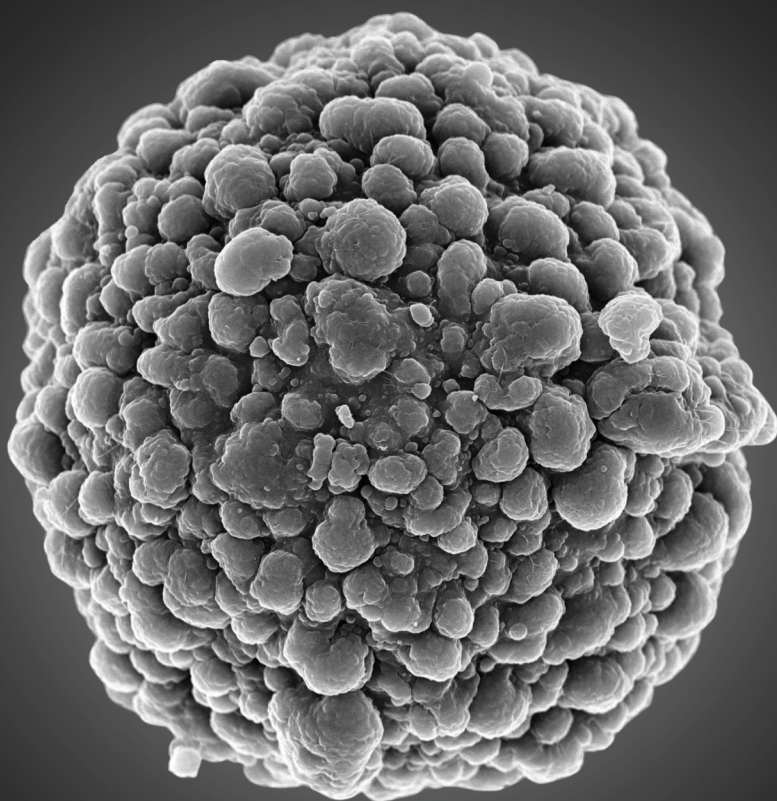


PROBING THE MORPHOLOGY, COMPOSITION
AND TEMPERATURE OF

**OLEFIN
POLYMERIZATION
CATALYST PARTICLES**

WITH **MICROSCOPY AND SPECTROSCOPY**



MAXIMILIAN J. WERNY

**PROBING THE MORPHOLOGY, COMPOSITION
AND TEMPERATURE OF**

**OLEFIN
POLYMERIZATION
CATALYST PARTICLES**
WITH **MICROSCOPY AND SPECTROSCOPY**

MAXIMILIAN J. WERNY

Werny, Maximilian James

Title: Probing the Morphology, Composition and Temperature of Olefin
Polymerization Catalyst Particles with Microscopy and Spectroscopy
ISBN: 978-94-6483-361-4
Cover design: Maximilian J. Werny
Layout design: Wiebke Keck, www.persoonlijkproefschrift.nl
Printed by: Ridderprint BV, www.ridderprint.nl

The work described in this PhD thesis was carried out at the Inorganic Chemistry and Catalysis Group, Institute for Sustainable and Circular Chemistry and Debye Institute for Nanomaterials Science, Utrecht University, The Netherlands.

Copyright © 2023 by Maximilian J. Werny. All rights reserved. Any unauthorized reprint or use of this material is prohibited. No part of this may be reproduced, stored or transmitted in any form or by any means, without written permission of the author or, when appropriate, of the publishers of the publications.

About the cover: The cover features an image of an individual pre-polymerized zirconocene-based catalyst particle, as acquired with scanning electron microscopy. Supported olefin polymerization catalysts, such as silica-supported metallocene and Ziegler-Natta catalysts, are known to undergo significant morphological and physicochemical changes during polymerization reactions. These changes govern the overall performance of the catalyst, as well as the quality and properties of the formed polymer.

Probing the Morphology, Composition and Temperature of Olefin Polymerization Catalyst Particles with Microscopy and Spectroscopy

Spectroscopie en Microscopie van de Morfologie, Samenstelling en Temperatuur
van Olefine Polymerisatie Katalysatordeeltjes
(met een samenvatting in het Nederlands)

Proefschrift

ter verkrijging van de graad van doctor aan de Universiteit Utrecht
op gezag van de rector magnificus, prof. dr. H. R. B. M. Kummeling,
ingevolge het besluit van het college voor promoties
in het openbaar te verdedigen op

woensdag 18 oktober 2023 des middags te 12:15 uur

door

Maximilian James Werny

geboren op 2 augustus 1994 te Hilden, Duitsland

Promotor:

Prof. dr. Bert M. Weckhuysen

Co-promotor:

Dr. Florian Meirer

Beoordelingscommissie:

Prof. dr. P. C. A. Bruijninx

Prof. dr. C. Copéret

Prof. dr. F. M. F. de Groot

Prof. dr. T. F. L. McKenna

Prof. dr. D. A. M. Vanmaekelbergh

The research in this PhD thesis was funded by a grant from the Dutch Polymer Institute (DPI, P.O. Box 902, 5600 AX Eindhoven, The Netherlands) and represents a part of the Research Program of DPI project no. 813.

Thesis Abstract

The economic importance of polyolefins is undeniable with the annual production of polyethylene, polypropylene and related materials currently falling in the range of 10^8 tons. Ever since supported transition metal-based catalysts were first used in the early 1950s to produce polyethylene under favorable process conditions, extensive research has been conducted to obtain a better structural and mechanistic understanding of these catalyst systems. Despite the undertaken efforts, several fundamental scientific questions, concerning the influence of the reaction conditions, heat and mass transfer, as well as the localized build-up of pressure on the activities and morphologies of supported olefin polymerization catalysts, remain. This PhD thesis describes how an analytical toolbox, consisting of various microscopy and spectroscopy techniques, was used to study the structure, composition and temperature of industrial-grade silica-supported ethylene polymerization catalysts, such as supported metallocene-based and Ziegler-Natta catalyst materials. Both families of heterogeneous catalysts were characterized in the early stages of active site genesis and polymer formation to elucidate structure-activity-morphology correlations at the single particle level. The acquired insights can ultimately contribute to the optimization of established catalyst systems, thereby improving both the catalyst productivity and the product quality. With the recycling of polymers gaining momentum, the potential of the previously mentioned toolbox for the characterization of heterogeneous catalysts in the field of chemical polyolefin recycling is also discussed.

Table of Contents

01	Catalysis, Spectroscopy and Olefin Polymerization	9
02	Correlations Between the Fragmentation Behavior and the Kinetics of Metallocene-Based Olefin Polymerization Catalysts	27
03	Assessing Morphological Heterogeneity in a Metallocene-Based Olefin Polymerization Catalyst with X-Ray Nanotomography	57
04	Elucidating the Sectioning Fragmentation Mechanism in Olefin Polymerization Catalysts with Laboratory-Based X-Ray and Electron Microscopy	85
05	Advancing the Compositional Analysis of Olefin Polymerization Catalysts with High-Throughput Fluorescence Microscopy	109
06	Monitoring the Temperature and Activity of an Olefin Polymerization Catalyst Using Luminescence Thermometry	131
07	Visualizing the Structure, Composition and Activity of Single Catalyst Particles for Olefin Polymerization and Polyolefin Decomposition	149
08	Summary, Conclusions and Future Perspectives	185
A	Appendices	199

Chapter 1

Catalysis, Spectroscopy and Olefin
Polymerization



Due to their versatility and outstanding physicochemical properties, polymers have become one of the most in-demand group of functional materials over the last decades. Commercially relevant polymers, such as polyethylene, are to a large extent produced via catalytic pathways. Supported transition metal-based catalysts are the materials of choice here and have been the focus of extensive research for decades. In this context, a combination of (micro-) spectroscopic techniques can be employed due to their non-invasive nature as well as their high spatial and temporal resolutions. The techniques yield insights into the structure, morphology, and composition of the catalyst materials. This first **Chapter** provides the reader with a brief introduction into the fields of catalysis, spectroscopy and industrially relevant olefin polymerization catalysts for the production of polyethylene. Furthermore, the individual chapters of the PhD thesis are briefly outlined.

1.1 Catalysis – Lowering Energy Barriers

Catalysis represents a key technology that lowers the environmental impact and increases the sustainability of industrial chemical processes.^[1-3] An estimated 90% of all industrial chemicals are produced with the help of a catalyst.^[4,5]

In general terms, a catalyst describes a substance that increases the rate or speed of a chemical reaction to a desired product without being consumed.^[6] In the absence of a catalyst, the activation energy, i.e., the amount of energy required for the conversion of reactants into their corresponding reaction products, is often high. Consequently, longer reaction times or harsher reaction conditions (i.e., elevated reaction temperatures and pressures) are required for the chemical reaction to take place. In the presence of a catalyst, however, the activation barrier is lowered via the formation of an energetically more favorable intermediate or transition state (**Figure 1.1**).^[7,8] This increases the rate of conversion (i.e., the reaction kinetics) and lowers the required reaction temperature.^[8] While a catalyst changes the kinetics of a reaction, the thermodynamics remain unaffected.^[7,8]

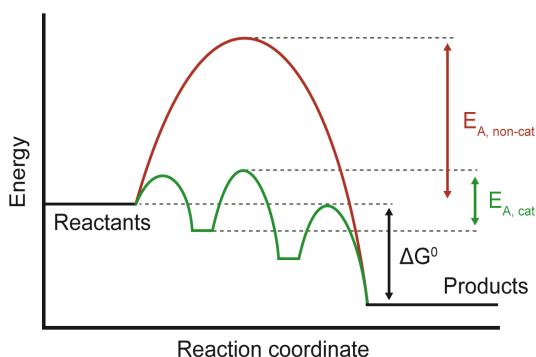


Figure 1.1 Energy diagram for the non-catalyzed (non-cat) and catalyzed (cat) conversion of reactants into reaction products. A catalyst provides an alternative, energetically favored kinetic pathway (i.e., lower activation energy E_A), thus increasing the reaction rate.

Catalysts are typically categorized into heterogeneous and homogeneous systems, depending on their physical aggregation state with respect to that of the reactants. A typical heterogeneous catalyst is a solid material that converts reactants in the liquid-phase or gas-phase. Reactions thus occur at solid–gas or solid–liquid interfaces, which, from a structural point of view, are typically complex.^[9] A homogeneous catalyst, on the other hand, operates in the same phase as the reactants. An estimated 90% of all chemical processes use heterogeneous catalysts.^[10] Heterogeneous catalysts are vital for the modern economy as they facilitate the energy-efficient and economic conversion of raw materials into value-added chemicals and fuels. They are generally preferred in industry as they enable a more facile product separation and catalyst recovery, while also demonstrating higher stability over prolonged time periods.^[11] This, however, often comes at the expense of a lower product selectivity and harsher reaction conditions.

The performance of catalysts is generally defined by three parameters: Activity, selectivity and stability. The activity of a catalyst describes the conversion of reactants per gram of catalyst over time. During most chemical transformations, several reaction products are formed in parallel. The role of a catalyst is to accelerate the formation of a specific reaction product that may not be thermodynamically favored, while suppressing the formation of undesired side-products.^[6] This is defined and quantified as the selectivity of a catalyst. Finally, a catalyst is only seen as commercially viable if it demonstrates sufficient long-term stability. In heterogeneously catalyzed reactions, harsh reaction conditions often lead to catalyst deactivation and degradation over time, thereby limiting the overall lifetime of the catalyst, which can range from seconds to several years. With the catalyst often representing a sizeable investment in an industrially operated chemical process, a combination of all three above-mentioned parameters is required for optimal performance.^[8,11]

1.2 Spectroscopy in Catalysis – Light(s), Camera, Action

Spectroscopy deals with the interactions between electromagnetic radiation and matter as a function of wavelength or frequency and represents a vital tool in modern catalysis research. Essentially, with the help of spectroscopy, active site structures, reaction mechanisms, as well as activation and deactivation pathways can be studied, both in heterogeneous and homogeneous catalyst systems.^[12,13] The applied spectroscopic techniques are usually non-invasive and allow for chemical processes to be followed at high temporal resolutions. In the case of heterogeneous catalysts, spectroscopy is often exercised in combination with microscopy, thereby delivering insights into heterogeneities taking place within catalytic solids at high spatial resolutions, ranging from the micron- to the nanoscale.^[13–20] Common examples include, amongst others, infrared (IR), Raman, fluorescence, UV-VIS, electron and X-ray microscopy. Furthermore, novel insights into structure and composition of catalysts, as well as associated local heterogeneities, are accessible by acquiring micro-spectroscopic data in 3D, e.g. via techniques such as transmission X-ray microscopy (TXM), X-ray fluorescence (XRF) tomography, coherent X-ray diffraction imaging (CXDI), X-ray holotomography and electron tomography.^[21–28]

In many cases, solid catalysts are known to undergo structural dynamics, not only under reaction conditions but also during the preceding activation and/or regeneration.^[6,9] This complicates any efforts to determine the true nature of a catalyst's active sites. The implementation of spectroscopic and microscopic methods under realistic reaction conditions (*in situ* mode of operation), coupled with the compositional analysis of formed products (*operando* mode of operation), is essential to study and characterize catalyst materials in their actual working state (**Figure 1.2**).^[6,29–31] The thereby obtained physicochemical insights form the basis for a more holistic understanding of existing catalyst materials, as well as the rational design of next-generation catalysts.

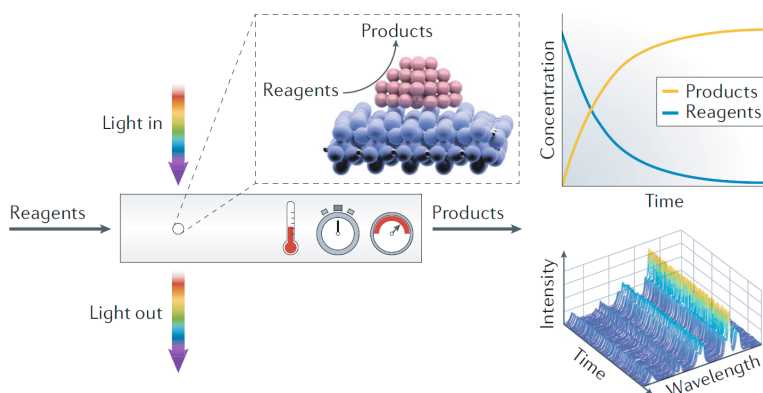


Figure 1.2 The aim of *operando* spectroscopy is to extract the structure and composition of catalyst materials in their actual working state (i.e., under realistic reaction conditions) while monitoring the formed reaction products. High temporal and spatial resolutions are vital for capturing the dynamics of catalytic processes. Reproduced from reference [25].

For catalysts to be suitable for technical processes, the active phase is often supported on a carrier material, and, in several cases, mixed with various additives and shaped into millimeter- or centimeter-sized bodies. This scale-up and integration of powder catalysts into more operationally friendly multi-component catalyst bodies introduces additional structural complexity and necessitates the investigation of the catalyst material at multiple different length scales, ranging from the active site level to the level of individual particles or even catalyst bodies.^[32]

Industrially established polymerization catalysts, such as supported Ziegler-Natta, Phillips and metallocene-based catalysts, are powder catalysts and have been intensively researched for multiple decades due to their economic importance.^[33–36] While chemical industry has made great progress in the design and controlled synthesis of related catalyst materials, yielding specific polyethylene (PE) and polypropylene (PP) grades, several open questions, in terms of the catalysts' structural development under reaction conditions, remain. In this context, spectroscopy and microscopy have great potential to make decisive contributions to this field of research^[37], ranging from the structural characterization of the active sites to tracking morphological changes within individual catalyst particles over the course of the olefin polymerization reaction.

1.3 Polymers – High Performance Materials

The 1953 Nobel Prize winner Herman Staudinger formally introduced the concept of a 'Makromolekül' (i.e., 'macromolecule') or polymer already in the 1920s^[38]: 'A molecule of high relative molecular mass, the structure of which essentially comprises the multiple repetition of units derived, actually or conceptually, from molecules of low relative molecular mass'^[39]. Since then, advances in research have revealed that these complex structural entities are abundantly present in nature. Examples include DNA, RNA, (hemi-)cellulose, lignin, chitin, proteins,

carbohydrates and rubber.^[40] Derived from the Greek words 'πολύ' ('poly', i.e., 'many') and 'μέρος' ('meros', i.e., 'parts'),^[41] the term polymer is not only used in the context of bio-based materials. In fact, various synthetic polymers, most notably PE and PP, are commercially available nowadays and have replaced traditional materials such as wood, stone, leather, metal and glass, especially in the packaging (41% market share), building and construction (20%), and automotive (9%) industries (**Figure 1.3**).^[42]

In 2017, the global production of synthetic polymers or plastics was reported as 438 Mt, with the compound annual growth rate (CAGR) of the total plastic production corresponding to 8.3% (i.e., calculated for the time period of 1950–2017).^[43,44] This represents a considerable growth in demand and can be attributed to the versatility and unique properties of these high-performance materials. Polymers are in fact often engineered to suit the specific needs of the intended field of application. Properties such as strength, durability, thermal and chemical stability, resistance to light, viscoelasticity, conductivity, as well as their tendency to form semi-crystalline structures or glasses,^[40,45] make them highly attractive to both industry and academia. Many polymers also form melts at reasonable temperatures (< 300 °C) and are thus easy to process, thereby opening up a wide range of practical applications.^[46]

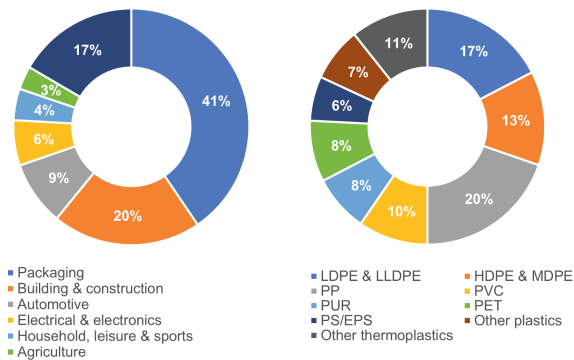





Figure 1.3 Left: Plastics demand in Europe in 2020 by industry or sector. Right: Plastics demand in Europe in 2020 by polymer type. Adapted from reference [42].

Today, a wide spectrum of synthetic polymer-based materials is commercially available. Mainly six types of polymers, namely PE, PP, polyvinyl chloride (PVC), (expanded) polystyrene (EPS/PS), polyurethanes (PUR) and polyethylene terephthalate (PET), account for over 80% of the total market demand in Europe (**Figure 1.3**).^[42] Amongst these, PE, due to its high chemical resistance, impact strength and stiffness at low temperatures, as well as good processability via molding or extrusion,^[34] represents the most important commodity polymer that is currently used (**Figure 1.3**).

1.4 Polyethylene – Properties and Processes

As the name suggests, PE is produced via polymerization of ethylene, a gaseous olefin that is pre-dominantly obtained from the steam cracking of naphtha and ethane. The three most commercially established grades of PE, based on the average density of the resin and the related polymer architecture, are low-density polyethylene (LDPE, 0.915–0.935 g/cm³), linear low-density polyethylene (LLDPE, 0.915–0.935 g/cm³), and high-density polyethylene (HDPE, 0.935–0.975 g/cm³).^[34] While HDPE consists of linear chains featuring very limited side-branching, LLDPE possesses short side branches. An even higher degree of branching is observed in LDPE, where the polymer backbone possesses comparatively long side chains in addition to the short side branches. The physico-chemical properties of the respective PE grades, such as the density, crystallinity and molding characteristics, are all dictated by the polymer architecture. This, in turn, is dependent on the applied olefin polymerization procedure, the experimental conditions and the type of catalyst (**Table 1.1**).^[34]

Table 1.1 Properties, production conditions and applications for different grades of polyethylene (PE) that are currently produced in the chemical industry.^[34]

	LDPE	LLDPE	HDPE
Molecular architecture			
Degree of branching	High	High	None to low
Type of branching	Short and long	Short	Short
Density (g/cm³)	0.915–0.935	0.915–0.935	0.935–0.975
Production process	Free radical in molten polymer	Slurry, gas-phase, solution-phase	Slurry, gas-phase, solution-phase
Pressure (bar)	690–2760	20–50	20–50
Catalysts	Oxygen, peroxides	Phillips, Ziegler-Natta, Metallocene	Phillips, Ziegler-Natta, Metallocene
Main applications	Films	Films	Blow/injection molding

Depending on the operating conditions, industrial polymerization processes for PE can be classified into 'high-pressure' and 'low-pressure' operations. Historically speaking, ethylene was first polymerized at an industrial scale in 1938 by Imperial Chemical Industries (ICI, Great Britain). The company used a high-pressure and high-temperature free radical polymerization process (150–300 °C, >> 50 bar) to produce LDPE – a process that is still economically viable and widely in use nowadays.^[47–49] In contrast to this, commercial processes for the production of HDPE and LLDPE were first developed in the 1950s and are typically operated at lower pressures and temperatures (≤ 250 °C, ≤ 50 bar) in the presence of a wide variety of heterogeneous and homogeneous catalysts, with heterogeneous catalysts dominating the field nowadays.

^[34,49–51] While HDPE is synthesized via the polymerization of pure ethylene, the production of LLDPE involves a co-polymerization reaction of ethylene with a second monomer (e.g., 1-butene, 1-hexene or 1-octene), which accounts for the side-branching.

1.5 Supported Olefin Polymerization Catalysts

Three different families of supported catalyst systems are commonly used for the production of HDPE and LLDPE: Phillips catalysts (e.g., $\text{CrO}_x/\text{SiO}_2$), Ziegler-Natta catalysts [e.g., $\text{TiCl}_4/\text{MgCl}_2$, in combination with organoaluminum compounds, such as triisobutyl aluminum (TiBA) or triethyl aluminum (TEA) as co-catalyst, as well as external or internal donor molecules] and metallocene-based catalysts (e.g., $\text{X}/\text{MAO}/\text{SiO}_2$, with X = metallocene complex and MAO = methylaluminoxane). Each catalyst produces PE with specific physical properties, which is related to the number and structural heterogeneity of active sites present in the catalyst. These determine the molecular weight distribution (MWD) of the formed polymer. The polydispersity (M_w/M_n) of the polymer, a measure for the width of the MWD, varies with the catalyst type: While the Phillips catalyst is capable of polydispersities in the range of ~ 8 –65, both Ziegler-Natta (~ 4.0) and metallocene-based catalysts (~ 2.0) are known to produce narrow MWDs.^[34] The respective MWDs, in turn, determine important processing parameters such as the flow characteristics of the molten resin.^[34,52] To illustrate this point in more detail: A PE grade with a broader MWD is well-suited to extrusion applications as the shorter polymer chains act as lubricants for the longer chains. As already mentioned, the type of catalyst material also determines the degree of long-chain branching, which also has implications for the product properties.^[53] While resins produced by Ziegler-Natta and Phillips-type catalysts dominate the linear PE market, metallocene catalysts have a strong foothold in specialty applications, such as low-density PE films.^[34]

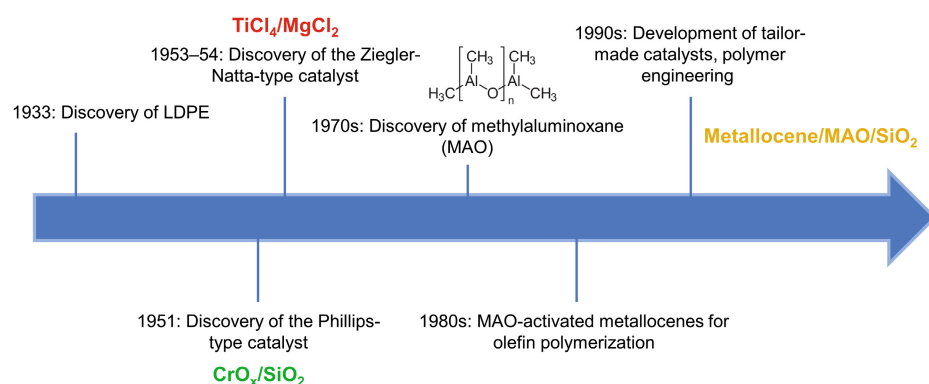


Figure 1.4 A timeline of a selection of major breakthroughs in the field of olefin polymerization. Adapted from reference [54].

1.5.1 Phillips Catalysts

In 1951, John P. Hogan and Robert L. Banks of the Phillips Petroleum Company reported that supported chromium oxide catalysts were highly active in the polymerization of propylene and ethylene to produce PP and HDPE respectively (**Figure 1.4**).^[55,56] In fact, the reactions required significantly milder reaction conditions in contrast to the capital-intensive ICI high-pressure process, which was considered to be a major breakthrough in the field. Over time, the Phillips-type catalyst has emerged to be a key catalyst material in the field of α -olefin polymerization, with 40–50% of worldwide HDPE production attributed to it.^[34] In total, over 50 different grades of HDPE and LLDPE are now available.^[57] Phillips-type catalysts also find application in the oligomerization of olefins when applied in combination with metal alkyl co-catalysts.^[34,58]

1.5.2 Ziegler-Natta Catalysts

In close succession to the breakthrough discovery of the Phillips-type catalyst, Karl Ziegler of the Max-Planck Institut in Mülheim, Germany showed that a mixture of transition metal compounds, i.e., titanium chlorides and aluminum alkyls, was able to polymerize ethylene in 1953 (**Figure 1.4**).^[59] Only a year later, Giulio Natta introduced the concept of stereospecific olefin polymerization by producing and characterizing isotactic PP (i-PP).^[60] Since its invention, the structure and composition of the Ziegler-Natta catalyst has been repeatedly adapted to enhance the catalyst's performance. The modern 4th generation Ziegler-Natta catalyst consists of TiCl_4 supported on MgCl_2 , in combination with a Lewis base (e.g., alcohol, amine, ester or ether) and an aluminum alkyl co-catalyst, such as TEA or TiBA.^[33]

1.5.3 Metallocene Catalysts

In the context of olefin polymerization catalysts, a metallocene refers to an organometallic complex of a group 4 transition metal (Zr, Hf, or Ti) and cyclopentadienyl-based ligands that requires activation via alkylation prior to polymerization.^[49] In general, metallocenes are often referred to as 'single-site catalysts' due to the well-defined, discrete nature of their active site, the metallocene complex.^[61,62] Metallocenes were first used for the polymerization of ethylene in 1957. At the time, a Cp_2TiCl_2 complex, in combination with an aluminum alkylating agent, was found to produce PE, albeit at a low activity.^[63] A major breakthrough, however, came in the 1980s when Sinn and Kaminsky discovered methylaluminoxane (MAO), an activator that turned out to be far superior in comparison to existing alkylating agents, such as TEA (**Figure 1.4**).^[64,65] In 1982, Brintzinger reported on the synthesis of so-called *ansa*-metallocenes, metallocenes that possess two interconnected ligands, thus giving rise to chirality at the metal center.^[66] With these novel catalysts, i-PP was synthesized for the first time. Since then, metallocenes have continuously evolved and become a popular class of polymerization catalysts. The steric and electronic properties of the catalysts can be tailored via the ligand framework, thus significantly influencing polymer composition and properties.^[36,60,67] This enables the synthesis of polymers with a highly defined microstructure (i.e., co-monomer distribution), tacticity and stereoregularity.^[60,61]

1.6 Role of the Particle Morphology During Olefin Polymerization On Supported Catalyst Systems

A common characteristic of supported olefin polymerization catalysts is their dynamic morphological behavior during the polymerization reaction. This has a significant impact on heat and mass transfer and is described in further detail in the following sections.

1.6.1 Catalyst Support Fragmentation

During the exothermic olefin polymerization reaction, the controlled morphological development of the catalyst system is a prerequisite for optimal performance. The evolution of a catalyst particle's morphology is dominated by a physicochemical process called fragmentation, which was first reported by Buls and Higgins in 1970.^[68] During this process, mechanical forces, linked to the formation of the solid polymer at the active sites of the catalyst, cause the catalyst support to break apart into smaller fragments. The catalyst support fragments are held together by the formed polymer phase. Over the course of the polymerization reaction, the support gradually disintegrates, exposing previously buried active sites to the reaction environment. This causes catalyst particles to grow up to 10-30 times their initial size, with the catalyst fragments actually remaining finely dispersed in the final product, i.e., the polymer particle.^[33,49] A catalyst particle that is 10 μm in diameter can thus grow to a size of 1 mm during a full polymerization run.^[69] Each spherical catalyst particle ideally yields a single polymer particle with a comparable shape – a phenomenon that is referred to as the 'replica effect'.^[49]

From a mechanistic point of view, two limiting pathways, namely the layer-by-layer and the sectioning fragmentation pathways (**Figure 1.5**), have been reported and discussed in literature.^[70-75] Layer-by-layer fragmentation involves progressive fragmentation of the catalyst particle and its constituent support granulates from the external surface to the interior. In the sectioning pathway, pronounced and coarser cracks are formed through the entire catalyst particle or support granulate, cleaving it into two or more larger fragments. While the morphology, porosity and mechanical rigidity of the support all significantly influence the process of fragmentation and, thus, the final polymer morphology and properties, the list of contributing experimental parameters is much more extensive. The chemical and physical properties of the active sites, the applied reaction conditions and the type of polymerization reactor and process all have a significant impact on the catalyst particle morphology (**Figure 1.6**).^[33,49,69,70,74-77] The highly complex relationship between this multitude of experimental parameters and experimentally observed fragmentation makes further experimental and theoretical investigations indispensable for catalyst and process optimization.

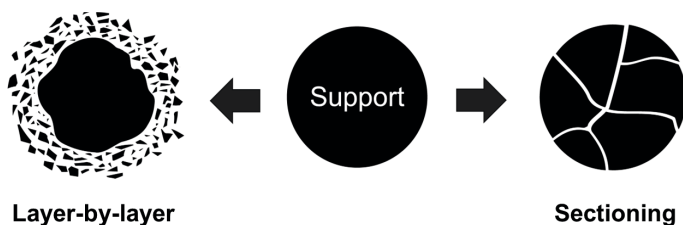


Figure 1.5 Simplified schematic of the layer-by-layer and sectioning fragmentation mechanisms. The support usually fragments in multiple iterations of the displayed pathways until it is finely dispersed in the formed polymer matrix.

It is important to note that the fragmentation of the support at reaction onset defines the morphological evolution of the particle during subsequent polymerization stages.^[75] Mild polymerization conditions and a uniform distribution of active sites promote more homogeneous support fragmentation. With mass and heat transfer limitations often the most significant during the initial pre-polymerization regime, certain catalysts are even pre-polymerized at lower temperatures and pressures in a separate reactor.^[75] This results in a more controlled morphological development of the particles and helps to avoid excessive hotspot formation.

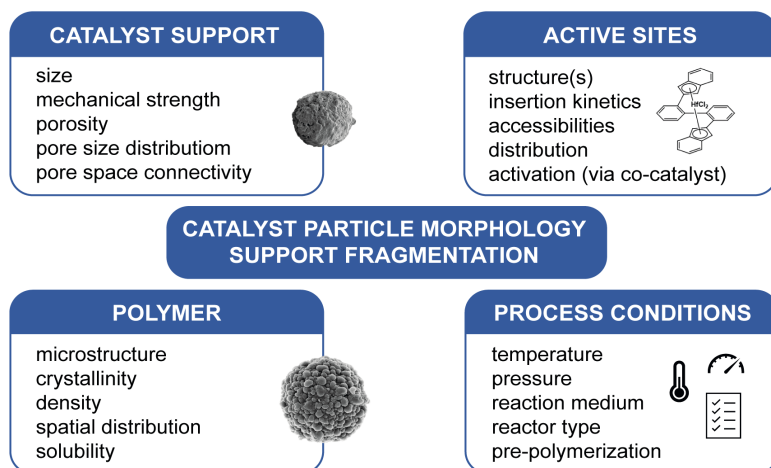


Figure 1.6 Overview of experimental and process parameters that have an influence on catalyst support fragmentation and morphology.

1.6.2 Mass Transport in Supported Olefin Polymerization Catalysts

Fragmentation is essential for overcoming mass transfer limitations that arise from the build-up of polymer and pore blocking and thus helps to maintain high catalyst activity and productivity, resulting in a high polymer yield.^[49,70] In essence, the monomer, the co-catalyst and, if employed, hydrogen, internal donors and external donors, have to be transported to the active sites of the catalyst for the olefin polymerization reaction to occur. The molecules diffuse through the pore space of the catalyst support, or, in the presence of polymer, through the polymer phase engulfing the active sites. As the rate of mass transport is significantly slower in the polymer phase than in the pore space,^[69] the particle's initial morphology (i.e., size, porosity, pore size distribution and connectivity, tortuosity), as well as the spatial distribution of the nascent polymer that is formed during polymerization, play a major role in controlling monomer diffusion. If the fragmentation of the catalyst support occurs too slowly, the accumulation of polymer can significantly limit the diffusion of the monomer and lead to a decline in the reaction rate or even completely inhibit the reaction.^[78] Naturally, the rate of diffusion also depends on the diffusion pathway length, resulting in particle size-dependent effects on the apparent rate of polymerization.^[70,74,79–83] In general, monomer diffusion and, as a result thereof, polymerization and fragmentation fronts, have been reported to occur preferentially in the larger macropores, only proceeding to the smaller meso- and nanopores with time.^[84–86] The degree of mass transfer resistance is further influenced by changes in the pore size distribution and porosity of the particle over time, as well as variations in the crystallinity of the formed polymers (commercial polyolefins are usually semi-crystalline).^[69] This polymer crystallinity is temperature-dependent: Lower polymerization temperatures induced higher crystallinities due to lower degrees of polymer chain entanglement.^[87,88]

Modern industrial-grade olefin polymerization catalysts are carefully engineered to deliver specific polymer yields and polymerization rate profiles. They rely on the interplay of kinetically fast active sites (up to 10^4 – 10^5 insertions per second^[77]), which play a major role in attaining sufficiently high polymer yields, and polymerization-grade silica gels with suitable porosities, pore size distributions, surface areas, and mechanical strengths, which facilitate adequate monomer diffusion and fragmentation behavior.^[69] A supported olefin polymerization catalyst will ideally polymerize and fragment in the absence of major monomer concentration and temperature gradients, thus ensuring a controlled expansion of the polymer-catalyst composite.

1.7 Scope and Outline of the PhD Thesis

The general aim of the research described in this PhD thesis was to (i) identify factors regulating the morphological and physicochemical evolution of industrial-grade silica-supported olefin polymerization catalysts, and (ii) employ existing and develop novel 2D and 3D microscopy and spectroscopy tools to establish structure-composition-performance correlations in supported olefin polymerization catalysts. To address these research goals, two distinct classes of catalyst materials, namely silica-supported metallocene catalysts (i.e., Zr/MAO/SiO₂ and Hf/MAO/SiO₂, with MAO = methylaluminoxane) and a silica-supported Ziegler-Natta catalyst (i.e., TiCl₄/MgCl₂/SiO₂), were investigated during ethylene polymerization under different reaction conditions. The individual research chapters of this PhD thesis (**Chapters 2–8**) are briefly described below:

In **Chapter 2**, the morphologies of two structurally analogous silica-supported hafnocene- and zirconocene-based catalyst materials were assessed at multiple stages of low-pressure, gas-phase ethylene polymerization (i.e., 1.6 bar) using focused ion beam-scanning electron microscopy (FIB-SEM) and infrared photoinduced force microscopy (IR PiFM). To establish correlations between the dominant fragmentation pathways of the catalysts (e.g., layer-by-layer fragmentation or sectioning) and the kinetics and accessibility of their active sites, bulk catalytic testing and probe molecule IR spectroscopy were performed. Thus, by adopting this multi-scale approach, the properties of the active sites were linked to the physicochemical behavior of the catalyst at the single particle level.

The morphological evolution of the hafnocene-based catalyst material during gas-phase ethylene polymerization (assessed in **Chapter 2**) was investigated more closely in **Chapter 3**. Here, hard X-ray holotomography, a synchrotron-based full-field imaging technique that delivers high imaging contrast (i.e., phase contrast) between the silica support of the catalyst and the formed polyethylene, was used. Due to the fast acquisition speed of the analytical technique, 12 individual catalyst particles were captured in 3D. The distribution of different phases (i.e., polymer, silica and macropores) was then assessed with advanced imaging segmentation and radial analysis, as well as visualized with dispersion plots. Furthermore, pore network modelling was performed to assess changes in macroporosity, pore space connectivity and tortuosity over time. This yielded more representative information on the catalyst's early-stage morphological development, as well as inter- and intraparticle heterogeneities.

In **Chapter 4**, the origin of the sectioning fragmentation mechanism in silica-supported olefin polymerization catalysts was analyzed in further detail. For this, two showcase catalyst systems, i.e., the above-mentioned silica-supported zirconocene catalyst and a silica-supported Ziegler-Natta catalyst, were studied during slurry-phase ethylene polymerization at elevated ethylene pressures (7.5–10 bar). By using a combination of laboratory-based nano computed tomography (nanoCT) and FIB-SEM, highly resolved 3D and 2D data were obtained. Three different factors that contribute to and regulate the occurrence of the sectioning fragmentation mechanism were identified.

In **Chapter 5**, a high-throughput characterization approach, based on confocal fluorescence microscopy (CFM) and advanced image processing, was employed to quantitatively assess the fragmentation behavior of the zirconocene-based catalyst material. The autofluorescent

catalyst was studied at multiple stages of slurry-phase ethylene polymerization (10 bar). The morphological screening of the catalyst via 2D and 3D CFM delivered quantitative data on the early-stage reactivity and fragmentation of a large number of catalyst particles. Furthermore, it provided representative insights into inter- and intraparticle heterogeneities. Due to its large sample throughput, the methodology is suitable for quality control on supported olefin polymerization catalysts before and after (pre-)polymerization.

In **Chapter 6**, *in situ* luminescence thermometry was employed as a novel analytical tool to assess the temperature and thus performance of the silica-supported zirconocene catalyst during gas-phase ethylene polymerization at high temporal resolutions. The use of $\text{NaYF}_4:\text{Er}^{3+},\text{Yb}^{3+}/\text{NaYF}_4$ core-shell nanoparticles as temperature sensors was evaluated, both in terms of their chemical compatibility with the sensitive olefin polymerization catalyst and their dispersion onto the catalyst particles. Differences in reactivity between testing runs could be assessed in a non-invasive manner using small sample amounts. The results described here lay the foundation for temperature mapping experiments under reaction conditions, which can potentially be used to visualize and quantify inhomogeneities in polymerization activity at the surface of individual catalyst particles.

Chapter 7 provides an overview of the state-of-the-art analytical techniques for the characterization of olefin polymerization and polyolefin decomposition catalysts. Recent studies, employing highly resolved 2D and 3D imaging techniques on individual catalyst particles, are highlighted. Furthermore, the potential of these techniques for *in situ* and *operando* as well as high-throughput experimentation is discussed.

Finally, the main findings and conclusions of this PhD thesis are summarized in **Chapter 8**. Future research directions in the field of supported olefin polymerization catalysts and the chemical imaging of individual catalyst particles at high spatial resolutions and sample throughput are proposed.

References

1. R. A. Sheldon, I. Arends, U. Hanefeld, *Green Chemistry and Catalysis*, Wiley-VCH, Weinheim, **2007**.
2. P. T. Anastas, M. M. Kirchhoff, T. C. Williamson, *Appl. Catal. A Gen.* **2001**, *221*, 3–13.
3. G. Centi, S. Perathoner, *Catal. Today* **2003**, *77*, 287–297.
4. J. N. Armor, *Catal. Today* **2011**, *163*, 3–9.
5. J. R. Ludwig, C. S. Schindler, *Chem* **2017**, *2*, 313–316.
6. R. Schlögl, *Angew. Chem. Int. Ed.* **2015**, *54*, 3465–3520.
7. I. Chorkendorff, J. W. Niemantsverdriet, *Concepts of Modern Catalysis and Kinetics*, 3rd Ed., Wiley-VCH, Weinheim, **2017**.
8. L. Lefferts, U. Hanefeld, *Catalysis: An Integrated Textbook for Students*, Wiley-VCH, Weinheim, **2018**.
9. A. Corma, *Angew. Chem. Int. Ed.* **2016**, *55*, 6112–6113.
10. J. M. Thomas, W. J. Thomas, *Principles and Practice of Heterogeneous Catalysis*, John Wiley & Sons, **2014**.
11. J. A. Dumesic, G. W. Huber, M. Boudart, in *Handbook of Heterogeneous Catalysis* (Eds.: G. Ertl, F. Schüth, H. Knözinger, J. Weitkamp), Wiley-VCH, Weinheim, **2008**, 1–15.
12. B. M. Weckhuysen, *Chem. Commun.* **2002**, 97–110.
13. I. L. C. Buurmans, B. M. Weckhuysen, *Nat. Chem.* **2012**, *4*, 873–886.
14. B. M. Weckhuysen, *Angew. Chem. Int. Ed.* **2009**, *48*, 4910–4943.
15. A. M. Beale, S. D. M. Jacques, B. M. Weckhuysen, *Chem. Soc. Rev.* **2010**, *39*, 4656–4672.
16. E. Stavitski, B. M. Weckhuysen, *Chem. Soc. Rev.* **2010**, *39*, 4615–4625.
17. J. Nelson, S. Misra, Y. Yang, A. Jackson, Y. Liu, H. Wang, H. Dai, J. C. Andrews, Y. Cui, M. F. Toney, *J. Am. Chem. Soc.* **2012**, *134*, 6337–6343.
18. J. C. Yang, M. W. Small, R. V. Grieshaber, R. G. Nuzzo, *Chem. Soc. Rev.* **2012**, *41*, 8179–8194.
19. J. D. Grunwaldt, J. B. Wagner, R. E. Dunin-Borkowski, *ChemCatChem* **2013**, *5*, 62–80.
20. B. M. Weckhuysen, *Natl. Sci. Rev.* **2015**, *2*, 147–149.
21. H. Friedrich, P. E. De Jongh, A. J. Verkleij, K. P. De Jong, *Chem. Rev.* **2009**, *109*, 1613–1629.
22. J. D. Grunwaldt, C. G. Schroer, *Chem. Soc. Rev.* **2010**, *39*, 4741–4753.
23. A. M. Wise, J. N. Weker, S. Kalirai, M. Farmand, D. A. Shapiro, F. Meirer, B. M. Weckhuysen, *ACS Catal.* **2016**, *6*, 2178–2181.
24. J. Ihli, R. R. Jacob, M. Holler, M. Guizar-Sicairos, A. Diaz, J. C. da Silva, D. Ferreira Sanchez, F. Krumeich, D. Grolimund, M. Taddei, W. -C. Cheng, Y. Shu, A. Menzel, *Nat. Commun.* **2017**, *8*, 809.
25. F. Meirer, B. M. Weckhuysen, *Nat. Rev. Mater.* **2018**, *3*, 324–340.
26. K. W. Bossers, R. Valadian, S. Zanon, R. Smeets, N. Friederichs, J. Garrevoet, F. Meirer, B. M. Weckhuysen, *J. Am. Chem. Soc.* **2020**, *142*, 3691–3695.
27. M. Gambino, M. Veselý, M. Filez, R. Oord, D. Ferreira Sanchez, D. Grolimund, N. Nesterenko, D. Minoux, M. Maquet, F. Meirer, B. M. Weckhuysen, *Angew. Chem. Int. Ed.* **2020**, *59*, 3922–3927.
28. M. Veselý, R. Valadian, L. Merten Lohse, M. Toepferwien, K. Spiers, J. Garrevoet, E. T. C. Vogt, T. Salditt, B. M. Weckhuysen, F. Meirer, *ChemCatChem* **2021**, *13*, 2494–2507.
29. B. M. Weckhuysen, *Phys. Chem. Chem. Phys.* **2003**, *5*, 4351–4360.
30. H. Topsøe, *J. Catal.* **2003**, *216*, 155–164.
31. C. Sansom, “Lights – camera – catalysis! | Research | Chemistry World,” <https://www.chemistryworld.com/opinion/lights-camera-catalysis/3009418.article>, **2018**.
32. S. Mitchell, N. L. Michels, J. Pérez-Ramírez, *Chem. Soc. Rev.* **2013**, *42*, 6094–6112.
33. L. L. Böhm, *Angew. Chem. Int. Ed.* **2003**, *42*, 5010–5030.
34. M. P. McDaniel, *Adv. Catal.* **2010**, *53*, 123–606.
35. G. G. Hlatky, *Chem. Rev.* **2000**, *100*, 1347–1376.

36. W. Kaminsky, *Polyolefins : 50 Years after Ziegler and Natta II, Polyolefins by Metallocenes and Other Single-Site Catalysts*, Springer-Verlag, Berlin, **2013**.
37. E. Groppo, K. Seenivasan, C. Barzan, *Catal. Sci. Technol.* **2013**, *3*, 858–878.
38. W. Quarles, *J. Chem. Educ.* **1951**, 120–122.
39. A. D. Jenkins, R. F. T. Stepto, P. Kratochvíl, U. W. Suter, *Pure Appl. Chem.* **1996**, *68*, 2287–2311.
40. R. J. Young, P. A. Lovell, *Introduction to Polymers*, CRC Press, Boca Raton, **2011**.
41. W. B. Jensen, *J. Chem. Educ.* **2008**, *85*, 624–625.
42. Plastics Europe Market Research Group and Conversio Market & Strategy GmbH, *Plastics – the Facts 2021*, **2021**.
43. R. Geyer, J. R. Jambeck, K. L. Law, *Sci. Adv.* **2017**, *3*, e1700782.
44. R. Geyer, in *Plast. Waste Recycl.*, Elsevier, **2020**, 13–32.
45. J. Mark, K. Ngai, W. Graessley, L. Mandelkern, E. Samulski, G. Wignall, J. Koenig, *Physical Properties of Polymers*, Cambridge University Press, Cambridge, **2004**.
46. L. F. Francis, in *Mater. Process. A Unified Approach to Process. Met. Ceram. Polym.* (Ed.: L. F. Francis), Academic Press, San Diego, **2016**, 105–249.
47. E. W. Fawcett, R. O. Gibson, M. W. Perrin, *Polymerization of Olefins*, **1939**, US2153553.
48. H. R. Sailors, J. P. Hogan, *J. Macromol. Sci. Part A - Chem.* **1981**, *15*, 1377–1402.
49. J. R. Severn, J. C. Chadwick, R. Duchateau, N. Friederichs, *Chem. Rev.* **2005**, *105*, 4073–4147.
50. B. M. Weckhuysen, R. A. Schoonheydt, *Catal. Today* **1999**, *51*, 215–221.
51. E. Groppo, C. Lamberti, S. Bordiga, G. Spoto, A. Zecchina, *Chem. Rev.* **2005**, *105*, 115–183.
52. W. Kaminsky, *Polyolefins : 50 Years after Ziegler and Natta II, Polyolefins by Metallocenes and Other Single-Site Catalysts*, Springer-Verlag, Berlin, **2013**.
53. J. B. P. Soares, T. F. L. McKenna, *Polyolefin Reaction Engineering*, Wiley-VCH, Weinheim, **2012**.
54. D. W. Sauter, M. Taoufik, C. Boisson, *Polymers* **2017**, *9*, 1–13.
55. J. P. Hogan, R. L. Banks, *Polymers and Production Thereof*, **1958**, US2825721.
56. J. P. Hogan, R. L. Banks, *Polymerization Catalyst and Production Thereof*, **1960**, US29511816.
57. R. G. Geitenbeek, A. E. Nieuwelink, T. S. Jacobs, B. B. V. Salzmans, J. Goetze, A. Meijerink, B. M. Weckhuysen, *ACS Catal.* **2018**, *8*, 2397–2401.
58. C. Barzan, E. Groppo, E. A. Quadrelli, V. Monteil, S. Bordiga, *Phys. Chem. Chem. Phys.* **2012**, *14*, 2239–2245.
59. G. Wilke, *Angew. Chem. Int. Ed.* **2003**, *42*, 5000–5008.
60. V. Busico, R. Cipullo, *Prog. Polym. Sci.* **2001**, *26*, 443–533.
61. W. Kaminsky, *J. Polym. Sci. Part A Polym. Chem.* **2004**, *42*, 3911–3921.
62. X. Cui, W. Li, P. Ryabchuk, K. Junge, M. Beller, *Nat. Catal.* **2018**, *1*, 385–397.
63. G. Natta, P. Pino, G. Mazzanti, U. Giannini, E. Mantica, M. Peraldo, *J. Polym. Sci.* **1957**, *26*, 120–123.
64. H. Sinn, W. Kaminsky, *Adv. Organomet. Chem.* **1980**, *18*, 99–149.
65. H. Sinn, W. Kaminsky, H. Vollmer, R. Woldt, *Angew. Chem. Int. Ed. English* **1980**, *19*, 390–392.
66. F. R. W. P. Wild, L. Zsolnai, G. Huttner, H. H. Brintzinger, *J. Organomet. Chem.* **1982**, *232*, 233–247.
67. G. W. Coates, *Chem. Rev.* **2000**, *100*, 1223–1252.
68. V. W. Buls, T. L. Higgins, *J. Polym. Sci. Part A-1 Polym. Chem.* **1970**, *8*, 1037–1053.
69. T. F. L. McKenna, A. Di Martino, G. Weickert, J. B. P. Soares, *Macromol. React. Eng.* **2010**, *4*, 40–64.
70. G. Fink, B. Steinmetz, J. Zechlin, C. Przybyla, B. Tesche, *Chem. Rev.* **2000**, *100*, 1377–1390.
71. G. Fink, B. Tesche, F. Korber, S. Knoke, *Macromol. Symp.* **2001**, *173*, 77–87.
72. B. Horáčková, Z. Grof, J. Kosek, *Chem. Eng. Sci.* **2007**, *62*, 5264–5270.
73. F. Machado, E. L. Lima, J. C. Pinto, T. F. McKenna, *Polym. Eng. Sci.* **2010**, *51*, 302–310.
74. M. A. Bashir, T. F. L. McKenna, in *Polym. React. Eng. Dispersed Syst. Vol. I* (Ed.: W. Pauer), Springer International Publishing, Cham, **2018**, 19–63.
75. A. Alizadeh, T. F. L. McKenna, *Macromol. React. Eng.* **2018**, *12*, 1700027.

76. G. Weickert, G. B. Meier, J. T. M. Pater, K. R. Westerterp, *Chem. Eng. Sci.* **1999**, *54*, 3291–3296.
77. T. F. McKenna, J. B. P. Soares, *Chem. Eng. Sci.* **2001**, *56*, 3931–3949.
78. S. W. Webb, E. L. Weist, M. G. Chiovetta, R. L. Laurence, W. C. Conner, *Can. J. Chem. Eng.* **1991**, *69*, 665–681.
79. V. F. Tisse, R. M. Briquel, T. F. L. McKenna, *Macromol. Symp.* **2009**, *285*, 45–51.
80. V. F. Tisse, F. Prades, R. Briquel, C. Boisson, T. F. L. McKenna, *Macromol. Chem. Phys.* **2010**, *211*, 91–102.
81. E. Tioni, J. P. Broyer, V. Monteil, T. McKenna, *Ind. Eng. Chem. Res.* **2012**, *51*, 14673–14684.
82. T. Taniike, T. Funako, M. Terano, *J. Catal.* **2014**, *311*, 33–40.
83. M. A. Bashir, V. Monteil, C. Boisson, T. F. L. McKenna, *AIChE J.* **2017**, *63*, 4476–4490.
84. M. P. McDaniel, *J. Polym. Sci. A1.* **1981**, *19*, 1967–1976.
85. M. P. McDaniel, in *Adv. Catal.* (Eds.: D. D. Eley, H. Pines, P. B. Weisz), Academic Press, San Diego, **1985**, 47–98.
86. P. Kittilsen, H. F. Svendsen, T. F. McKenna, *AIChE J.* **2003**, *49*, 1495–1507.
87. P. Smith, H. D. Chanzy, B. P. Rotzinger, *J. Mater. Sci.* **1987**, *22*, 523–531.
88. J. Loos, M. Arndt-Rosenau, U. Weingarten, W. Kaminsky, P. J. Lemstra, *Polym. Bull.* **2002**, *48*, 191–198.

Chapter 2

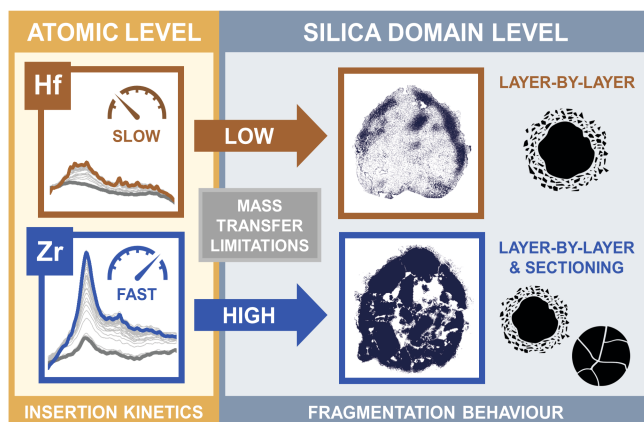
Correlations Between the Fragmentation Behavior and the Kinetics of Metallocene-Based Olefin Polymerization Catalysts

This **Chapter** is based on the following scientific articles:

M. J. Werny*, J. Zarupski*, I. C. ten Have, A. Piovano, C. Hendriksen, N. H. Friederichs, F. Meirer, E. Groppo, B. M. Weckhuysen, *JACS Au* **2021**, *1*, 1996–2008. Copyright © 2021 Werny *et al.*, published by American Chemical Society.

M. J. Werny*, J. Zarupski*, I. C. ten Have, A. Piovano, C. Hendriksen, N. H. Friederichs, F. Meirer, E. Groppo, B. M. Weckhuysen, *JACS Au* **2023**. DOI: 10.1021/jacsau.3c00266. Copyright © 2023 Werny *et al.*, published by American Chemical Society.

*Both authors contributed equally to this work.



This **Chapter** focuses on the early-stage fragmentation and related kinetics of silica-supported bridged bis-indenyl hafnocene- and zirconocene-based catalysts for the gas-phase polymerization of ethylene. While a combination of focused ion beam-scanning electron microscopy (FIB-SEM) and nanoscale infrared photoinduced force microscopy (IR PiFM) revealed notable differences in the distribution of the support, polymer, and composite phases between the two catalyst materials, time-resolved probe molecule IR spectroscopy delivered information on the kinetic behavior and accessibility of the active sites of both catalyst systems. The rate of polymer formation, a property that is inherently related to the kinetics of an olefin polymerization catalyst and the applied reaction conditions, ultimately governs mass transfer and thus the degree of homogeneity achieved during support fragmentation. In the absence of strong mass transfer limitations, a layer-by-layer mechanism was found to dominate at the level of the individual catalyst support domains, while contributions from the sectioning mechanism were more subdued.

2.1 Introduction

In supported olefin polymerization catalysts, the process of support fragmentation is essential for maintaining high catalyst activity, controlling the morphology of the polymer particles, and achieving a homogeneous distribution of catalyst residues throughout the polymer matrix.^[1,2] During catalyst particle fragmentation, mechanical forces, which arise from the formation of solid polymer at the active sites of the catalyst, cause the support to disintegrate into smaller fragments. As both polymerization and fragmentation proceed, new active sites are continuously exposed to the reaction environment. Ultimately, mass transfer limitations, due to the build-up of polymer and pore blocking, can be partially overcome and the catalyst activity can be sustained or even increased. Since the early reaction stages are critical in defining the morphology of the final polymer particles, several studies have been dedicated toward understanding the process mechanistically. Two simplified models, namely, the layer-by-layer and sectioning models, are often used to describe experimentally observed fragmentation pathways during early reaction stages.^[3-9] While the layer-by-layer model involves the progressive fragmentation of the support from its external surface to the interior, the sectioning model is described by a more pronounced and coarser crack formation through the entire catalyst particle, thereby cleaving it into multiple larger fragments. Generally speaking, the morphology, porosity, and mechanical rigidity of the catalyst support all critically affect fragmentation and, hence, the final polymer morphology and properties.^[1,3,10-12] The process also strongly depends on the inherent properties of the catalyst's active sites, the applied reaction conditions, as well as heat and mass transfer limitations.^[6,8,9,11,13,14] Thus, with the aim of obtaining a more comprehensive understanding for the process of fragmentation and the key factors behind it, characterization approaches covering both the scale of the single polymerizing particle and the atomic scale of the active sites must be adopted.

In this **Chapter**, we introduce a multiscale approach that links the morphological evolution of individual catalyst particles to the kinetic behavior of their active sites. Two structurally analogous, silica-supported bridged bis-indenyl metallocene catalysts, pre-activated with methylaluminoxane (MAO) as co-catalyst (M/MAO/SiO₂, M = Hf/Zr), were examined. Despite the structural similarity of the hafnocene and zirconocene precursors, the two catalysts yielded substantially different productivities when tested in gas-phase ethylene polymerization, with Zr/MAO/SiO₂ displaying a more than 40 times higher productivity than Hf/MAO/SiO₂. The lower activity of hafnocene complexes compared to zirconocene complexes has long been attributed to an inherently lower chain propagation rate, resulting from a stronger metal-carbon bond.^[15-18] More recently, a correlation with the predominantly ionic character of the Hf-C bond was established.^[19] MAO is also known to be a poor activator for hafnocene complexes as it forms rather stable hetero-dinuclear compounds with 'free' trimethylaluminum (TMA) in equilibrium with its oligomeric part.^[20,21] The structurally analogous Hf/MAO/SiO₂ and Zr/MAO/SiO₂ catalysts, representing two extremes in terms of activity, are thus expected to behave differently during the early stages of the reaction and are therefore ideal candidates for testing our multiscale approach.

The conceptual approach of our work is illustrated in **Figure 2.1**. A combination of focused ion beam-scanning electron microscopy (FIB-SEM) and infrared photoinduced force microscopy (IR PiFM) was employed to assess the morphology of individual catalyst particle cross-sections (i.e., the spatial distribution of support and polymer phases as well as macropores), during the early stages of gas-phase ethylene polymerization (**Figure 2.1A**). At the same time, IR spectroscopy, in the presence of d-acetonitrile (d-ACN, CD_3CN) as a probe molecule, was used to evaluate the fraction of accessible metal sites and their ability to insert electron-rich molecules into the $\text{M}-\text{CH}_3$ bond. The latter represents an elementary step in olefin polymerization catalysis (**Figure 2.1B**). Finally, by comparing the morphological data obtained at the single-particle level to the compositional and kinetic data collected at the atomic scale, correlations between catalyst performance and the properties of the active sites were established.

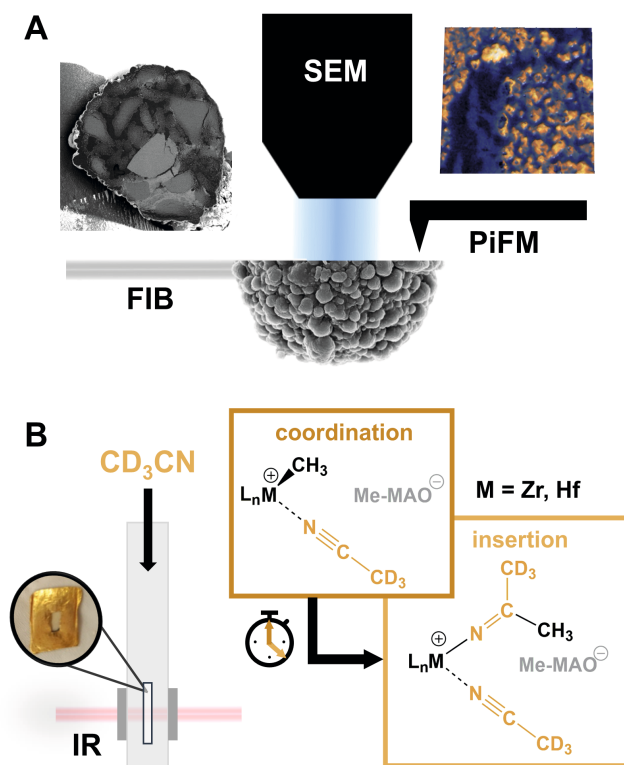


Figure 2.1 Schematic overview of the multiscale characterization approach applied to the $\text{M}/\text{MAO}/\text{SiO}_2$ ($\text{M} = \text{Hf}$ or Zr , MAO = methylaluminoxane) ethylene polymerization catalysts and the information provided by each technique. (A) Correlated focused ion beam-scanning electron microscopy (FIB-SEM) and infrared photoinduced force microscopy (IR PiFM). (B) Time-resolved IR spectroscopy in the presence of d-acetonitrile (CD_3CN) as a probe molecule.

2.2 Experimental Methods

2.2.1 Catalyst Preparation

The hafnocene-based (i.e., Hf/MAO/SiO₂) and zirconocene-based (i.e., Zr/MAO/SiO₂) catalyst materials under investigation were synthesized by SABIC (Saudi Basic Industries Corporation). Both catalyst materials were prepared following a two-step procedure. The bis-indenyl metallocene complex (2,2'-biphenylenebis-2-indenyl hafnium or zirconium dichloride) was first suspended in dried toluene (Braun solvent purification system) and contacted with methylaluminoxane (MAO, co-catalyst, 30 wt%, Chemtura; Al/M molar ratio = 150). Then, ES757 silica (PQ Corporation, D₅₀ = 25.0 μm, S_{BET} = 295 m²/g, V_{Pore} = 1.6 mL/g) was added to the solution to form a slurry. The remaining solvent was removed by a stream of N₂ at room temperature for 20 h to produce a free-flowing powder. Prior to impregnation, the ES757 silica was calcined for 4 h at 600 °C. All synthetic procedures were performed under inert N₂ atmosphere. The hafnocene-based and zirconocene-based catalyst materials contained ~ 0.59 wt% Hf and ~ 0.30 wt% Zr, respectively as determined via X-ray fluorescence (XRF) analysis.

2.2.2 Catalyst Testing

Catalytic tests were performed using a medium-throughput testing set-up consisting of 8 parallel reactors (450 mL autoclaves), equipped with helical stirrers, under reaction conditions that are displayed in **Table 2.1**.

Table 2.1 Reaction conditions employed during the high-pressure gas-phase polymerization of ethylene over the hafnocene-based and zirconocene-based catalysts and their respective polyethylene (PE) yields.

Catalyst	Catalyst mass (mg)	C ₂ H ₄ pressure (bar)	Temp. (°C)	Time (min)	Volume TiBA, 3.2 mmol/L (mL)	Stir rate (rpm)	Mass NaCl (g)	Yield (g)
Hf/MAO/SiO ₂	12	15	87	60	3.6	600	50	1.8
Zr/MAO/SiO ₂	6	15	87	60	3.6	600	50	38

Due to the technical complexity of conducting gas-phase polymerizations at the lab scale, a methodology described by the group of McKenna,^[22–24] involving the addition of NaCl to the reactors, was adopted to ensure a better dispersion of the catalyst as well as improved heat transfer during the polymerization reaction. NaCl sits at the base of the reactors and is stirred by helical stirrers. The catalyst is then added on top and is dispersed throughout the reactor volume.

For a typical gas-phase ethylene polymerization experiment, the following procedure was applied. NaCl was dried in an oven at 130 °C for two days prior to transfer to the autoclave. The autoclave was closed and kept at 110 °C, while the reactor was flushed 20 times with N₂ to remove impurities. After removal of all impurities, the reactor was conditioned to the required temperature and pressurized to the required ethylene pressure. A slurry of 50 mg catalyst in 2.5 mL pentamethylheptane (PMH) was prepared in the glovebox and the required catalyst amount taken up by a robotic needle. The robotic needle goes through an antechamber to enter the reactor

and injects the catalyst slurry using a nitrogen overpressure of 0.5–1.0 bar. Upon injection of the catalyst into the autoclave, the reaction is started. The ethylene pressure is controlled by means of GC analysis of the reactor headspace with an integrated feedback control of the reactor feeds. After 60 min of polymerization, a quench gas was added at overpressure to terminate the reaction. After three venting/vacuum/nitrogen flushing cycles, the reactor was opened.

2.2.3 Catalyst Pre-Polymerization

Pre-polymerized samples of the hafnocene-based and zirconocene-based catalysts were prepared under mild conditions via gas-phase ethylene polymerization at 1.6 bar ethylene pressure and room temperature. For this purpose, 6.7 mg of the respective catalyst was added to a dedicated glass-reactor (~ 100 mL, **Figure 2.2**) and subjected to constant ethylene pressure for the designated time periods (i.e., 10 min, 30 min and 60 min) using a gas line inside a N₂-filled glovebox.



Figure 2.2 Image of a glass-reactor used in the gas-phase ethylene pre-polymerization of the investigated metallocene-based catalyst materials.

In preparation for each pre-polymerization, the catalyst powder was well dispersed over the glass surface to reduce particle agglomeration and overheating during the exothermic polymerization reaction. All gas-phase polymerizations were performed under static conditions (i.e., no fluidization or stirring). The polymer yields were determined by weighing the catalyst powder before and after pre-polymerization (**Table 2.2**). Further information on the set-up can be found in previous work by our group.^[8]

Table 2.2 Polyethylene (PE) yields in g_{PE}/g_{cat} as obtained during the gas-phase polymerization of ethylene over the hafnocene-based and zirconocene-based catalysts in a dedicated glass-reactor set-up (1.6 bar C₂H₄, room temperature).

Catalyst yield (g_{PE}/g_{cat})	10 min	30 min	60 min
Hf/MAO/SiO ₂	1.4	2.6	6.7
Zr/MAO/SiO ₂	1.4	3.2	5.8

2.2.4 Focused Ion Beam-Scanning Electron Microscopy

Focused ion beam-scanning electron microscopy (FIB-SEM) was performed using a FEI Helios NanoLab G3 UC scanning electron microscope following a conventional procedure from the literature.^[25] All catalyst samples were dispersed onto double-sided adhesive, conductive carbon tape, which was then stuck onto an aluminum SEM stub. A Pt coating of ~ 6 nm was subsequently applied in a Cressington 208HR sputter coater. During the process of FIB cutting, slices were milled perpendicularly or horizontally to the SEM stub surface using a 45° angled SEM stub at different stage tilt angles. Cross-sectional SEM images were recorded in backscattered electron (BSE) mode using the Through the Lens Detector (TLD) in combination with an immersion lens at 2 kV and 0.1 nA. Overview images were acquired in secondary electron (SE) mode at the same acceleration voltage and current using an Everhart-Thornley detector. Image segmentation was performed using the Avizo™ software package by Thermo Fisher Scientific Inc. For images displaying full particle cross-sections, manual thresholds were applied to ensure a correct segmentation of the cross-section into support (light gray), polymer (dark gray) and pore space (predominantly black). Manual adjustments were made to include light gray regions within the pores that correspond to the inner walls of the pore as well as white regions that correspond to Ga or Pt deposits from the FIB cutting procedure. This ensured a correct segmentation of the pore space in 2D. Automatic thresholding algorithms falsely segment the pore space as solid phase due to the algorithms' inability to correctly interpret the 3D geometry of the pore system as well as due to Pt and Ga deposition in the pores during sputter coating and FIB cutting, respectively (Ga ion beam used for FIB cutting). All close-up images were segmented using Otsu's method.

2.2.5 Infrared Photoinduced Force Microscopy

Infrared photoinduced force microscopy (IR PiFM) was performed on the cross-sections of a single 30 min pre-polymerized Hf/MAO/SiO₂ particle using a VistaScope photoinduced force microscope (PiFM) from Molecular Vista Inc. (San Jose, CA, USA). The instrument is equipped with a Block Engineering tunable quantum cascade laser (QCL) unit for spectral acquisition in the range of 775-1950 cm⁻¹ at 1 cm⁻¹ spectral resolution. Atomic force microscopy (AFM) topography images, IR maps and IR point spectra were recorded in dynamic non-contact PiF mode (60 accumulations, 500 ms pixel dwell time, 1 cm⁻¹ spectral resolution) at a set point amplitude ratio of 80–85% (i.e., in relation to the free space value) using NCHR Au-coated cantilevers (force constant: ~ 40 N/m).

Prior to acquiring an IR map at a specific wavenumber, a preliminary low-resolution scan was performed. A point spectrum was then taken in the mapped area to determine the wavenumber of the targeted vibrational band (i.e., the wavenumber at which the band has its maximum intensity).

To record phase maps of the corresponding areas, however, the set point of the PiFM instrument was lowered to 60% to enhance tip-sample contact (contact mode), unless specified otherwise. These set point values were chosen based on the shift of the cantilever frequency relative to its eigenfrequency^[26] (**Table 2.3**), an indicator for the degree of tip-sample interaction. For both the silica and PE phases, set points greater than 60% resulted in a shift to

lower frequencies. This implied that net attractive forces were acting on the cantilever tip. The attractive forces were the highest at a set point of 80%. Repulsive tip-sample interactions, on the other hand, started to dominate at a set point of 60% and led to higher frequencies.

Table 2.3 Cantilever frequency recorded at different amplitude ratio set points on silica- [1030 cm^{-1} , $\nu(\text{Si-O})$] and polyethylene (PE)-rich [1472 cm^{-1} , $\delta(\text{C-H})$] domains of a hafnocene-based catalyst particle cross-section (cantilever eigenfrequency: 265.287 kHz, drive amplitude: 3 nm).

Set point	Frequency [1030 cm^{-1}] (kHz)	Frequency [1472 cm^{-1}] (kHz)
90%	264.087	264.087
80%	263.987	263.987
70%	264.787	264.787
60%	265.687	266.787

Spatial resolutions in the range of 10–40 nm were achieved at a probing depth of approximately 30 nm^[27]. Some of the point spectra feature a band at 1264 cm^{-1} , which is linked to the $\delta(\text{Si-CH}_3)$ ^[28,29] vibration in polydimethylsiloxane (PDMS) – a common contamination on AFM tips.

All acquired data were analyzed using the VistaScan 3.9 and SurfaceWorks 3.0 software packages from Molecular Vista Inc. Spectra recorded on the hafnocene-based catalyst particle cross-sections were generally saved without normalization or smoothing.

2.2.6 Fourier-Transform Infrared Spectroscopy

Fourier-transform infrared (FTIR) spectroscopy in the presence of d-acetonitrile (d-ACN) as a probe molecule was performed in transmission mode by using a Bruker Vertex 70 instrument equipped with a mercury-cadmium-telluride (MCT) detector at a spectral resolution of 2 cm^{-1} . The samples were measured in the form of thin, self-supporting pellets, made inside the glovebox by using a manual pelletizer. After the pellet was prepared, it was inserted into a gold envelope and placed inside a quartz cell equipped with two KBr windows. In order to monitor the evolution of the spectra in the presence of d-acetonitrile, the quartz cell, interfaced with the spectrophotometer, was directly connected to a vacuum line. Experiments were performed at room temperature at different d-acetonitrile pressures (concentrations). Before dosing d-acetonitrile, the sample was outgassed in high vacuum for 15 min in order to remove N_2 from the glovebox. During outgassing, small amounts of toluene, used as a solvent during the synthesis, were also removed. After d-acetonitrile was dosed, spectra were collected every 5 min for 3 h.

2.3 Results and Discussion

2.3.1 Assessing Catalyst Performance

The Hf/MAO/SiO₂ and Zr/MAO/SiO₂ catalysts were tested in the gas-phase polymerization of ethylene by using pressurized reactors. Under the adopted experimental conditions ($T = 87^\circ\text{C}$, $P_{\text{C}_2\text{H}_4} = 15$ bar, and triisobutylaluminum (TiBA) as scavenger; **Table 2.1**), Zr/MAO/SiO₂ displayed a productivity of about 6300 g of polyethylene (PE) per g of catalyst [$g_{\text{PE}}/(g_{\text{cat}} \cdot \text{h})$], while the Hf/MAO/SiO₂ system displayed a productivity of 150 $g_{\text{PE}}/(g_{\text{cat}} \cdot \text{h})$. The high temperatures and

pressures that were employed during these initial catalytic tests resulted in fast reaction kinetics and high polymer yields (**Table 2.1**, see ethylene uptake profiles in **Figure 2.3**), thereby impeding any studies on the early-stage fragmentation of the two catalyst systems under industrial conditions.

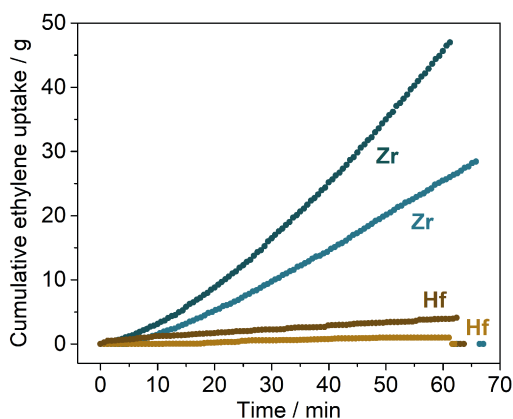


Figure 2.3 Cumulative ethylene uptake in gram (g) during the high-pressure gas-phase polymerization of ethylene over the hafnocene-based and zirconocene-based catalysts under study (two runs per catalyst).

2.3.2 Investigating the Internal Morphologies of Catalyst Particles

In order to obtain low polymer yield samples that are representative for the initial stages of ethylene polymerization (i.e., the pre-polymerization regime), the two catalysts were pre-polymerized in gas-phase under mild conditions (i.e., 1.6 bar C_2H_4 and room temperature; **Table 2.2**). Remarkably, the two catalysts displayed very similar productivities after 60 min of ethylene polymerization under the given pre-polymerization conditions, contrary to the previously mentioned gas-phase polymerization experiments (Hf/MAO/SiO₂: 6.7 g_{PE}/g_{cat} , Zr/MAO/SiO₂: 5.8 g_{PE}/g_{cat} ; **Table 2.2**). By means of FIB cutting according to a procedure from the literature,^[25] the cross-sections of randomly selected catalyst particles were accessed and consequently imaged at nanometer-scale resolution using SEM and IR PiFM. The SEM images were segmented for the improved visualization of the fragmentation process (**Figures 2.4** and **2.5**).

Figures 2.4 and **2.5** show representative cross-sectional SEM images of the Hf/MAO/SiO₂ and Zr/MAO/SiO₂ catalyst materials, respectively, at multiple reaction stages (i.e., pristine as well as after 10, 30 and 60 min of ethylene polymerization). As can be seen in the SEM images of the pristine catalyst particles (**Figures 2.4A** and **2.4A'**, **Figures 2.5A** and **2.5A'**), the spherical support of the particles is constituted by several larger domains of silica that are bound to each other by a phase with a different density, presumably alkali silicate.^[3] Furthermore, the catalyst particles feature numerous macropores that are postulated to be partially connected. This interconnected pore network is highly beneficial for ethylene diffusion into the particle interior, especially in the initial reaction stages.

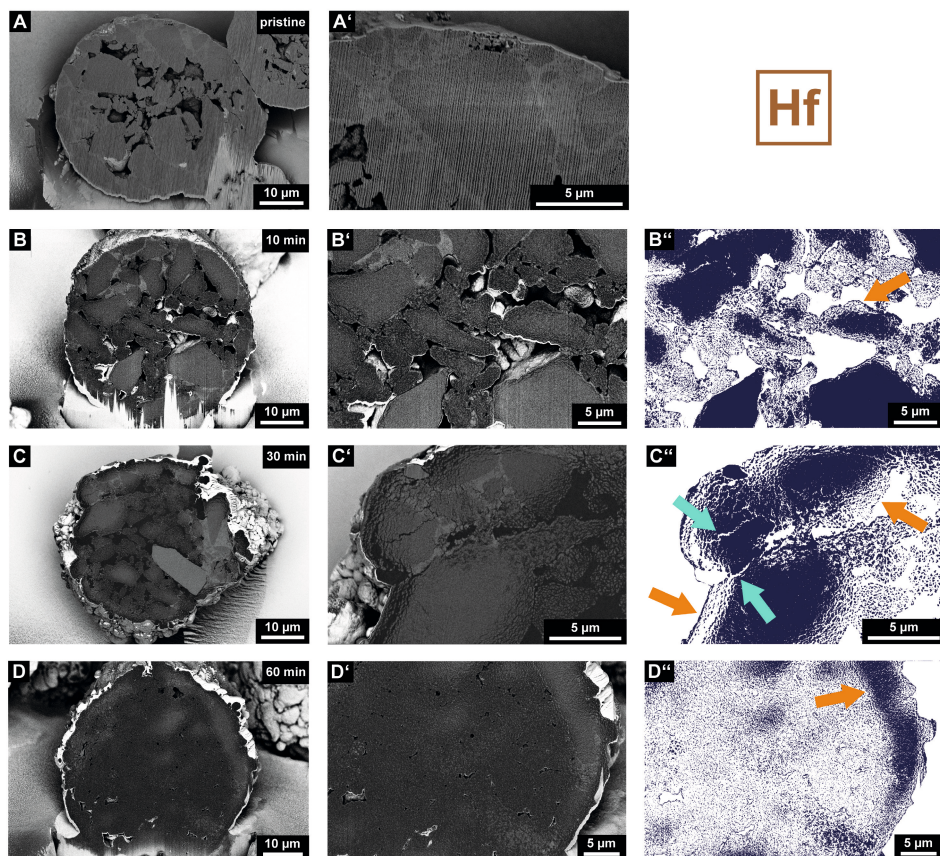


Figure 2.4 Scanning electron microscopy (SEM) images displaying the cross-sections of a pristine (A and A'), 10 min (B and B'), 30 min (C and C') and 60 min (D and D') pre-polymerized particle of the Hf/MAO/SiO₂ catalyst material (with MAO = methylaluminoxane) acquired in backscattered electron mode (BSE; silica support: light gray; polyethylene: dark gray; pores: predominantly black). The close-up images (B', C', and D') were segmented (B'', C'', and D'') to clearly illustrate fragmentation events and the morphology of the particles (silica support is represented in dark blue, layer-by-layer and sectioning pathways are indicated by orange and turquoise arrows, respectively). Vertical lines, which originate from the focused ion beam (FIB) cutting procedure, are visible in certain SEM images.

The segmented SEM images of the 10 min pre-polymerized Hf/MAO/SiO₂ and Zr/MAO/SiO₂ particle cross-sections (**Figures 2.4B–B''**, **Figures 2.5B–B''**) do indeed indicate ethylene polymerization activity in the particle interior. In the case of the Hf/MAO/SiO₂ system, most of the larger constituent silica domains (light gray in the backscattered electron mode, BSE) display mild fragmentation in their outer sphere after 10 min of polymerization (**Figures 2.4B–B''**). The smaller silica domains, on the other hand, feature a more advanced degree of fragmentation that penetrates the entire silica domain. Up to this reaction stage, we assume that gas-phase ethylene can freely diffuse into the internal pore space of the particle and polymerize on all exposed external and internal surface areas of the catalyst particle.

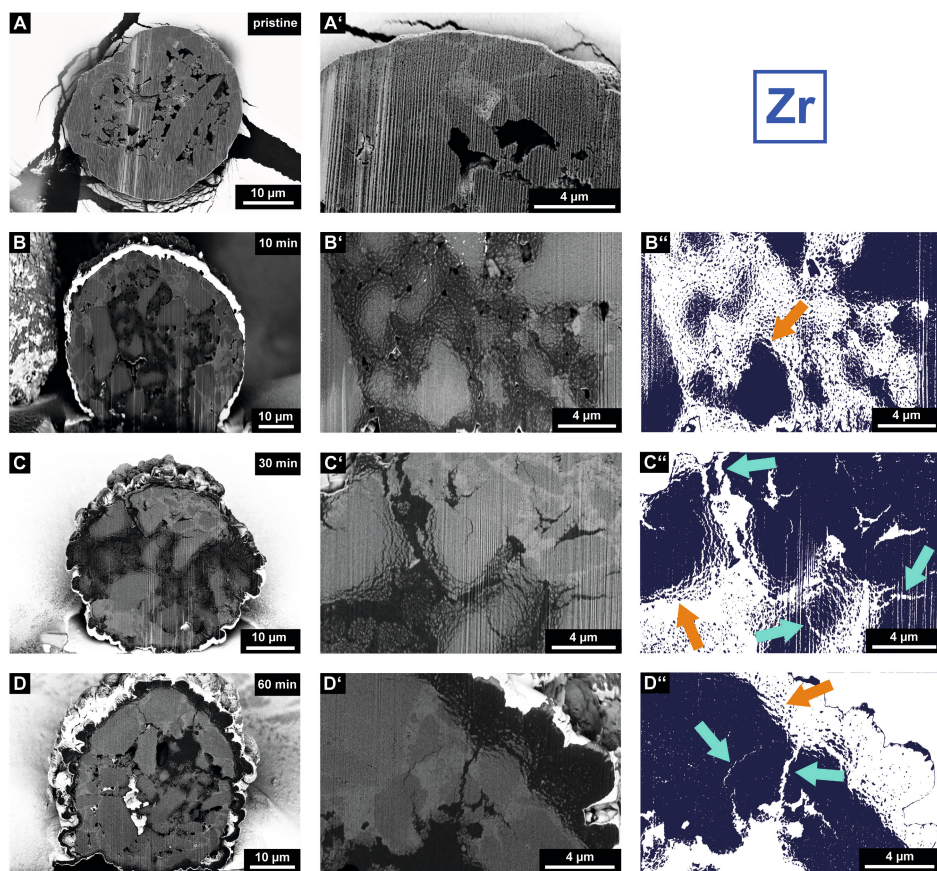


Figure 2.5 Scanning electron microscopy (SEM) images displaying the cross-sections of a pristine (A and A'), 10 min (B and B'), 30 min (C and C') and 60 min (D and D') pre-polymerized particle of the Zr/MAO/SiO₂ catalyst material (with MAO = methylaluminoxane) acquired in backscattered electron mode (BSE; silica support: light gray; polyethylene: dark gray; pores: predominantly black). The close-up images (B', C', and D') were segmented (B'', C'', and D'') to clearly illustrate fragmentation events and the morphology of the particles (silica support is represented in dark blue, layer-by-layer and sectioning pathways are indicated by orange and turquoise arrows, respectively). Vertical lines, which originate from the focused ion beam (FIB) cutting procedure, are visible in certain SEM images.

In general, only a limited amount of PE (dark gray in BSE mode) was formed while large macropores were still clearly visible in the particle. Under given reaction conditions, the individual silica domains seem to fragment according to a layer-by-layer mechanism (indicated by an orange arrow in **Figure 2.4B''**), provided that ethylene gas can access the inner volume of the particle.

Further polymerization evidently leads to a significant decrease in the macropore volume and more pronounced fragmentation. While the 30 min polymerized catalyst particle (**Figures 2.4C–C''**) still features larger isolated fragments of the support in the size range of micrometers, the 60 min polymerized particle (**Figures 2.4D–D''**) is characterized by a high degree of homogeneous support fragmentation. In fact, the cross-section shows nanometer-sized fragments that are finely dispersed in the PE matrix (**Figure 2.4D''**). Remnants of the support in the outer sphere of the catalyst point to an active involvement of the particle interior in the polymerization process, presumably due to the absence of strong mass transfer limitations (**Figure 2.4D''**). While the catalyst has predominantly fragmented according to a layer-by-layer mechanism (**Figures 2.4B''**, **2.4C''** and **2.4D''**; indicated by orange arrows), local diffusion limitations and stress build-up may, to a limited extent, induce the formation of larger cracks in the support matrix at higher PE yields (i.e., sectioning at the support granulate level, indicated by turquoise arrows in **Figure 2.4C''**).

When comparing the Zr/MAO/SiO₂ catalyst system to the Hf/MAO/SiO₂ system, no pronounced differences in catalyst support fragmentation are apparent after 10 min of ethylene polymerization (**Figures 2.5B–B''**). Similar to the Hf/MAO/SiO₂ catalyst material, accessible silica domains begin to fragment according to a layer-by-layer mechanism upon exposure to ethylene (**Figure 2.5B''**, indicated by an orange arrow). Indications of a more heterogeneous fragmentation pathway are, however, observed in the later reaction stages (**Figures 2.5C–C''** and **Figures 2.5D–D''**). In contrast to the Hf/MAO/SiO₂ system, large unfragmented support domains are still visible after 30 min for the Zr/MAO/SiO₂ system (**Figures 2.5C–C''**). Interestingly, the cross-section of the 60 min pre-polymerized particle also features sizeable pristine support domains along with a thick polymer layer that covers the outer surface of the catalyst particles (**Figures 2.5D–D''**). While the layer-by-layer mechanism dominates fragmentation in the early reaction stages at both silica domain and particle level (indicated by orange arrows in **Figure 2.5**), the sectioning mechanism contributes more strongly under the imposed mass transfer limitations at later reaction stages (indicated by turquoise arrows in **Figure 2.5**). With the particle practically enveloped in a growing layer of PE yet still active in certain domains, a significant accumulation of stress in the particle becomes inevitable. This pressure build-up induces ruptures and more pronounced crack formation,^[30] resulting in the cleavage of larger support fragments (indicated by turquoise arrows in **Figures 2.5C''** and **2.5D''**). It must be noted that the outer layers of the catalyst particles in both catalyst systems seem to fragment gradually according to a layer-by-layer mechanism (as indicated by an orange arrow for Zr/MAO/SiO₂ in **Figure 2.5D''**).

To verify our observations, additional particles of the two 60 min pre-polymerized catalysts were investigated (**Figure 2.6**). While most of the particles within a particular batch demonstrated the expected fragmentation behavior, a certain degree of interparticle heterogeneity was nevertheless apparent. A strong correlation between catalyst particle fragmentation and the particle size^[31–33] as well as the dimensions, accessibility, and connectivity of the macro-pore network is expected. This can account for differences in the fragmentation degree and, possibly, the involvement of a particular fragmentation mechanism.

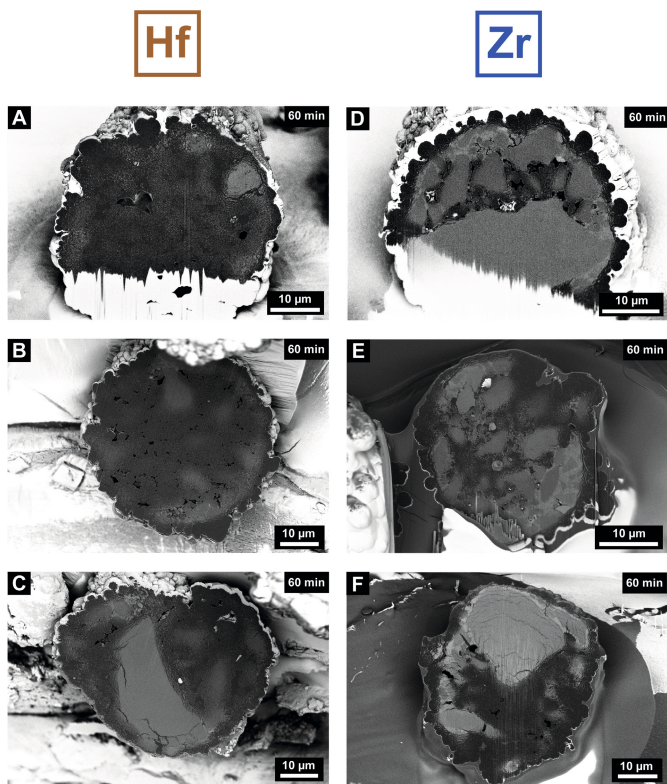


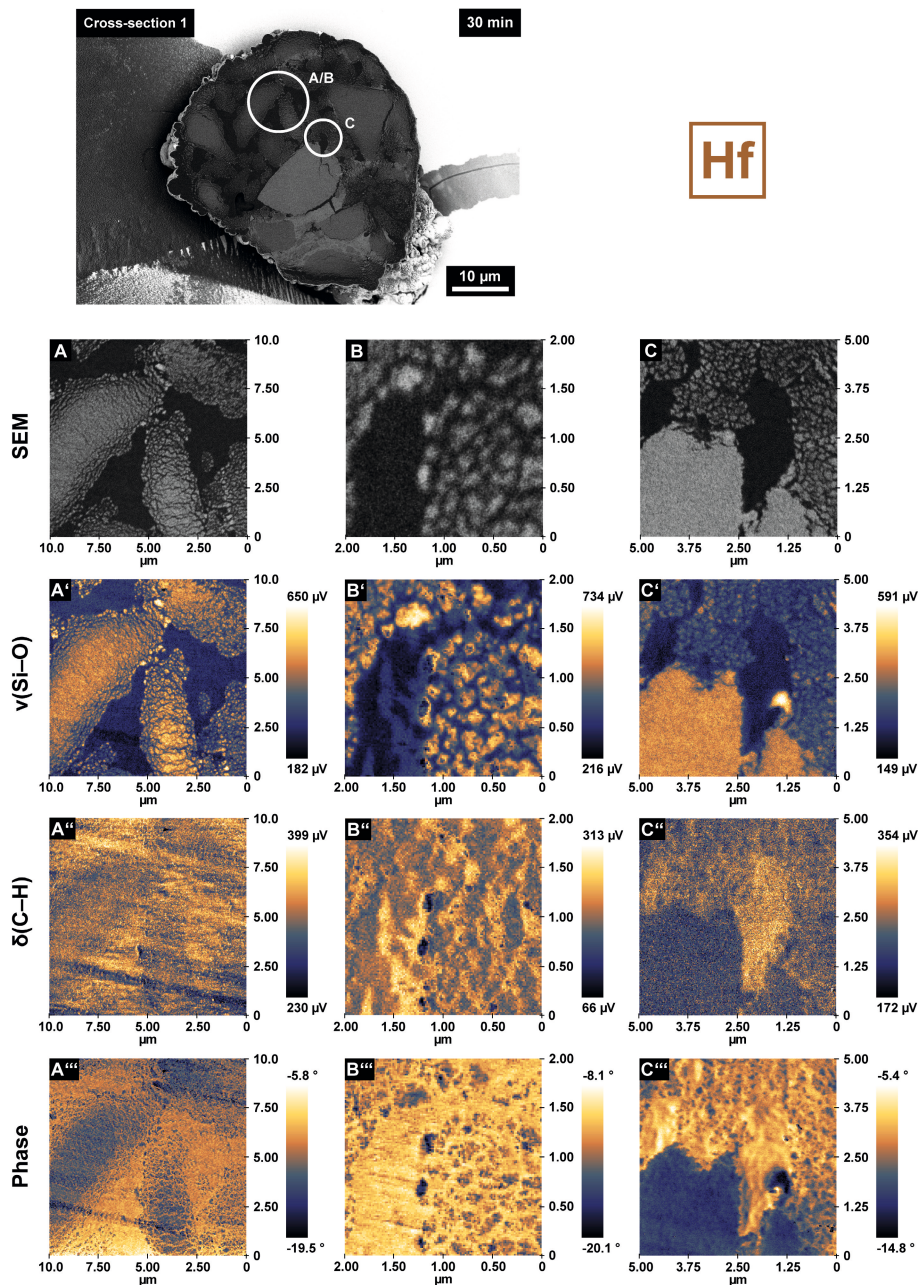
Figure 2.6 Scanning electron microscopy (SEM) images displaying the cross-sections of 60 min pre-polymerized hafnocene-based (A–C) and zirconocene-based (D–F) catalyst particles (1.6 bar C_2H_4 , gas-phase, room temperature).

2.3.3 Examining the Catalyst Composition at a Sub-20 nm Resolution

In principle, the analysis of the SEM images of both catalyst systems (**Figures 2.4, 2.5 and 2.6**), via segmentation into their constituent phases (i.e., PE, silica and pore space), should yield the relative composition of each cross-section. However, the analysis is hampered by (i) the limited number of particles that are assessed per reaction stage; (ii) the 2D nature of the data; (iii) the degree of polymerization, which varies between particles (**Figure 2.6**); and (iv) the detection limit (resolution) of the applied SEM technique. Indeed, at high degrees of polymerization and fragmentation, such as in the 30 min and 60 min pre-polymerized Hf/MAO/SiO₂ cross-sections, a substantial amount of silica fragments remains undetected due to their high dispersion and limited size (nanometer regime).

A nanoscale chemical imaging technique that is arguably better suited to uncovering structural and compositional heterogeneities in our challenging composite materials is IR PiFM. In the field of polymer science and related disciplines, IR PiFM^[34,35] has been used together with atomic force microscopy-infrared spectroscopy (AFM-IR)^[36–40] to characterize multicomponent polymer materials at high spatial resolutions. Inspired by this, we used IR PiFM to characterize the cross-section of a single 30 min pre-polymerized Hf/MAO/SiO₂ particle at multiple locations (**Figures 2.7 and 2.8**). Nanoscale infrared and topographic imaging^[26,27,34,35,41–45] yielded information on both the chemical composition and morphology of the sample at a sub-20 nm resolution.

Figure 2.7 shows correlated SEM images, IR PiFM and phase shift maps collected at different locations on the above-mentioned particle cross-section (the image in panel B was recorded in the same area as panel A but at a higher magnification). The IR PiFM maps were recorded in non-contact mode^[26] (amplitude ratio set point of 80%, attractive van der Waals force regime; **Table 2.3**) at characteristic wavenumbers for the Si–O stretching vibration^[46,47] (maps recorded at single wavenumbers in the range of 1050–1030 cm⁻¹, $\nu(\text{Si-O})$, **Figure 2.7A'–C'**) and the symmetric C–H bending vibration of the methylene group^[37–39] (maps recorded at single wavenumbers in the range of 1472–1460 cm⁻¹, $\delta(\text{C-H})$, **Figure 2.7A''–C''**). The IR PiFM data stand in excellent agreement with the corresponding SEM images and yield a remarkably clear differentiation between the silica and PE phases. Multiple larger domains of the silica support have partially fragmented following the layer-by-layer mechanism. Silica fragments smaller than 50 nm, infused with polymer that was presumably formed upon exposure of new active sites to ethylene gas, can be observed in the periphery of these domains (**Figures 2.7A'** and **2.7B'**). **Figures 2.7C–C''** shows a polymer-rich domain in close proximity to a larger network of cracks in the support (**Figure 2.8**). It is conceivable that the emergence of larger amounts of polymer in this particular area resulted in the accumulation of stress in the support, ultimately inducing the formation of cracks. At the same time, the build-up of stress over the entire particle may have also contributed. Irrespective of the exact formation pathway, the emergence of large, partially unfilled cracks in the pristine support (**Figure 2.8**) exposes new active sites that will consequently contribute to the polymerization and fragmentation of the particle.



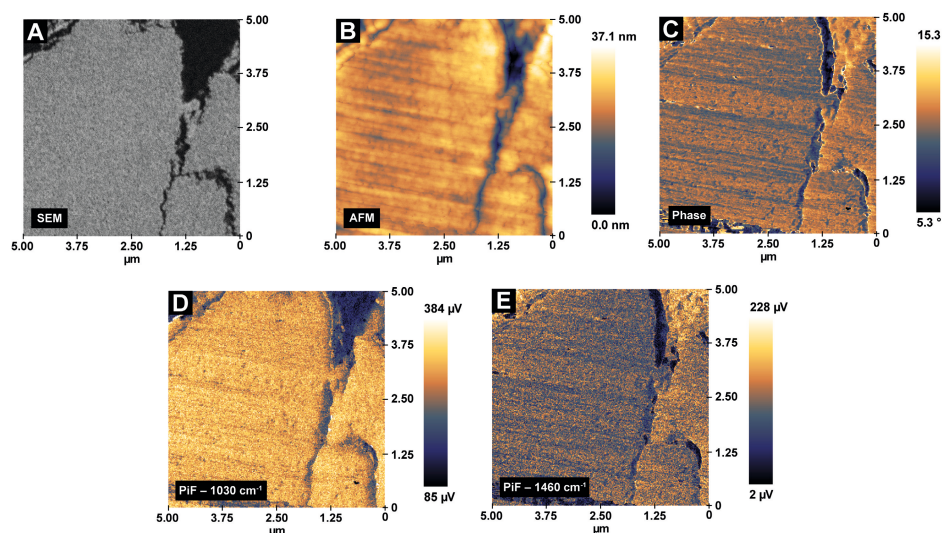


Figure 2.8 Scanning electron microscopy (SEM; A), topography (atomic force microscopy, AFM; B), phase shift (C) and infrared photoinduced force microscopy (IR PiFM, $\nu(\text{Si-O})$: 1030 cm^{-1} and $\delta(\text{C-H})$, 1460 cm^{-1} ; D, E) images recorded on a single area of a 30 min pre-polymerized hafnocene-based catalyst particle cross-section (in close vicinity to measurement area shown in Figures 2.7C–C’’, set point amplitude ratio = 81%). The presence of a partially empty network of cracks in the silica support is discernible.

Interestingly, the phase shift maps in **Figures 2.7A’’–C’’** display a striking amount of detail, revealing a complex network of overlapping, thread-like PE domains in close vicinity to the formed fragments. In general, the phase channel represents a promising complementary imaging tool^[48,49] due to its correlation with mechanical material properties. It corresponds to the absolute difference in phase between the external excitation (driver) and the tip response and is governed by the dissipation of energy from the tip to the sample.^[44] This energy dissipation is strongly affected by mechanical material properties such as stiffness, adhesion and viscoelasticity.^[50–52] In general, the set point and drive amplitude of the cantilever must be optimized to obtain qualitative insights into the mechanical properties of a given material.^[53,54] In our case, phase maps were recorded at a set point of 60% and 3 nm drive amplitude to enhance the tip-sample contact^[26] (hard tapping regime, repulsive interactions dominant; **Table 2.3**).

As is evident from **Figures 2.7A’’–C’’**, higher phase shift values were obtained for PE, hereby indicating a lower repulsion of the tip from the polymer-rich domains relative to the silica fragments. This is assumed to be a result of the lower mechanical stiffness and higher viscoelasticity of the PE phase. The overall negative phase shift values result from the net repulsive and dissipative force experienced during heavy tapping (**Table 2.3**).

Point spectra, recorded of PE- and silica-rich regions (**Figure 2.9**) as well as reference materials (**Figure 2.10**), further helped to unambiguously assign the imaged phases. Due to the high degree of intermixing of silica and PE, it was not possible to acquire point spectra of pure PE on the pre-polymerized catalyst cross-section. Furthermore, the PE phase displayed high sensitivity towards the incident IR laser beam. As can be seen in **Figure 2.10**, its partial degradation, upon prolonged exposure to the laser beam, was apparent from the emergence of new bands in the IR point spectrum. The bands at around 924 cm^{-1} and 1594 cm^{-1} can be linked to $\delta(\text{C}=\text{C}-\text{H})^{[55]}$ and $\nu(\text{C}=\text{C})^{[55-58]}$ while the band at 1376 cm^{-1} can be assigned to methyl groups^[55,57]. This suggests that a scission of the polymer chains can occur over time.

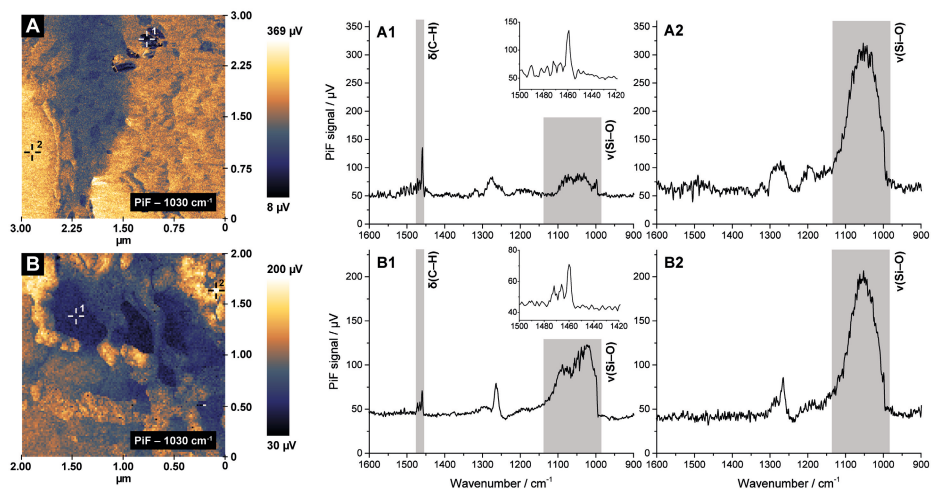


Figure 2.9 Infrared photo-induced force microscopy (IR PiFM) maps of two different areas of the 30 min pre-polymerized hafnocene-based catalyst particle cross-section recorded at 1030 cm^{-1} [$\nu(\text{Si}-\text{O})$]. Point spectra (A1, A2, B1 and B2) that were taken at the locations indicated in the IR maps feature vibrational bands of polyethylene (PE) and silica (SiO_2). A 2nd-order Savitzky-Golay filter (5 points) was applied to decrease the level of background noise in the acquired spectra.

Despite this, IR PiFM proved to be suitable for the detection and differentiation of pristine and fragmented support domains, the bulk polymer phase, and related composite phases at an unparalleled spatial resolution ($< 20\text{ nm}$), while also yielding insights into fragmentation events and the associated release of buried active sites.

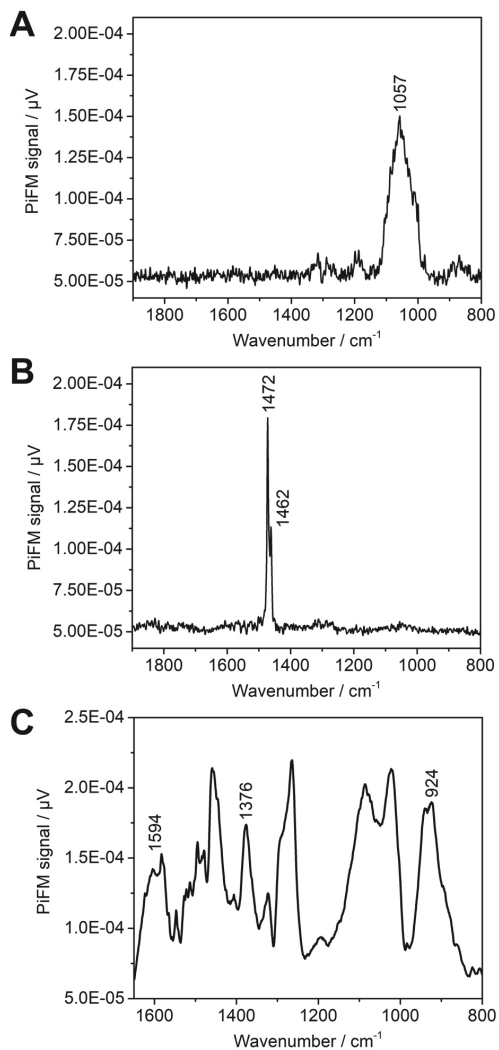


Figure 2.10 Infrared (IR) point spectrum recorded with infrared photoinduced force microscopy (IR PiFM) on the horizontal cross-section of a pristine hafnocene-based catalyst particle (A), a high-density polyethylene (PE) bead (Sigma-Aldrich, B), and on a PE/SiO₂ composite damaged by the IR laser (C). A 2nd-order Savitzky-Golay filter (20 points) was applied to decrease the level of background noise in spectrum C.

2.3.4 Probing the Kinetics of Insertion into the Metal–Methyl Bond

To elucidate the reasons for the different fragmentation behavior of the two catalyst systems and their similar productivities under pre-polymerization conditions, we designed a series of FTIR spectroscopy experiments in the presence of acetonitrile as a probe molecule. FTIR spectroscopy of adsorbed probes is one of the most sensitive methods to retrieve information on the properties of surface sites and has been largely used to characterize heterogeneous catalysts at a molecular level.^[59,60] This also applies to heterogeneous olefin polymerization catalysts such as the Phillips^[61,62] and Ziegler-Natta^[63–66] catalysts. Owing to its mildly basic character, CO is often used as a molecular probe to differentiate between sites based on their acidity. Previous works demonstrated that CO at 100 K is indeed able to probe Lewis acid sites (LAS) belonging to MAO/TMA in metallocene/MAO/SiO₂ catalyst materials, while it has more difficulty reaching the metallocene cations.^[67–69] By being inserted into metal alkyl bonds, CO can also form acyl species.^[70] Furthermore, CO has traditionally been used to quantify the number of active sites in olefin polymerization catalysts.^[71–77]

In this work, acetonitrile was chosen as a probe molecule over CO due to its comparatively higher basicity.^[78–83] Hence, it is better suited to probing metal cations. More importantly, acetonitrile can also insert into transition metal alkyl bonds to form aza-alkenylidenes, as has been demonstrated for different cationic titanium and zirconium complexes.^[84–87] By using acetonitrile as a probe molecule, the acidity and number of the active sites and their ability to insert electron-rich molecules can be assessed simultaneously. All are critical factors in the context of olefin polymerization. It is important to note that the insertion of acetonitrile into the metal alkyl bond is not affected by diffusion limitations (related to the build-up of polymer at the particle surface). Therefore, the insertion rates evaluated by this method provide direct insights into the inherent insertion ability of the active sites. To the best of our knowledge, there are no similar reports in the open literature on the use of acetonitrile as probe or insertion molecule for silica-supported metallocene-based catalyst materials.

The insertion rate of acetonitrile and thus the reactivity of the Hf/MAO/SiO₂ and Zr/MAO/SiO₂ catalyst materials was determined by means of time-resolved FTIR spectroscopy. A blank experiment was also conducted on a MAO/SiO₂ material for comparison. Deuterated acetonitrile (d-ACN) was used in order to overcome band doubling due to Fermi resonance effects.^[79] As a consequence of its interaction with the LAS sites, the $\nu(\text{C}=\text{N})$ vibrational mode is expected to increase in energy with respect to the vibrational mode of the free molecule (2265 cm⁻¹). This shift is proportional to the strength of the Lewis acid-base couple. Moreover, the $\nu(\text{C}=\text{N})$ vibration of the aza-alkenylidene species is expected to feature in another well-defined spectral region (1720–1600 cm⁻¹), without overlapping with the bands of chemisorbed d-ACN. **Figure 2.11** shows the sequence of FTIR spectra for MAO/SiO₂, Hf/MAO/SiO₂ and Zr/MAO/SiO₂ upon exposure to d-ACN over a period of 3 h in the spectral region of 2400–1300 cm⁻¹. The insets show a magnification of the same spectra in the 1720–1600 cm⁻¹ range to highlight the bands assigned to the Zr and Hf aza-alkenylidene species (spectra are reported after the subtraction of the spectrum collected before the introduction of d-ACN).

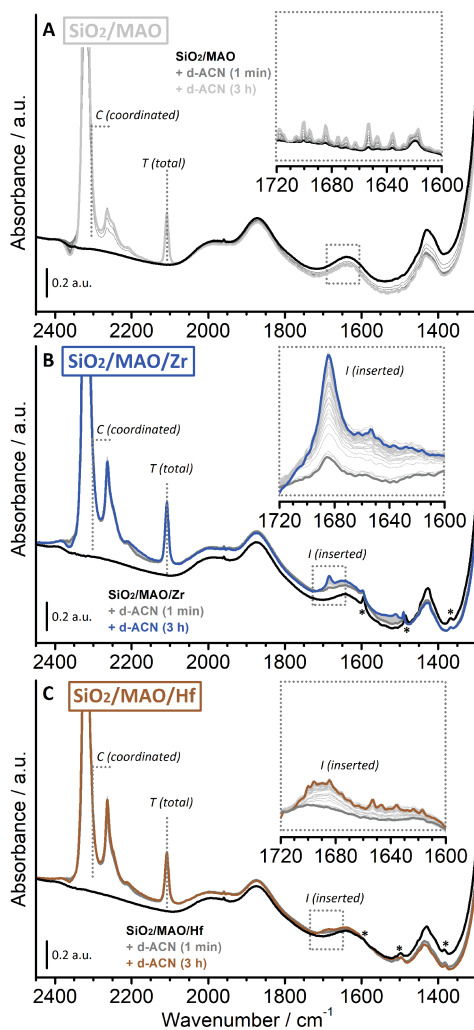


Figure 2.11 Fourier-transform infrared (FTIR) spectra recorded of the methylaluminoxane (MAO)/ SiO_2 reference material before (black) and after (gray) interaction with d-acetonitrile (d-ACN) at room temperature over a time period of 3 h (light gray) (A). The inset shows the 1720–1600 cm^{-1} region for the same sequence of FTIR spectra after subtraction of the spectrum collected prior to the introduction of d-ACN. Comparable FTIR spectra are also shown for the Zr/MAO/ SiO_2 (B) and Hf/MAO/ SiO_2 (C) catalyst materials. The bands labelled with asterisks (*) are attributed to vibrations of the indenyl ligands in Zr/MAO/ SiO_2 and Hf/MAO/ SiO_2 , respectively.

The initial spectra of the MAO/SiO₂, Zr/MAO/SiO₂ and Hf/MAO/SiO₂ catalyst materials (black in **Figure 2.11**) are very similar to each other and are dominated by the vibrational features of silica. In addition to these, a limited number of low intensity bands can be observed. The bands at 1500–1350 cm⁻¹ are assigned to the bending vibrational modes of CH₃ groups belonging to MAO (i.e., Al–CH₃ species), Si–CH₃, or Si–O–Al(CH₃)₂ species, which might originate from the reaction of MAO/TMA with siloxane bridges at the silica surface. According to Ystenes *et al.*^[88], the $\delta_{\text{asym}}(\text{CH}_3)$ vibrations of terminal Al–CH₃ in MAO are expected to appear at approximately 1435 cm⁻¹, while the corresponding $\delta_{\text{sym}}(\text{CH}_3)$ vibrational mode is expected to appear at around 1300 cm⁻¹. The latter is hence not detectable due to the broad and intense modes of SiO₂, which dominate the spectral region below 1350 cm⁻¹. The $\delta_{\text{asym}}(\text{CH}_3)$ mode of –OCH₃ species is expected to contribute at around 1470 cm⁻¹,^[88] but is barely identifiable in our spectra (low intensity and broad band). Finally, the very weak and narrow bands labeled with asterisks are attributed to the vibrations of the indenyl ligands in the activated zirconocene and hafnocene complexes.

In all cases, several intense absorption bands immediately appeared in the 2400–2000 cm⁻¹ region upon introduction of d-ACN, which are discussed as follows:

- i. The absorption band at 2108 cm⁻¹ (indicated as *T*, *total* in **Figure 2.11**) is due to $\nu(\text{CD}_3)$. This band is insensitive to the absorption sites^[80] and thus not analytically relevant. It will therefore be used as an internal standard to quantify the total amount of d-ACN on the sample, comprising d-ACN coordinated to the LAS sites (belonging to both MAO/TMA and the methylated metallocenes) and physisorbed d-ACN. The concentration of d-ACN in the sample depends on both the equilibrium pressure and the sample mass, the latter being difficult to evaluate due to the complexity of the experimental procedure.
- ii. In the $\nu(\text{C}=\text{N})$ region (2400–2200 cm⁻¹), all spectra are dominated by an intense and symmetric absorption band centered at 2320 cm⁻¹ (i.e., upward shifted by 55 cm⁻¹ with respect to free d-ACN at 2265 cm⁻¹), which is due to the interaction of d-ACN with LAS sites. The band accounts for both the LAS sites of MAO/TMA species and the Zr or Hf cations (for comparison, d-ACN adsorbed on coordinatively unsaturated Al(III) sites on a triethylaluminum (TEAL)-pre-treated SiO₂ features a band at 2317 cm⁻¹).^[89] We expect that the MAO/TMA species are predominantly probed by d-ACN because of their much higher relative content in the two samples (Al/M = 150). Since the associated band rapidly goes out of scale, the total amount of accessible LAS sites was derived from the spectral intensity at 2300 cm⁻¹ for each experiment (indicated as *C*, *coordinated*, in **Figure 2.11**).
- iii. A second absorption band was observed in the same spectral region at 2265 cm⁻¹, with a shoulder at around 2250 cm⁻¹. The former is ascribed to liquid-like d-ACN and is the only absorption band that decreases in intensity upon degassing (not shown).^[90] The assignment of the shoulder is more challenging. The low frequency of the $\nu(\text{C}=\text{N})$ band suggests a bridging coordination mode, as has been observed for other ligands and suggested for nitriles in interaction with two cations in zeolites.^[91] The appearance of this absorption band indicates the presence of LAS sites that are close enough to each other to be simultaneously complexed by both the nitrogen lone pair and the π -type

bonding electrons of the same acetonitrile molecule. A similar absorption band was also observed for d-ACN adsorbed on a Cr(II)/SiO₂ Phillips catalyst material activated with TEAL and attributed to a Cr(II)···Al(III) bimetallic species.^[89]

- iv. In the presence of d-ACN, the Zr/MAO/SiO₂ (**Figure 2.11B**) and Hf/MAO/SiO₂ (**Figure 2.11C**) catalyst materials feature additional weak absorption bands that appear in the 1700–1300 cm⁻¹ spectral region and slowly grow in intensity over time. In particular, two well-defined absorption bands appear at 1684 cm⁻¹ and 1690 cm⁻¹ for the Zr/MAO/SiO₂ and Hf/MAO/SiO₂ catalyst materials, respectively (labeled as band *I*, *inserted*; **Figures 2.11B** and **2.11C**). These absorption bands are attributed to the ν(C=N) of an aza-alkenyldiene species that is formed due to the insertion of d-ACN into the Zr-CH₃ and Hf-CH₃ bonds (**Figure 2.1B**). At the same time, all the absorption bands ascribed to the activated metallocene complexes (asterisks) were perturbed. For example, the absorption bands of Zr/MAO/SiO₂ at 1593 cm⁻¹ and 1485 cm⁻¹ are upward shifted by a few inverse centimeters, while the absorption band at 1370 cm⁻¹ has decreased in intensity. Altogether, this suggests that the coordination modes of the indenyl ligand are changing concomitantly to the coordination of d-ACN to the Zr or Hf cation and its subsequent insertion into the metal alkyl bond.

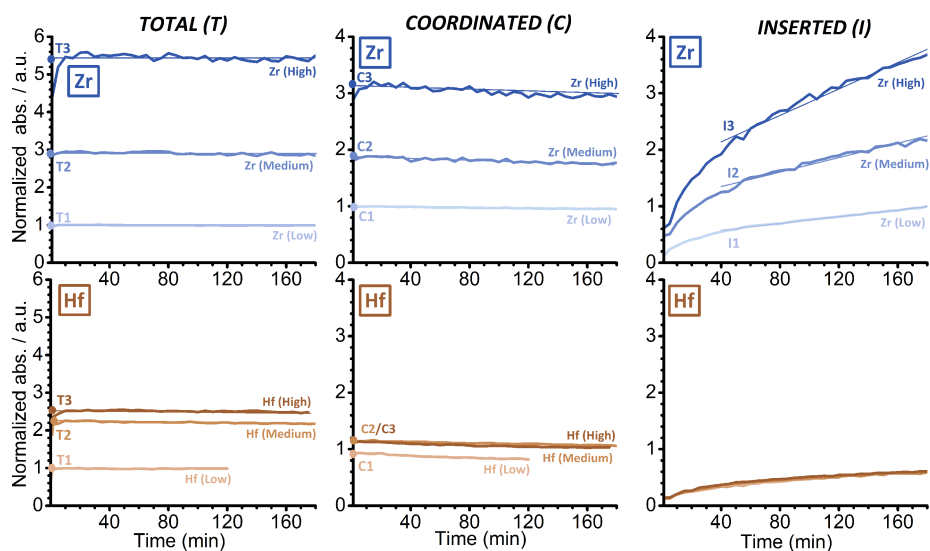


Figure 2.12 Evolution of the intensities of the Fourier-transform infrared (FTIR) absorption bands *T* (total amount of d-ACN), *C* (coordinated d-ACN) and *I* (inserted d-ACN) as a function of time, derived from a series of experiments in which Zr/MAO/SiO₂ (top) and Hf/MAO/SiO₂ (bottom) were treated with d-ACN at three different concentrations (High, Medium, and Low) (MAO= methylaluminoxane). The data were normalized to the optical thickness of the pellets and rescaled with respect to the Zr (Low) experiment for comparison.

In fact, the two absorption bands at 1684 cm^{-1} and 1690 cm^{-1} , which are ascribed to the Zr and Hf aza-alkenylidene species respectively, grow at different rates. A significantly faster increase was observed for the Zr/MAO/SiO₂ system in comparison to the Hf/MAO/SiO₂ system. Interestingly, the rate of insertion of d-ACN in the M-CH₃ bond correlates well with the catalyst productivity in ethylene polymerization, as determined by the previously mentioned gas-phase experiments (15 bar ethylene, 87 °C), and not with those determined from the relatively mild pre-polymerization experiments. Based on the literature,^[19–21] our experimental observations may be explained by both: (1) a lower number of active species in the Hf/MAO/SiO₂ catalyst material due to the formation of stable heterodinuclear compounds with TMA, and (2) a different inherent insertion ability of the electron-rich d-ACN in the M-CH₃ bonds in the two catalysts.

To clarify the reasons behind the different behaviors of the two structurally analogous catalysts, a series of FTIR spectroscopy experiments with different d-ACN concentrations, similar to those discussed in **Figure 2.11**, were conducted. In total, three experiments were performed for each catalyst (High, Medium and Low d-ACN concentration). Some of the experiments were repeated to verify the reproducibility of the results. In all experiments, the intensities of the bands *T* (total amount of d-ACN), *C* (coordinated d-ACN) and *I* (inserted d-ACN) were monitored as a function of time (**Figure 2.12**, after normalization to the optical pellet thickness and rescaled to the Zr (Low) experiment for comparison).

For both the Zr/MAO/SiO₂ system and the Hf/MAO/SiO₂ system, the *T* and *C* bands almost immediately reach their maximum intensity (left and middle in **Figure 2.12**, respectively), irrespective of the d-ACN concentration. Based on this, we conclude that there are no intrinsic diffusion limitations. The *C* bands, on the other hand, slightly decrease in intensity over time due to the gradual insertion of coordinated d-ACN into the M-CH₃ bond. The maximum intensities of the *T* and *C* bands were determined by extrapolating the linear part at time zero ($t = 0$) and are reported in **Figure 2.13**. In contrast to these, band *I* (right in **Figure 2.12**) grew at an almost constant rate after the first 30 min, and did not saturate even after 3 h of reaction. This observation is in agreement with the very slow insertion kinetics of d-ACN in other zirconocene and hafnocene complexes, as reported in the literature.^[84–87] The insertion rate was derived from the slope of a linear fit that was applied to the curves and can also be found in **Figure 2.13**.

For the Zr/MAO/SiO₂ system, the amount of coordinated d-ACN was found to depend on the total d-ACN concentration (**Figures 2.12 and 2.13**): The higher the concentration or pressure of the electron-rich probe, the higher the fraction of the sites able to coordinate it (comprising both the LAS sites of MAO/TMA and the zirconocene cations). This correlation, however, was not linear: A threefold increase in the total concentration (from T1 to T2) led to twice the amount of coordinated d-ACN (from C1 to C2), while a further twofold increase (from T2 to T3) only resulted in 1.6 times the number of coordinated species (from C2 to C3). Interestingly, the d-ACN insertion rates scale perfectly with the fraction of sites able to coordinate d-ACN, i.e., *I* increases by a factor of 2 from I1 to I2 and by a factor of 1.7 from I2 to I3.

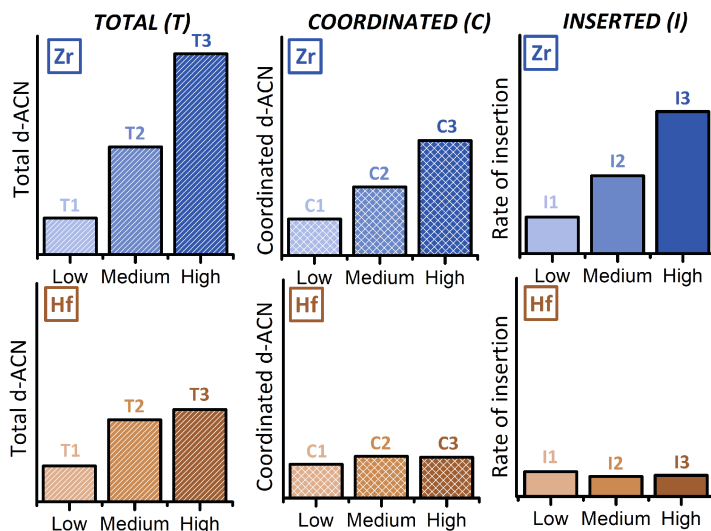


Figure 2.13 For each of the experiments reported in Figure 2.12, the maximum intensity of the Fourier-transform infrared (FTIR) bands T and C was determined by extrapolating the linear part of the curves (indicated as T_n and C_n , where $n = 1, 2, 3$ refers to the experiments at low, medium and high d-ACN concentration). The insertion rate was derived from the slope of the linear part of the I curves (I_n , with $n = 1, 2$ and 3).

Contrary to the Zr/MAO/SiO₂ system, the intensities of the three bands T, C and I in the Hf/MAO/SiO₂ system rapidly reached a saturation level (Figures 2.12 and 2.13). Moreover, for comparable d-ACN total concentrations (T), the amount of coordinated d-ACN CAN was lower for Hf/MAO/SiO₂ than for Zr/MAO/SiO₂. This difference became more pronounced at higher d-ACN concentrations. The data stand in agreement with the reported detrimental effect of MAO/TMA on hafnocene complexes, relative to comparable zirconocene complexes.^[20,21] However, this only partly explains the lower insertion rate for the Hf/MAO/SiO₂ system. A comparison of the experiments performed on the two catalysts at low d-ACN concentrations (T1) revealed that the number of sites coordinating d-ACN (C1) in the Hf/MAO/SiO₂ system correspond to 90% of those found in the Zr/MAO/SiO₂ system, while the insertion rate (I1) is only 75% of that observed for the Zr/MAO/SiO₂ system. These findings indicate that the insertion kinetics of d-ACN in the Hf/MAO/SiO₂ system are inherently slower than in the Hf/MAO/SiO₂ system. As recently suggested,^[19] this is explained by the more pronounced ionic character of the Hf–C bond compared to the Zr–C bond, and, consequently, the larger enthalpic contribution to the activation barrier of the Hf–C bond cleavage.

As a final comment, the limited amount of d-ACN that can adsorb on Hf/MAO/SiO₂ (i.e., T and C signals do not increase significantly when moving to a high d-ACN concentration) might be also explained by a filling of the pore channels that facilitate the diffusion of d-ACN. This hypothesis is compatible with the above discussed theory on stable heterodinuclear compounds that are formed with TMA.

2.3.5 Correlating Data from Different Length Scales

Based on the time-resolved FTIR data, which collected in the presence of d-acetonitrile, we conclude that the insertion kinetics of the Zr/MAO/SiO₂ catalyst material are notably faster compared to those of the Hf/MAO/SiO₂ catalyst material. This is mainly due to the following two reasons: (i) The active sites are more accessible (i.e., less stable hetero-dinuclear compounds with TMA) in Zr/MAO/SiO₂, and (ii) the active sites are intrinsically faster. According to the FIB-SEM and IR PiFM data, the faster kinetics of the Zr/MAO/SiO₂ catalyst material result in the build-up of large amounts of PE at the particle surface as well as in any accessible pores. The imposed diffusion limitations restrict the access of ethylene molecules to the particle interior, thereby limiting polymerization and concurrent fragmentation under the given experimental conditions. In contrast to this, the kinetically slower Hf/MAO/SiO₂ catalyst system seems to be less affected by diffusion limitations, which is manifested in a more homogeneous fragmentation of the catalyst support.

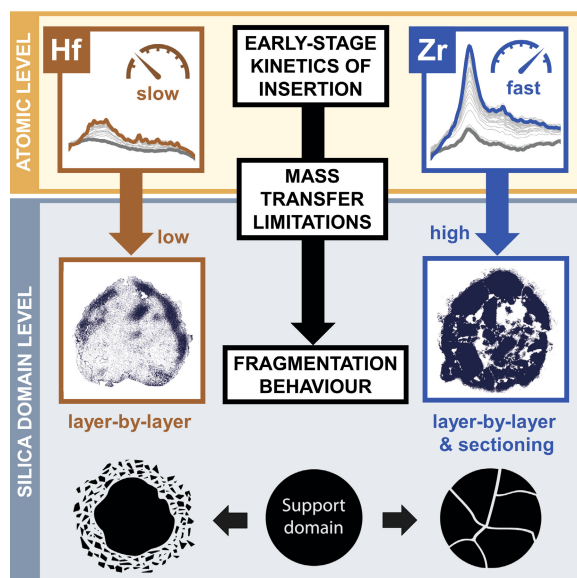


Figure 2.14 Schematic illustration of the main insights gained from the multiscale microscopy-spectroscopy approach described in this Chapter. Insertion kinetics and associated mass transfer limitations are critical for the homogeneity of catalyst support fragmentation during the early stages of ethylene polymerization over metallocene-based catalysts.

This hypothesis is also reflected by the unexpectedly low PE yield of the kinetically superior Zr/MAO/SiO₂ catalyst in comparison to that of the Hf/MAO/SiO₂ catalyst under pre-polymerization conditions, i.e., 5.8 g_{PE}/g_{cat} vs. 6.7 g_{PE}/g_{cat} (**Table 2.2**). In fact, low PE yields, which are linked with the build-up of polymer at the particle surface and thus mass transfer limitations, have also recently been reported by Zanoni *et al.*^[9] for a comparable silica-supported zirconocene during gas-phase ethylene polymerization at 9 bar and 15 bar.

2.4 Conclusions

The developed multiscale combined microscopy and spectroscopy approach, which is based on focused ion beam-scanning electron microscopy (FIB-SEM), infrared photoinduced force microscopy (IR PiFM), and time-resolved IR spectroscopy of adsorbed d-acetonitrile (d-ACN), delivered new mechanistic insights into the early-stage fragmentation of two structurally analogous, silica-supported bridged bis-indenyl metallocene catalysts, pre-activated with methylaluminoxane (MAO) as co-catalyst (M/MAO/SiO₂, M = Hf/Zr). The two catalyst materials displayed different catalytic performances and kinetic profiles during the gas-phase polymerization of ethylene.

As summarized in **Figure 2.14**, insertion kinetics and associated mass transfer limitations were identified as being critical for the homogeneity of catalyst support fragmentation during early reaction stages of ethylene polymerization. In the absence of strong mass transfer limitations that are imposed by the surface build-up of polyethylene as well as pore filling, the individual support domains disintegrate more uniformly according to a layer-by-layer mechanism, as was observed for the kinetically slower Hf/MAO/SiO₂ catalyst material. Stronger mass transfer limitations, as evident for the faster Zr/MAO/SiO₂ catalyst material, significantly inhibit or delay fragmentation during the initial reaction stages of ethylene polymerization under the given experimental conditions. This is postulated to induce higher stress accumulation and thus a larger contribution from the sectioning mechanism at the level of the individual silica domains and, possibly, at the particle level.

Time-resolved IR spectroscopy in the presence of d-ACN provided an explanation for the different experimentally observed insertion kinetics. Not only are the active sites of Hf/MAO/SiO₂ less accessible (due to more stable heterodinuclear adducts with TMA), they are also intrinsically slower than the active sites of Zr/MAO/SiO₂. It is worth noticing that these conclusions are in agreement with theoretical and experimental data reported in the literature. This unprecedented spectroscopic approach can also be applied to similar catalysts to evaluate their accessibility and insertion behavior.

The correlated FIB-SEM-IR PiFM approach, on the other hand, delivered highly resolved morphological information and facilitated the spectroscopic identification of support, polymer, and composite phases. It represents a novel analytical approach that can also be extended to other industrial-grade catalysts for obtaining information on structure, chemical composition, and mechanical parameters at unparalleled spatial resolutions and, in the case of full catalyst particles, at variable probing depths via FIB cutting.

Acknowledgments

Derek Nowak (Molecular Vista Inc.) is gratefully acknowledged for his advice on the IR PiFM method.

References

1. J. R. Severn, J. C. Chadwick, R. Duchateau, N. Friederichs, *Chem. Rev.* **2005**, *105*, 4073–4147.
2. J. B. P. Soares, T. F. L. McKenna, *Polyolefin Reaction Engineering*, Wiley-VCH, Weinheim, **2012**.
3. G. Fink, B. Steinmetz, J. Zechlin, C. Przybyla, B. Tesche, *Chem. Rev.* **2000**, *100*, 1377–1390.
4. G. Fink, B. Tesche, F. Korber, S. Knoke, *Macromol. Symp.* **2001**, *173*, 77–87.
5. B. Horáčková, Z. Grof, J. Kosek, *Chem. Eng. Sci.* **2007**, *62*, 5264–5270.
6. F. Machado, E. L. Lima, J. C. Pinto, T. F. McKenna, *Polym. Eng. Sci.* **2010**, *51*, 302–310.
7. K. W. Bossers, R. Valadian, S. Zaroni, R. Smeets, N. Friederichs, J. Garrevoet, F. Meirer, B. M. Weckhuysen, *J. Am. Chem. Soc.* **2020**, *142*, 3691–3695.
8. K. W. Bossers, R. Valadian, J. Garrevoet, S. van Malderen, R. Chan, N. Friederichs, J. Severn, A. Wilbers, S. Zaroni, M. K. Jongkind, B. M. Weckhuysen, F. Meirer, *JACS Au* **2021**, *1*, 852–864.
9. S. Zaroni, N. Nikolopoulos, A. Welle, A. Vantomme, B. M. Weckhuysen, *Catal. Sci. Technol.* **2021**, *11*, 5335–5348.
10. G. Weickert, G. B. Meier, J. T. M. Pater, K. R. Westerterp, *Chem. Eng. Sci.* **1999**, *54*, 3291–3296.
11. T. F. McKenna, J. B. P. Soares, *Chem. Eng. Sci.* **2001**, *56*, 3931–3949.
12. L. L. Böhm, *Angew. Chem. Int. Ed.* **2003**, *42*, 5010–5030.
13. T. McKenna, V. Mattioli, *Macromol. Symp.* **2001**, *173*, 149–162.
14. T. F. L. McKenna, A. Di Martino, G. Weickert, J. B. P. Soares, *Macromol. React. Eng.* **2010**, *4*, 40–64.
15. L. Resconi, L. Cavallo, A. Fait, F. Piemontesi, *Chem. Rev.* **2000**, *100*, 1253–1345.
16. J. A. Ewen, L. Haspelslagh, H. Zhang, J. L. Atwood, *J. Am. Chem. Soc.* **1987**, *109*, 6544–6545.
17. B. Rieger, C. Troll, J. Preuschen, *Macromolecules* **2002**, *35*, 5742–5743.
18. A. Laine, M. Linnolahti, T. A. Pakkanen, J. R. Severn, E. Kokko, A. Pakkanen, *Organometallics* **2010**, *29*, 1541–1550.
19. M. R. Machat, A. Fischer, D. Schmitz, M. Vöst, M. Drees, C. Jandl, A. Pöthig, N. P. M. Casati, W. Scherer, B. Rieger, *Organometallics* **2018**, *37*, 2690–2705.
20. V. Busico, R. Cipullo, R. Pellecchia, G. Talarico, A. Razavi, *Macromolecules* **2009**, *42*, 1789–1791.
21. C. Ehm, R. Cipullo, P. H. M. Budzelaar, V. Busico, *Dalt. Trans.* **2016**, *45*, 6847–6855.
22. G. B. Meier, G. Weickert, W. P. M. van Swaaij, *J. Polym. Sci. Part A Polym. Chem.* **2001**, *39*, 500–513.
23. M. Namkajorn, A. Alizadeh, E. Somsook, T. F. L. McKenna, *Macromol. Chem. Phys.* **2014**, *215*, 873–878.
24. A. R. Martins, A. J. Cancelas, T. F. L. McKenna, *Macromol. React. Eng.* **2017**, *11*, 1600011.
25. D. A. M. De Winter, F. Meirer, B. M. Weckhuysen, *ACS Catal.* **2016**, *6*, 3158–3167.
26. R. A. Murdick, W. Morrison, D. Nowak, T. R. Albrecht, J. Jahng, S. Park, *Jpn. J. Appl. Phys.* **2017**, *56*, 08LA04.
27. D. Nowak, W. Morrison, H. K. Wickramasinghe, J. Jahng, E. Potma, L. Wan, R. Ruiz, T. R. Albrecht, K. Schmidt, J. Frommer, D. P. Sanders, S. Park, *Sci. Adv.* **2016**, *2*, e1501571.
28. F. Huth, A. Govyadinov, S. Amarie, W. Nuansing, F. Keilmann, R. Hillenbrand, *Nano Lett.* **2012**, *12*, 3973–3978.
29. H. A. Bechtel, S. C. Johnson, O. Khatib, E. A. Muller, M. B. Raschke, *Surf. Sci. Rep.* **2020**, *75*, 100493.
30. Z. Grof, J. Kosek, M. Marek, *AIChE J.* **2005**, *51*, 2048–2067.
31. V. F. Tisse, F. Prades, R. Briquel, C. Boisson, T. F. L. McKenna, *Macromol. Chem. Phys.* **2010**, *211*, 91–102.
32. T. Taniike, T. Funako, M. Terano, *J. Catal.* **2014**, *311*, 33–40.
33. M. A. Bashir, V. Monteil, C. Boisson, T. F. L. McKenna, *AIChE J.* **2017**, *63*, 4476–4490.
34. K. L. Gu, Y. Zhou, W. A. Morrison, K. Park, S. Park, Z. Bao, *ACS Nano* **2018**, *12*, 1473–1481.
35. C. Sun, F. Pan, H. Bin, J. Zhang, L. Xue, B. Qiu, Z. Wei, Z. G. Zhang, Y. Li, *Nat. Commun.* **2018**, *9*, 743.
36. A. Dazzi, C. B. Prater, Q. Hu, D. B. Chase, J. F. Rabolt, C. Marcott, *Appl. Spectrosc.* **2012**, *66*, 1365–1384.
37. T. Eby, U. Gundusharma, M. Lo, K. Sahagian, C. Marcott, K. Kjoller, *Spectrosc. Eur.* **2012**, *24*, 18–21.
38. F. Tang, P. Bao, Z. Su, *Anal. Chem.* **2016**, *88*, 4926–4930.

39. M. Kelchtermans, M. Lo, E. Dillon, K. Kjoller, C. Marcott, *Vib. Spectrosc.* **2016**, *82*, 10–15.
40. P. Nguyen-Tri, P. Ghassemi, P. Carriere, S. Nanda, A. A. Assadi, D. D. Nguyen, *Polymers* **2020**, *12*, 1–28.
41. D. Fu, K. Park, G. Delen, Ö. Attila, F. Meirer, D. Nowak, S. Park, J. E. Schmidt, B. M. Weckhuysen, *Chem. Commun.* **2017**, *53*, 13012–13014.
42. G. Delen, M. Monai, F. Meirer, B. M. Weckhuysen, *Angew. Chem. Int. Ed.* **2021**, *60*, 1620.
43. J. Li, J. Jahng, J. Pang, W. Morrison, J. Li, E. S. Lee, J. J. Xu, H. Y. Chen, X. H. Xia, *J. Phys. Chem. Lett.* **2020**, *11*, 1697–1701.
44. M. A. Almajhadi, S. M. A. Uddin, H. K. Wickramasinghe, *Nat. Commun.* **2020**, *11*, 5691.
45. I. C. ten Have, A. J. A. Duijndam, R. Oord, H. J. M. van Berlo-van den Broek, I. Vollmer, B. M. Weckhuysen, F. Meirer, *Chemistry-Methods* **2021**, *1*, 205–209.
46. M. Ocaña, V. Fornés, C. J. Serna, *J. Non. Cryst. Solids* **1989**, *107*, 187–192.
47. R. M. Almeida, *Phys. Rev. B - Condens. Matter Mater. Phys.* **1996**, *53*, 14656–14658.
48. V. J. Ruddick, J. P. S. Badyal, *J. Phys. Chem. B* **1997**, *101*, 1791–1793.
49. G. K. H. Pang, K. Z. Baba-Kishi, A. Patel, *Ultramicroscopy* **2000**, *81*, 35–40.
50. I. Schmitz, M. Schreiner, G. Friedbacher, M. Grasserbauer, *Appl. Surf. Sci.* **1997**, *115*, 190–198.
51. S. N. Magonov, V. Elings, M. H. Whangbo, *Surf. Sci.* **1997**, *375*, L385–L391.
52. W. W. Scott, B. Bhushan, *Ultramicroscopy* **2003**, *97*, 151–169.
53. G. Bar, Y. Thomann, R. Brandsch, H. J. Cantow, M. H. Whangbo, *Langmuir* **1997**, *13*, 3807–3812.
54. L. Wang, *Surf. Sci.* **1999**, *429*, 178–185.
55. F. Carrasco, P. Pagès, S. Pascual, X. Colom, *Eur. Polym. J.* **2001**, *37*, 1457–1464.
56. T. C. K. Yang, S. S. Y. Lin, T. H. Chuang, *Polym. Degrad. Stab.* **2002**, *78*, 525–532.
57. G. Lazar, K. Zellama, I. Vascan, M. Stamate, I. Lazar, I. Rusu, *J. Optoelectron. Adv. Mater.* **2005**, *7*, 647–652.
58. M. Gardette, A. Perthue, J. L. Gardette, T. Janecska, E. Földes, B. Pukánszky, S. Therias, *Polym. Degrad. Stab.* **2013**, *98*, 2383–2390.
59. A. Zecchina, C. Otero Areán, *Chem. Soc. Rev.* **1996**, *25*, 187–197.
60. C. Lamberti, A. Zecchina, E. Groppo, S. Bordiga, *Chem. Soc. Rev.* **2010**, *39*, 4951–5001.
61. E. Groppo, C. Lamberti, S. Bordiga, G. Spoto, A. Zecchina, *Chem. Rev.* **2005**, *105*, 115–183.
62. E. Groppo, G. A. Martino, A. Piovano, C. Barzan, *ACS Catal.* **2018**, *8*, 10846–10863.
63. V. A. Zakharov, E. A. Paukshtis, T. B. Mikenas, A. M. Volodin, E. N. Vitus, A. G. Potapov, *Macromol. Symp.* **1995**, *89*, 55–61.
64. K. S. Thushara, M. D'Amore, A. Piovano, S. Bordiga, E. Groppo, *ChemCatChem* **2017**, *9*, 1782–1787.
65. M. D'Amore, K. S. Thushara, A. Piovano, M. Causà, S. Bordiga, E. Groppo, *ACS Catal.* **2016**, *6*, 5786–5796.
66. P. Pletcher, A. Welle, A. Vantomme, B. M. Weckhuysen, *J. Catal.* **2018**, *363*, 128–135.
67. M. E. Z. Velthoen, A. Muñoz-Murillo, A. Bouhmadi, M. Cecius, S. Diefenbach, B. M. Weckhuysen, *Macromolecules* **2018**, *51*, 343–355.
68. V. N. Panchenko, I. G. Danilova, V. A. Zakharov, E. A. Paukshtis, *Kinet. Catal.* **2004**, *45*, 547–553.
69. J. A. Marsella, C. J. Curtis, J. E. Bercaw, K. G. Caulton, *J. Am. Chem. Soc.* **1980**, *102*, 7244–7246.
70. A. Piovano, J. Zarupski, E. Groppo, *J. Phys. Chem. Lett.* **2020**, *11*, 5632–5637.
71. X. Desert, J. F. Carpentier, E. Kirillov, *Coord. Chem. Rev.* **2019**, *386*, 50–68.
72. Y. Doi, M. Murata, K. Yano, T. Keii, *Ind. Eng. Chem. Prod. Res. Dev.* **1982**, *21*, 580–585.
73. T. Taniike, S. Sano, M. Ikeya, V. Q. Thang, M. Terano, *Macromol. React. Eng.* **2012**, *6*, 275–279.
74. A. Thakur, T. Wada, P. Chammingkwan, M. Terano, T. Taniike, *Polymers* **2019**, *11*, 1012.
75. G. Bukatov, V. Goncharov, V. Zakharov, *Die Makromol. Chemie* **1986**, *187*, 1041–1051.
76. T. Shiono, M. Ohgizawa, K. Soga, *Die Makromol. Chemie* **1993**, *194*, 2075–2085.
77. I. Tritto, M. C. Sacchi, P. Locatelli, *Die Makromol. Chemie, Rapid Commun.* **1983**, *4*, 623–627.
78. H. Knözinger, *Elem. React. Steps Heterog. Catal.* **1993**, 267–285.

79. H. Knoezinger, H. Krietenbrink, *J. Chem. Soc. Faraday Trans. 1* **1975**, *71*, 2421–2430.
80. C. Morterra, M. Peñarroya Mentrui, G. Cerrato, *Phys. Chem. Chem. Phys.* **2002**, *4*, 676–687.
81. C. Morterra, G. Cerrato, E. Novarino, M. Peñarroya Mentrui, *Langmuir* **2003**, *19*, 5708–5721.
82. E. Escalona Platero, M. Peñarroya Mentrui, C. Morterra, *Langmuir* **1999**, *15*, 5079–5087.
83. M. Cerruti, V. Bolis, G. Magnacca, C. Morterra, *Phys. Chem. Chem. Phys.* **2004**, *6*, 2468–2479.
84. M. Bochmann, L. M. Wilson, *J. Chem. Soc. Chem. Commun.* **1986**, 1610–1611.
85. R. F. Jordan, C. S. Bajgur, W. E. Dasher, A. L. Rheingold, *Organometallics* **1987**, *6*, 1041–1051.
86. M. Bochmann, L. M. Wilson, M. B. Hursthouse, M. Motevalli, *Organometallics* **1988**, *7*, 1148–1154.
87. Y. W. Alelyunas, R. F. Jordan, S. F. Echols, S. L. Borkowsky, P. K. Bradley, *Organometallics* **1991**, *10*, 1406–1416.
88. M. Ystenes, J. L. Eilertsen, J. Liu, M. Ott, E. Rytter, J. A. Støvneng, *J. Polym. Sci. Part A Polym. Chem.* **2000**, *38*, 3106–3127.
89. G. A. Martino, A. Piovano, C. Barzan, J. Rabeah, G. Agostini, A. Bruekner, G. Leone, G. Zanchin, T. Monoi, E. Groppo, *ACS Catal.* **2020**, *10*, 2694–2706.
90. A. Zecchina, E. Guglielminotti, S. Coluccia, E. Borello, *J. Chem. Soc. A* **1969**, 2196–2199.
91. T. Montanari, M. Bevilacqua, G. Busca, *Appl. Catal. A Gen.* **2006**, *307*, 21–29.

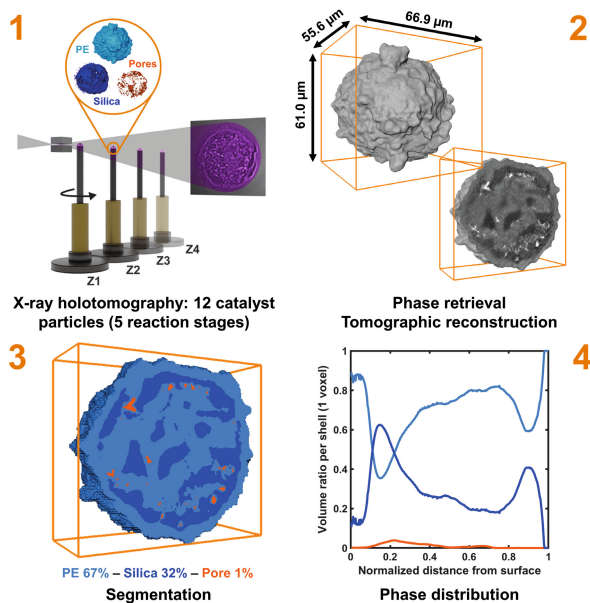
Chapter 3

Assessing Morphological Heterogeneity in a Metallocene-Based Olefin Polymerization Catalyst with X-Ray Nanotomography

This **Chapter** is based on the following scientific article:

M. J. Werny*, R. Valadian*, L. M. Lohse, A.-L. Robisch, S. Zanoni, C. Hendriksen, B. M. Weckhuysen, F. Meirer, *Chem Catalysis* **2021**, *1*, 1413–1426. Copyright © 2021 Elsevier Inc, published by Elsevier.

*Both authors contributed equally to this work.



This **Chapter** describes the use of non-destructive hard X-ray holotomography to quantitatively assess the 3D morphology of multiple silica-supported hafnocene-based catalyst particles during the early stages of gas-phase ethylene polymerization. Image processing and pore network modeling were employed to assess variations in the dimensions and interconnectivities of pristine and pre-polymerized particles' macropore networks. Clear differences in the fragmentation behavior of pre-polymerized particles were also identified. Both suggest that the reactivity and morphological evolution of individual catalyst particles are largely dictated by their unique support and pore space architectures. By minimizing the structural heterogeneity among pristine catalyst particles, more uniform particle morphologies may be obtained. Significant polymerization activity that was observed in the interiors of the catalyst particles further implies that appropriate polymerization conditions and catalyst kinetics can guarantee sufficiently high particle accessibilities and thus more homogeneous support fragmentation.

3.1 Introduction

In supported olefin polymerization catalysts, polymer formation at the active sites leads to the disintegration of the porous catalyst support, thereby yielding a complex composite material that is composed of the obtained polymer and fragments of the support. With early-stage support fragmentation known to play a vital role in maintaining catalytic activity as well as determining the final polymer particle morphology and properties^[1-7], significant research efforts have been directed towards visualizing the morphology of olefin polymerization catalyst particles. From a mechanistic point of view, experimentally observed support fragmentation depends on the catalyst properties (i.e., active sites, support properties, and kinetics), the applied reaction conditions (i.e., pressure, temperature and process type) as well as the properties of the formed polymer (i.e., crystallinity, viscoelasticity). To obtain novel insights into this complex process, well-defined morphological studies, focused on the variation of a limited number of parameters during the initial stages of olefin polymerization, are required. While the morphology of olefin polymerization catalysts is usually assessed in 2D by means of microtoming and scanning electron microscopy (SEM)^[2,8-13], high resolution 3D imaging techniques can contribute decisively by delivering quantitative information on the fragmentation of entire catalyst particles.^[7,14,15]

Over the years, X-ray microscopy has become an invaluable tool for the characterization of catalyst particles due to its non-invasive and non-destructive nature, its capacity to enable full 3D imaging due to the high penetration power of hard X-rays, as well as its steadily increasing spatial resolution.^[16-20] While several investigations have been performed on the 3D distribution of metals within catalyst particles^[14,21-27], mapping the 3D distribution of low atomic number (Z) materials with hard X-ray tomography remains challenging.^[28] In the field of olefin polymerization catalysis, synchrotron- and lab-based hard X-ray computed tomography (CT) techniques have been successfully used in the past to determine the morphology of both low Z polymer and the support in individual catalyst particles.^[29-37] In most of these studies, however, high polymer yield samples were investigated at resolutions in the order of several micrometers. A high-resolution tomography of a large number of Ziegler-type catalyst particles ($\text{MgCl}_2/\text{TiCl}_4$; pristine: $D_{50} = 3.64 \mu\text{m}$) was only recently acquired by our group using hard X-ray ptychography, a phase-contrast-based scanning technique that provides sufficient sensitivity for low Z elements.^[15] Despite the technique's capacity to deliver sub-100 nm resolutions^[15,38,39], it is limited by its long measurement times (e.g., 22 h for $120 \times 120 \times 20 \mu\text{m}^3$ in reference 15, $\sim 220 \mu\text{m}^3/\text{min}$). This can complicate the characterization of more extensive sample sets, especially when multiple (larger) particles from different batches or reaction stages are subject to investigation.

In this **Chapter**, full-field hard X-ray holotomography is used to further assess the morphological evolution of the silica-supported hafnocene-based catalyst ($\text{Hf}/\text{MAO}/\text{SiO}_2$) during the initial stages of gas-phase ethylene polymerization, as previously discussed in **Chapter 2**. Inline holograms, collected at different angles and sample-detector distances, were used to reconstruct 3D representations of individual catalyst particles, with grayscale values that are proportional to the particles' relative electron density distributions.^[40] Holotomography

relies on propagation-based phase contrast and is thus suitable for visualizing low Z materials at sub-micrometer spatial resolution^[26,28,40–45]. Moreover, its superior acquisition speed (2.5 h for 90 x 90 x 81 μm^3 , 4 distances, $\sim 4400 \mu\text{m}^3/\text{min}$) enables high sample throughput. Thus, we were able to analyze multiple catalyst particles from five different reaction stages *ex situ* (pristine, 1 min, 10 min, 30 min and 60 min). In contrast to the mesoporous MgCl_2 support of the previously discussed Ziegler-type catalyst^[15], the silica support of the here examined catalyst is significantly larger (pristine: $D_{50} = 25.0 \mu\text{m}$) and less friable. These properties, together with the support's extensive macropore networks, are assumed to have a direct impact on the process of support fragmentation. To assess this, the porosity, composition and phase distribution of the individual catalyst particles were determined based on the mapped relative electron density differences between the constituent phases. Furthermore, the dimensions and connectivity of the particles' respective macropore networks were evaluated by means of pore network modeling.^[21–23] This in-depth analysis not only provided valuable insights into the morphological heterogeneity among pristine catalyst particles but also revealed notable differences in reaction progress and morphology among pre-polymerized particles of the same batch. The divergent behavior among individual catalyst particles implies correlations between the particles' reactivities and their initial support morphologies, which, in turn, can severely affect mass and heat transfer during ethylene polymerization. Fragmentation was generally observed to occur in large portions of the catalyst particles, thus implying a sufficient accessibility of the particle interior for ethylene gas under the given experimental conditions.

3.2 Experimental Methods

3.2.1 Sample Preparation

The hafnocene-based catalyst material was synthesized via impregnation of a polymer-grade silica with a solution of a 2,2'-biphenylene-bis-2-indenyl HfCl_2 complex and methylaluminoxane (MAO). The catalyst was then pre-polymerized in gas-phase with ethylene for different amounts of time to obtain low polymer yield samples that were suitable for our investigations (1 min/10 min/30 min/60 min, 1.6 bar ethylene, room temperature, yielding 0.7–6.4 $\text{g}_{\text{PE}}/\text{g}_{\text{cat}}$, PE = polyethylene; **Table 3.1**).

Table 3.1 Polyethylene (PE) yields in $\text{g}_{\text{PE}}/\text{g}_{\text{cat}}$ as obtained during the gas-phase polymerization of ethylene over the hafnocene-based catalyst in a dedicated glass-reactor set-up (1.6 bar C_2H_4 , room temperature).

Time (min)	1	10	30	60
Catalyst yield ($\text{g}_{\text{PE}}/\text{g}_{\text{cat}}$)	0.7	1.4	2.6	6.7

Further details on the synthesis and pre-polymerization of the catalyst, as well as its characterization via focused ion beam-scanning electron microscopy (FIB-SEM) can be found in **Chapter 2** of this PhD thesis.

3.2.2 Hard X-Ray Holotomography

X-ray holotomography was performed on multiple pristine and pre-polymerized hafnocene-based catalyst particles using the Göttingen Instrument for Nano-Imaging with X-Rays (GINIX) set-up at the P10 beamline, located at the PETRA III storage ring, Deutsches Elektronen Synchrotron (DESY), Hamburg, Germany.^[46] The set-up is highly suitable for near-field phase-contrast imaging at high magnification and resolution. All measurements were performed at a photon energy of 8 keV using a Si(111) channel-cut monochromator. The X-ray beam was focused by Kirkpatrick-Baez (KB) mirrors to a size of approximately 300 x 300 nm². A 1 mm long silicon waveguide with a sub-100 nm guiding layer, fabricated by e-beam lithography (Eulitha, Switzerland) and capped by wafer bonding, was placed in the focal plane of the KB mirror to reduce high-frequency artifacts arising from inhomogeneities on the mirror surface, improve the focal spot size and to increase the coherence of the X-ray beam.^[46] A Zyla 5.5 sCMOS detector (Andor) with a pixel size of 6.5 μm was employed approximately 5 m after the sample. In general, holograms were acquired at a minimum of one and at a maximum of four different source-to-sample distances, leading to slightly different effective propagation distances. The acquisition of holograms at multiple distances yielded missing information on specific spatial frequencies due to the zero crossings of the contrast transfer function (CTF)^[40,47], which describes the image formation for homogenous, weakly absorbing objects with a slowly varying phase. Depending on the source-to-sample distance, an effective pixel size between 53.5 nm and 79.0 nm was obtained. Approximately 2–4 h were required per sample for mounting, alignment and holotomography. At every source-to-sample distance, 1000 projections were acquired over an angular range of 180°. In terms of sample preparation, the individual polymerization catalyst particles were either embedded in X-ray transparent epoxy glue (Araldite® Rapid epoxy) and mounted on top of a graphite pin, or loaded inside a polyimide (Kapton, d = 360 μm) capillary.

3.2.3 Phase Retrieval, Image Reconstruction and Segmentation

As mentioned above, holotomography requires the acquisition of multiple holograms at different propagation distances. Phase retrieval performed on these holograms yields two-dimensional (2D) images of the projected phase shift of the sample, which form the basis for the tomographic reconstruction of the three-dimensional (3D) relative electron density distribution of the sample (obtained phase shift is approximately proportional to the relative electron density).^[40] Due to the large size of the files, the projections were binned by a factor of 2 prior to phase retrieval. All projections were also scaled to the same pixel size and aligned to each other in Fourier space. Phase retrieval was performed from dark and empty beam corrected holograms, using a non-linear adaptation of the contrast transfer function (CTF) method based on Tikhonov regularization (NL-CTF).^[48,49] The code package HoloTomoToolbox was employed for this.^[49] A filtered back-projection (FBP) algorithm with standard Ram-Lak filter was utilized for the tomographic reconstruction of the retrieved phase images. All reconstructed 32-bit images (2D virtual slices) were converted to 16-bit integer format. In general, the images are visualized with a grayscale colormap, in which white and black pixels (voxels) correspond to low and high electron density values, respectively.

The Avizo™ software package by Thermo Fisher Scientific Inc. was employed for post-processing of the reconstructed images. After determining the total particle volume (TPV, i.e., binary representation of a particle's volume including pore space) for every particle, the 16-bit integer images were masked with the TPV. In the case of ring or streak artifacts, a non-local means filter was applied to make the TPV generation easier. The masked images were then segmented into their corresponding pore space and solid phase using k-means clustering^[50] (MATLAB™). In the case of artifacts or incorrect segmentation of the pore space, manual thresholding was applied.

For epoxy-embedded catalyst particles consisting of silica and detectable amounts of polymer, a MATLAB™-based k-means clustering approach^[50], previously used by our group^[15], was adopted to distinguish between phases based on their relative electron densities (ED). Three clusters ($k = 3$) were used to segment the masked grayscale images into a silica-dominant phase (high relative ED), a polymer-dominant phase (intermediate relative ED) and the macropore space (low relative ED). Due to the resolution limitations of the technique and the high degree of intermixing of silica, polymer and macropores, the silica-dominant phase is overestimated. Polymer, support and macropores that are smaller than the determined resolutions go undetected or are excluded from the analysis of the segmented images. Polyethylene (PE) in the micro- and mesopores as well as in some of the macropores of the denser silica granulates can thus also not be accounted for.

The binarized TPV and segmented pore space of each particle were used to determine its equivalent spherical diameter (ESD) [$ESD = (6V/\pi)^{1/3}$, V is equivalent to TPV], assuming spherical geometry, as well as its porosity and macropore volume (V_{mp}) in MATLAB™.

3.2.4 Determination of Spatial Resolutions

The spatial resolution was estimated per catalyst particle based on 12 line profiles fitted over well-defined features in the 2D virtual slices using a 10%–90% criterion (line scan analysis). Following a method described by Holler *et al.*^[51] and Vesely *et al.*^[28], the edge resolution was determined from the horizontal distance between the vertical lines that pass through the line profile at 10% and 90%, respectively.

3.2.5 Radial Phase Distribution Analysis

The radial phase distribution analysis was performed on the segmented data sets with an in-house developed MATLAB™ code. All calculations were carried out in relation to the central voxel of a given particle. This was determined by generating a distance map of a particle's inverted TPV. Here, the Euclidean distance of every voxel (voxel value = 0) to the closest particle surface (voxel value = 1) is calculated. The voxel with the maximum Euclidean distance is then taken as the central voxel. Following this, the TPV is divided into shells, each possessing a thickness of 1 voxel. The shells are concentrically arranged around the central voxel. The relative fraction of a particular phase (i.e., silica-dominant phase, polymer-dominant phase or pore space) within a shell is determined by taking the ratio of the phase's corresponding voxel count to the total number of voxels within the shell (normalized by the shell volume). The final 5–10% of the radial analysis are typically ignored due to the limited number of voxels

per shell at low remaining particle volumes (statistically insignificant regime). More information on this radial phase distribution analysis can be found in a publication by Meirer *et al.*^[21]

3.2.6 Pore Network Models

Pore network models (PNMs) were generated from the binarized (segmented) pore space images of the reconstructed catalyst particles. Due to their large size, the images were binned two times (binning factor = 4) before pore network analysis. First, a thinning procedure was applied to the pore space of a particle to obtain its corresponding skeleton, i.e., a set of lines of 1 voxel thickness, connecting the geometric centers of the corresponding pore space voxels. The skeleton is then transformed into a pore network model.

Each pore network model consists of a set of geometrical spatial graphs called sub-graphs. Two sub-graphs, although in the same network, are not connected. A sub-graph can be defined as a set of nodes (branching segment points or dead-end segment points) and segments (set of lines connecting the nodes). Each segment is constituted by segment points to account for the curvature of the pores. The volume of each segment corresponds to the volume of a cylinder with a radius equal to the average radius of all segment points (i.e., radius of cylinders connecting segment points) and a length equal to the Euclidean distance between two specific nodes.

In general, the pore networks of most particles feature sub-graphs that are isolated from the largest graph. These sub-graphs represent isolated pores or cavities in the catalyst particles. The number of sub-graphs is an indicator for the interconnectivity of a catalyst particle's pore space. Another metric that can be used to describe the connectivity of the macropores is the nodes connectivity ratio (NCR). This is derived by the formula $NCR = N_c / (n^2 - n)$, where N_c corresponds to the number of connected nodes and n represents the total number of nodes. A high NCR value indicates extensive macropore connectivity.

Based on the radii of the segments within the pore network model of a given particle, an approximate pore size distribution (PSD) can be determined. Due to the resolution limitations of holotomography, the PSDs only account for the macropores of the respective catalyst particles.

3.2.7 Binning Simulation

A simulation was performed to study the effect of binning on the analysis of the grayscale images as well as the pore network model analysis. The original reconstructed holotomography data (binned twice) of particle E_0 was binned iteratively at increasing binning factors (2 and 4). The spatial resolution of the data set was thus effectively lowered. For each binning factor, image processing and pore network analysis were performed.

3.2.8 Dispersion Plots

The 3D distribution of the catalyst particles' constituent phases (silica-dominant, polymer-dominant phases or pore space) was visualized in MATLAB™ in so-called dispersion plots. Here, the corresponding sub-volumes of a particular phase (i.e., connected voxels) are visualized as small spheres, with the color of a sphere indicating the sub-volume's distance to the particle centroid, which is visualized as a red cross in the figures. The center of each sphere is positioned at the centroid of the corresponding sub-volume and scales directly with the sub-volume's dimensions. The sphere representing the largest sub-volume therefore has the largest diameter and is labelled as '1' while sub-volumes smaller than 1% of the largest sub-volume ($V_{\text{threshold}} = 0.01 \times V_{\text{max}}$) are visualized as spheres with a fixed diameter.

3.3 Results and Discussion

3.3.1 Investigating the 3D Structure of Polymerization Catalyst Particles

Holotomographic scans (**Figure 3.1A**) were performed on randomly selected pristine and pre-polymerized catalyst particles (**Figure 3.1B**) at the GINIX end station of the PETRA III storage ring, DESY, Hamburg. The particles were either embedded in epoxy glue (denoted as 'E', **Figure 3.1C**) or mounted in Kapton capillaries (denoted as 'K', **Figure 3.1C**) and scanned at a low photon energy of 8 keV at multiple distances (Z1–Z4) to the detector. The combination of these two preparation techniques allowed us to identify optimal measurement conditions for the low Z polyethylene (PE)/silica composite materials. A total of 12 pristine and pre-polymerized particles, labeled as E_0 , K_0 , E_1 , K_1 , E_{10} , K_{10} , K_{30-1} , K_{30-2} , E_{60-1} , E_{60-2} , K_{60-1} and K_{60-2} in accordance with their respective reaction stages, were measured and reconstructed (**Figure 3.1C**). Prior to image segmentation and post-processing, the data sets were binned by a factor of 2 to reduce their size. The particles' corresponding grayscale volumes were subsequently segmented into pore space and solid phase to study the particles' microstructure in 3D as well as their respective macropore networks.

As can be seen in **Figure 3.1C**, all catalyst particles possess a well-defined external and internal morphology. In fact, the pristine and 60 min pre-polymerized catalyst particles are comparable to particles from the same batch (refer to FIB-SEM data in **Figures 3.1B** and **3.2**). While the pristine (E_0 , K_0) and 1 min pre-polymerized (E_1 , K_1 ; $0.7 \text{ g}_{\text{PE}}/\text{g}_{\text{cat}}$) catalyst particles possess smooth external surfaces, the 60 min pre-polymerized particles (E_{60-1} , E_{60-2} , K_{60-1} , K_{60-2} ; $6.4 \text{ g}_{\text{PE}}/\text{g}_{\text{cat}}$) feature a cauliflower-like morphology, indicating a significant build-up of PE at the surface. The surface morphologies of particles E_{10-1} , K_{10-1} , K_{30-1} and K_{30-2} vary and may be indicative of their respective polymerization degrees.

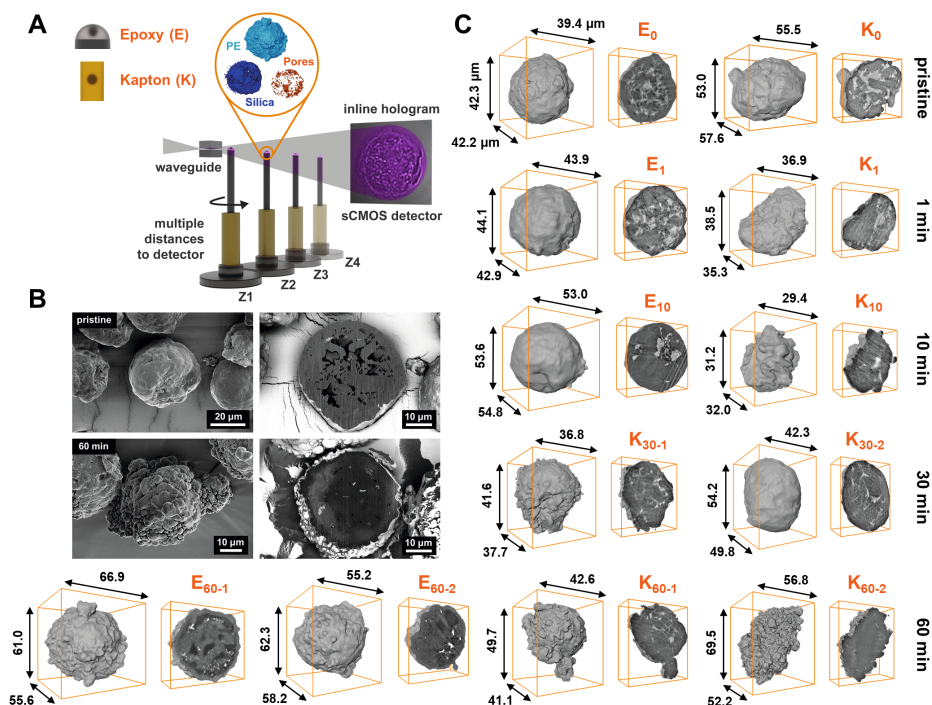


Figure 3.1 Morphological characterization of multiple pristine and pre-polymerized hafnocene-based catalyst particles using hard X-ray holotomography. (A) Schematic of the propagation-based phase contrast imaging set-up (GINIX) at the P10 beamline of the PETRA III storage ring, DESY. Monochromatic X-rays are focused by Kirkpatrick-Baez (KB) mirrors (not shown here) onto a waveguide. The polymerization catalyst particle, which is either embedded in epoxy glue or mounted inside a Kapton capillary, is illuminated by a cone beam from this coherent point source and rotated for tomographic measurements. A scientific complementary metal-oxide semiconductor (sCMOS) camera, placed approximately 5 m behind the sample, is used for detection. Scans are performed at multiple distances from the detector (maximum of 4). A phase-retrieval procedure is applied to the collected holograms to obtain the corresponding 2D phase shift images (related to the relative electron density distribution), which are then used to reconstruct the scanned specimen via a filtered back-projection algorithm. (B) Scanning electron microscopy (SEM) images of a pristine and 60 min pre-polymerized hafnocene-based catalyst particle (gas-phase, 1.6 bar, room temperature) (light gray: silica support, dark gray: PE). (C) Reconstructed volumes of the pristine (E_0 , K_0), 1 min (E_1 , K_1), 10 min (E_{10} , K_{10}), 30 min (K_{30-1} , K_{30-2}) and 60 min pre-polymerized (E_{60-1} , E_{60-2} , K_{60-1} , K_{60-2}) hafnocene-based catalyst particles as well as their corresponding virtual particle cross-sections (white/light gray, low relative electron density, macropores; gray, intermediate relative electron density, PE-dominant phase; dark gray, high relative electron density, silica-dominant phase).

In general, the obtained phase contrast and thus the ability to differentiate between phases in the particle interior were found to depend on the type of sample preparation. In the case of the pre-polymerized particles mounted in Kapton capillaries, the PE and silica phases could not be differentiated at 8 keV. This is presumably related to a large difference in refractive index between the particle and the surrounding air. Significantly higher contrast was, however, achieved by embedding the catalyst particles in epoxy glue. As is evident from the reconstructed cross-sections of the 60 min pre-polymerized catalyst particles E_{60-1} and E_{60-2} (Figure 3.1C), macropores (low relative electron density (ED), white/light gray), a PE-dominant

phase (intermediate relative ED, gray) and a silica-dominant phase (high relative ED, dark gray), featuring pristine and fragmented support granulates, are distinguishable at more advanced reaction stages.

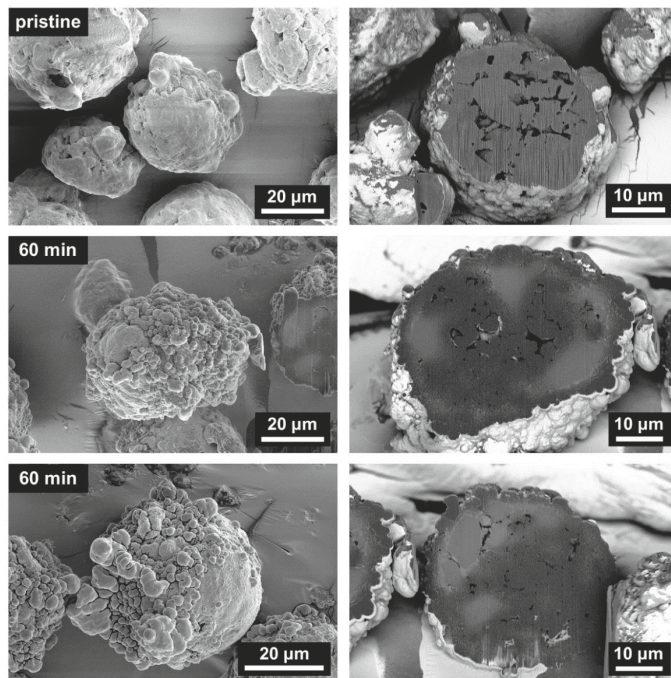


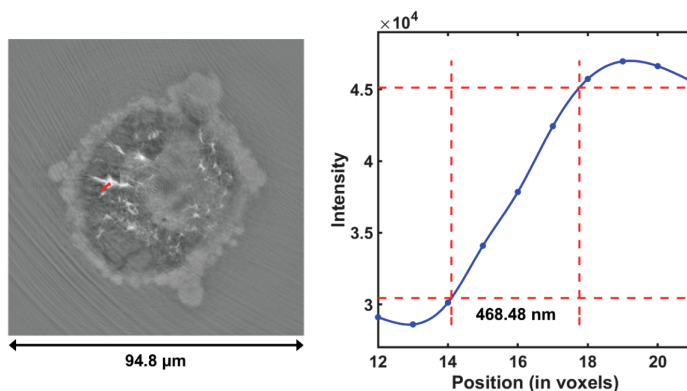
Figure 3.2 Scanning electron microscopy (SEM) images of pristine and 60 min pre-polymerized hafnocene-based catalyst particles (gas-phase, 1.6 bar, room temperature) and their corresponding cross-sections (left: recorded in secondary electron (SE) mode, right: recorded in back-scattered electron (BSE) mode). The full particle and cross-sectional images were acquired at different stage tilt and rotation angles. The vertical stripes in the cross-sectional images are artifacts from focused ion beam (FIB) cutting.

The classification into PE- and silica-dominant phases was adopted to account for the resolution limitations of the technique (**Table 3.2**) as well as the high degree of intermixing of the PE and silica phases (**Figures 3.1B** and **3.2**), which together effectively inhibit the differentiation of the two phases at length scales below the achieved spatial resolutions. This results in the denser silica-dominant phase being overestimated.

To segment these three phases, a k-means clustering algorithm ($k = 3$), that has previously been used by our group for comparable systems^[15], was applied to the corresponding data sets. This ensured comparability of the extracted data between the measured catalyst particles. Silica fragments, polymer domains, and pores smaller than the determined spatial resolutions (246–546 nm via line scan analysis, **Table 3.2** and **Figure 3.3**) were excluded from the analysis of the segmented images. It must be noted that polymer could not be detected in the remaining epoxy-embedded particles E_1 and E_{10} , presumably due to the low amounts of PE that were formed and resolution limitations.

Table 3.2 Spatial resolutions of the reconstructed hafnocene-based catalyst particles as determined via the 10%–90% criterion.

Particle	E ₀	K ₀	E ₁	K ₁	E ₁₀	K ₁₀	K ₃₀₋₁	K ₃₀₋₂	E ₆₀₋₁	E ₆₀₋₂	K ₆₀₋₁	K ₆₀₋₂
Resolution (nm)	491	365	315	246	290	465	285	387	491	417	422	546

**Figure 3.3** Line scan analysis performed on a 2D virtual slice of catalyst particle E₆₀₋₁ following the 10%–90% criterion. A resolution of 468.5 nm was determined from the corresponding edge profile.

3.3.2 Analysis of the Catalyst Particles' Macropore Networks

Based on the segmented grayscale images, the porosity and macropore volume (V_{mp}) of each particle were determined (Table 3.3). As expected, a gradual decline in porosity is generally observed with increasing polymerization degree. While the pristine particles E₀ and K₀ and the 1 min pre-polymerized particle E₁ ($0.7 \text{ g}_{PE}/\text{g}_{cat}$) feature comparatively high porosities in the range of 12–13%, the porosities of the 60 min pre-polymerized particles E₆₀₋₁, E₆₀₋₂ and K₆₀₋₂ ($6.4 \text{ g}_{PE}/\text{g}_{cat}$) fall in the range of 1–3%. In order to obtain a more thorough understanding for the spatial distribution of the macropores, radial analysis^[22,52,53] was applied to all particles (Figures 3.4A and 3.4B). Here, the porosity of each concentric single-pixel shell of the catalyst particles was plotted as a function of the normalized Euclidean distance to the particle surfaces (d_s ; $d_{s,surface} = 0$, $d_{s,central\ voxel} = 1$). All catalyst particles display low porosity in close vicinity to their respective surfaces ($d_s \leq 0.1$) and a subsequent increase in porosity when moving toward to the particle center. The observed fluctuations can be attributed to structural heterogeneity within the individual catalyst particles. The previously discussed decrease in porosity, as a function of reaction progress, is easily discernible from the two radial analysis plots (Figures 3.4A and 3.4B).

Table 3.3 Metrics for the pristine (E_0 , K_0), 1 min (E_1 , K_1), 10 min (E_{10} , K_{10}), 30 min (K_{30-1} , K_{30-2}) and 60 min pre-polymerized (E_{60-1} , E_{60-2} , K_{60-1} , K_{60-2}) hafnocene-based catalyst particle reconstructions, as derived via image segmentation, pore network modeling (PNM) and analysis.

Particle	Equivalent spherical diameter, ESD (μm)	Porosity	Macropore volume, V_{mp} (μm^3)	Number of subgraphs	Graph nodes connectivity ratio (NCR)	Mean distance (μm)	Mean Euclidean distance (μm)	Mean tortuosity
E_0	38.3	0.13	3819	106	0.93	197.5	105.2	1.91
K_0	40.2	0.12	4069	350	0.74	329.6	144.2	2.31
E_1	35.2	0.12	2750	149	0.89	240.8	115.2	2.16
K_1	23.7	0.08	561	206	0.72	163.0	79.3	2.09
E_{10}	43.1	0.08	3352	288	0.79	296.7	130.5	2.27
K_{10}	18.6	0.08	268	130	0.37	138.8	54.1	2.58
K_{30-1}	29.3	0.04	529	418	0.25	169.3	70.4	2.49
K_{30-2}	34.9	0.07	1563	1890	0.76	363.9	134.1	2.76
E_{60-1}	60.4	0.01	1155	361	0.03	51.8	28.7	1.73
E_{60-2}	52.6	0.03	2291	202	0.09	142.9	60.9	2.29
K_{60-1}	35.1	0.06	1359	517	0.60	268.9	94.0	2.95
K_{60-2}	49.4	0.02	1259	586	0.04	75.6	39.3	1.89

All metrics are defined in the text. Both the mean distance and mean Euclidean distance are calculated for the connected nodes of a pore network model.

To further assess the properties of the catalyst particles' respective macropore networks, pore network models (PNMs), representing the macropore volume of the measured catalyst particles, were generated based on the binarized (segmented) pore space images (images for PNMs binned by a total factor of 4). Each PNM is based on a set of geometrical spatial graphs, commonly referred to as sub-graphs, that consist of nodes (i.e., branching points) and segments (i.e., a cylinder with pore-specific radius and length connecting two nodes). Using these sub-graphs, the connectivity and tortuosity of the catalyst particles' macropore networks were determined (**Table 3.3**). Note that pores smaller than the obtained spatial resolutions were not assessed. To determine the average connectivity of all nodes in the respective PNMs, the nodes connectivity ratio (NCR) was calculated for each network. This corresponds to the ratio of connected nodes to the total number of nodes in all sub-graphs of a pore network. While a large NCR value denotes a high connectivity of a PNM's nodes, a small value indicates a lower connectivity of the pore space. The tortuosity of the pore networks was also deduced from the average ratio of the mean real distance between connected nodes (i.e., the distance along open pores) to the corresponding mean Euclidean distance between nodes.

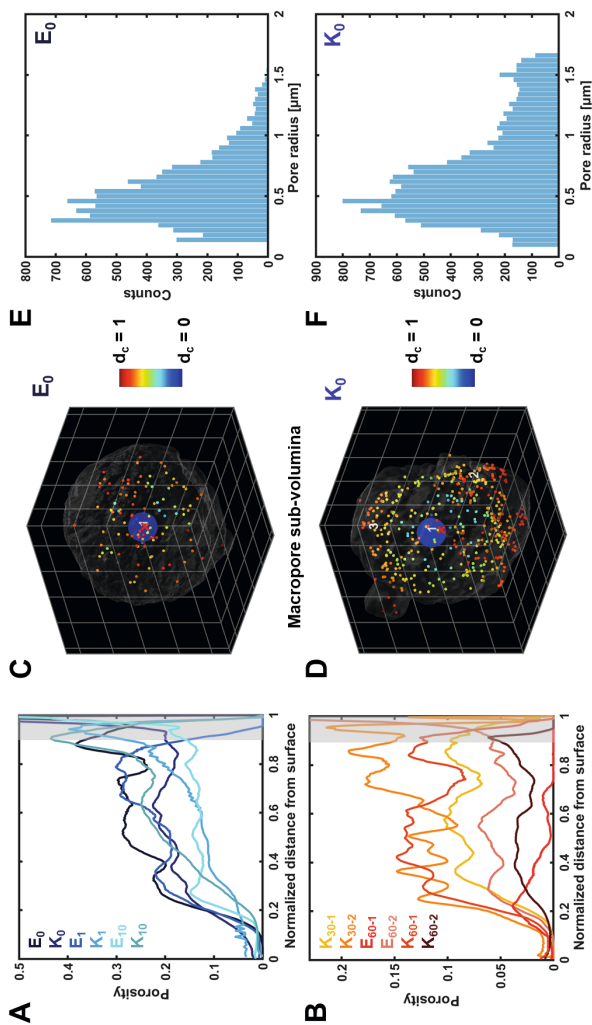


Figure 3.4 Quantitative analysis of the catalyst particles' macropore networks. (A) and (B) Radial analysis of the reconstructed catalyst particles' porosity. The porosity of each concentric single-voxel shell is plotted as a function of the normalized distance from the particle surface (d ; center: $d_c = 1$, surface: $d_c = 0$). The final 5–10% of the radial analysis (light gray) are typically ignored due to the limited number of voxels per shell at low remaining particle volumes (statistically insignificant regime). (C) Dispersion plot for the macropore space sub-volumes of particle E_0 ($V_{\text{max}} = 3800 \mu\text{m}^3$, $V_{\text{threshold}} = 38 \mu\text{m}^3$). D_c denotes the distance of a pore space sub-volume to the particle's centroid. (D) Dispersion plot for the macropore space of particle K_0 ($V_{\text{max}} = 3816 \mu\text{m}^3$, $V_{\text{threshold}} = 38 \mu\text{m}^3$). (E) Pore size distribution of particle E_0 , as determined from the pore network model (PNM). (F) Pore size distribution of particle K_0 .

By performing a binning simulation, a limited effect of the binning procedure on the results of the pore network model and grayscale image analysis was determined. As can be seen in **Figure 3.5** and **Table 3.4**, higher resampling (i.e., lower resolutions) did not significantly affect the porosity, pore space interconnectivity or radial analysis of particle E_0 . The features that are assessed in our data sets are thus considerably larger than the achieved spatial resolutions.

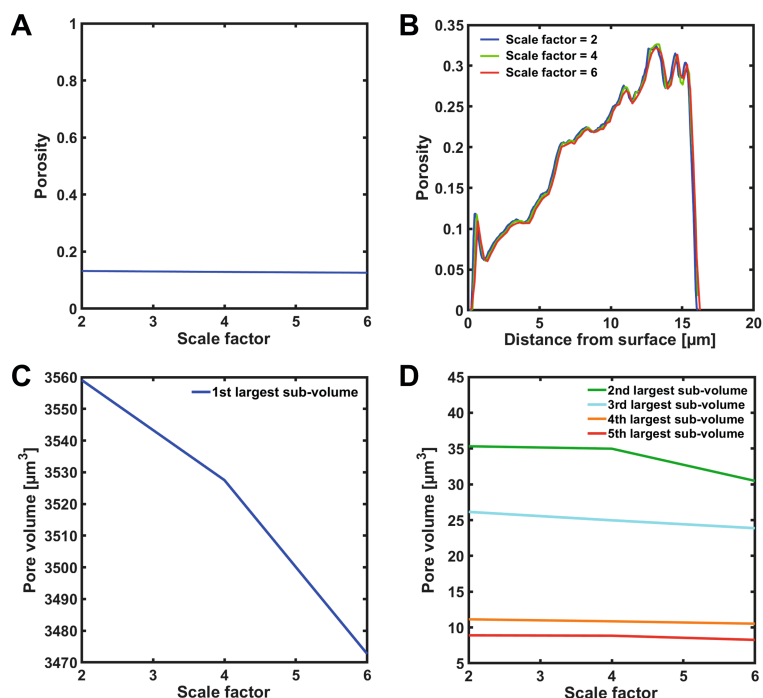


Figure 3.5 Effect of a reduced spatial resolution on the grayscale images analysis for catalyst particle E_0 . A total binning of 2, 4 and 6 is equivalent to an increase of the voxel size by a factor of 2, 4 and 6. The binning was performed via bicubic interpolation of the 2-times binned reconstructed data. (A) Effect of binning on the particle porosity. (B) Effect of binning on the radial porosity analysis. (C) Effect of binning on the volume of the particle's largest macropore space sub-volume. (D) Effect of binning on the volume of the 2nd–5th largest sub-volume of the particle's macropore space.

High NCRs (≥ 0.74) and porosities ($\geq 12\%$) (**Table 3.3**) were obtained for the pristine catalyst particles E_0 and K_0 and the pre-polymerized catalyst particle E_r , thus implying that the particles feature accessible and interconnected macropore networks at reaction onset. These allow ethylene to diffuse to large portions of the catalyst body. In contrast to this, the pre-polymerized catalyst particles E_{60-1} , E_{60-2} and K_{60-2} were evaluated to have relatively low NCR values (≤ 0.09) and porosities ($\leq 3\%$) (**Table 3.3**). This considerable reduction in macropore connectivity and porosity at low PE yields is assumed to impede mass transport throughout the catalyst particles at a relatively early reaction stage. No clear trend in tortuosity was observed as a function of reaction time.

Table 3.4 Metrics derived from the pore network model (PNM) for catalyst particle E_0 at multiple different binning factors.

Binning factor	2	4	6
Number of subgraphs	111	106 (-4%)	101 (-9%)
NCR	0.93	0.93 (0%)	0.91 (-2%)
Mean distance between all nodes (μm)	15.23	14.85 (-2%)	14.72 (-3%)
Longest segment (μm)	2.33	2.18 (-6%)	2.14 (-8%)
Mean tortuosity between all nodes	1.98	1.91 (-3%)	1.89 (-4%)

In general, the strong divergence of the above-mentioned metrics (i.e., porosity, NCR, tortuosity; **Table 3.3**) among catalyst particles from the same batch clearly indicates morphological heterogeneity, both in pristine and pre-polymerized particles. For the latter, such variations can be attributed to differences in reactivity. For example, the 10 min pre-polymerized catalyst particle K_{10} , in contrast to particle E_{10} , possesses a comparatively low NCR value (0.37). This, together with its uneven surface morphology (polymer-rich, **Figure 3.1**), suggests that the particle is more polymerized. A possible explanation is given by its rather small dimensions (ESD = 18.6 μm), which may have facilitated a relatively fast diffusion of ethylene throughout the particle. Another notable deviation was observed for catalyst particle K_{60-1} , which, considering its reaction stage, features a comparatively high porosity (0.06) and NCR (0.60). We postulate that this could be related to its initial support morphology. A similar observation also applies to catalyst particle K_{30-2} , which possesses a high NCR (0.76) and intermediate porosity (0.07). All in all, these outliers suggest that the reactivity of individual catalyst particles is related to their initial support and pore space architectures, which, in turn, govern mass and heat transport within the particles.

Because olefin polymerization and concurrent fragmentation are both expected to be correlated to the spatial arrangement of macropores, we visualized the 3D distribution of pore space sub-volumes (i.e., connected pore space voxels) and their relative distances to the catalyst particles' centroids (i.e., geometric center) in so-called dispersion plots (**Figures 3.4C, 3.4D** and **3.6**). Here, all pore space sub-volumes of the catalyst particles are visualized as small spheres, with the color of a sphere indicating the sub-volume's distance to the catalyst particle's centroid, denoted with a red cross in the respective figures. Each sphere is positioned at the centroid of the corresponding sub-volume and scales directly with the sub-volume's dimensions. The sphere representing the largest sub-volume therefore has the largest diameter and is labelled as '1' while sub-volumes smaller than 1% of the largest sub-volume ($V_{\text{threshold}} = 0.01 \times V_{\text{max}}$) are visualized as spheres with a fixed diameter (without a label). As is apparent from **Figures 3.4C** and **3.4D**, the pristine catalyst particles E_0 and K_0 are dominated by a single, extensive pore space sub-volume. In addition to this, smaller sub-volumes that are disconnected from the largest sub-volume are visible throughout the two particles. While particle E_0 features a low number of disconnected sub-volumes, particle K_0 features a significantly higher concentration of disconnected sub-volumes.

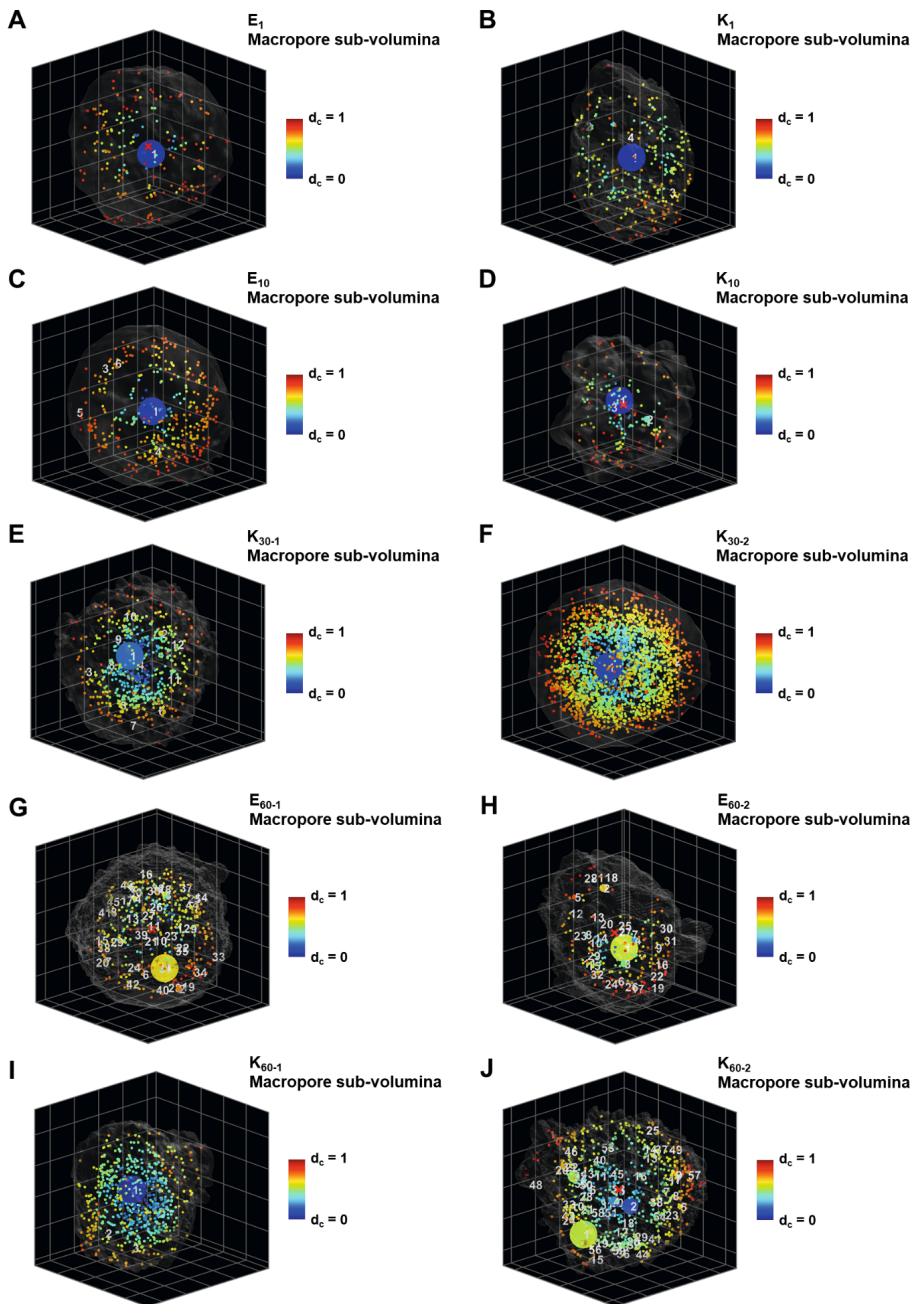


Figure 3.6 Dispersion plots for the macropore space sub-volumes of the pre-polymerized catalyst particles E_1 (A, $V_{\max} = 2,636 \mu\text{m}^3$, $V_{\text{threshold}} = 26 \mu\text{m}^3$), K_1 (B, $V_{\max} = 498 \mu\text{m}^3$, $V_{\text{threshold}} = 5.0 \mu\text{m}^3$), E_{10} (C, $V_{\max} = 2,843 \mu\text{m}^3$, $V_{\text{threshold}} = 28 \mu\text{m}^3$), K_{10} (D, $V_{\max} = 187 \mu\text{m}^3$, $V_{\text{threshold}} = 1.9 \mu\text{m}^3$), K_{30-1} (E, $V_{\max} = 303 \mu\text{m}^3$, $V_{\text{threshold}} = 3.0 \mu\text{m}^3$), K_{30-2} (F, $V_{\max} = 1,237 \mu\text{m}^3$, $V_{\text{threshold}} = 12 \mu\text{m}^3$), E_{60-1} (G, $V_{\max} = 658 \mu\text{m}^3$, $V_{\text{threshold}} = 6.6 \mu\text{m}^3$), E_{60-2} (H, $V_{\max} = 447 \mu\text{m}^3$, $V_{\text{threshold}} = 4.5 \mu\text{m}^3$), K_{60-1} (I, $V_{\max} = 1,215 \mu\text{m}^3$, $V_{\text{threshold}} = 12 \mu\text{m}^3$) and K_{60-2} (J, $V_{\max} = 183 \mu\text{m}^3$, $V_{\text{threshold}} = 1.8 \mu\text{m}^3$). D_c denotes the distance of a particle's pore space sub-volumes to its centroid.

This is also reflected by the larger number of sub-graphs in the PNM of particle K_0 (350) relative to particle E_0 (106) (Table 3.3). Both metrics indicate a lower degree of connectivity in catalyst particle K_0 , where approximately 6% of the macropore volume is disconnected from the central macropore system ($(V_{mp} - V_{max})/V_{mp}$), versus 0.5% in catalyst particle E_0 . Similar conclusions, in terms of connectivity, were also drawn from the calculated NCRs (lower NCR for K_0 relative to E_0). We expect such variations in pore space connectivity to lead to differences in reactivity during the initial reaction stages.

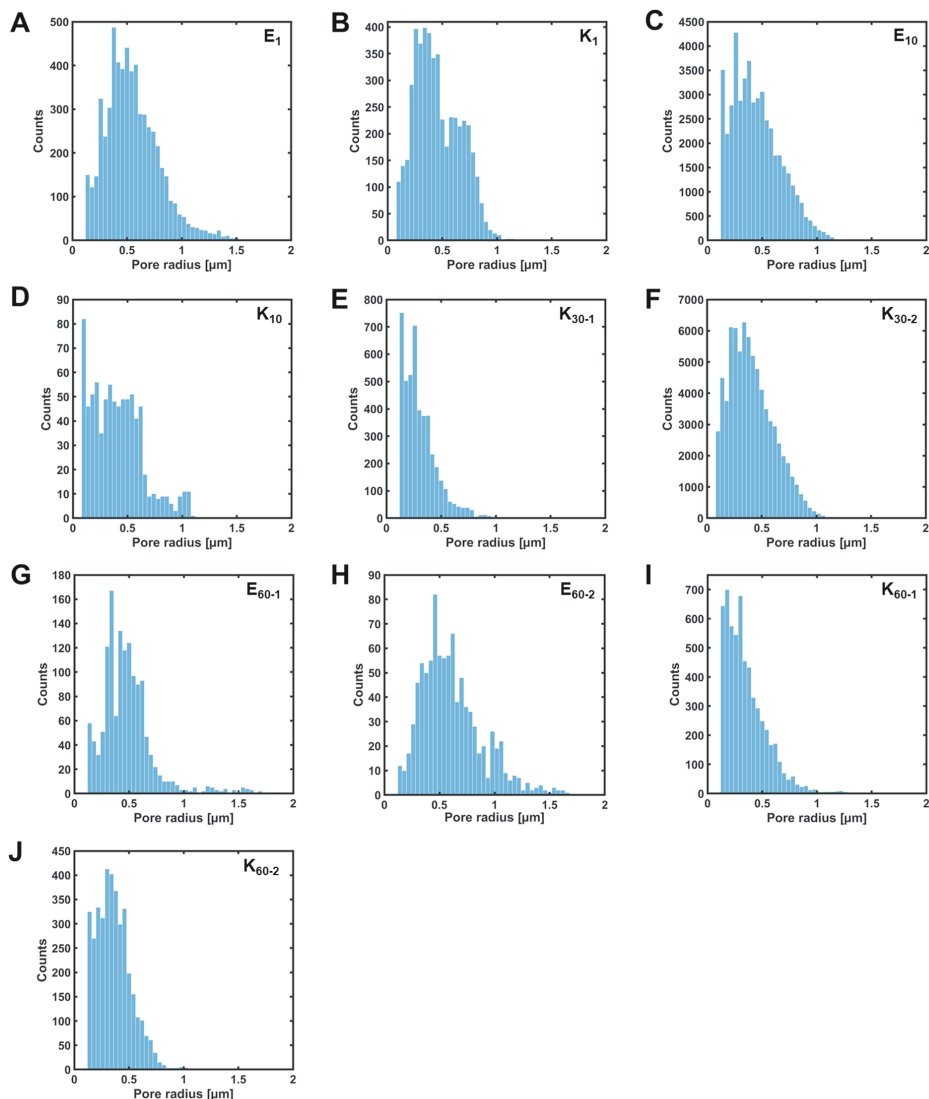


Figure 3.7 Pore size distributions (PSD) of the pre-polymerized catalyst particles E_1 (A), K_1 (B), E_{10} (C), K_{10} (D), K_{30-1} (E), K_{30-2} (F), E_{60-1} (G), E_{60-2} (H), K_{60-1} (I) and K_{60-2} (J). The PSDs only represent the macropores of the respective particles.

Finally, the established PNMs were used to approximate the catalyst particles' respective (macro)pore size distributions (PSDs) (**Figures 3.4E, 3.4F and 3.7**). As can be seen in **Figures 3.4E and 3.4F**, both pristine catalyst particles feature pores with diameters of 0.2 μm –3.4 μm , with a majority of the pore diameters falling in the range of 0.6–1.6 μm . The data stands in agreement with the pore size distribution of a comparable silica-supported metallocene, which was assessed via mercury porosimetry (**Figure 3.8**). By using the pore diameters from the pore network model as input values, the average volume of the pristine catalyst's detectable macropores (i.e., macropores that were successfully resolved with holotomography) was derived from the mercury porosimetry data. A total pore volume of ~ 0.2 mL/g was determined for all macropores in the range of 0.2–3.4 μm , which corresponds to a porosity of approximately 24%. Considering the porosities of particles E_0 and K_0 ($\leq 13\%$, **Table 3.3**), we believe that the detection and quantification of the macropore space is also affected by resolution limitations and the high degree of intermixing of support, polymer and macropores.

In contrast to the pristine particles, the pre-polymerized catalyst particles differed more strongly in terms of their PSDs (**Figure 3.7**). In general, the PSDs, together with the previously discussed radial analysis (**Figure 3.4**), NCRs (**Table 3.3**) and dispersion plots (**Figures 3.4 and 3.5**), clearly illustrate the variations in dimensions, interconnectivity and spatial distribution of the macropores in both pristine and pre-polymerized catalyst particles. This has considerable implications for both mass transport and reaction kinetics at the single particle level and can explain the morphological heterogeneity in pre-polymerized catalyst samples.

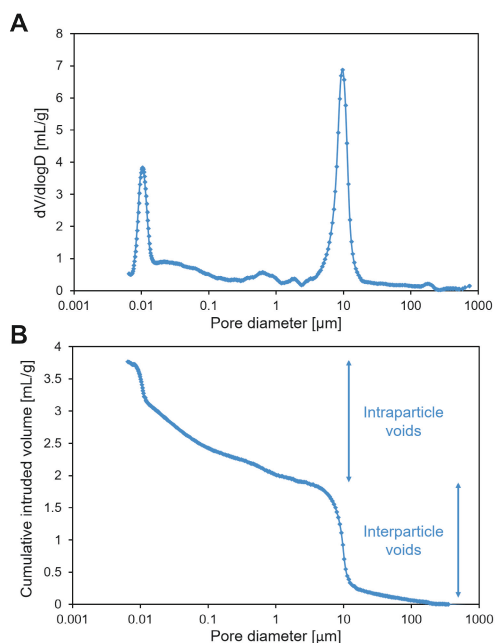


Figure 3.8 Mercury porosimetry data of a comparable ES757-supported zirconocene catalyst (Al/Zr molar ratio = 150 eq., 0.3 wt% Zr): (A) Pore size distribution of the catalyst, (B) Cumulative intrusion volume as a function of pore diameter.

3.3.3 Assessing Catalyst Particle Composition and Phase Distributions

As mentioned above, the 3D distribution of PE- and silica-dominant phases as well as macropores was determined for the pre-polymerized catalyst particles E_{60-1} and E_{60-2} ($6.4 \text{ g}_{\text{PE}}/\text{g}_{\text{cat}}$), based on the reconstructed and segmented X-ray holotomography data (Figure 3.9A–D). This yielded quantitative information on the particles' composition as well as phase distribution. While the two catalyst particles feature very similar percentages of pore space (1% versus 3%), particle E_{60-1} consists of a higher percentage of PE-dominant phase (67%) than particle E_{60-2} (59%). Radial phase distribution analysis revealed a high concentration of PE-dominant phase at the external surface of the catalyst particles (Figures 3.9E and 3.9F). In fact, both catalyst particles are enveloped by a thick layer of polymer-dominant phase. As can be deduced from the corresponding radial analysis plots, the polyethylene-rich shell occupies 15–20% in diameter of particle E_{60-2} , while the value is slightly lower for particle E_{60-1} . In both particles, diffusion limitations are likely to arise due to this pronounced surface build-up of polymer and consequent pore blocking.

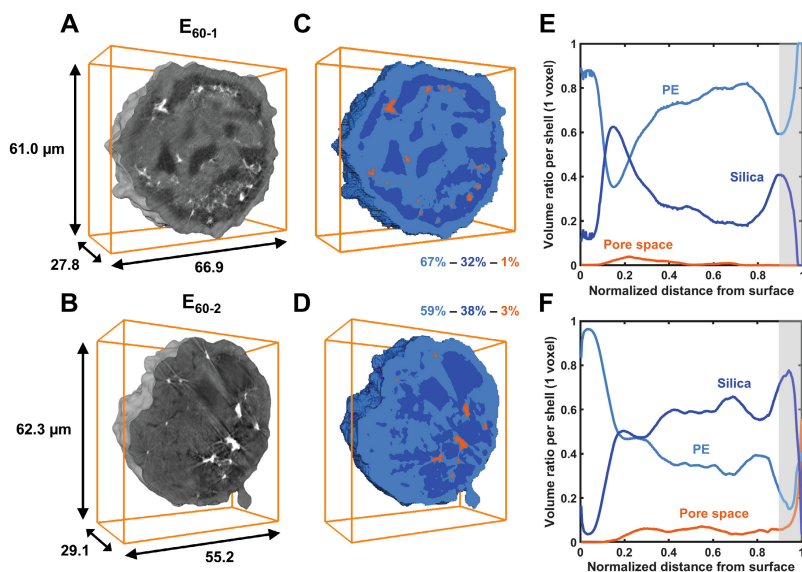


Figure 3.9 Assessment of the phase composition and distribution for catalyst particles E_{60-1} and E_{60-2} . (A) and (B) Reconstructed volumes and cross-sections of particles E_{60-1} and E_{60-2} (grayscale). (C) and (D) Segmented volumes and cross-sections of particles E_{60-1} and E_{60-2} (light blue, polymer-dominant phase; dark blue, silica-dominant phase; orange, macropores). (E) and (F) Radial analysis of the particle composition for E_{60-1} and E_{60-2} (d_s : central voxel, $d_s = 1$; surface: $d_s = 0$). The final 5–10% of the radial analysis (light gray) are typically ignored due to the limited number of voxels per shell at low remaining particle volumes (statistically insignificant regime).

Further notable differences, in terms of composition and phase distribution, become apparent when inspecting the respective interiors of the catalyst particles. Particle E_{60-1} exhibits a higher concentration of residual silica-dominant phase close to its surface, directly below

the layer of PE. The particle interior is, however, primarily composed of PE-dominant phase. Similar phase distributions were also observed for other catalyst particles that were assessed qualitatively in 2D with FIB-SEM (**Figures 3.1B** and **3.2**). The presence of substantial amounts of polymer-dominant phase in the particle interior as well as larger residual support-dominant phase in its outer sphere both indicate a strong involvement of the catalyst particle interior's accessible active sites in the polymerization process. Similar conclusions can also be drawn from reports by Conner *et al.*^[29,31] and Ruddick and Badyal^[54], who detected residual support fragments at the surface of other silica-supported catalyst systems at comparatively high PE yields.

The internal morphology of particle E_{60-2} differs strongly in comparison to that of particle E_{60-1} . In fact, its inner volume is constituted by more than 50% silica-dominant phase, thus indicating a less advanced degree of fragmentation. The surface build-up of polymer, in combination with potentially unfavorable dimensions and connectivity of the catalyst particle's macropore network, may have induced diffusion limitations, which consequently lead to a lower accessibility of the particle interior for gaseous ethylene monomer. A similar catalyst particle morphology was indeed also reported by Zaroni *et al.* for a gas-phase pre-polymerized zirconocene-based catalyst.^[55] Hence, we conclude that even under mild experimental conditions and at low polymer yields, diffusion limitations are highly likely to influence the polymerization rate and fragmentation of individual catalyst particles during gas-phase ethylene polymerization.

To further investigate the non-uniform fragmentation behavior of the two catalyst particles of interest, the number and average volume of silica-dominant and PE-dominant sub-volumes was determined as a function of their distance to the particles' respective centroids (d_c) (**Figure 3.10**). The analysis was performed using the segmented grayscale images. In both catalyst particles, the largest support- and polymer-dominant sub-volumes are located close to the particle centroids. This is also apparent from their corresponding dispersion plots (support-dominant sub-volumes, **Figures 3.10B** and **3.10F**; polymer-dominant sub-volumes, **Figures 3.10D** and **3.10H**). Featuring average volumes in the order of 10^4 – $10^5 \mu\text{m}^3$, these extensive silica- or PE-dominant sub-volumes occupy large portions of the catalyst particles' volumes. It is important to note, however, that the sub-volumes are irregular in shape and size.

When considering the remaining smaller sub-volumes, notable differences can be observed between particle E_{60-1} and particle E_{60-2} . As is evident from the corresponding histograms, the interior of catalyst particle E_{60-1} ($d_c < 0.8$) mainly features a limited number of low and intermediate volume silica-dominant sub-volumes ($10^{-3} \mu\text{m}^3 < V_{\text{avg, support}} < 10^1 \mu\text{m}^3$) while its periphery ($d_c > 0.8$) is constituted by a comparatively high number of low volume silica-dominant sub-volumes ($10^{-3} \mu\text{m}^3 < V_{\text{avg, support}} < 10^0 \mu\text{m}^3$) (**Figures 3.10A** and **3.10B**). PE-dominant sub-volumes, mostly low in volume ($10^{-3} \mu\text{m}^3 < V_{\text{avg, polymer}} < 10^0 \mu\text{m}^3$), are predominantly found in the outer sphere of the particle ($d_c > 0.8$) (**Figures 3.10C** and **3.10D**). Catalyst particle E_{60-2} , on the other hand, possesses a substantially higher number of low volume silica-dominant sub-volumes ($10^{-3} \mu\text{m}^3 < V_{\text{avg, support}} < 10^0 \mu\text{m}^3$) that are dispersed throughout the particle (**Figures 3.10E** and **3.10F**). In contrast to particle E_{60-1} , the PE-dominant sub-volumes of particle E_{60-2} are mostly located in the particle interior ($d_c < 0.8$) and have a limited volume ($10^{-3} \mu\text{m}^3 < V_{\text{avg, polymer}} < 10^0 \mu\text{m}^3$) (**Figures 3.10G** and **3.10H**).

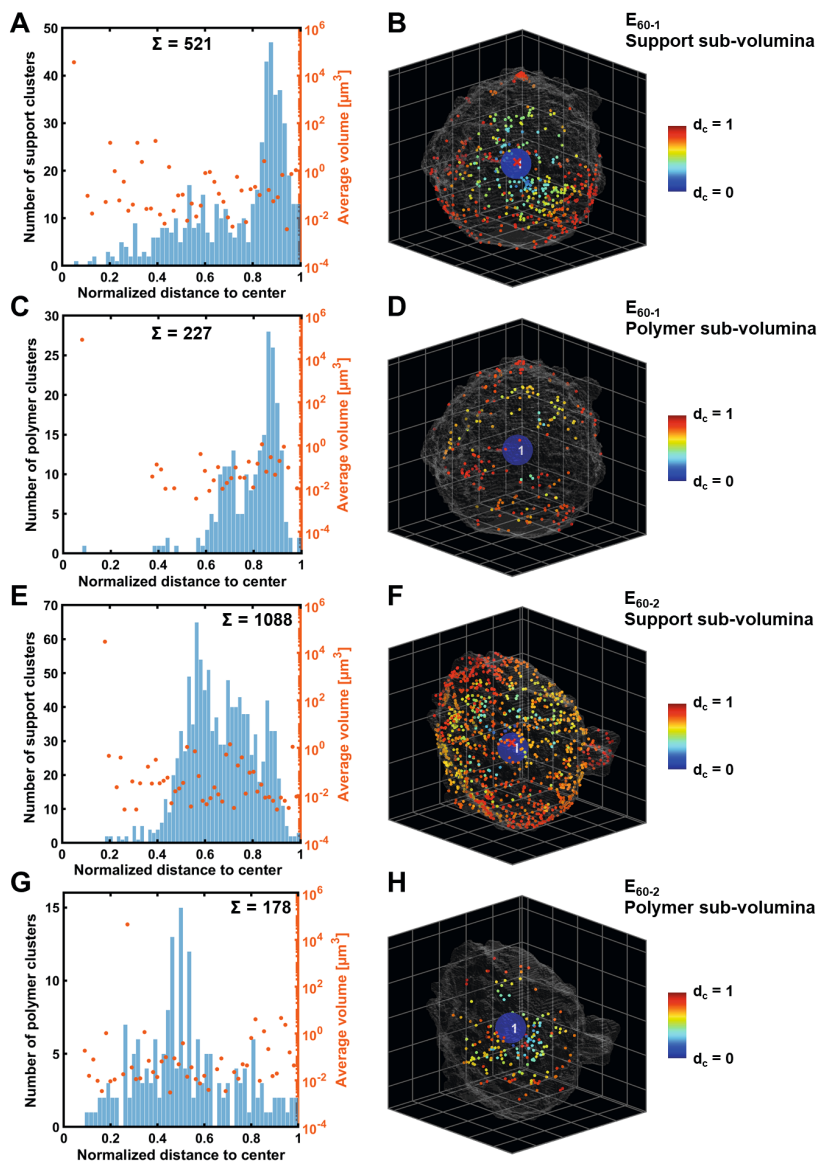


Figure 3.10 Number, volume and distribution of silica-dominant and polyethylene (PE)-dominant sub-volumes in catalyst particles E_{60-1} and E_{60-2} . (A) Number and average volume (V_{avg}) of silica-dominant sub-volumes (per bin) as a function of the normalized distance to the particle centroid (d_c) for particle E_{60-1} (center, $d_c = 0$; surface, $d_c = 1$). The total number of sub-volumes per particle is denoted as Σ . (B) Dispersion plot for the silica-dominant sub-volumes of particle E_{60-1} ($V_{\text{max}} = 36,371 \mu\text{m}^3$, $V_{\text{threshold}} = 364 \mu\text{m}^3$). (C) Number and average volume (V_{avg}) of PE-dominant sub-volumes for particle E_{60-1} . (D) Dispersion plot for the PE-dominant sub-volumes of particle E_{60-1} ($V_{\text{max}} = 77,089 \mu\text{m}^3$, $V_{\text{threshold}} = 771 \mu\text{m}^3$). (E) Number and average volume (V_{avg}) of silica-dominant sub-volumes for particle E_{60-2} . (F) Dispersion plot for the silica-dominant sub-volumes of particle E_{60-2} ($V_{\text{max}} = 29,152 \mu\text{m}^3$, $V_{\text{threshold}} = 292 \mu\text{m}^3$). (G) Number and average volume (V_{avg}) of PE-dominant sub-volumes for particle E_{60-2} . (H) Dispersion plot for the PE-dominant sub-volumes of particle E_{60-2} ($V_{\text{max}} = 44,726 \mu\text{m}^3$, $V_{\text{threshold}} = 447 \mu\text{m}^3$).

The higher total number (denoted as Σ) and dispersion of detectable silica-dominant sub-volumes in particle E_{60-2} , compared to particle E_{60-1} , further support the assumption that the particle is in a less advanced reaction stage. As previously observed in the radial analysis, both catalyst particles feature higher concentrations of residual support fragments close to the particle surface (represented by red and orange spheres in corresponding dispersion plots, **Figures 3.10B** and **3.10F**), where layer-by-layer fragmentation is assumed to be dominant (**Figure 3.2**).^[2]

With the collected tomography data clearly indicating strong morphological heterogeneity among pristine catalyst particles, we ascribe the differences in fragmentation and reactivity between particles E_{60-1} and E_{60-2} mainly to the specific arrangement and connectivity of their pristine silica support granulates. Mass transport and reaction kinetics at the single particle level are governed by the resulting non-ordered macropore networks and their corresponding accessibilities. In this context, we refer to findings by Abboud *et al.*^[56] and Machado *et al.*^[57], who observed non-uniform fragmentation behavior for silica-supported Ziegler-Natta and metallocene-based catalysts, respectively. While a catalyst's support structure is key to its morphological evolution, heterogeneous fragmentation pathways may also be partially introduced by the higher local accessibility of a certain particle domain or surface for incoming monomer gas at the onset of the reaction. These differences in accessibility may arise from particles' contact with other catalyst particles (agglomeration) or even the walls of the reactor. Consideration must also be given to the distribution of the metallocene complex, which may not be homogeneous at the sub-micrometer scale and will thus affect the local activity and fragmentation phenomena.

The absence of significant ruptures, propagating through the entire volume of the respective catalyst particles, leads us to believe that a pronounced sectioning pathway rarely occurs at particle level^[14,35,58] under the given experimental conditions (1.6 bar, room temperature, gas-phase). Instead, a strong involvement of a layer-by-layer fragmentation mechanism^[2,35,58] is postulated, both at the particle and individual silica domain level,^[55] due to the high accessibility of the particles' interior volume for ethylene gas (**Figures 3.1B**, **3.1C** and **3.2**). While the interior of catalyst particle E_{60-1} is assumed to have polymerized to a significant degree following this mechanism, the fragmentation of the interior of catalyst particle E_{60-2} was presumably impeded by diffusion limitations. In this case, the onset of more pronounced mass transfer limitations may lead to a larger involvement of the sectioning mechanism, which would otherwise remain more subdued under mild experimental conditions.

Based on our data, we postulate that a high degree of homogeneous support fragmentation may be achieved by means of (i) controlled pre-polymerization under carefully selected operating conditions (i.e., low temperature and pressure) and (ii) by using a catalyst with appropriate kinetics. Alternatively, a pre-polymerization with a less reactive monomer (e.g., propylene) can be performed, which is expected to yield similar results. In addition to the already discussed support configuration, both the applied experimental conditions and catalyst kinetics are instrumental in determining the accessibility of the silica granulates during the initial stages of the reaction.

The divergence in reactivity and fragmentation behavior that is observed within individual catalyst batches (i.e., reaction stages) does, however, underline the need for further studies using 3D imaging techniques such as holotomography, in which the morphology and fragmentation of a statistically relevant number of particles is assessed. Besides characterizing larger samples sets, the observed morphological heterogeneity also calls for the implementation of novel support synthesis strategies that lower the divergence in initial catalyst particle morphology. As the resolution of X-ray-based imaging techniques improves, polymer formation in the meso- and micropores may also be imaged, thereby yielding vital insights into their contributions to the morphological evolution of supported olefin polymerization catalysts. Finally, our work provides the foundation for future *in situ* studies to directly establish correlations between the initial catalyst particle structure and observed fragmentation pathways. The obtained quantitative data may also be useful for researchers working on the computational simulation of catalyst support fragmentation, possibly providing means of validating and expanding their computational models.

3.4 Conclusions

In this **Chapter**, full-field hard X-ray holotomography was shown to be highly suitable for obtaining quantitative information on the morphological evolution of supported olefin polymerization catalysts due to high spatial resolution (down to 246 nm), relatively low measurement times, and good sensitivity for low Z elements. The high acquisition speed of this analytical technique facilitated the characterization of multiple hafnocene-based catalyst particles at five different stages of ethylene polymerization. Image processing and analysis delivered quantitative insights into the particles' composition and porosity as well as the 3D distribution of support- and polymer-dominant sub-volumes within. This was further refined with a radial analysis of the support, polymer and macropore space distribution. Differences in pore space interconnectivity, tortuosity and pore size distribution were revealed by means of pore network modeling among both pristine and pre-polymerized catalyst particles. Furthermore, deviations in catalyst support fragmentation were evident at more advanced reaction stages. Based on the above-mentioned analysis and results, we conclude that the notable interparticle heterogeneity, observed both in terms of fragmentation degree and pathway, can be attributed to the unique configuration of the particles' respective supports and pore space networks. The general decrease in porosity and macropore space connectivity that was observed with increasing polymer yields underlines the importance of controlled catalyst support fragmentation in overcoming potential mass transfer limitations. A high degree of homogeneous support fragmentation, mainly manifested in form of a layer-by-layer mechanism, was achieved by means of (pre-)polymerization under mild conditions. On the whole, holotomography is suitable for obtaining highly resolved morphological and chemical information not only on olefin polymerization catalysts at high sample throughput, but also, on other heterogeneous catalyst system, such as polyolefin depolymerization catalysts, even under reaction conditions.

Acknowledgments

Tim Salditt (University of Göttingen) is gratefully acknowledged for his guidance and assistance in performing the X-ray holotomography experiments. Michael Sprung (DESY), Fabian Westermeier (DESY) and Markus Osterhoff (University of Göttingen) are thanked for their experimental support at the P10 beamline (PETRA III, DESY). Marina Eckermann (University of Göttingen) and Marianna Gambino (Utrecht University) are acknowledged for their assistance during sample preparation. Our appreciation also goes to Nicolaas Friederichs (SABIC) for his feedback on the collected data and manuscript. Delft Solids Solutions are acknowledged for the mercury porosimetry measurements.

References

1. G. Weickert, G. B. Meier, J. T. M. Pater, K. R. Westerterp, *Chem. Eng. Sci.* **1999**, *54*, 3291–3296.
2. G. Fink, B. Steinmetz, J. Zechlin, C. Przybyla, B. Tesche, *Chem. Rev.* **2000**, *100*, 1377–1390.
3. T. F. McKenna, J. B. P. Soares, *Chem. Eng. Sci.* **2001**, *56*, 3931–3949.
4. L. L. Böhm, *Angew. Chem. Int. Ed.* **2003**, *42*, 5010–5030.
5. J. R. Severn, J. C. Chadwick, R. Duchateau, N. Friederichs, *Chem. Rev.* **2005**, *105*, 4073–4147.
6. Z. Grof, J. Kosek, M. Marek, *AIChE J.* **2005**, *51*, 2048–2067.
7. T. F. L. McKenna, A. Di Martino, G. Weickert, J. B. P. Soares, *Macromol. React. Eng.* **2010**, *4*, 40–64.
8. J. T. M. Pater, G. Weickert, J. Loos, W. P. M. van Swaaij, *Chem. Eng. Sci.* **2001**, *56*, 4107–4120.
9. S. Knoke, F. Korber, G. Fink, B. Tesche, *Macromol. Chem. Phys.* **2003**, *204*, 607–617.
10. J. M. Zhou, N. H. Li, N. Y. Bu, D. T. Lynch, S. E. Wanke, *J. Appl. Polym. Sci.* **2003**, *90*, 1319–1330.
11. H. Hammawa, S. E. Wanke, *Polym. Int.* **2006**, *55*, 426–434.
12. H. L. Rönkkö, T. Korpela, H. Knuutila, T. T. Pakkanen, P. Denifl, T. Leinonen, M. Kemell, M. Leskelä, *J. Mol. Catal. A Chem.* **2009**, *309*, 40–49.
13. T. Taniike, V. Q. Thang, N. T. Binh, Y. Hiraoka, T. Uozumi, M. Terano, *Macromol. Chem. Phys.* **2011**, *212*, 723–729.
14. K. W. Bossers, R. Valadian, S. Zanoni, R. Smeets, N. Friederichs, J. Garrevoet, F. Meirer, B. M. Weckhuysen, *J. Am. Chem. Soc.* **2020**, *142*, 3691–3695.
15. K. W. Bossers, R. Valadian, J. Garrevoet, S. van Malderen, R. Chan, N. Friederichs, J. Severn, A. Wilbers, S. Zanoni, M. K. Jongkind, B. M. Weckhuysen, F. Meirer, *JACS Au* **2021**, *1*, 852–864.
16. J. D. Grunwaldt, C. G. Schroer, *Chem. Soc. Rev.* **2010**, *39*, 4741–4753.
17. F. Meirer, B. M. Weckhuysen, *Nat. Rev. Mater.* **2018**, *3*, 324–340.
18. I. D. Gonzalez-Jimenez, K. Cats, T. Davidian, M. Ruitenbeek, F. Meirer, Y. Liu, J. Nelson, J. C. Andrews, P. Pianetta, F. M. F. de Groot, B. M. Weckhuysen, *Angew. Chem. Int. Ed.* **2012**, *51*, 11986–11990.
19. S. R. Bare, M. E. Charochak, S. D. Kelly, B. Lai, J. Wang, Y. C. K. Chen-Wiegart, *ChemCatChem* **2014**, *6*, 1427–1437.
20. Y. S. Zhang, X. Lu, R. E. Owen, G. Manos, R. Xu, F. R. Wang, W. C. Maskell, P. R. Shearing, D. J. L. Brett, *Appl. Catal. B Environ.* **2020**, *263*, 118329.
21. F. Meirer, S. Kalirai, D. Morris, S. Soparawalla, Y. Liu, G. Mesu, J. C. Andrews, B. M. Weckhuysen, *Sci. Adv.* **2015**, *1*, e1400199.
22. F. Meirer, D. T. Morris, S. Kalirai, Y. Liu, J. C. Andrews, B. M. Weckhuysen, *J. Am. Chem. Soc.* **2015**, *137*, 102–105.
23. Y. Liu, F. Meirer, C. M. Krest, S. Webb, B. M. Weckhuysen, *Nat. Commun.* **2016**, *7*, 12634.
24. J. Ihli, R. R. Jacob, M. Holler, M. Guizar-Sicairos, A. Diaz, J. C. Da Silva, D. Ferreira Sanchez, F. Krumeich, D. Grolimund, M. Taddei, W. -C. Cheng, Y. Shu, A. Menzel, J. A. van Bokhoven, *Nat. Commun.* **2017**, *8*, 809.
25. J. Ihli, D. Ferreira Sanchez, R. R. Jacob, V. Cuartero, O. Mathon, F. Krumeich, C. Borca, T. Huthwelker, W. C. Cheng, Y. Y. Shu, S. Pascarelli, D. Grolimund, A. Menzel, J. A. van Bokhoven, *Angew. Chem. Int. Ed.* **2017**, *56*, 14031–14035.
26. P. Sprenger, T. L. Sheppard, J. P. Suuronen, A. Gaur, F. Benzi, J. D. Grunwaldt, *Catalysts* **2018**, *8*, 356.
27. M. Gambino, M. Veselý, M. Filez, R. Oord, D. Ferreira Sanchez, D. Grolimund, N. Nesterenko, D. Minoux, M. Maquet, F. Meirer, B. M. Weckhuysen, *Angew. Chem. Int. Ed.* **2020**, *59*, 3922–3927.
28. M. Veselý, R. Valadian, L. Merten Lohse, M. Toepperwien, K. Spiers, J. Garrevoet, E. T. C. Vogt, T. Salditt, B. M. Weckhuysen, F. Meirer, *ChemCatChem* **2021**, *13*, 2494–2507.
29. W. Curtis Conner, S. W. Webb, P. Spanne, K. W. Jones, *Macromolecules* **1990**, *23*, 4742–4747.
30. K. W. Jones, P. Spanne, S. W. Webb, W. C. Conner, R. A. Beyerlein, W. J. Reagan, F. M. Dautzenberg, *Nucl. Inst. Methods Phys. Res. B* **1991**, *56–57*, 427–432.
31. K. W. Jones, P. Spanne, W. B. Lindquist, W. C. Conner, M. Ferrero, *Nucl. Instruments Methods Phys. Res. Sect. B Beam Interact. with Mater. Atoms* **1992**, *68*, 105–110.

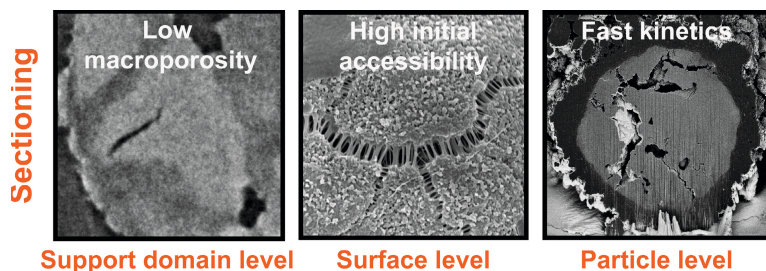
32. M. A. Ferrero, R. Sommer, P. Spanne, K. W. Jones, W. C. Conner, *J. Polym. Sci. Part A Polym. Chem.* **1993**, *31*, 2507–2512.
33. S. Boden, M. Bieberle, G. Weickert, U. Hampel, *Powder Technol.* **2008**, *188*, 81–88.
34. L. Seda, A. Zubov, M. Bobak, J. Kosek, A. Kantzas, *Macromol. React. Eng.* **2008**, *2*, 495–512.
35. J. B. P. Soares, T. F. L. McKenna, *Polyolefin Reaction Engineering*, Wiley-VCH, Weinheim, **2012**.
36. L. Meisterová, A. Zubov, K. Smolná, F. Štěpánek, J. Kosek, *Macromol. React. Eng.* **2013**, *7*, 277–288.
37. A. Alizadeh, T. F. L. McKenna, *Macromol. React. Eng.* **2018**, *12*, 1700027.
38. A. Diaz, P. Trtik, M. Guizar-Sicairos, A. Menzel, P. Thibault, O. Bunk, *Phys. Rev. B - Condens. Matter Mater. Phys.* **2012**, *85*, 020104(R).
39. F. Pfeiffer, *Nat. Photonics* **2018**, *12*, 9–17.
40. P. Cloetens, W. Ludwig, J. Baruchel, D. van Dyck, J. van Landuyt, J. P. Guigay, M. Schlenker, *Appl. Phys. Lett.* **1999**, *75*, 2912–2914.
41. O. Coindreau, G. Vignoles, P. Cloetens, *Nucl. Instruments Methods Phys. Res. B* **2003**, *200*, 308–314.
42. T. F. Morgeneyer, H. Proudhon, P. Cloetens, W. Ludwig, Q. Roirand, L. Laiarinandrasana, E. Maire, *Polymer* **2014**, *55*, 6439–6443.
43. A. Khimchenko, C. Bikis, A. Pacureanu, S. E. Hieber, P. Thalmann, H. Deyhle, G. Schweighauser, J. Hench, S. Frank, M. Müller-Gerbl, G. Schulz, P. Cloetens, B. Muller, *Adv. Sci.* **2018**, *5*, 1870036.
44. M. Töpperwien, F. van der Meer, C. Stadelmann, T. Salditt, *Proc. Natl. Acad. Sci. U. S. A.* **2018**, *115*, 6940–6945.
45. A.-L. Robisch, M. Eckermann, M. Töpperwien, F. van der Meer, C. Stadelmann-Nessler, T. Salditt, *J. Med. Imaging* **2020**, *7*, 013501.
46. T. Salditt, M. Osterhoff, M. Krenkel, R. N. Wilke, M. Priebe, M. Bartels, S. Kalbfleisch, M. Sprung, *J. Synchrotron Radiat.* **2015**, *22*, 867–878.
47. S. Zabler, P. Cloetens, J. P. Guigay, J. Baruchel, M. Schlenker, *Rev. Sci. Instrum.* **2005**, *76*, 073705.
48. V. Davidoiu, B. Sixou, M. Langer, F. Peyrin, *Proc. - Int. Symp. Biomed. Imaging* **2012**, *19*, 106–109.
49. L. M. Lohse, A. L. Robisch, M. Töpperwien, S. Maretzke, M. Krenkel, J. Hagemann, T. Salditt, *J. Synchrotron Radiat.* **2020**, *27*, 852–859.
50. D. Arthur, S. Vassilvitskii, in *Proc. Annu. ACM-SIAM Symp. Discret. Algorithms*, **2007**, 1027–1035.
51. M. Holler, A. Diaz, M. Guizar-Sicairos, P. Karvinen, E. Färm, E. Härkönen, M. Ritala, A. Menzel, J. Raabe, O. Bunk, *Sci. Rep.* **2014**, *4*, 3857.
52. F. Meirer, S. Kalirai, D. Morris, S. Soparawalla, Y. Liu, G. Mesu, J. C. Andrews, B. M. Weckhuysen, *Sci. Adv.* **2015**, *1*, e1400199.
53. F. Meirer, S. Kalirai, J. N. Weker, Y. Liu, J. C. Andrews, B. M. Weckhuysen, *Chem. Commun.* **2015**, *51*, 8097–8100.
54. V. J. Ruddick, J. P. S. Badyal, *J. Phys. Chem. B* **1997**, *101*, 1791–1793.
55. S. Zanoni, N. Nikolopoulos, A. Welle, A. Vantomme, B. M. Weckhuysen, *Catal. Sci. Technol.* **2021**, *11*, 5335–5348.
56. M. Abboud, P. Denifl, K. H. Reichert, *Macromol. Mater. Eng.* **2005**, *290*, 558–564.
57. F. Machado, E. L. Lima, J. C. Pinto, T. F. McKenna, *Polym. Eng. Sci.* **2010**, *51*, 302–310.
58. B. Horáčková, Z. Grof, J. Kosek, *Chem. Eng. Sci.* **2007**, *62*, 5264–5270.

Chapter 4

Elucidating the Sectioning Fragmentation Mechanism in Olefin Polymerization Catalysts with Laboratory-Based X-Ray and Electron Microscopy

This **Chapter** is based on the following scientific article:

M. J. Werny, D. Müller, C. Hendriksen, R. Chan, N. H. Friederichs, C. Fella, F. Meirer, B. M. Weckhuysen, *ChemCatChem* **2022**, *14*, e202200067. Copyright © 2022 Werny *et al.*, published by Wiley-VCH GmbH



Strict morphological control over growing polymer particles is an indispensable requirement in many catalytic olefin polymerization processes. In catalysts with mechanically stronger supports, e.g., polymerization-grade silicas, the emergence of extensive cracks via the sectioning fragmentation mechanism requires severe stress build-up in the polymerizing catalyst particle. In this **Chapter**, three factors that influence the degree of sectioning in silica-supported olefin polymerization catalysts are reported. Laboratory-based X-ray nano-computed tomography (nanoCT) and focused ion beam-scanning electron microscopy (FIB-SEM) were employed to study catalyst particle morphology and crack propagation in two showcase catalyst systems, i.e., a zirconocene-based catalyst (i.e., Zr/MAO/SiO₂, with Zr = 2,2'-biphenylene-bis-2-indenyl zirconium dichloride and MAO = methylaluminoxane) and a Ziegler-Natta catalyst (i.e., TiCl₄/MgCl₂/SiO₂), during slurry-phase ethylene polymerization. The absence of extensive macropores in some of the catalysts' larger constituent silica support granulates, a sufficient accessibility of the catalyst particle interior at reaction onset, and a high initial polymerization rate were found to favor the occurrence of the sectioning pathway at different length scales. While sectioning is beneficial for reducing diffusion limitations, its appearance in mechanically stronger catalyst supports can indicate a suboptimal support structure or unfavorable reaction conditions.

4.1 Introduction

Industrial olefin polymerization catalysts are well-established catalyst materials that have been in use for decades to produce some of mankind's most in demand high-performance materials, such as polyethylene and polypropylene.^[1] Despite the associated research field being quite mature, further insights into the functionality of these 'single-use' systems at the onset of polymerization remain highly desirable. It is during this critical stage that both the activity and final product morphology are determined by the concurrently occurring processes of polymer formation and support fragmentation.^[2] The stress-induced 'breaking apart' of the catalyst support not only exposes new active sites, but is also instrumental in overcoming mass and heat transfer limitations.^[3,4] Thus, to rationally design the next generation of supported olefin polymerization catalysts, it is paramount to further characterize and elucidate support fragmentation from a mechanistic point of view.

Various accounts from literature^[2,4-8], including recent studies by our group,^[9-13] report on the synergy of the layer-by-layer and sectioning mechanisms in facilitating the morphological evolution of supported olefin polymerization catalysts. Depending on the type of support and the reaction conditions that are employed, the contributions of either mechanism may become dominant (**Figure 4.1**). For instance, various groups have reported an instantaneous break-up of the relatively fragile MgCl_2 support in conventional Ziegler-Natta catalysts during propylene polymerization (**Figure 4.1**, particle morphologies **a** and **b**).^[8,14-18] Recent high-resolution 3D tomography studies on the fragmentation of comparable MgCl_2 -supported Ziegler-Natta and Ziegler-type catalysts, employed in slurry-phase propylene and ethylene polymerization, further confirmed that the sectioning mechanism is heavily involved in MgCl_2 -supported systems.^[9,10] In contrast to this, the fragmentation of metallocene-based catalysts, usually supported on mechanically firmer, less fragmentable SiO_2 supports, is often dominated by the layer-by-layer mechanism at the particle surface as well as at the level of the support's constituent granulates or domains, especially during ethylene polymerization (**Figure 4.1**, particle morphology **c**).^[6,11,12,19,20] Irrespective of the type of support, industrial operating conditions (i.e., high pressures and temperatures) or highly active catalytic sites can lead to more extensive contributions from the sectioning mechanism as a result of pronounced polymer build-up, mass transfer limitations and stress accumulation (e.g., particle morphologies **a** and **d** in **Figure 4.1**).^[8,11,12]

To obtain novel insights into the origins of the sectioning fragmentation mechanism, we investigated two industrial-grade silica-supported olefin polymerization catalysts, namely a zirconocene-based catalyst (i.e., $\text{Zr}/\text{MAO}/\text{SiO}_2$, with $\text{Zr} = 2,2'$ -biphenylene-bis-2-indenyl zirconium dichloride and $\text{MAO} = \text{methylaluminumoxane}$) and a Ziegler-Natta catalyst (i.e., $\text{TiCl}_4/\text{MgCl}_2/\text{SiO}_2$), that were both used in slurry-phase ethylene polymerization. The catalysts' respective morphologies were assessed using a combination of laboratory-based nano-computed tomography (nanoCT) and focused ion beam-scanning electron microscopy (FIB-SEM) (**Figure 4.2**). While FIB-SEM is widely employed for the morphological analysis of heterogeneous catalysts^[21-26], high resolution laboratory-based nanoCT represents a less frequently used yet accessible methodology for obtaining structural information and chemical information in 3D.

In recent years, nanoCT has successfully been employed to characterize a supported liquid metal catalyst for alkane dehydrogenation^[27], a zeolite material^[28], as well as electrochemical devices such as fuel cells^[29,30].

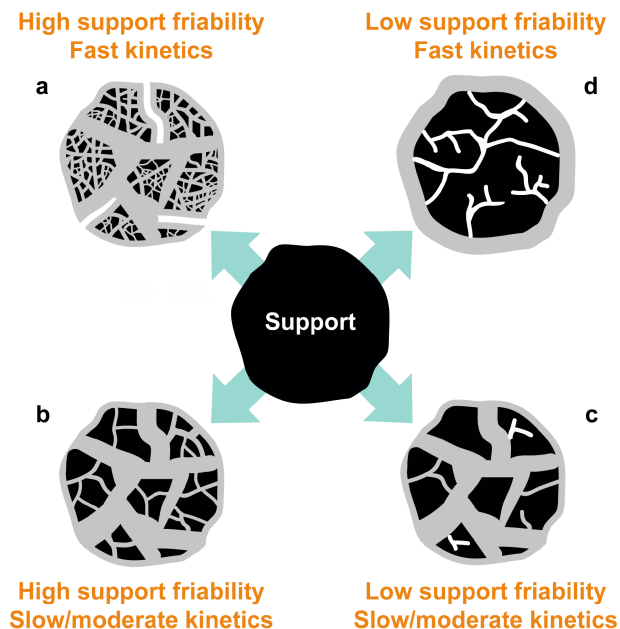


Figure 4.1 Schematic of the sectioning mechanism's contributions during catalytic olefin polymerization (black, support; gray, polymer; white, formed cracks; pores are not shown for simplification). The relative involvement of the sectioning mechanism is influenced by the friability of a catalyst's support, the catalyst's kinetics and the applied reaction conditions. Significant mass transfer limitations and stress generation lead to pronounced manifestations of the sectioning mechanism [particle morphologies (a) and (d)], while less pronounced mass transfer limitations and stress generation will lead to a more controlled fragmentation of the support, often involving the layer-by-layer mechanism (not shown for simplification) to a comparatively large extent [particle morphologies (b) and (c)]. The morphologies displayed above represent simplified showcases (post reaction onset) and do not address the full complexity of experimentally observed support fragmentation.

From an instrumental point of view, a handful of different technologies exist for laboratory-based nanoCT. This includes lens-based full-field microscopes^[28,31] as well as devices that operate in projection-based magnification, either featuring adapted SEM devices as the source^[32] or a nanofocus X-ray source^[33]. These devices can achieve 3D resolutions in the range of 50–150 nm. Due to the availability of various imaging technologies with different photon energies and fields of view, the choice of instrument ultimately depends on the sample and the required imaging parameters.

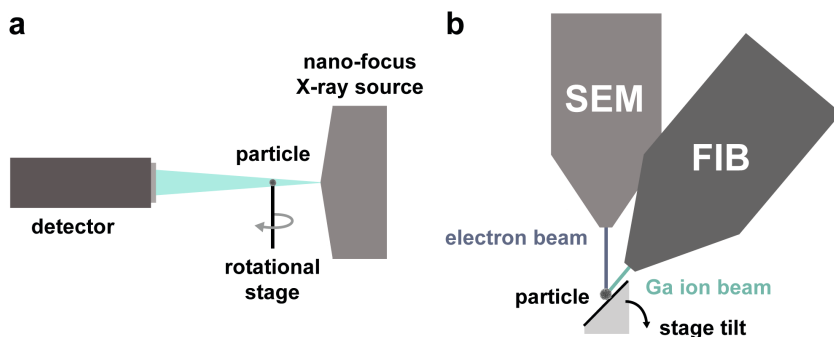


Figure 4.2 Schematic illustrations of the (a) nano-computed tomography (nanoCT) and (b) focused ion beam-scanning electron microscopy (FIB-SEM) set-ups that were used to characterize pristine and pre-polymerized particles of the Zr/MAO/SiO₂ (with MAO = methylaluminoxane) and TiCl₄/MgCl₂/SiO₂ catalysts.

The CT set-up employed in this study features a nanofocus X-ray source, covering an energy range of 5–110 keV.^[33–35] A variety of samples can be imaged under ambient conditions at 2D and 3D spatial resolutions of up to 150 nm and 170 nm, respectively.^[33–35] Specifically in the context of supported olefin polymerization catalysts, the technique delivers comprehensive information on the extent and magnitude of large-scale fragmentation phenomena (i.e., crack formation and propagation) and the 3D structure and phase distribution of individual particles^[2,4,36,37] – more so than other laboratory-based techniques such as SEM, which only yields 2D information^[11,17,19,38–42].

Thus, by using nanoCT in combination with FIB-SEM, we were able to identify three important factors that, in addition to the friability of a given support, are responsible for suboptimal monomer diffusion and stress generation, thus leading to a more frequent occurrence of the sectioning fragmentation mechanism in silica-supported olefin polymerization catalysts. The three contributing factors that we will discuss in this **Chapter** are: (i) A low degree of macroporosity at the level of the constituent support domains or particle level, (ii) a high particle accessibility during the initial reaction stages, and (iii) fast catalyst kinetics.

4.2 Experimental Methods

4.2.1 Sample Preparation

The silica-supported zirconocene catalyst was prepared according to the synthesis procedure described in **Chapter 2** of this PhD thesis.

The Ziegler-Natta catalyst ($\text{TiCl}_4/\text{MgCl}_2/\text{SiO}_2$) was synthesized by SABIC (Saudi Basic Industries Corporation) according to US patent 4374753 (Pullukat *et al.*). ES70X silica (PQ Corporation, $D_{50} = 50.0 \mu\text{m}$, $S_{\text{BET}} \approx 295 \text{ m}^2/\text{g}$, $V_{\text{pore}} \approx 1.6 \text{ mL/g}$), dried at $200 \text{ }^\circ\text{C}$ for 2 h, was first treated with hexamethyldisilazane (HMDS). After removal of unreacted HMDS and residual ammonia (NH_3), the support was subsequently impregnated with solutions of dibutylmagnesium/triethylaluminum in heptane ($\text{MgBu}_2/\text{TEA}/\text{heptane}$), 1-butanol (1-BuOH) and titanium tetrachloride (TiCl_4). A free flowing powder was obtained after drying the slurry under nitrogen flow at elevated temperatures. A weight loading of $\sim 3.8 \pm 0.2 \text{ wt}\%$ Ti was determined via X-ray Fluorescence Analysis (XRF), thus yielding a Mg/Ti ratio of 1.0 ± 0.1 .

To study the sectioning mechanism, a number of samples were prepared via slurry- or gas-phase ethylene polymerization at different pressures. The high-pressure polymerizations of the silica-supported zirconocene-based catalyst $\text{Zr}/\text{MAO}/\text{SiO}_2$ were performed at 10 bar or 15 bar ethylene pressure. The reactions were carried out at room temperature in a Parr autoclave set-up under stirring (570 rpm). For this, the autoclave was first loaded inside a nitrogen glovebox. Approximately 10 mL heptane and $3 \mu\text{L}$ triisobutylaluminum (TiBA, scavenger) were added to 10 mg of catalyst powder in a glass reactor. This glass reactor was then placed inside the autoclave. After removal from the glovebox, the autoclave was pressurized for approximately 10 s under continuous stirring to reach the desired pressure. The inlet valve was then closed. The period of pressurization is included in the total polymerization time (**Table 4.1**). To terminate the reaction, the valves of the autoclave were opened, and the formed polymer immediately removed from the glass reactor. The polymer was dried under air flow and weighed. Samples with yields of 2.1 g polyethylene (PE) per g catalyst were prepared at both 10 bar and 15 bar (**Table 4.1**).

The pre-polymerization of the $\text{Zr}/\text{MAO}/\text{SiO}_2$ catalyst at 1 bar was performed in a fume hood-based polymerization set-up at room temperature under inert conditions. 250 mL of dried hexane were added to a glass flask and saturated with ethylene (5 L/h) for 10 min while stirring at 300 rpm. A suspension of 180 mg of the catalyst in 10 mL hexane were then added with a pipet, while keeping the ethylene flow constant. The polymerization was terminated after 45 s by turn off the ethylene feed. The formed polymer was dried under nitrogen flow. The yield of the batch was derived from the equation $\text{CY} = (D_{\text{pol}}/(D_0 \times R_f))^3$, where CY = catalyst yield, $D_{\text{pol}} = D_{50}$ of the pre-polymerized catalyst sample ($D_{\text{pol}} = 26.1 \mu\text{m}$), $D_0 = D_{50}$ of the pristine catalyst sample ($D_0 = 25.0 \mu\text{m}$) and R_f = replication factor (defined as $R_f \approx 1$ due to the short polymerization time and limited average particle growth). The D_{50} of the pre-polymerized catalyst sample (D_{pol}) was derived from SEM images of 200 catalyst particles using ImageJ.

The pre-polymerization of the $\text{Zr}/\text{MAO}/\text{SiO}_2$ catalyst at 1.6 bar was performed at room temperature in a dedicated glass reactor ($\sim 100 \text{ mL}$) inside the glovebox. A mixture of $3 \mu\text{L}$ TiBA and 10 mL heptane was first added to 10 mg of the catalyst. The reactor was then briefly

evacuated and pressurized with ethylene for 1 min under stirring (500 rpm). The reaction mixture was also continuously stirred during the reaction. After 7.5 min, the reaction was terminated by removing the ethylene under vacuum. The reactor was then opened, the solvent decanted, and the pre-polymerized catalyst sample exposed to air. The yield was determined after drying the sample in air (**Table 4.1**). Additional details on the set-up can be found in previous work by our group.^[10,12]

The silica-supported Ziegler-Natta catalyst $\text{TiCl}_4/\text{MgCl}_2/\text{SiO}_2$ was pre-polymerized in slurry-phase at 7.5 bar ethylene pressure following the autoclave-based procedure as stated above. 13 μL TiBA (co-catalyst, 6.5 molar eq., $n(\text{Al})/n(\text{Ti}) = 6.5$) in 10 mL heptane were added to the catalyst in the glass reactor. Ethylene was introduced approximately 10 min after contacting the catalyst with the co-catalyst. The polymer was dried under air flow and weighed (**Table 4.1**).

The pre-polymerization of the $\text{TiCl}_4/\text{MgCl}_2/\text{SiO}_2$ catalyst at 0.6 bar ethylene pressure was also performed at room temperature in the glovebox-based glass reactor set-up as described above. 13 μL TiBA and 5 mL heptane were added to the glass reactor. The system was then pressurized with ethylene for 5 min under stirring (300 rpm). After turning the stirring off, the reactor was opened. 10 mg of the catalyst in 5 mL heptane were subsequently added. The reactor was repressurized with ethylene for 1 min under stirring. The reaction mixture was continuously stirred during the reaction. After 10 min, the reaction was terminated by removing the ethylene under vacuum. The reactor was then opened, the solvent decanted, and the pre-polymerized catalyst sample exposed to air. The weight of the polymer powder was determined after drying the sample in air (**Table 4.1**).

Table 4.1 Polyethylene (PE) yields in $g_{\text{PE}}/g_{\text{cat}}$ as obtained during the slurry-phase polymerization of ethylene with the Zr/MAO/ SiO_2 (with MAO = methylaluminoxane) and $\text{TiCl}_4/\text{MgCl}_2/\text{SiO}_2$ catalysts at room temperature.

Catalyst	p (bar)	t (min)	n(TiBA):n(M)	Yield ($g_{\text{PE}}/g_{\text{cat}}$)
Zr/MAO/ SiO_2	10	1.0	0.36	2.1
	15	1.0	0.36	2.1
	1	0.75	0	1.1*
	1.6	7.5	0.36	2.1
$\text{TiCl}_4/\text{MgCl}_2/\text{SiO}_2$	7.5	0.5	6.50	2.4
	7.5	1.0	6.50	6.4
	0.6	11	6.50	2.8

*PE yield determined from the D_{50} of the pre-polymerized catalyst sample.

The gas-phase pre-polymerization of the $\text{TiCl}_4/\text{MgCl}_2/\text{SiO}_2$ catalyst at 1 bar ethylene pressure and room temperature was performed in a stainless steel reaction cell. After impregnating the catalyst inside the glovebox with 3.25 molar eq. of TiBA in heptane, the catalyst was dried and loaded into the reaction cell. The cell was then taken out of the glovebox and connected to gas lines. After flushing the bypass of the cell with nitrogen (10 mL/min) for 10 min, ethylene was introduced to the cell at a flow rate of 1 mL/min. The reaction was terminated after approximately 60 min.

4.2.2 Nano-Computed Tomography

Nano-computed tomography (nanoCT) measurements were conducted using a laboratory-based X-ray computed tomography set-up based on lens-free X-ray projection magnification.^[33–35] The set-up features an Excillum Nanotube N2 110 kV (Excillum AB, Kista, Sweden) with a 500 nm thick tungsten transmission target as X-ray source and a DECTRIS EIGER2 R hybrid photon counting detector (DECTRIS AG, Baden-Daettwil, Switzerland) with a CdTe sensor. Additional details on the instrumentation can be found in the publications [32–34]. For each measurement, a pre-polymerized catalyst particle was mounted on the tip of a needle-shaped sample holder using epoxy glue, brought close to the X-ray source and scanned over a range of 360°. Voxel samplings in the range of 93–136.4 nm were used. The nanoCT data was reconstructed using an in-house developed filtered back-projection (FBP) algorithm, after which a phase retrieval was applied.^[33] Both sample drift and irregularities in the sensitivity of the detector pixels were corrected for. An average 3D spatial resolution of 177 nm was obtained based on Fourier Shell Correlation (FSC) analysis in IMAGIC FSC (Image Science Software GmbH, Berlin, Germany) using the half-bit criterion (1/2 bit of information per voxel, **Figure 4.3**).^[43]

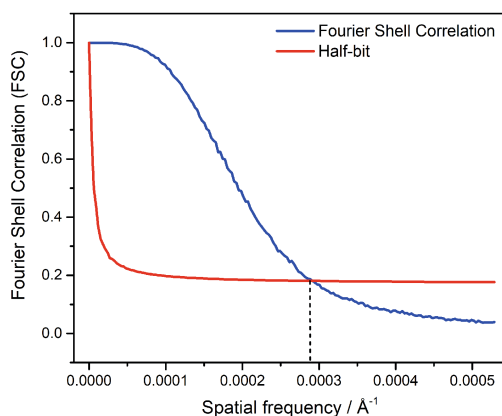


Figure 4.3 Fourier Shell Correlation (FSC) plot for particle $\text{ZN}_{7.5-1}$. The FSC curve and the 1/2-bit curve intersect at 342.9 nm, yielding an estimated 3D resolution of 171 nm.

For this, the original 2D projections of each data set were divided by angle into even and odd projections. Each set of projections was reconstructed using the FBP algorithm. The 3D Fourier transforms of both reconstructions were then used to determine their statistical correlation (i.e., normalized cross-correlation coefficient over their corresponding shells) in Fourier space as a function of spatial frequency (1/voxel size). By using the half-bit criterion as FSC threshold, the resolution was estimated as the intersection of the half-bit threshold curve with the FSC. The FSC analysis was performed on the reconstructed data sets prior to further image processing such as phase retrieval. Only reconstructed particles with well-defined features (e.g., macropores) delivered resolution values in an appropriate range. The resolutions of particles with low degrees of macroporosity were neglected. Additional information on the procedure can be found in

previous work by Müller and co-workers.^[33] Post processing and visualization of the reconstructed catalyst particles was performed using the Avizo™ software package by Thermo Fisher Scientific.

4.2.3 Focused Ion Beam-Scanning Electron Microscopy

Focused ion beam-scanning electron microscopy (FIB-SEM) experiments were performed according to the method described in **Chapter 2** of this thesis.

4.2.4 Diffuse Reflectance Infrared Fourier Transform Spectroscopy

Diffuse Reflectance Infrared Fourier Transform Spectroscopy (DRIFTS) experiments were performed *in situ* using a Bruker Tensor 37 spectrometer, equipped with a nitrogen cooled MCT (mercury cadmium telluride) detector, and a Harrick Praying Mantis™ High Temperature Reaction Chamber. For each measurement, the sample cup of the reaction chamber was loaded inside a nitrogen glovebox with a small amount of glass wool, a VICI Jour® stainless steel frit and 12 mg of the catalyst. While the Zr/MAO/SiO₂ catalyst did not require any form of activation, the TiCl₄/MgCl₂/SiO₂ catalyst was treated with 1.5 eq. triisobutylaluminum (TiBA) in pentane and subsequently dried. For each experimental run, the loaded reaction cell was transferred to the spectrometer and connected to the gas lines. All experiments were performed in gas-phase at room temperature using an ethylene flow of 5 mL/min at 1 bar. To avoid contamination and deactivation of the sample, the gas lines were flushed with nitrogen for 10 min before introducing ethylene to the reaction cell. FTIR spectra were recorded in 30 s intervals in the spectral range of 900–4500 cm⁻¹ with a 4 cm⁻¹ resolution and 16 s scan time. The data were evaluated using an in-house developed MATLAB™ code. First, the spectra were normalized to the highest band at approximately 1279 cm⁻¹. A background subtraction was then performed on all spectra using a normalized spectrum recorded of the catalyst under nitrogen atmosphere before the reaction. After reducing the spectral range to 2800–3200 cm⁻¹, Principal Component Analysis (PCA) was applied to the first five spectra that were recorded in the presence of ethylene. The first Eigenspectrum (first principal component) of each data set was fitted via a Least Squares Linear Combination (LSLC) fitting with 8 manually assigned pseudo-Voigt peaks (2851, 2890, 2920, 2958, 2988, 3011, 3077 and 3124 cm⁻¹; 2800 cm⁻¹ and 3200 cm⁻¹ defined as boundaries for fitting). The area of the peak fitted to the symmetric CH₂ stretching vibration band at 2851 cm⁻¹ was evaluated as a function of time. A polymerization rate was obtained from the first time derivative of this time evolution. All reported activity plots are based on the most active runs of the respective catalysts and were verified with a second measurement.

4.3 Results and Discussion

As is described in Section 4.2.1, the two silica-supported olefin polymerization catalysts under study (Zr/MAO/SiO₂, TiCl₄/MgCl₂/SiO₂) were synthesized according to two different procedures. Despite both catalysts being composed of compositionally identical polymerization-grade silicas with the same pore volume and surface area (refer to **Figure 4.4** for external and internal particle morphologies), the average particle sizes of the silica supports (Zr/MAO/

SiO₂: D₅₀ = 25 μm, TiCl₄/MgCl₂/SiO₂: D₅₀ = 50 μm) and, moreover, the chemical compositions of the supported metal-organic phases, differ significantly. It is thus difficult to draw parallels between these two catalyst systems when determining structure-activity correlations. However, novel insights related to the sectioning fragmentation mechanism were gained from investigating the morphologies of both catalysts. These are presented side-by-side in this **Chapter** to deliver a comprehensive overview of the different factors that can contribute to the sectioning pathway.

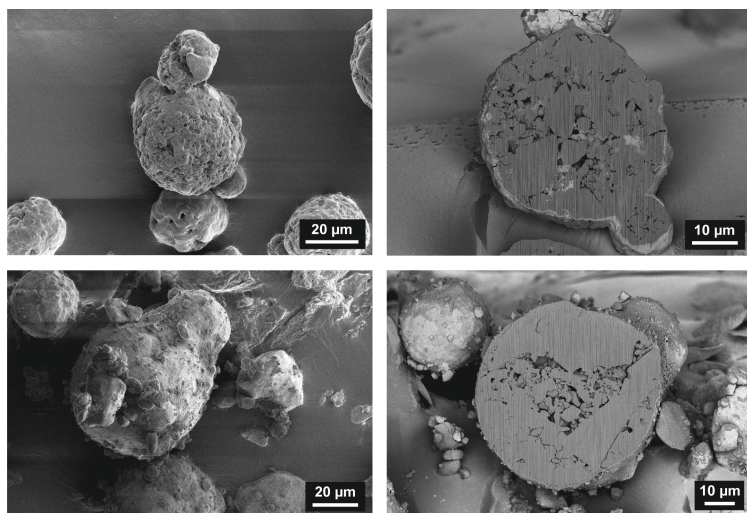


Figure 4.4 Scanning Electron Microscopy (SEM) images of the pristine Zr/MAO/SiO₂ catalyst (with MAO = methylaluminoxane) (top) and the pristine TiCl₄/MgCl₂/SiO₂ catalyst (bottom).

The catalysts were primarily studied after slurry-phase ethylene polymerization at room temperature and different pressures. Pre-polymerizations were performed for short time periods in an autoclave reactor at 7.5–15 bar ethylene, or in a fume hood-based polymerization set-up at ambient pressure, with the latter used to obtain low polymer yield samples ($\leq 6.4 \text{ g}_{\text{PE}}/\text{g}_{\text{cat}}$, PE = polyethylene; **Table 4.1**).

4.3.1 The Absence of Large Macropores Promotes Sectioning in the Catalyst Support Granulates

The silica-supported zirconocene-based catalyst was pre-polymerized for 1 min in slurry-phase at 10 bar and 15 bar ethylene pressure in the presence of low amounts of tri-isobutylaluminum (TiBA) as scavenger (obtained yield for both reactions: $2.1 \text{ g}_{\text{PE}}/\text{g}_{\text{cat}}$, **Table 4.1**). NanoCT was employed to characterize the 3D morphology of four particles from the sample pre-polymerized at 10 bar (Zr₁₀₋₁–Zr₁₀₋₄) at sub-180 nm spatial resolution. The tomographies and reconstructed cross-sections (i.e., virtual slices) of particles Zr₁₀₋₁–Zr₁₀₋₄ (**Figures 4.5a** and **4.6**) show that the catalyst particles' respective surfaces as well as large portions of

their interiors have fragmented due to the formation of polymer, presumably following the layer-by-layer mechanism.^[11,12]

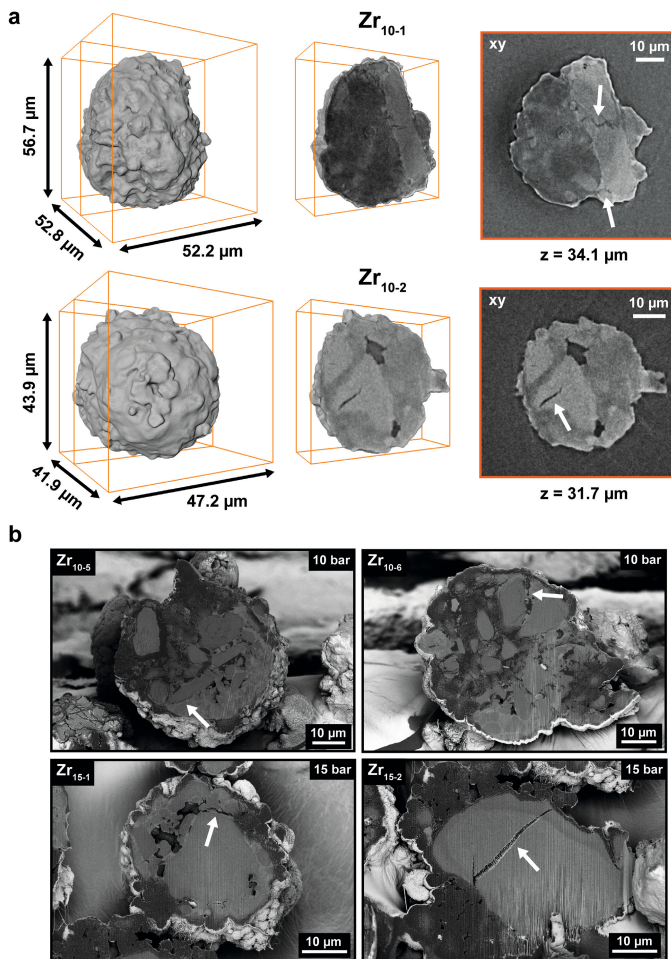


Figure 4.5 Morphological characterization of the Zr/MAO/SiO₂ catalyst (with MAO = methylaluminoxane) after slurry-phase pre-polymerization for 1 min at 10 bar and 15 bar ethylene pressure, respectively (room temperature, obtained yields: 2.1 g_{PE}/g_{cat}): (a) Reconstructed tomographies and corresponding virtual cross-sections of the two particles Zr₁₀₋₁ and Zr₁₀₋₂ from the 10 bar pre-polymerized batch. The light gray phase can be classified as support-dominant phase, while the dark gray phases correspond to the remaining particle volume (i.e., polymer-dominant phase + pore space). z is the depth of a given cross-section (xy) with z = 0 μm corresponding to the top of the particle. The formation of large cracks (i.e., sectioning) is indicated by white arrows. (b) Scanning electron microscopy (SEM; light gray, silica support; dark gray, polymer) images of selected catalyst particle cross-sections from the 10 bar (Zr₁₀₋₅, Zr₁₀₋₆) and 15 bar (Zr₁₅₋₁, Zr₁₅₋₂) batches.

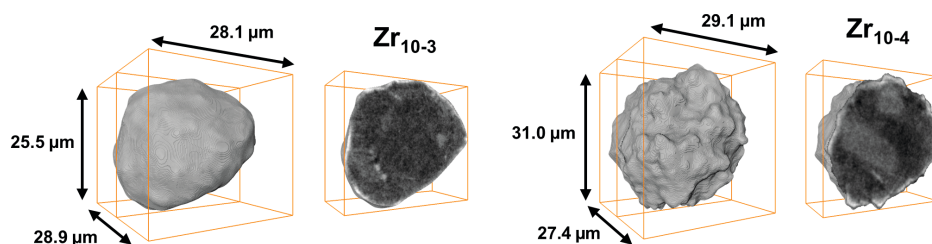


Figure 4.6 Reconstructed tomographies and corresponding virtual cross-sections of the two particles Zr_{10-3} and Zr_{10-4} from the 10 bar pre-polymerized $Zr/MAO/SiO_2$ ($MAO = \text{methylaluminoxane}$) catalyst batch. The light gray phase can be classified as support-dominant phase while the dark gray phase corresponds to the remaining particle volume (i.e., polymer-dominant domains + remaining pore space).

To verify our assumptions, FIB-SEM was performed on the two pre-polymerized catalyst batches (i.e., 10 and 15 bar; **Figure 4.5b**). All catalyst particles, to different extents, featured contributions from the sectioning mechanism. While its involvement may be subtle in the case of particle Zr_{10-5} , it is much more apparent in the remaining particles (Zr_{10-6} , Zr_{15-1} and Zr_{15-2}). Significant cracks were presumably formed in the affected domains due to high polymerization activity in adjacent regions (Zr_{10-5} , Zr_{10-6}), inherent structural weaknesses of the support (e.g., in close vicinity to the macropore space; Zr_{15-1}) as well as high polymerization rates at the particle surface (Zr_{15-1} , Zr_{15-2}). With most of the affected support domains lacking significant macroporosity, mass transport is limited, hence leading to more pronounced stress generation and crack formation.

The reconstructions of particles Zr_{10-1} and Zr_{10-2} , however, also clearly indicate a parallel involvement of the sectioning mechanism at silica granulate level, as is schematically illustrated in **Figure 4.1** (particle morphology **c**). Several larger silica domains, visibly lacking large macropores, have been penetrated and divided by extensive cracks (indicated by white arrows in **Figure 4.5a**). Sectioning in these polymer-embedded support granulates is attributed to the build-up of relatively large amounts of strain within the polymerizing particle. The support domains lack extensive macropore networks, which resulted in a lower accessibility of their active sites and increased the probability of significant local mass transfer limitations. The sectioning of the silica granulates effectively helped in overcoming these mass transfer limitations while instantaneously exposing a large amount of ‘buried’ active sites, which subsequently participate in the polymerization reaction. Contributions from the sectioning mechanism at the scale of several microns are vital for overcoming mass transfer limitations, especially under vigorous reaction conditions, i.e., at high monomer concentrations and temperatures, or in the presence of highly active catalytic sites.

The effect of severe mass transfer limitations is particularly obvious in particle Zr_{15-2} , which is cleaved by a substantial crack. This may have been related to a rapid build-up of polymer at the particle surface at high ethylene pressure (15 bar). With certain domains of the particle continuing to react, albeit at presumably lower rates, significant stress may have generated. This leads to a severe rupturing of the silica domain. Significant localized stress build-up and concurrent sectioning are also apparent in particles pre-polymerized at 1.6 bar ($2.1 \text{ g}_{PE}/\text{g}_{cat}$, **Table 4.1**; **Figure 4.7**), suggesting that the sectioning mechanism does also contribute to a

certain extent under milder conditions (i.e., at lower ethylene pressure and thus concentration). In general, this form of sectioning can take place at any stage of the reaction, provided mass transfer limitations and stress buildup are sufficient. Naturally, mass transfer limitations will be larger at higher polymer yields.

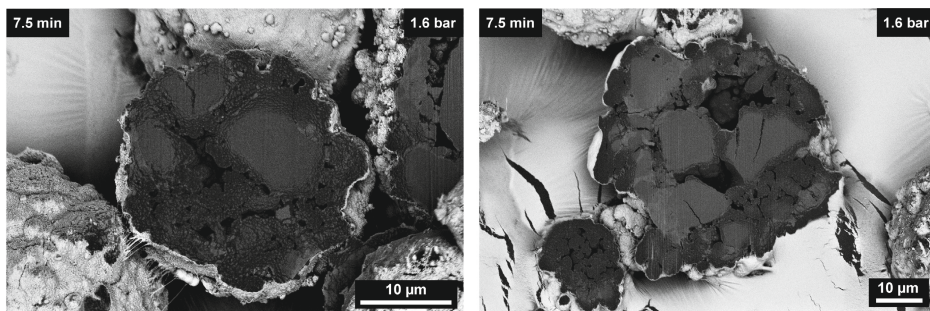


Figure 4.7 Scanning Electron Microscopy (SEM) images of the cross-sections of two Zr/MAO/SiO₂ (with MAO = methylaluminoxane) catalyst particles that were pre-polymerized in slurry-phase for 7.5 min at 1.6 bar ethylene pressure (room temperature, heptane, obtained yield: 2.1 g_{PE}/g_{cat}).

4.3.2 A High Initial Catalyst Particle Accessibility Facilitates Surface-Based Sectioning

To study the morphology of the Zr/MAO/SiO₂ catalyst at reaction onset, it was pre-polymerized in slurry-phase for 45 s at 1 bar ethylene pressure. Interestingly, a pronounced fragmentation of some of the particles' surfaces was observed (**Figure 4.8**). Due to the dimensions and spatial arrangement of the cracks, the process can be defined as surface-based sectioning. Strands of polyethylene are visible in these cracks (**Figure 4.8**, close-ups of particles Zr₁₋₁ and Zr₁₋₂, outlined in orange) and were presumably formed due to polymerization in the sub-surface layers of the particle. Subsequent crack formation caused the PE to be stretched.^[44] Polymer fibrils are also visible at the surface of particle Zr₁₋₁ (see areas in close vicinity to crack in close-up image), which rules out the scenario of extensive surface deactivation^[11].

Comparable particle morphologies, in terms of crack formation, have been reported by the group of McKenna, who used short stop reactors to pre-polymerize silica- and MgCl₂-supported olefin polymerization catalysts for extremely short reaction periods at elevated pressures.^[8,45–47] Similar observations were also made by Weist *et al.* for a silica-supported Phillips-type catalyst pre-polymerized in gas-phase at 1 bar ethylene pressure.^[48]

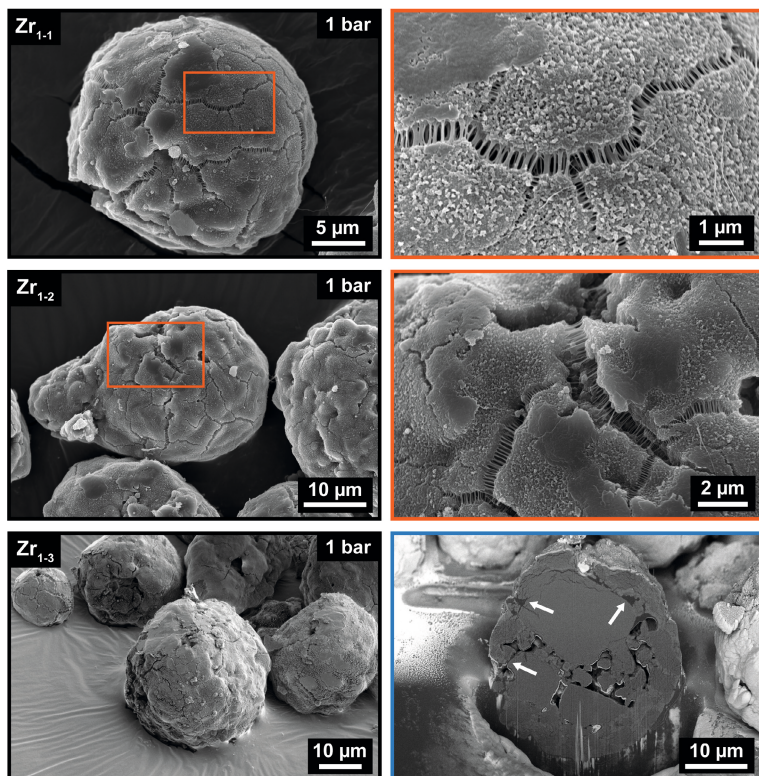


Figure 4.8 Morphological characterization of the Zr/MAO/SiO₂ catalyst (with MAO = methylaluminoxane) that was pre-polymerized in slurry-phase at 1 bar ethylene pressure (45 s, room temperature, estimated yield: 1.1 g_{PE}/g_{cat}): Scanning electron microscopy (SEM; light gray, silica support; dark gray, polymer) images of catalyst particles Zr₁₋₁, Zr₁₋₂ and Zr₁₋₃, including zoom-ins of catalyst particles Zr₁₋₁ and Zr₁₋₂ (orange) as well as the cross-section of catalyst particle Zr₁₋₃ (blue). In the latter, formed polymer is indicated by white arrows.

The formation of these cracks is presumed to be caused by the diffusion of ethylene throughout the macroporous catalyst particle, consequently leading to polymerization activity at all accessible active sites within the particle. The resulting strain from the expanding polymer-silica composite matrix initiates the large-scale fragmentation of the catalyst particles by opening up the compact catalyst support, exposing previously buried active sites and further enhancing the accessibility of the particle's interior for the incoming monomer. This is, in fact, evident from the cross-sectional analysis of a catalyst particle displaying surface fractures (Zr₁₋₃). The formation of polymer in the particle interior has led to significant stress-build up and fragmentation in the outer sphere of the catalyst particle (**Figure 4.8**, indicated by white arrows in the corresponding SEM image, outlined in blue; also refer to **Figure 4.9**). We believe that this form of fragmentation generally requires a high accessibility of the catalyst particle interior at the beginning of the reaction to ensure sufficient polymer formation in the interior. At higher ethylene pressures or at more advanced reaction stages, the accumulation of polymer at the particle surface is likely to fill the cracks. Fast catalyst

kinetics may even reduce the accessibility of the particle interior at reaction onset to such an extent that surface-based sectioning is suppressed.

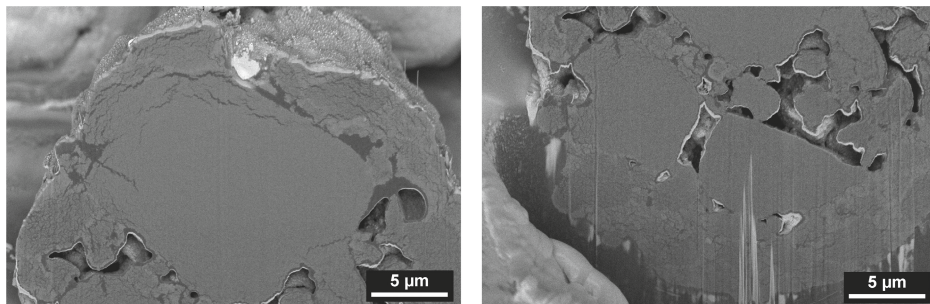


Figure 4.9 Scanning Electron Microscopy (SEM) images of the cross-section of catalyst particle $Zr_{1.3}$, pre-polymerized in slurry-phase for 45 s at 1 bar ethylene pressure (room temperature, hexane, obtained yield: $1.1 \text{ g}_{PE}/\text{g}_{cat}$).

4.3.3 Fast Polymerization Kinetics Induce Sectioning at the Particle Level

The sectioning mechanism was observed to play an instrumental role in the morphological evolution of a silica-supported Ziegler-Natta catalyst ($TiCl_4/MgCl_2/SiO_2$), pre-polymerized in slurry-phase for 1 min at 7.5 bar ethylene pressure (obtained yield: $6.4 \text{ g}_{PE}/\text{g}_{cat}$, **Table 4.1**). Before introducing ethylene, the catalyst was pre-contacted with 6.5 eq. TiBA (co-catalyst) in heptane for approximately 10 min. The catalyst's productivity (i.e., polyethylene yield) implies that the catalyst is kinetically faster than the Zr/MAO/ SiO_2 catalyst ($TiCl_4/MgCl_2/SiO_2$, $6.4 \text{ g}_{PE}/\text{g}_{cat}$, 7.5 bar, 1 min; Zr/MAO/ SiO_2 , $2.1 \text{ g}_{PE}/\text{g}_{cat}$, 10 bar, 1 min; **Table 4.1**). This was corroborated with diffuse reflectance infrared Fourier transform spectroscopy (DRIFTS), which delivered kinetic data on the formation of PE on the catalyst bed surface during gas-phase ethylene polymerization (**Figure 4.10**). As can be seen in **Figures 4.10a** and **4.10b**, the introduction of gaseous ethylene (see vibrational and roto-vibrational modes between 2980 and 3200 cm^{-1}) leads to the emergence of several bands in the $\nu(CH_x)$ spectral region (2800 – 3000 cm^{-1})^[49,50], indicative of methylene (CH_2) and methyl (CH_3) groups and thus the growth of PE chains. The rate of PE formation was calculated by integrating the $\nu_s(CH_2)$ band at 2851 cm^{-1} in the background corrected and fitted spectra (**Figures 4.10a** and **4.10b**) and subsequently forming the first time derivative thereof.

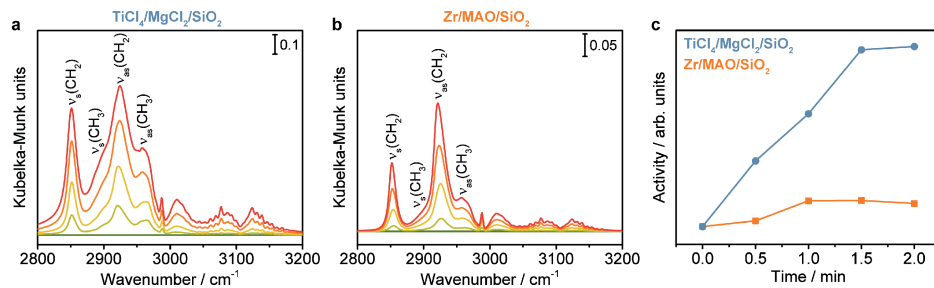


Figure 4.10 Diffuse reflectance infrared Fourier transform spectroscopy (DRIFTS) data collected on the $\text{TiCl}_4/\text{MgCl}_2/\text{SiO}_2$ (1.5 eq. triisobutylaluminum, TiBA) and $\text{Zr}/\text{MAO}/\text{SiO}_2$ catalysts (with MAO = methylaluminoxane) during gas-phase ethylene polymerization (1 bar ethylene, 5 mL/min, room temperature, 12 mg catalyst): (a) Background subtracted DRIFTS spectra of the $\text{TiCl}_4/\text{MgCl}_2/\text{SiO}_2$ catalyst (5 spectra, 2.0 min reaction time, transition from green to red), (b) Background subtracted DRIFTS spectra of the $\text{Zr}/\text{MAO}/\text{SiO}_2$ catalyst (5 spectra, 2.0 min reaction time, transition from green to red), and (c) Activities of the two catalysts plotted versus time, based on individual testing runs. The activities of the catalysts were determined as the time derivative of the $\nu_s(\text{CH}_2)$ stretching vibration band (2851 cm^{-1}) area, which represents the rate of polyethylene formation on the catalyst bed surface. Only spectra recorded in the first 2.0 min of ethylene polymerization were used for comparison due to an oversaturation of the DRIFTS signal after 2.0 min in the case of the $\text{TiCl}_4/\text{MgCl}_2/\text{SiO}_2$ catalyst (high rate of polyethylene formation).

As is evident in **Figure 4.10c**, the activity of the Ziegler-Natta catalyst increases significantly within the first 1.5 min of polymerization, especially when compared to the, under these conditions, markedly slower $\text{Zr}/\text{MAO}/\text{SiO}_2$ catalyst (**Figure 4.10b**). In fact, the technique can only be used to monitor the start of the polymerization reaction on the $\text{TiCl}_4/\text{MgCl}_2/\text{SiO}_2$ catalyst as the catalyst bed rises within minutes due to PE formation (**Figure 4.11**), leading to a strong baseline drift in the recorded spectra and an oversaturation of the IR signal. The relative decrease in activity after 1.5–2 min may be attributed to the onset of mass transfer limitations that are typical for this reaction stage (i.e., the pre-polymerization and induction regimes).^[19]

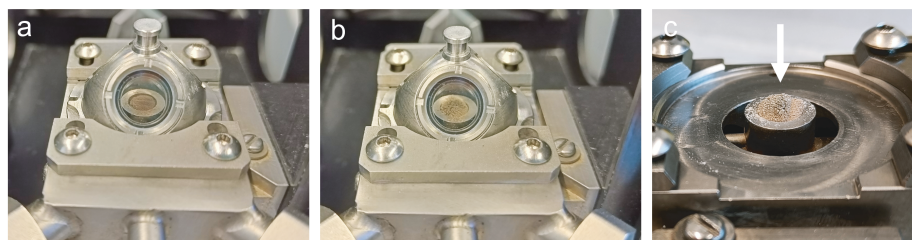


Figure 4.11 Images of a Harrick reaction cell loaded with 12 mg of the activated $\text{TiCl}_4/\text{MgCl}_2/\text{SiO}_2$ catalyst (1.5 eq triisobutylaluminum, TiBA) before (a) and after polymerization (b) with ethylene (5 mL/min, room temperature). The formation of polyethylene (PE) led to a visible expansion of the catalyst bed, as indicated by the white arrow (c).

To assess the impact of the $\text{TiCl}_4/\text{MgCl}_2/\text{SiO}_2$ catalyst's markedly faster rate of PE formation, the morphologies of two pre-polymerized catalyst particles were assessed with nanoCT ($\text{ZN}_{7.5-1}$, $\text{ZN}_{7.5-2}$; **Figure 4.12**). Both particles feature distinct shells of polyethylene that were formed via polymerization and layer-by-layer fragmentation in the peripheral regions of the particles. SEM images taken at an earlier reaction stage indicate that the polyethylene shell is directly formed upon exposure to ethylene (**Figure 4.13**). Since the polymer shell is formed at reaction onset, the access of both the monomer (i.e., ethylene) and the co-catalyst (i.e., TiBA) to the particle interior is restricted at an early reaction stage.^[51]

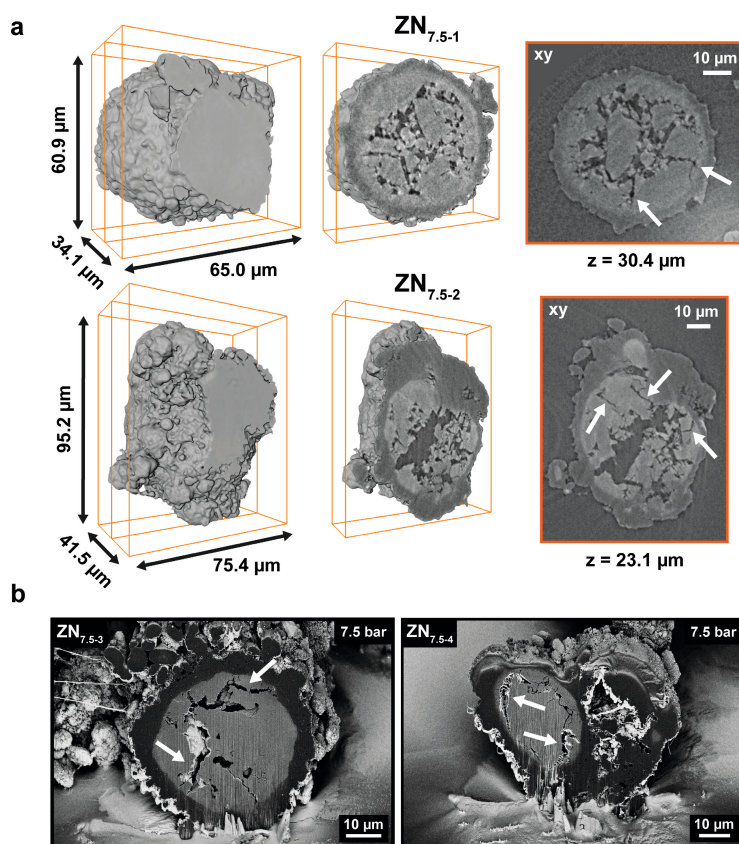


Figure 4.12 Morphological characterization of the $\text{TiCl}_4/\text{MgCl}_2/\text{SiO}_2$ catalyst pre-polymerized at 7.5 bar ethylene pressure (1 min, room temperature, slurry-phase, 6.5 eq. triisobutylaluminum (TiBA), obtained yield: $6.4 \text{ g}_{\text{PE}}/\text{g}_{\text{cat}}$): (a) Reconstructed tomographies and corresponding virtual cross-sections of two particles designated as $\text{ZN}_{7.5-1}$ and $\text{ZN}_{7.5-2}$. The light gray phase can be classified as support-dominant phase, while the dark gray phases correspond to the remaining particle volume (i.e., polymer-dominant phase + pore space). z is the depth of a given cross-section (xy) with $z = 0 \mu\text{m}$ corresponding to the top of the particle. The formation of large cracks (i.e., sectioning) is indicated by white arrows. (b) Scanning electron microscopy (SEM; light gray, silica support; dark gray, polymer) images of the cross-sections of two particles from the same batch ($\text{ZN}_{7.5-3}$ and $\text{ZN}_{7.5-4}$).

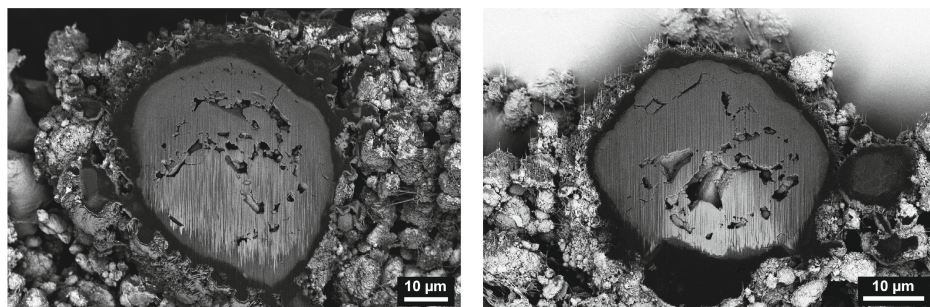


Figure 4.13 Scanning Electron Microscopy (SEM) images of the cross-sections of two $\text{TiCl}_4/\text{MgCl}_2/\text{SiO}_2$ catalyst particles that were pre-polymerized in slurry-phase for 0.5 min at 7.5 bar ethylene pressure (room temperature, heptane, 6.5 eq. triisobutylaluminum, obtained yield: $2.4 \text{ g}_{\text{PE}}/\text{g}_{\text{cat}}$).

Similar morphologies were also observed for other catalyst particles with FIB-SEM. As can be seen in **Figure 4.12b**, the remaining silica supports (light gray) of particles $\text{ZN}_{7.5-3}$ and $\text{ZN}_{7.5-4}$ feature extensive cracks and are enveloped by thick layers of polyethylene (dark gray), leading to higher stress accumulation and lower stress dissipation within the particle (**Figure 4.1**, particle morphology **d**). Interestingly, the presence of fines (i.e., smaller polymer spheres, **Figures 4.14** and **4.15**) in the pre-polymerized catalyst is suggestive of high or even uncontrolled catalyst activity at reaction onset (**Figure 4.10c**). The high monomer concentration at 7.5 bar, together with a relatively high concentration of co-catalyst (6.5 eq. TiBA), is likely to have contributed to substantial polymerization rates at the particles' surfaces. Similar morphologies were, however, also observed at low pressures (i.e., 0.6 bar; **Figures 4.14** and **4.15**). This leads us to believe that the catalyst's high reaction rate is inherently related to the kinetics of its active sites. The presence of smaller silica spheres in the pristine catalyst (**Figure 4.4**) may also contribute the formation of smaller polymer spheres.

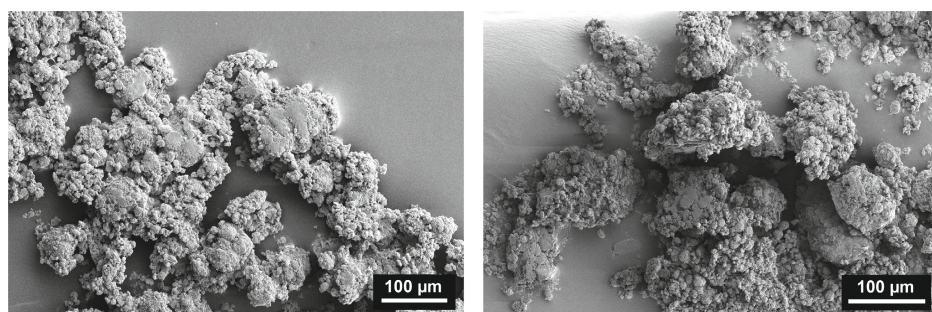


Figure 4.14 Scanning Electron Microscopy (SEM) overview images of the $\text{TiCl}_4/\text{MgCl}_2/\text{SiO}_2$ catalyst that was pre-polymerized in slurry-phase for 1 min at 7.5 bar ethylene pressure (left; room temperature, heptane, 6.5 eq. triisobutylaluminum, obtained yield: $6.4 \text{ g}_{\text{PE}}/\text{g}_{\text{cat}}$), and 11 min at 0.6 bar ethylene pressure (right; room temperature, heptane, 6.5 eq. TiBA, obtained yield: $2.8 \text{ g}_{\text{PE}}/\text{g}_{\text{cat}}$).

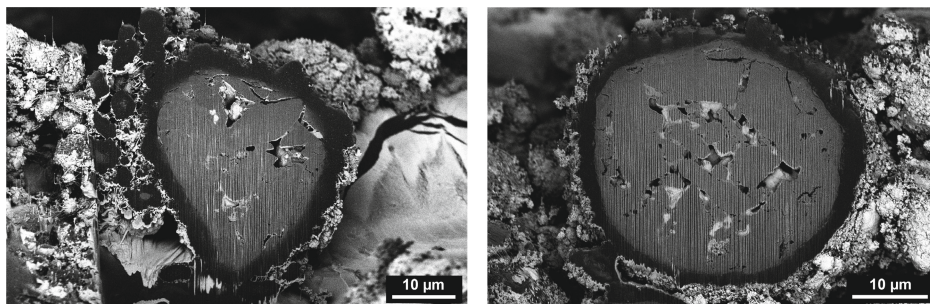


Figure 4.15 Scanning Electron Microscopy (SEM) images of two $\text{TiCl}_4/\text{MgCl}_2/\text{SiO}_2$ catalyst particles that were pre-polymerized in slurry-phase for 11 min at 0.6 bar ethylene pressure (room temperature, heptane, 6.5 eq. triisobutylaluminum, obtained yield: $2.8 \text{ g}_{\text{PE}}/\text{g}_{\text{cat}}$).

In addition to the surface build-up of polyethylene, the particles possess radial fractures ($> 10 \mu\text{m}$ in size) that are indicative of the sectioning fragmentation mechanism (indicated by white arrows in **Figure 4.12a**). Most notably in $\text{ZN}_{7.5-2}$, substantial crack formation is observed throughout the silica support. The cracks propagate several microns through the particle, thus suggesting that significant strain was generated due to polymer build-up and concurrent polymerization activity in the particle interior.

In general, the morphology of the pre-polymerized $\text{TiCl}_4/\text{MgCl}_2/\text{SiO}_2$ catalyst is a good example for illustrating correlations between high reaction rates and more extensive contributions from the sectioning mechanism at particle level. By adopting milder reaction conditions, diffusion limitations, imposed on both the monomer and the co-catalyst, may be reduced. This can facilitate a more controlled fragmentation of the catalyst via a layer-by-layer mechanism at particle and support domain (granulate) level. In fact, for a $\text{TiCl}_4/\text{MgCl}_2/\text{SiO}_2$ catalyst sample pre-polymerized in gas-phase at ambient pressure and at lower co-catalyst concentration (3.25 eq. TiBA, room temperature, **Figure 4.16**), layer-by-layer fragmentation was predominantly observed in the particle interiors. In addition to this, no thick surface layer of polymer was formed. This proves that the reaction conditions significantly affect mass transport and thus the degree to which a particular fragmentation pathway contributes. The formation of large void spaces, as observed for particles $\text{ZN}_{7.5-2}$ and $\text{ZN}_{7.5-4}$, may be linked to the dominance of the sectioning mechanism and may be contained by polymerizing under milder conditions, hence ensuring a higher bulk density of the product.

The morphological insights acquired on the high activity $\text{TiCl}_4/\text{MgCl}_2/\text{SiO}_2$ catalyst are also consistent with recent investigations by our group that revealed correlations between faster catalyst kinetics and a higher relative contribution of the sectioning mechanism during gas-phase ethylene polymerization in metallocene-based catalysts.^[12]

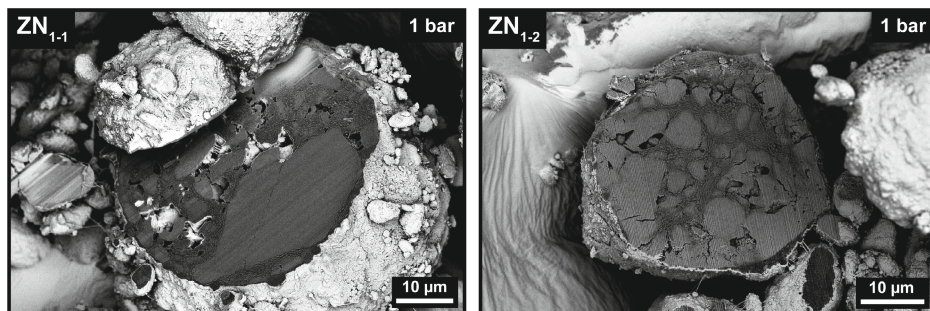


Figure 4.16 Scanning electron microscopy (SEM; light gray, silica support; dark gray, polymer) images of two $\text{TiCl}_4/\text{MgCl}_2/\text{SiO}_2$ catalyst particles (ZN_{1-1} and ZN_{1-2}) that were pre-polymerized in gas-phase for 60 min at 1 bar ethylene pressure (1 mL/min, room temperature, 3.25 eq. triisobutylaluminum, yield not determined).

4.4 Conclusions

New insights into the factors regulating the fragmentation behavior of industrial-grade, silica-supported olefin polymerization catalysts were gained using a combination of X-ray microscopy (i.e., laboratory-based nanoCT) and electron microscopy (FIB-SEM). A low macroporosity of the support, a high accessibility of a particle's interior volume during the early reaction stages, as well as fast polymerization kinetics were found to favor the occurrence of the sectioning mechanism, both at silica domain and catalyst particle level. In general, the contributions of the sectioning pathway to the fragmentation of a given catalyst particle are governed by the degree of mass transfer limitations and stress imposed upon a catalyst particle, which, in turn, are related to the catalyst's chemical and physical properties, as well as the applied polymerization conditions. While the cross-sectional analysis via FIB-SEM delivered highly resolved morphological information in 2D, the acquired nanoCT data provided more comprehensive insights into the composition of the catalyst particles, the spatial distribution of residual support domains and fragments, as well as crack formation and distribution in 3D. The results described in this **Chapter** demonstrate the suitability of laboratory-based nanoCT for research on heterogeneous catalysts, where high resolution morphological and structural data is desired.

Acknowledgments

Jochem Wijten (Utrecht University) is acknowledged for recording some of the SEM data on the pre-polymerized $\text{Zr}/\text{MAO}/\text{SiO}_2$ catalyst.

References

1. D. W. Sauter, M. Taoufik, C. Boisson, *Polymers* **2017**, *9*, 185.
2. J. B. P. Soares, T. F. L. McKenna, *Polyolefin Reaction Engineering*, Wiley-VCH, Weinheim, **2012**.
3. J. R. Severn, J. C. Chadwick, R. Duchateau, N. Friederichs, *Chem. Rev.* **2005**, *105*, 4073–4147.
4. A. Alizadeh, T. F. L. McKenna, *Macromol. React. Eng.* **2018**, *12*, 1700027.
5. G. Weickert, G. B. Meier, J. T. M. Pater, K. R. Westerterp, *Chem. Eng. Sci.* **1999**, *54*, 3291–3296.
6. X. Zheng, M. Smit, J. C. Chadwick, J. Loos, *Macromolecules* **2005**, *38*, 4673–4678.
7. B. Horáčková, Z. Grof, J. Kosek, *Chem. Eng. Sci.* **2007**, *62*, 5264–5270.
8. F. Machado, E. L. Lima, J. C. Pinto, T. F. McKenna, *Polym. Eng. Sci.* **2010**, *51*, 302–310.
9. K. W. Bossers, R. Valadian, S. Zaroni, R. Smeets, N. Friederichs, J. Garrevoet, F. Meirer, B. M. Weckhuysen, *J. Am. Chem. Soc.* **2020**, *142*, 3691–3695.
10. K. W. Bossers, R. Valadian, J. Garrevoet, S. van Malderen, R. Chan, N. Friederichs, J. Severn, A. Wilbers, S. Zaroni, M. K. Jongkind, B. M. Weckhuysen, F. Meirer, *JACS Au* **2021**, *1*, 852–864.
11. S. Zaroni, N. Nikolopoulos, A. Welle, A. Vantomme, B. M. Weckhuysen, *Catal. Sci. Technol.* **2021**, *11*, 5335–5348.
12. M. J. Werny, J. Zarupski, I. C. ten Have, A. Piovano, C. Hendriksen, N. H. Friederichs, F. Meirer, E. Groppo, B. M. Weckhuysen, *JACS Au* **2021**, *1*, 1996–2008.
13. M. J. Werny, R. Valadian, L. M. Lohse, A.-L. Robisch, S. Zaroni, C. Hendriksen, B. M. Weckhuysen, F. Meirer, *Chem Catalysis* **2021**, *1*, 1413–1426.
14. V. W. Buls, T. L. Higgins, *J. Polym. Sci Part A-1 Polym. Chem.* **1970**, *8*, 1037–1053.
15. M. Kakugo, H. Sadatoshi, M. Yokoyama, K. Kojima, *Macromolecules* **1989**, *22*, 547–551.
16. M. A. Ferrero, R. Sommer, P. Spanne, K. W. Jones, W. C. Conner, *J. Polym. Sci. Part A Polym. Chem.* **1993**, *31*, 2507–2512.
17. J. T. M. Pater, G. Weickert, J. Loos, W. P. M. van Swaaij, *Chem. Eng. Sci.* **2001**, *56*, 4107–4120.
18. X. Zheng, J. Loos, in *Macromol. Symp.*, **2006**, 249–258.
19. G. Fink, B. Steinmetz, J. Zechlin, C. Przybyla, B. Tesche, *Chem. Rev.* **2000**, *100*, 1377–1390.
20. Y. J. Jang, C. Naundorf, M. Klapper, K. Müllen, *Macromol. Chem. Phys.* **2005**, *206*, 2027–2037.
21. C. Wu, P. T. Williams, *Appl. Catal. B Environ.* **2010**, *96*, 198–207.
22. C. Ziegler, S. Thiele, R. Zengerle, *J. Power Sources* **2011**, *196*, 2094–2097.
23. R. Singh, A. R. Akhgar, P. C. Sui, K. J. Lange, N. Djilali, *J. Electrochem. Soc.* **2014**, *161*, F415–F424.
24. D. A. M. De Winter, F. Meirer, B. M. Weckhuysen, *ACS Catal.* **2016**, *6*, 3158–3167.
25. Y. Fam, T. L. Sheppard, A. Diaz, T. Scherer, M. Holler, W. Wang, D. Wang, P. Brenner, A. Wittstock, J. D. Grunwaldt, *ChemCatChem* **2018**, *10*, 2858–2867.
26. R. Mayorga-González, M. Rivera-Torrente, N. Nikolopoulos, K. W. Bossers, R. Valadian, J. Yus, B. Seoane, B. M. Weckhuysen, F. Meirer, *Chem. Sci.* **2021**, *12*, 8458–8467.
27. J. Wirth, S. Englisch, D. Drobek, B. Apeleo Zubiri, M. Wu, N. Taccardi, N. Raman, P. Wasserscheid, E. Spiecker, *Catalysts* **2021**, *11*, 810.
28. B. Apeleo Zubiri, J. Wirth, D. Drobek, S. Englisch, T. Przybilla, T. Weissenberger, W. Schwieger, E. Spiecker, *Adv. Mater. Interfaces* **2021**, *8*, 2001154.
29. Q. Meyer, J. Hack, N. Mansor, F. Iacoviello, J. J. Bailey, P. R. Shearing, D. J. L. Brett, *Fuel Cells* **2019**, *19*, 35–42.
30. T. M. M. Heenan, C. Tan, J. Hack, D. J. L. Brett, P. R. Shearing, *Mater. Today* **2019**, *31*, 69–85.
31. T. M. M. Heenan, D. P. Finegan, B. Tjaden, X. Lu, F. Iacoviello, J. Millichamp, D. J. L. Brett, P. R. Shearing, *Nano Energy* **2018**, *47*, 556–565.
32. F. Lutter, P. Stahlhut, K. Dremel, S. Zabler, J. Fell, H. G. Herrmann, R. Hanke, *Nucl. Instruments Methods Phys. Res. Sect. B Beam Interact. with Mater. Atoms* **2021**, *500–501*, 10–17.
33. D. Müller, J. Graetz, A. Balles, S. Stier, R. Hanke, C. Fella, *Crystals* **2021**, *11*, 677.

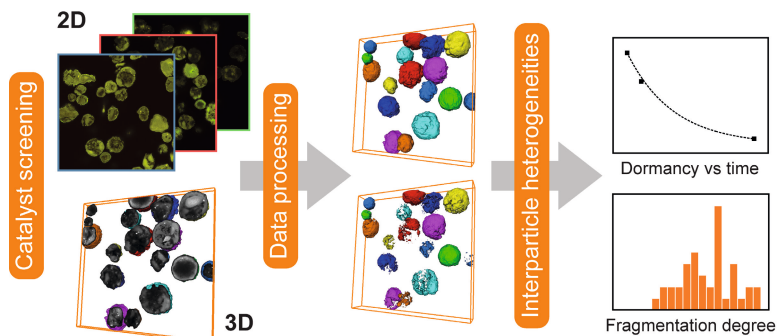
34. C. Fella, J. Dittmann, D. Muller, T. Donath, D. Murer, T. Tuohimaa, A. Sofiienko, S. Zabler, R. Hanke, *Microsc. Microanal.* **2018**, *24*, 234–235.
35. J. Graetz, D. Müller, A. Balles, C. Fella, *J. Instrum.* **2021**, *16*, P01034–P01034.
36. L. Seda, A. Zubov, M. Bobak, J. Kosek, A. Kantzas, *Macromol. React. Eng.* **2008**, *2*, 495–512.
37. L. Meisterová, A. Zubov, K. Smolná, F. Štěpánek, J. Kosek, *Macromol. React. Eng.* **2013**, *7*, 277–288.
38. G. Fink, B. Tesche, F. Korber, S. Knoke, *Macromol. Symp.* **2001**, *173*, 77–87.
39. S. Knoke, D. Ferrari, B. Tesche, G. Fink, *Angew. Chem. Int. Ed.* **2003**, *42*, 5090–5093.
40. J. M. Zhou, N. H. Li, N. Y. Bu, D. T. Lynch, S. E. Wanke, *J. Appl. Polym. Sci.* **2003**, *90*, 1319–1330.
41. X. Zheng, M. Smit, J. C. Chadwick, J. Loos, *Macromolecules* **2005**, *38*, 4673–4678.
42. H. Hammawa, S. E. Wanke, *Polym. Int.* **2006**, *55*, 426–434.
43. M. Van Heel, M. Schatz, *J. Struct. Biol.* **2005**, *151*, 250–262.
44. G. A. H. Nooijen, *Catal. Today* **1991**, *11*, 35–46.
45. F. M. Silva, J. P. Broyer, C. Novat, E. L. Lima, J. C. Pinto, T. F. McKenna, *Macromol. Rapid Commun.* **2005**, *26*, 1846–1853.
46. A. Di Martino, G. Weickert, T. F. L. McKenna, *Macromol. React. Eng.* **2007**, *1*, 165–184.
47. T. F. L. McKenna, E. Tioni, M. M. Ranieri, A. Alizadeh, C. Boisson, V. Monteil, *Can. J. Chem. Eng.* **2013**, *91*, 669–686.
48. E. L. Weist, A. H. Ali, B. G. Naik, W. C. Conner, *Macromolecules* **2002**, *22*, 3244–3250.
49. A. Piovano, K. S. Thushara, E. Morra, M. Chiesa, E. Groppo, *Angew. Chem. Int. Ed.* **2016**, *55*, 11203–11206.
50. A. Piovano, P. Pletcher, M. E. Z. Velthoen, S. Zanoni, S. H. Chung, K. Bossers, M. K. Jongkind, G. Fiore, E. Groppo, B. M. Weckhuysen, *ChemPhysChem* **2018**, 2662–2671.
51. G. A. H. Nooijen, *Eur. Polym. J.* **1994**, *30*, 11–15.

Chapter 5

Advancing the Compositional Analysis of Olefin Polymerization Catalysts with High-Throughput Fluorescence Microscopy

This **Chapter** is based on the following scientific article:

M. J. Werny, K. B. Siebers, N. H. Friederichs, C. Hendriksen, F. Meirer, and B. M. Weckhuysen, *J. Am. Chem. Soc.*, **2022**, *144*, 21287–21294. Copyright © 2022 Werny *et al.*, published by American Chemical Society.



To optimize the performance of supported olefin polymerization catalysts, novel methodologies are required to evaluate the composition, structure and morphology of both pristine and pre-polymerized samples in a resource-efficient, high-throughput manner. In this **Chapter**, we report on a unique combination of laboratory-based confocal fluorescence microscopy and advanced image processing that allowed us to quantitatively assess support fragmentation in a large number of autofluorescent metallocene-based catalyst particles. Using this approach, significant inter- and intraparticle heterogeneity was detected and quantified in a representative number of pre-polymerized catalyst particles (2D: ≥ 135 , 3D: 40). The heterogeneity that was observed over several stages of slurry-phase ethylene polymerization (10 bar) is primarily attributed to the catalyst particles' diverse support structures and to inhomogeneities in the metallocene distribution. From a mechanistic point of view, the 2D and 3D analyses revealed extensive contributions from a layer-by-layer fragmentation mechanism in synergy with a less pronounced sectioning mechanism. A significant number of catalyst particles were found to display limited support fragmentation at the onset of the reaction (i.e., at low polymer yields). This delay in activity or 'dormancy' is believed to contribute to a broadening of the particle size distribution during the early stages of polymerization. Extensive 2D and 3D screening via confocal fluorescence microscopy represents an accessible and fast approach to characterize the structure of heterogeneous catalysts and assess the distribution of their fluorescent fluorescent components and reaction products. The automation of both image segmentation and post-processing with machine learning results can yield a powerful diagnostic tool for future research as well as quality control on industrial catalysts.

5.1 Introduction

Silica-supported metallocenes represent a promising class of industrial olefin polymerization catalysts due to their high activities and their ability to produce polyolefins with tailored properties.^[1,2] The single-site character of their active sites essentially facilitates the production of narrow molecular weight polymers with well-defined tacticity and co-monomer incorporation.^[3,4] Industrial, supported metallocene-based catalysts typically consist of high porosity, amorphous silica particles in a size range of 20–100 μm , impregnated with a group 4 transition metal complex, usually zirconium-based, and methylaluminoxane (MAO) as a co-catalyst.^[5] The immobilization of the metallocene limits reactor fouling and, moreover, ensures a uniform morphology and high bulk density of the produced polymer particles.^[6]

The activity and morphological evolution of supported catalysts are both governed by the phenomenon of fragmentation, i.e., the disintegration of the catalyst support due to polymer formation.^[7,8] The process releases new active sites and promotes homogeneous particle growth (replica effect), thereby limiting the formation of fines, which also contribute to reactor fouling.^[9–11] Fragmentation plays an important role in overcoming mass and heat transfer limitations, which would otherwise severely affect catalyst performance and product properties.^[6,8] Thus, to optimize existing catalyst designs as well as to improve the physical and mechanical properties of the formed polymers, a more comprehensive understanding of the factors controlling the process of support fragmentation is necessary.

A common approach to evaluate the internal morphology of supported polymerization catalyst particles involves accessing particle cross-sections via microtoming or focused ion beam (FIB) cutting and subsequent imaging via scanning electron microscopy (SEM).^[12–19] Despite yielding highly resolved morphological data, this approach remains laborious, destructive and, moreover, does not provide 3D resolved data. Synchrotron- and laboratory-based X-ray nanotomography experiments, on the other hand, provide unparalleled 3D imaging capabilities at high spatial resolutions but are elaborate in terms of sample preparation, experimental execution and data analysis.^[20–23] Both approaches, moreover, deliver limited physicochemical and catalytic information due to their low sample throughput. While multiple olefin polymerization catalyst particles have recently been studied with hard X-ray nanotomography^[21], the characterization of a large number of particles was facilitated by the comparatively small average particle size of the investigated catalyst (i.e., 5.9 μm).

In this **Chapter**, we present a more accessible approach for multiparticle analysis based on confocal fluorescence microscopy (CFM). The laboratory-based technique can deliver both 2D and 3D morphological data at high sample throughput due to its large field of view (FOV) and short measurement times (2D: < 1 min for 178 μm x 178 μm FOV, 3D: ~ 2 h for 178 μm x 178 μm x 30 μm) (**Figure 5.1**). Fluorescence microscopy is widely used in biology and in the life sciences to selectively visualize cellular components and processes, usually in combination with fluorescent probe molecules.^[24–27] Its application in the field of catalysis is, however, more recent and ranges from the investigation of, amongst others, the pore space architecture in catalyst extrudates to mapping Brønsted acidity in industrial catalysts.^[28–35] Specifically in the context of olefin polymerization catalysis, fluorescence microscopy has been employed

to visualize monomer incorporation and the formation of nascent polymer^[36–39], as well as to qualitatively assess support fragmentation in individual catalyst particles^[40–43]. Building on this, we employed fluorescence microscopy in combination with advanced image processing to obtain quantitative insights into the morphology of a large number of silica-supported zirconocene-based catalyst particles that display autofluorescence.

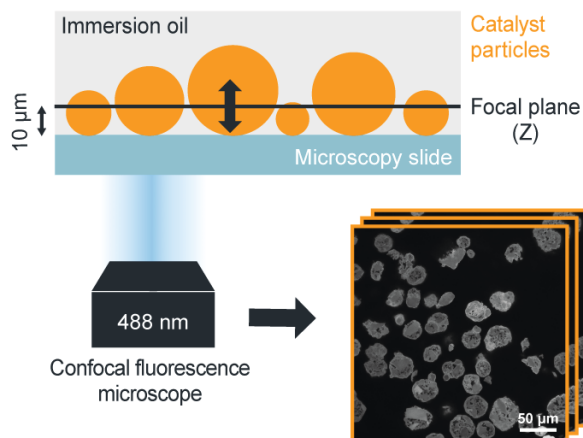


Figure 5.1 Schematic illustration of the high-throughput confocal fluorescence microscopy (CFM) approach that was employed for the characterization of the autofluorescent Zr/MAO/SiO₂ catalyst samples. Multiple metallocene-based catalyst particles were excited with a 488 nm laser and scanned at different focal depths using an oil immersion objective to obtain Z-stacks of fluorescence microscopy images. These Z-stacks were then converted into 3D tomographies by means of image processing. To record and compare 2D data, all samples were measured at a fixed focal depth of 10 μm.

As CFM does not require intensive sample preparation and, moreover, facilitates high-throughput experimentation, it represents an attractive laboratory-based alternative to X-ray-based experimentation for assessing the morphology of extensive sample sets. Ultimately, it can be used as a high-throughput tool to assess the quality and state of different heterogeneous catalysts after synthesis, as well as after reaction. Taking the autofluorescent zirconocene-based catalyst as an example, the spatial distribution of the metallocene on the support delivers information on the quality of the pristine catalyst after synthesis. Ideally, the support is homogeneously impregnated with the metallocene. In pre-polymerized particles, the fluorescence of the metallocene directly yields the distribution of the catalyst support. This, retrospectively, delivers information on the catalyst's morphological behavior during polymerization. Similar insights may be gained for other heterogeneous catalysts, either, via staining approaches with chemosensitive- and/or size-selective probes, or, by forming fluorescent reaction products (e.g., coke, thiophene or styrene oligomerization products, and fluorophore-tagged polymers), thus enabling a selective visualization of specific catalyst domains, pore space architectures and catalytic reactions.^[34,38,44–48] Automating the data acquisition and analysis with machine learning could ultimately yield statistically relevant insights

into the behavior of heterogeneous catalysts, and possibly, enable us to derive quantitative structure-activity correlations.

5.2 Experimental Methods

5.2.1 Sample Preparation

In this **Chapter**, we investigated the silica-supported bis-indenyl zirconocene-based catalyst (Zr/MAO/SiO₂) that was previously studied during gas-phase^[19] (**Chapter 2**) and slurry-phase (**Chapter 4**) ethylene polymerization. The catalyst was synthesized by suspending a 2,2'-bi-phenylene-bis-2-indenyl ZrCl₂ complex and methylaluminoxane (MAO, Al:M ratio = 150) in dried toluene, subsequently adding polymer-grade SiO₂ (D₅₀ = 25.0 μm, pre-calcination at 600 °C) to form a slurry, and removing the solvent under nitrogen flow. Further details can be found in **Chapter 2** of this thesis.

To obtain samples that were suitable for our investigations, the Zr/MAO/SiO₂ catalyst was pre-polymerized at room temperature in slurry-phase at 10 bar ethylene pressure in a Parr autoclave set-up under stirring (570 rpm). In a first step, the autoclave was loaded inside a nitrogen glovebox. Approximately 10 mL heptane and 3 μL triisobutylaluminum (TiBA, scavenger) were added to 10 mg of catalyst powder in a glass reactor. This glass reactor was then placed inside the autoclave. After removal from the glovebox, the autoclave was pressurized for ~ 10 s under continuous stirring to reach the desired pressure. The inlet valve was then closed. The period of pressurization is included in the total polymerization time. To terminate the reaction, the valves of the autoclave were opened, and the formed polymer immediately removed from the glass reactor. The polymer was dried under air flow and weighed. Polymer yields were calculated by subtracting the initial mass of catalyst from the final mass of the polyethylene-catalyst composite.

5.2.2 Particle Size Analysis

Optical microscopy was employed to determine the particle size distribution, average particle sizes and D₅₀ values of the pristine and pre-polymerized catalyst batches. A Zyla camera, installed on a Nikon A1 confocal fluorescence microscope, was used. The analysis of the acquired images was performed with ImageJ. For each sample batch, the largest 2D Feret diameters of 200 particles were assessed. The 2D Feret diameter describes the distance between a pair of parallel tangential lines that confine a given particle in 2D.

5.2.3 Confocal Fluorescence Microscopy

Instrumentation and Measurement Settings

Confocal fluorescence microscopy (CFM) experiments were performed using a Nikon A1 confocal microscope, configured with an Eclipse Ti2-E inverted microscope body, at 488 nm excitation. The system is equipped with a pin hole to filter out-of-focus light and suitable dichroic mirrors (405 nm/488 nm). A Nikon oil immersion objective (Nikon CFI Plan Apo Lambda 60x Oil, NA = 1.4) was employed in combination with a Nikon type F immersion oil for index matching

(refractive index oil = 1.518, refractive index HDPE \approx 1.51–1.54^[49–51], refractive index amorphous silica \approx 1.45–1.47^[52–54]). In terms of sample preparation, the pristine and pre-polymerized samples of the Zr/MAO/SiO₂ catalyst (air-exposed) were placed on top of a microscopy slide, immersed in oil and covered with a slide of 170 μ m thickness.

All 2D CFM images were acquired at a focal depth of 10 μ m. To obtain the data for the 3D reconstructions, Z-stacks of multiple 2D CFM images were acquired at a step size of 0.125 μ m. By applying a scan size of 2048 x 2048 pixels to a 178.0 μ m x 178.0 μ m field of view (pixel size = 86.90 nm, Nyquist sampling), a lateral resolution of \sim 470 nm was obtained. The resolution was determined based on 15 line profiles that were fitted over well-defined features in the 2D CFM images of the pristine Zr/MAO/SiO₂ catalyst following a 10%–90% criterion^[55,56] (line scan analysis). More detailed information on the measurement settings can be found in **Table 5.1**. For a qualitative assessment of the catalyst's morphological evolution over several reaction stages, overview images were measured using 1024 x 1024 pixels and a field of view of 294.6 μ m x 294.6 μ m.

Table 5.1 Settings used for the 2D and 3D confocal fluorescence microscopy (CFM) measurements of the Zr/MAO/SiO₂ catalyst.

Setting	Value
Excitation wavelength (nm)	488
Laser power (%)	7.5
Spectral detection range (nm)	508–748
Si grating resolution (nm)	10
Scan size (pixels)	2048 x 2048
Frames per second	1/32
Averaging	No averaging
Pinhole size (μ m)	35.8
Si HV	180

Image Processing and Segmentation

Post processing of the 2D confocal fluorescence microscopy (CFM) images and visualization of the reconstructed catalyst particles was performed using self-developed code written in MATLAB™ and the Avizo™ software package by Thermo Fisher Scientific Inc. In a first step, the 2D CFM images (.nd2 files) were exported as 16-bit grayscale TIF images using MATLAB™. All images were subsequently filtered with a non-local means filter. Depending on the nature of the data (2D/3D), the total particle areas (TPAs) or total particle volumes (TPVs) of the particles were determined. The TPV is defined as the total volume of a particle including matter and pores. Particles that were in contact with each other were separated manually in Avizo™. The particle areas or volumes and their corresponding largest 2D or 3D Feret diameters were then calculated.

After masking the original images with their corresponding TPAs or TPVs, the 2D and 3D data sets were collectively normalized (value range of 0–255). An automated thresholding procedure (threshold value: 2D = 36, 3D = 24) was then applied to segment the high inten-

sity regions in the collected 2D and 3D CFM data sets. All thresholds were chosen based on visual inspection. Due to the high degree of intermixing of support and polymer phase, as well as resolution limitations, these high intensity regions correspond to the sum of pure silica and silica-dominant mixed phase and were classified as silica-dominant phase (A_s/V_s). The low intensity regions, on the other hand, represent a combination of polyethylene, polyethylene-dominant mixed phase and macropore space and are collectively denoted as V_p .

A comparison of the $V_{PE+macropores}/V_{SiO_2}$ volume ratios extracted from the 2D and 3D CFM data to the PE yield-derived volume ratios revealed the PE phase to be significantly underestimated (**Table 5.2**). This can theoretically be addressed by choosing a higher threshold value during segmentation. However, higher threshold values only result in a sub-optimal overlap of the segmented regions with the high intensity domains of the particles. Given that the fluorescence intensity decreases strongly, even after 0.5 min of polymerization, we believe that a large amount of the formed PE phase goes undetected due to resolution limitations. This affects any quantification, as is apparent below.

Table 5.2 Polyethylene (PE) to silica (SiO_2) volume ratios, as derived from the yields of the 0.5 min, 1 min and 5 min pre-polymerized samples [assuming $\delta(PE) = 0.95 \text{ g/cm}^3$, $\delta(SiO_2) = 1.60\text{--}1.90 \text{ g/cm}^3$, denoted as V_{PE}/V_{SiO_2} (yield)], compared to the volume ratios derived from the 2D and 3D confocal fluorescence microscopy (CFM) data analysis.

Yield (g_{PE}/g_{cat})	V_{PE}/V_{SiO_2} (yield)	$V_{PE+macropores}/V_{SiO_2}$ (2D CFM)	$V_{PE+macropores}/V_{SiO_2}$ (3D CFM)
0.8	1.35–1.60	0.39	/
2.1	3.54–4.20	0.68	1.49
4.8	8.08–9.60	2.42	/

Differences in fluorescence intensity can generally be observed between individual particles in the pristine catalyst material. Due to the strong decrease in fluorescence intensity upon the formation of non-fluorescent polymer, these differences seem to have limited influence on the segmentation of the data. The accuracy of the data analysis was ensured by measuring a large number of particles per reaction stage.

In the 2D data, areas constituting less than approximately 80% of the total approximated area of a given particle's cross-section were categorized as partial cross-sections. As is demonstrated in **Table 5.3**, the percentage of partial cross-sections is low for all reaction stages.

Table 5.3 Percentage of partial particle cross-sections per characterized reaction stage as measured by 2D confocal fluorescence microscopy (CFM).

Time (min)	0.5	1	5
Percentage of partial cross-sections (%)	7.4	6.2	5.9

Particles that were insufficiently imaged in 3D were excluded from the data analysis. This guaranteed an accurate size determination in 3D. Agglomerated particles that could not be clearly separated based on the fluorescence images were separated manually to approximate their size (see red and blue particles in **Figure 5.9B**).

5.2.4 Focused Ion Beam-Scanning Electron Microscopy

Focused ion beam-scanning electron microscopy (FIB-SEM) experiments were performed following the procedure that is described in **Chapter 2** of this thesis.

5.2.5 Scanning Electron Microscopy-Energy Dispersive X-Ray Spectroscopy

Scanning electron microscopy-energy dispersive X-ray spectroscopy (SEM-EDX) was performed with a FEI Helios NanoLab G3 UC scanning electron microscope at 10 keV and a ZEISS Gemini SEM 450 at 5 keV. The latter was used to characterize particle cross-sections that were accessed following the FIB procedure mentioned in **Chapter 2**.

5.3 Results and Discussion

5.3.1 Catalyst Pre-Polymerization

The Zr/MAO/SiO₂ catalyst was pre-polymerized in dried heptane in an autoclave at 10 bar ethylene pressure for 0.5 min, 1 min, 5 min and 15 min respectively (room temperature). As can be seen in **Table 5.4** and **Figure 5.2**, the average particle size increases with reaction time. Furthermore, a concurrent broadening of the particle size distribution (PSD), as indicated by an increasing standard deviation (SD), points to kinetic differences amongst the individual particles of the pre-polymerized batches. This stands in agreement with other works, where optical microscopy revealed kinetic differences amongst individual catalyst particles.^[57-63]

Table 5.4 Yields, D₅₀ values and average particle sizes of the pristine and selected 10 bar pre-polymerized Zr/MAO/SiO₂ catalyst samples, as determined via optical microscopy for 200 catalyst particles.

Sample	Yield (g _{PE} /g _{cat})	D ₅₀ (μm)	d _{avg} (μm)	SD (%)
pristine	0	25.8	26.7	8.4
1 min	2.1	38.4	39.8	11.7
5 min	4.8	51.1	52.1	15.2
15 min	18.5	74.2	74.5	25.7

d_{avg} = average particle diameter and SD = standard deviation.

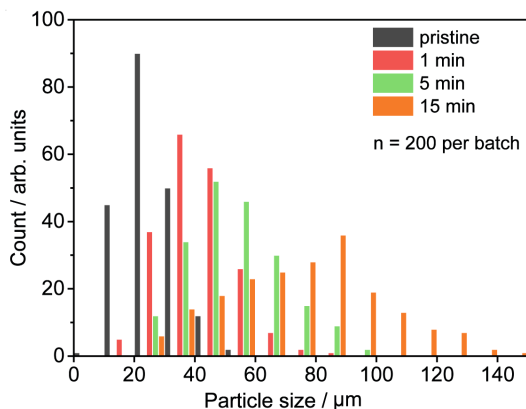


Figure 5.2 Particle size distribution of the pristine (black), 1 min (red), 5 min (green) and 15 min (orange) pre-polymerized Zr/MAO/SiO₂ catalyst samples (slurry-phase, 10 bar ethylene, room temperature). A total of 200 catalyst particles was assessed per batch.

5.3.2 Screening the Fragmentation Degree and Catalyst Particle Dormancy Over Multiple Reaction Stages with 2D Confocal Fluorescence Microscopy

2D CFM was used to qualitatively and quantitatively assess the morphology and fragmentation degree of the Zr/MAO/SiO₂ catalyst at multiple reaction stages (**Figures 5.3** and **5.4**, samples exposed to air). In contrast to previous CFM studies performed on similar systems,^[40,41,64] no chemical modification of the catalyst, i.e., via impregnation with suitable fluorophores, had to be performed due to the autofluorescent nature of the Zr/MAO/SiO₂ catalyst (**Figure 5.3**, SiO₂ and MAO/SiO₂ are both non-fluorescent).

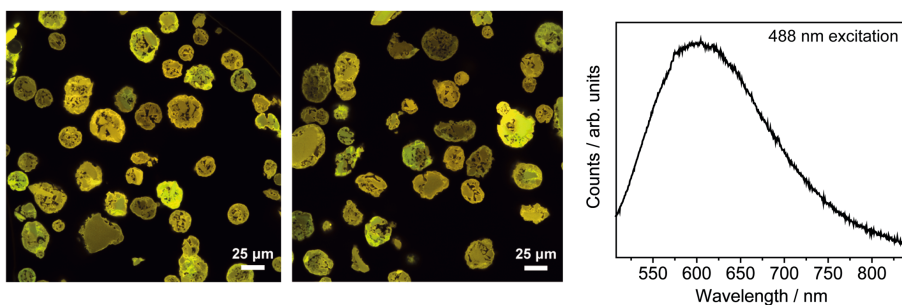


Figure 5.3 Left and center: 2D confocal fluorescence microscopy (CFM) images of multiple pristine Zr/MAO/SiO₂ catalyst particles (488 nm excitation, 1024 x 1024 pixels, dichroics: 405 nm/488 nm/561 nm/640 nm). Right: Emission spectrum of the pristine Zr/MAO/SiO₂ catalyst recorded at 488 nm excitation (no dichroics).

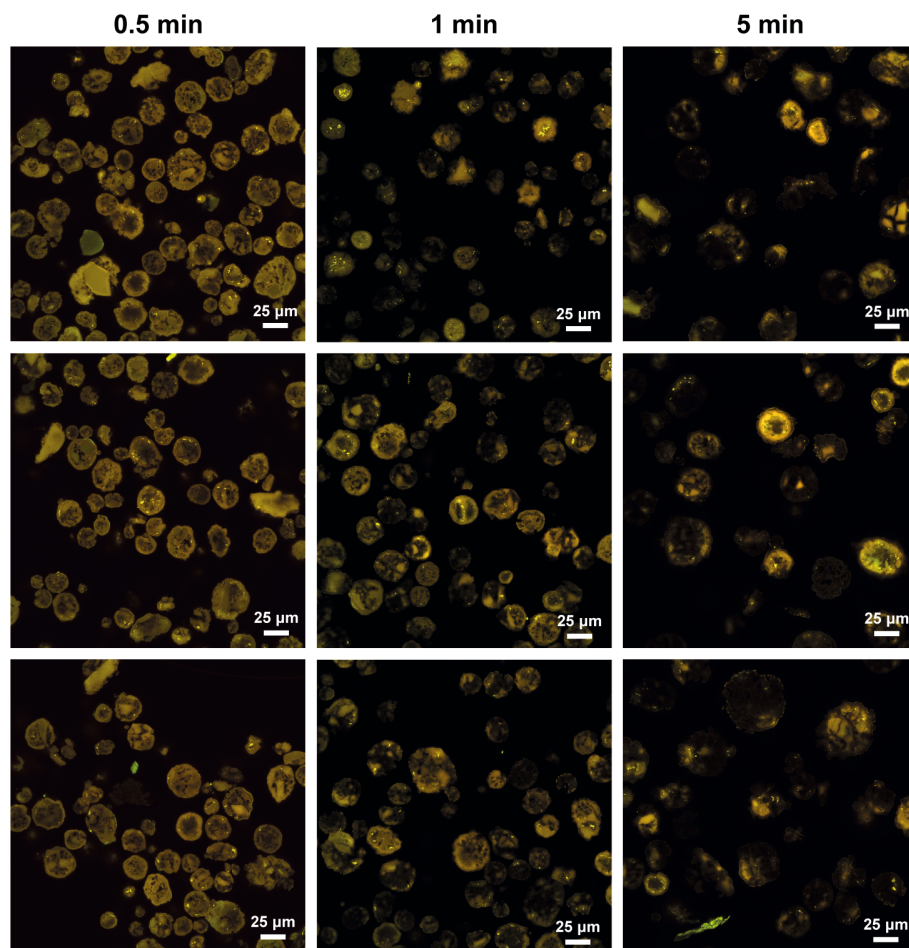


Figure 5.4 A selection of 2D confocal fluorescence microscopy (CFM) images of multiple 0.5 min, 1 min and 5 min pre-polymerized Zr/MAO/SiO₂ catalyst particles (488 nm excitation, 1024 x 1024 pixels, dichroics: 405 nm/488 nm/561 nm/640 nm).

The CFM data was interpreted based on the cross-sectional analysis of randomly selected pre-polymerized catalyst particles with FIB-SEM (**Figure 5.5**): High fluorescence intensity regions represent support-dominant domains (pure silica + silica-dominant mixed phase, denoted as A_s) while low fluorescence intensity regions are predominantly constituted by polyethylene (PE), PE-dominant mixed phase and the macropore space (in sum denoted as A_p). In general, a decrease in fluorescence intensity was observed in areas where the support is diluted with the formed polymer (**Figure 5.4**). All images for analysis were acquired using a large FOV (178 μm x 178 μm) at a fixed focal depth of ~ 10 μm. The latter helped to obtain fluorescence intensities that are still sufficiently high for reliable characterization and image

processing, while also ensuring comparability of the data. A lateral resolution of ~ 470 nm was determined via line scan analysis of the 2D images of the pristine catalyst (Figure 5.6).

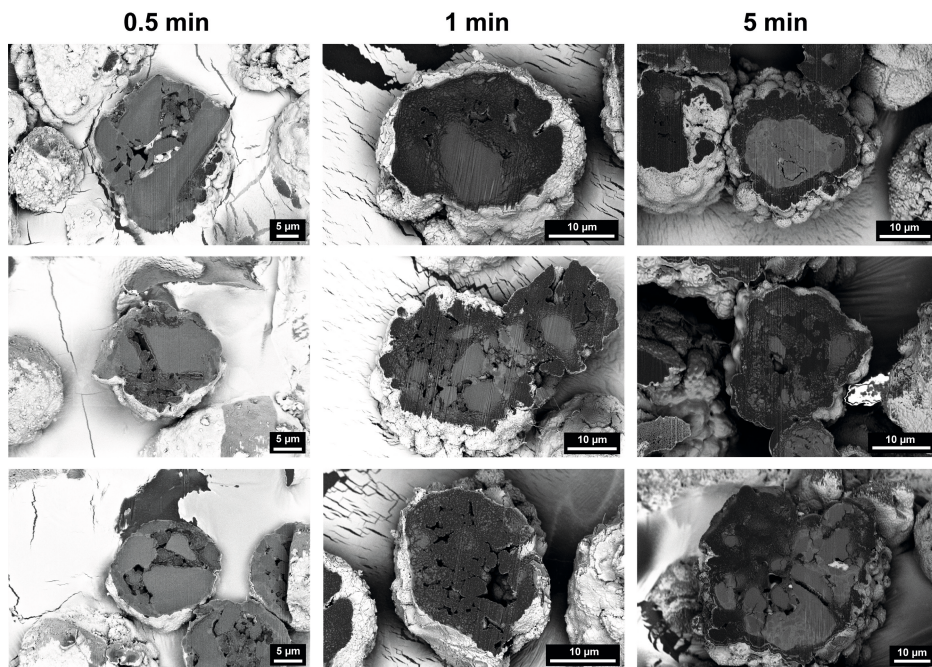


Figure 5.5 Scanning electron microscopy (SEM) images displaying the horizontal cross-sections of Zr/MAO/SiO₂ catalyst particles that were pre-polymerized in slurry-phase for 0.5 min, 1 min and 5 min at 10 bar ethylene (room temperature).

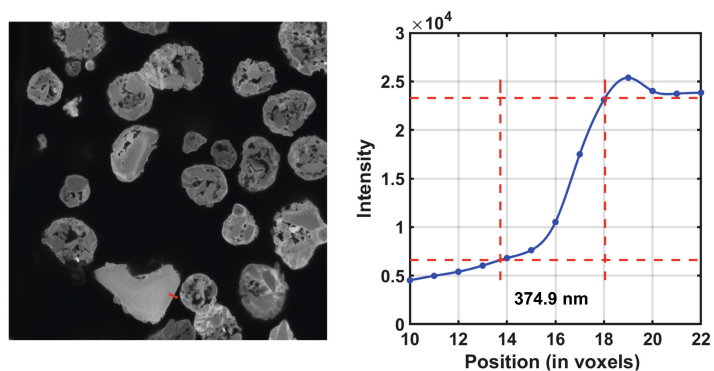


Figure 5.6 Line scan analysis performed on a single particle of the pristine Zr/MAO/SiO₂ catalyst using the 10%–90% criterion. A resolution of 374.9 nm was determined from the edge profile.

The 2D CFM images of the 0.5 min, 1 min and 5 min pre-polymerization stages (**Figure 5.4**) show that both the polymerization degree (i.e., the amount of formed polymer and the degree of internal support fragmentation) and average particle size increased with reaction progress. From a qualitative point of view, a large degree of inter- and intraparticle heterogeneity is clearly evident. In most particles, the layer-by-layer fragmentation mechanism dominates at both particle and silica domain level (**Figure 5.4**). This is evident from a gradual change in fluorescence intensity at the perimeter of the catalyst particles' constituent support granulates, indicating progressing polymerization and support fragmentation (refer to the differences in fluorescence intensity between pristine and pre-polymerized catalyst particles in **Figures 5.3** and **5.4** for clarification, also refer to the SEM images in **Figure 5.5**). The sectioning mechanism, on the other hand, is less prominent. In fact, it is mostly involved in cleaving larger, inaccessible support fragments with low degrees of macroporosity, as has recently been reported and discussed by our group.^[23]

To quantify the degree of internal support fragmentation of a given particle, we introduced a fragmentation parameter F (**Equation 5.1**).

$$F = 1 - \left(\frac{A_S}{TPA} \right) = \frac{A_P}{TPA} \quad (\text{Eq. 5.1})$$

This corresponds to 1 minus the ratio between the area of high intensity, silica-dominant domains (A_S), as determined via a manually assigned threshold, and the total particle area (TPA) (**Figure 5.7**), thus yielding the sum of the areas of the polymer-dominant domains and the macropore space (A_p) divided by the TPA.

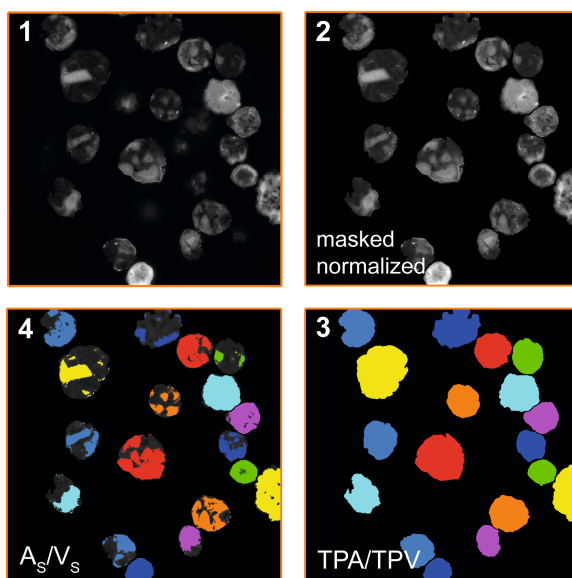


Figure 5.7 Overview of the image processing applied to the 2D and 3D confocal fluorescence microscopy

(CFM) data sets. The 16-bit grayscale images (1) were filtered with a non-local means filter and masked with the TPAs/TPVs (2) of the particles. After collectively normalizing the masked 2D and 3D CFM data (3), the data sets were segmented into high- and low-intensity regions using manually defined thresholds. The high-intensity regions (4) represent silica-dominant domains (A_s/V_s).

As can be derived from the histograms of the particles' fragmentation parameters at different reaction stages (**Figures 5.8A–5.8F**), as well as the corresponding standard deviations (**Table 5.5**), interparticle heterogeneity is clearly evident and becomes more pronounced with reaction progress. The average A_p/TPA ratio (F_{avg}) was found to increase from 0.30 at $0.8 \text{ g}_{PE}/\text{g}_{cat}$ (0.5 min) to 0.73 at $4.8 \text{ g}_{PE}/\text{g}_{cat}$ (5 min) (**Table 5.5, Figure 5.8G**). In fact, this average fragmentation parameter F_{avg} is linearly correlated with the polymer yield in this low polymer yield regime (**Figure 5.8H**, linear relationship may not apply at higher polymer yields/larger average particle sizes).

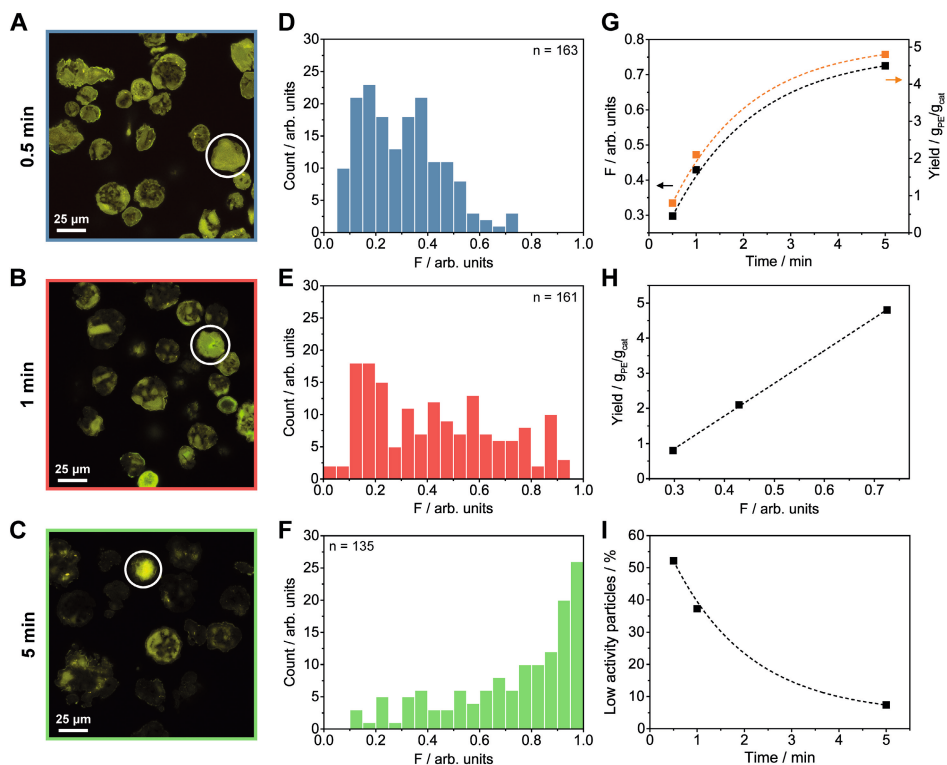


Figure 5.8 2D confocal fluorescence microscopy (CFM) data acquired of the Zr/MAO/SiO₂ catalyst at different reaction stages (0.5 min, 1 min, 5 min; 10 bar ethylene; room temperature; $0.8\text{--}4.8 \text{ g}_{PE}/\text{g}_{cat}$). (A)–(C): 2D CFM images of the characterized particles, (D)–(F): Histogram of the particles' respective fragmentation parameters with $F = A_p/TPA$, (G): Average F and polyethylene (PE) yield per reaction stage plotted versus the pre-polymerization time, (H): Average F per reaction stage plotted versus the corresponding PE yield, and (I): Percentage of particles with a value of F smaller than the average F value of the 0.5 min pre-polymerized batch ($F < 0.30$), indicating a lower degree of polymerization and thus lower relative activity. (i.e., dormancy). For each reaction stage, a dormant catalyst particle has been marked with a circle (Figures 5.8A–5.8C).

Table 5.5 Quantitative data extracted via 2D confocal fluorescence microscopy (CFM) and image processing for the 0.5 min, 1 min and 5 min pre-polymerized Zr/MAO/SiO₂ catalyst batches (10 bar ethylene).

Sample	Yield (g _{PE} /g _{cat})	n	F _{avg}	SD (%)	d _{Feret, avg} (μm)	PCC
0.5 min	0.8	163	0.30	15.2	26.6	-0.20
1 min	2.1	161	0.43	24.7	29.0	-0.14
5 min	4.8	135	0.73	24.7	35.8	-0.15

n = total number of full or partial particle cross-sections, F_{avg} = average fragmentation parameter F of all particles belonging to a sample, SD = standard deviation of F, d_{Feret, avg} = average 2D Feret diameter of a sample, and PCC = Pearson's correlation coefficient for F and d_{Feret}.

The average fragmentation parameter of the 0.5 min pre-polymerized batch (F = 0.30) was used as a threshold to categorize all particles of a given sample according to their respective fragmentation degrees. This allowed us to quantify the number of low activity or 'dormant' particles with F < 0.30 during the early reaction stages. The share of dormant catalyst particles was found to be significant after 0.5 min (52.1%) and 1 min (37.3%) of polymerization (**Figure 5.8I**). These differences in reactivity at reaction onset partly explain the large spread in particle sizes observed at more advanced reaction stages (**Figure 5.2**). Even after 5 min of polymerization (4.8 g_{PE}/g_{cat}), 7.4% of the characterized particles possess F values smaller than 0.30, implying that they have only fragmented to a limited extent.

While the 2D analysis generally does not deliver accurate compositional data for a single particle, it is useful for extracting trends in composition and reactivity over several catalyst batches (or reaction stages) based on average compositional values for each batch. The linear relationship between F and the polymer yield can furthermore be used to determine the unknown polymer yield of a given catalyst batch with minimal sample amounts. In contrast to techniques such as video microscopy, which has pre-dominantly been applied during gas-phase polymerization experiments, 2D CFM is suitable for assessing internal support fragmentation and catalyst particle activity in both gas-phase and slurry pre-polymerized samples, making it a useful tool for catalyst characterization and quality control.

5.3.3 Assessing Interparticle Heterogeneity and Size-Dependent Morphological Correlations with 3D Confocal Fluorescence Microscopy

With the 2D analysis clearly indicating differences in morphology between individual particles, further efforts were made to extract more accurate quantitative data with 3D CFM. 40 catalyst particles of the 1 min pre-polymerized batch were thus scanned over a range of 25 μm in depth (Z) using a step size of 0.125 μm. The Z-stacks of 2D images were consequently segmented to determine the particles' respective volumes (i.e., total particle volume = TPV; **Figures 5.9A–5.9C**) and treated with a manual thresholding algorithm to isolate the high intensity regions representing the silica-dominant phase V_s (**Figure 5.9D–5.9F, Figure 5.7**). After visual inspection of the reconstructed particles, the data sets were adapted to only include particles with sufficiently large volumes within the field of view. As previously observed in the 2D analysis, the particles' internal fragmentation parameters (F = V_p/TPV, analogous

to **Equation 5.1**) varied significantly ($F = 0.26\text{--}0.93$, $F_{\text{avg}} = 0.61$, **Figure 5.9G**). The fragmentation parameter values of selected particles can be extracted from **Figures 5.9D–5.9F**. By applying a k-means clustering algorithm to the data set (3 clusters with following centroids: $F = 0.37/0.52/0.75$), the particles were roughly classified in relation to each other based on their F values. Out of 40 particles, 7, 13 and 20 particles displayed weak, moderate and strong degrees of fragmentation, respectively. 29 of the 40 catalyst particles (72.5%) were found to be composed of more than 50% PE ($F > 0.50$), while only 9 catalyst particles (22.5%) contained more than 75% PE ($F > 0.75$).

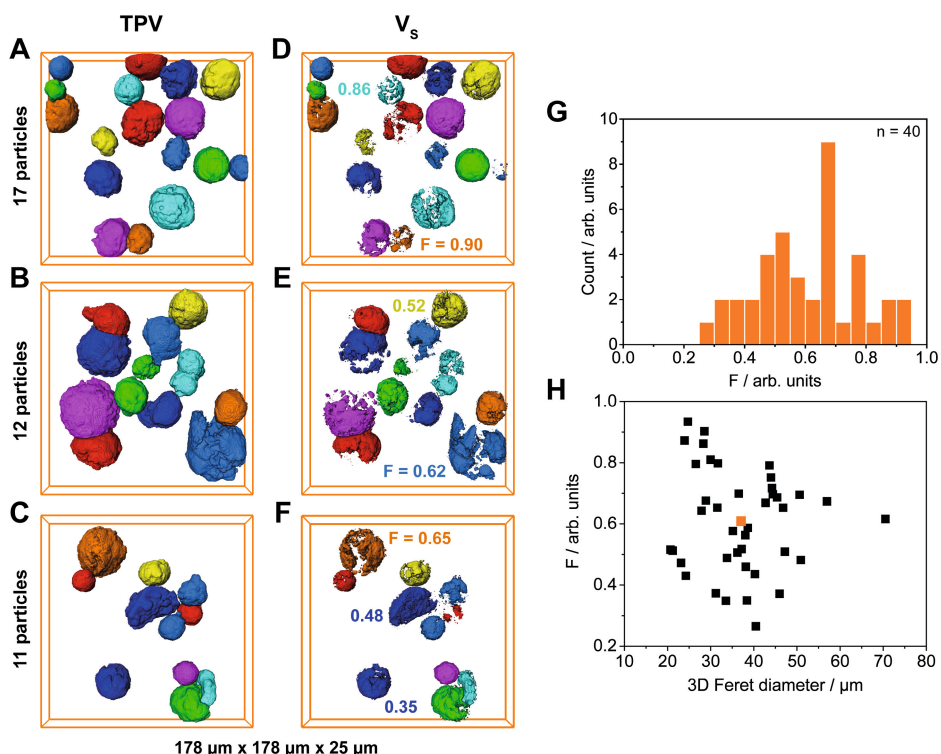


Figure 5.9 3D confocal fluorescence microscopy (CFM) data acquired of 40 particles of the 1 min pre-polymerized Zr/MAO/SiO₂ catalyst (10 bar ethylene, room temperature, 2.1 $g_{\text{PE}}/g_{\text{cat}}$). (A)–(C): Total particle volumes (TPV) of the characterized particles, (D)–(F): Segmented high intensity regions of the particles, which represent the silica-dominant phase (V_s), (G): Histogram of the particles' respective fragmentation parameters ($F = V_p/TPV$), and (H): Largest 3D Feret diameters of the particles plotted versus their respective fragmentation parameters F (average value plotted in orange).

In the past, inverse correlations between the particle size and catalyst activity have been reported and were generally attributed to a higher diffusion resistance in larger particles. [13,65–70] To determine whether the here observed morphological heterogeneity is actually linked to the size of the particles, the particles' respective fragmentation parameters (F) were set in relation to their largest 3D Feret diameters (**Figure 5.9H**). The 3D Feret diameter describes

the distance between a pair of parallel tangential planes that confine a given object in 3D and is therefore a representative measure for the true particle size. The average Feret diameter of the 40 pre-polymerized particles was determined as 37.1 μm (**Table 5.6**), which is comparable to the average particle size that was obtained via optical microscopy (39.8 μm , **Table 5.4**). The small deviation in value may be explained by the lower number of particles that was characterized with CFM. By plotting the particles' F values against their respective Feret diameters (**Figure 5.4H**), marked differences in polymerization degree between similarly sized particles became apparent. No clear size dependency could, however, be established based on a Pearson's correlation coefficient of -0.11 (**Table 5.6**).

Table 5.6 Quantitative data extracted via 3D confocal fluorescence microscopy (CFM) and image processing for the 1 min pre-polymerized Zr/MAO/SiO₂ catalyst batch (10 bar ethylene).

Sample	n	F _{avg}	SD (%)	d _{Feret, avg} (μm)	PCC
1 min	40	0.61	16.8	37.1	-0.11

n = total number of particles, F_{avg} = average fragmentation parameter F of all particles, SD = standard deviation of F, d_{Feret, avg} = average 3D Feret diameter, and PCC = Pearson's correlation coefficient for F and d_{Feret}.

The large spread in fragmentation parameter values ($F = 0.26\text{--}0.93$, $F_{\text{avg}} = 0.61$, **Figure 5.9G**) leads us to believe that the structural heterogeneity of the particles' supports (**Figure 5.3**), rather than the particle size, is the more dominant factor in controlling the monomer diffusion and, thus, the kinetics and morphological evolution of the catalyst particles during these early reaction stages. At more advanced reaction stages and under higher mass transfer limitations, size-dependent effects may become more pronounced, as previously reported in literature.^[13,65–70] The cross-sectional data acquired at 10 μm depth, despite yielding a far less reliable size determination, further corroborates our hypothesis that the interparticle heterogeneity is not solely attributable to the particle size (see Pearson's correlation coefficients in **Table 5.5**, **Figure 5.10**).

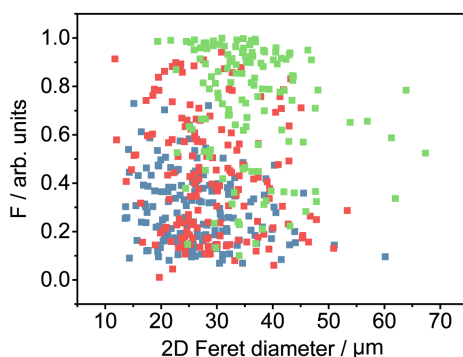


Figure 5.10 Largest 2D Feret diameters of the 0.5 min (blue), 1 min (red) and 5 min (green) pre-polymerized Zr/MAO/SiO₂ catalyst particles that were characterized with 2D confocal fluorescence microscopy (CFM), plotted versus their respective fragmentation parameters (F).

5.3.4 Qualitative Interpretation of the Morphology Data

The significant inter- and intraparticle heterogeneity observed in the Zr/MAO/SiO₂ catalyst at multiple stages of slurry-phase ethylene polymerization (**Figure 5.4**) confirms our conclusions from previous studies on gas-phase pre-polymerized metallocenes.^[19,22] As is postulated in these recent works, the morphological evolution of an individual catalyst particle is strongly correlated to its initial support architecture and pore space configuration. These effectively determine the degree of mass transport and, thus, reaction kinetics at the single particle level. Particles with smaller, accessible support domains (higher macroporosity and pore space interconnectivity) are expected to display a more advanced fragmentation degree than catalyst particles that are predominantly constituted by large granulates with limited macroporosity (i.e., higher mass transfer resistance).

Interestingly, olefin polymerization is often observed to a greater extent in a specific sub-volume of the particles (**Figures 5.9A–5.4F**). Higher accessibilities may exist for specific support domains, which could be related to their spatial arrangement within the particle. While interactions with other particles (i.e., agglomeration) or with the walls of the reactor should also be considered, their effects are expected to be limited as the reaction mixture was continuously stirred, even before ethylene addition. Low to moderate variations in fluorescence intensity amongst the pristine catalyst particles (**Figure 5.3**) indicate different metallocene loadings, which can potentially lead to differences in reactivity amongst individual particles.

Tran *et al.* recently reported inhomogeneities in the radial distributions of a zirconocene complex and methylaluminumoxane in the cross-sections of individual silica-supported catalyst particles.^[71] Higher concentrations of the metallocene complex in the periphery of the catalyst particles were found to lead to a more pronounced formation of fines, thus indicating correlations between the metallocene distribution, local polymerization activity and morphology. Knoke *et al.* and Velthoen *et al.* also proposed an inhomogeneous distribution of MAO amongst catalyst particles as a possible cause for variations in reactivity and morphology.^[16,72] With the Zr/MAO/SiO₂ catalyst featuring ~ 15 wt% aluminum, inter- and intraparticle heterogeneity, in terms of the distribution of MAO, should be minimal.^[72] This was confirmed with SEM-EDX (**Figure 5.11**).

The 2D and 3D data representatively show that the layer-by-layer fragmentation mechanism dictates the fragmentation of the catalyst particles under the given reaction conditions (slurry-phase ethylene polymerization, 10 bar). A synergy with the, in this case, more subdued sectioning mechanism is also apparent. The contribution of this mechanism is, however, limited to particles with significant mass transfer limitations and is responsible for the formation of more extensive cracks in the catalyst support.

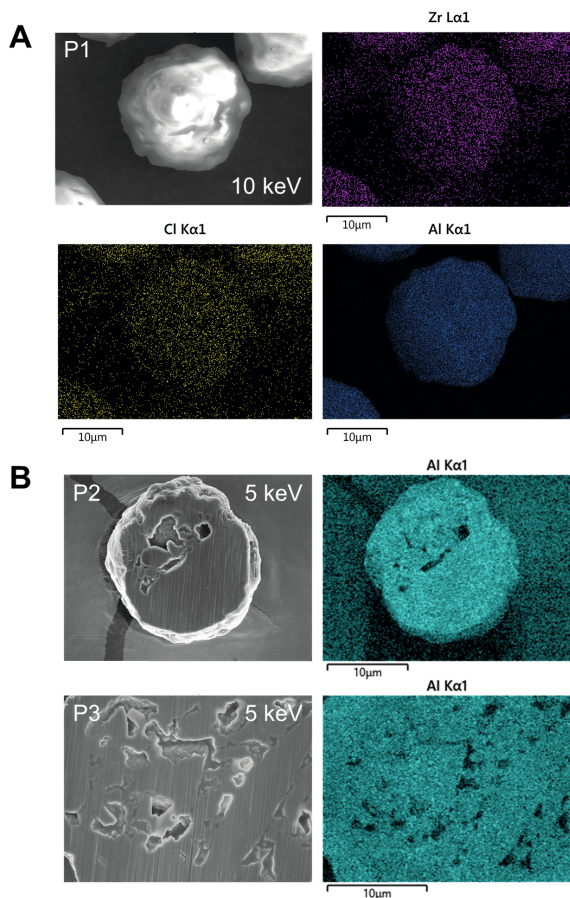


Figure 5.11 Scanning electron microscopy-energy dispersive X-ray (SEM-EDX) spectroscopy data recorded of three particles of the pristine Zr/MAO/SiO₂ catalyst. (A) SEM-EDX data of a full catalyst particle acquired with a FEI Helios NanoLab G3 UC scanning electron microscope at 10 keV, (B) SEM-EDX data of two particle cross-sections acquired with a ZEISS GeminiSEM 450 at 5 keV. The EDX images display the distribution of zirconium (Zr) and chlorine (Cl), representative for the zirconocene complex, as well as aluminum (Al), which is representative for the co-catalyst methylaluminoxane (MAO).

5.4 Conclusions

Due to its fast measurement times and comparatively large FOV, laboratory-based confocal fluorescence microscopy represents an efficient, non-invasive diagnostic tool to obtain quantitative information on the relative composition and morphology of pristine and pre-polymerized olefin polymerization catalyst particles, both in 2D and 3D. By delivering statistically more relevant mechanistic insights into the morphological evolution of a given catalyst system, it represents an attractive complementary method to hard X-ray-based nanotomography techniques, which are often limited by their FOV, long measurement periods and elaborate data reconstruction and analysis.

Our studies on a silica-supported zirconocene-based catalyst material revealed large differences in reactivity between individual catalyst particles at the onset of ethylene polymerization. The dormant behavior of selected catalyst particles during the early reaction stages leads to delays in particle growth, which partly accounts for size-based differences in the final polymer product. The acquired 2D and 3D data, collected on a representative number of catalyst particles, furthermore revealed significant inter- and intraparticle heterogeneity during the early stages of polymerization. A strong correlation of fragmentation with the support and pore space architecture of the individual catalyst particles is apparent from our investigations on samples that were pre-polymerized to low polymer yields.

In general, the linear correlation between the polymer yield and the fragmentation parameter F can be exploited to determine unknown polymer yields of samples. Provided that several reaction stages are evaluated in 3D, the polymer yield of individual catalyst particles could be derived from their respective fragmentation parameters. This represents a novel approach to estimate the activities of individual polymerization catalyst particles.

By means of rational catalyst design and material-specific staining procedures^[41,43], the methodology can also be extended to other supported olefin polymerization catalysts, where morphological screening at high sample throughput is desired. In fact, the approach is applicable to any type of macroporous catalyst system, where representative structural and chemical insights are desired at the single particle level. By using autofluorescent metallocene-based catalysts (several metallocenes display fluorescence), or other support-stained polymerization catalysts, in combination with fluorescence-based particle screening,^[73] it may also be possible to sort pristine polymerization catalyst particles according to their support structure and metallocene concentration. Hence, by minimizing this disparity between particles, a greater control over a given polymerization catalyst's activity and morphological evolution may be achieved. Finally, with machine learning gaining momentum, fully automated image segmentation and post-processing could greatly improve the efficiency of the data analysis.

Acknowledgments

Our appreciation goes to Eric Hellebrand (Utrecht University, UU) for some of the SEM-EDX measurements and Erik Maris (UU) for the conversion of the .nd2 data to .tif format. We would also like to thank Thomas van Swieten (UU) for measuring the emission spectrum of the pristine Zr/MAO/SiO₂ catalyst and Roozbeh Valadian (UU) for his assistance with the line scan analysis.

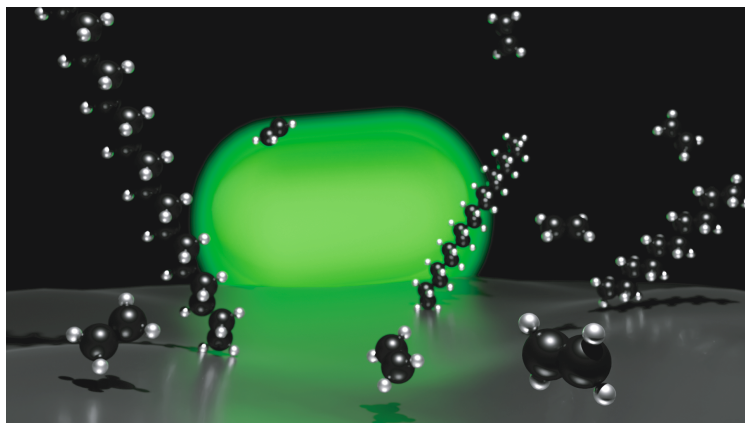
References

1. W. Kaminsky, A. Laban, *Appl. Catal. A Gen.* **2001**, 222, 47–61.
2. W. Kaminsky, *J. Polym. Sci. Part A Polym. Chem.* **2004**, 42, 3911–3921.
3. H. H. Brintzinger, D. Fischer, R. Mülhaupt, B. Rieger, R. M. Waymouth, *Angew. Chem. Int. Ed.* **1995**, 34, 1143–1170.
4. G. W. Coates, *Chem. Rev.* **2000**, 100, 1223–1252.
5. L. Resconi, L. Cavallo, A. Fait, F. Piemontesi, *Chem. Rev.* **2000**, 100, 1253–1345.
6. J. R. Severn, J. C. Chadwick, R. Duchateau, N. Friederichs, *Chem. Rev.* **2005**, 105, 4073–4147.
7. T. F. L. McKenna, A. Di Martino, G. Weickert, J. B. P. Soares, *Macromol. React. Eng.* **2010**, 4, 40–64.
8. A. Alizadeh, T. F. L. McKenna, *Macromol. React. Eng.* **2018**, 12, 1700027.
9. G. G. Hlatky, *Chem. Rev.* **2000**, 100, 1347–1376.
10. L. L. Böhm, *Angew. Chem. Int. Ed.* **2003**, 42, 5010–5030.
11. J. B. P. Soares, T. F. L. McKenna, *Polyolefin Reaction Engineering*, Wiley-VCH, Weinheim, **2012**.
12. J. T. M. Pater, G. Weickert, J. Loos, W. P. M. van Swaaij, *Chem. Eng. Sci.* **2001**, 56, 4107–4120.
13. G. Fink, B. Steinmetz, J. Zechlin, C. Przybyla, B. Tesche, *Chem. Rev.* **2000**, 100, 1377–1390.
14. G. Fink, B. Tesche, F. Korber, S. Knoke, *Macromol. Symp.* **2001**, 173, 77–87.
15. J. M. Zhou, N. H. Li, N. Y. Bu, D. T. Lynch, S. E. Wanke, *J. Appl. Polym. Sci.* **2003**, 90, 1319–1330.
16. S. Knoke, F. Korber, G. Fink, B. Tesche, *Macromol. Chem. Phys.* **2003**, 204, 607–617.
17. H. Hammawa, S. E. Wanke, *Polym. Int.* **2006**, 55, 426–434.
18. S. Zanoni, N. Nikolopoulos, A. Welle, A. Vantomme, B. M. Weckhuysen, *Catal. Sci. Technol.* **2021**, 11, 5335–5348.
19. M. J. Werny, J. Zarupski, I. C. ten Have, A. Piovano, C. Hendriksen, N. H. Friederichs, F. Meirer, E. Groppo, B. M. Weckhuysen, *JACS Au* **2021**, 1, 1996–2008.
20. K. W. Bossers, R. Valadian, S. Zanoni, R. Smeets, N. Friederichs, J. Garrevoet, F. Meirer, B. M. Weckhuysen, *J. Am. Chem. Soc.* **2020**, 142, 3691–3695.
21. K. W. Bossers, R. Valadian, J. Garrevoet, S. van Malderen, R. Chan, N. Friederichs, J. Severn, A. Wilbers, S. Zanoni, M. K. Jongkind, B. M. Weckhuysen, F. Meirer, *JACS Au* **2021**, 1, 852–864.
22. M. J. Werny, R. Valadian, L. M. Lohse, A.-L. Robisch, S. Zanoni, C. Hendriksen, B. M. Weckhuysen, F. Meirer, *Chem Catalysis* **2021**, 1, 1413–1426.
23. M. J. Werny, D. Müller, C. Hendriksen, R. Chan, N. H. Friederichs, C. Fella, F. Meirer, B. M. Weckhuysen, *ChemCatChem* **2022**, 14, e202200067.
24. J. W. Lichtman, J. A. Conchello, *Nat. Methods* **2005**, 2, 910–919.
25. Z. Földes-Papp, U. Demel, G. P. Tilz, *Int. Immunopharmacol.* **2003**, 3, 1715–1729.
26. J. Zhang, R. E. Campbell, A. Y. Ting, R. Y. Tsien, *Nat. Rev. Mol. Cell Biol.* **2002**, 3, 906–918.
27. K. M. Marks, G. P. Nolan, *Nat. Methods* **2006**, 3, 591–596.
28. B. M. Weckhuysen, *Angew. Chem. Int. Ed.* **2009**, 48, 4910–4943.
29. G. De Cremer, B. F. Sels, D. D. De Vos, J. Hofkens, M. B. J. Roefsaers, *Chem. Soc. Rev.* **2010**, 39, 4703–4717.
30. P. Chen, X. Zhou, H. Shen, N. M. Andoy, E. Choudhary, K. S. Han, G. Liu, W. Meng, *Chem. Soc. Rev.* **2010**, 39, 4560–4570.
31. T. Tachikawa, T. Majima, *Chem. Soc. Rev.* **2010**, 39, 4802–4819.
32. I. L. C. Buurmans, B. M. Weckhuysen, *Nat. Chem.* **2012**, 4, 873–886.
33. F. C. Hendriks, F. Meirer, A. V. Kubarev, Z. Ristanović, M. B. J. Roefsaers, E. T. C. Vogt, P. C. A. Bruijninx, B. M. Weckhuysen, *J. Am. Chem. Soc.* **2017**, 139, 13632–13635.
34. G. T. Whiting, N. Nikolopoulos, I. Nikolopoulos, A. D. Chowdhury, B. M. Weckhuysen, *Nat. Chem.* **2019**, 11, 23–31.
35. J. J. E. Maris, D. Fu, F. Meirer, B. M. Weckhuysen, *Adsorption* **2021**, 27, 423–452.
36. D. Wöll, H. Uji-i, T. Schnitzler, J. I. Hotta, P. Dedecker, A. Herrmann, F. C. De Schryver, K. Müllen, J. Hofkens, *Angew. Chem. Int. Ed.* **2008**, 47, 783–787.

37. N. M. Esfandiari, S. A. Blum, *J. Am. Chem. Soc.* **2011**, *133*, 18145–18147.
38. T. Cordes, S. A. Blum, *Nat. Chem.* **2013**, *5*, 993–999.
39. Q. T. Easter, S. A. Blum, *Angew. Chem. Int. Ed.* **2017**, *56*, 13772–13775.
40. Y. Jang, K. Bieber, C. Naundorf, N. Nenov, M. Klapper, K. Müllen, D. Ferrari, S. Knoke, G. Fink, *e-Polymers* **2005**.
41. Y. J. Jang, C. Naundorf, M. Klapper, K. Müllen, *Macromol. Chem. Phys.* **2005**, *206*, 2027–2037.
42. M. Klapper, D. Joe, S. Nietzel, J. W. Krumpfer, K. Müllen, *Chem. Mater.* **2014**, *26*, 802–819.
43. R. Dorresteyn, S. Nietzel, D. Joe, Y. Gerkmann, G. Fink, M. Klapper, K. Müllen, *J. Polym. Sci. Part A Polym. Chem.* **2014**, *52*, 450–459.
44. D. Mores, E. Stavitski, M. H. F. Kox, J. Kornatowski, U. Olsbye, B. M. Weckhuysen, *Chem. Eur. J.* **2008**, *14*, 11320–11327.
45. I. Vollmer, M. J. F. Jenks, R. Mayorga González, F. Meirer, B. M. Weckhuysen, *Angew. Chem. Int. Ed.* **2021**, *60*, 16101–16108.
46. I. L. C. Buurmans, J. Ruiz-Martínez, W. V. Knowles, D. van Der Beek, J. A. Bergwerff, E. T. C. Vogt, B. M. Weckhuysen, *Nat. Chem.* **2011**, *3*, 862–867.
47. M. Gambino, M. Veselý, M. Filez, R. Oord, D. Ferreira Sanchez, D. Grolimund, N. Nesterenko, D. Minoux, M. Maquet, F. Meirer, B. M. Weckhuysen, *Angew. Chem. Int. Ed.* **2020**, *59*, 3922–3927.
48. A. E. Nieuwelink, M. E. Z. Velthoen, Y. C. M. Nederstigt, K. L. Jagtenberg, F. Meirer, B. M. Weckhuysen, *Chem. Eur. J.* **2020**, *26*, 8546–8554.
49. D. R. Smith, E. V. Loewenstein, *Appl. Opt.* **1975**, *14*, 1335.
50. Y. Lin, E. Bilotti, C. W. M. Bastiaansen, T. Peijs, *Polym. Eng. Sci.* **2020**, *60*, 2351–2376.
51. F. J. Rodriguez-Gonzalez, B. A. Ramsay, B. D. Favis, *Polymer* **2003**, *44*, 1517–1526.
52. Y. Guo, Z. Y. Wang, Q. Qiu, J. Su, Y. Wang, S. Shi, Z. Yu, *J. Non. Cryst. Solids* **2015**, *429*, 198–201.
53. *Silica, Amorphous [MAK Value Documentation, 1991]* in *The MAK-Collection for Occupational Health and Safety*, Wiley-VCH, Weinheim, **2012**, 158–179.
54. B. N. Khlebtsov, V. A. Khanadeev, N. G. Khlebtsov, *Langmuir* **2008**, *24*, 8964–8970.
55. M. Holler, A. Diaz, M. Guizar-Sicairos, P. Karvinen, E. Färm, E. Härkönen, M. Ritala, A. Menzel, J. Raabe, O. Bunk, *Sci. Rep.* **2014**, *4*, 3857.
56. M. Veselý, R. Valadian, L. Merten Lohse, M. Toepferwien, K. Spiers, J. Garrevoet, E. T. C. Vogt, T. Salditt, B. M. Weckhuysen, F. Meirer, *ChemCatChem* **2021**, *13*, 2494–2507.
57. K. Zöllner, K. H. Reichert, *Chem.-Ingenieur-Technik* **2001**, *73*, 849–852.
58. K. Zöllner, K. H. Reichert, *Chem. Eng. Sci.* **2001**, *56*, 4099–4106.
59. K. Zöllner, K. H. Reichert, *Chem. Eng. Technol.* **2002**, *25*, 707–710.
60. S. Knoke, D. Ferrari, B. Tesche, G. Fink, *Angew. Chem. Int. Ed.* **2003**, *42*, 5090–5093.
61. J. T. M. Pater, G. Weickert, W. P. M. van Swaaij, *AIChE J.* **2003**, *49*, 450–464.
62. M. Abboud, K. Kallio, K. H. Reichert, *Chem. Eng. Technol.* **2004**, *27*, 694–698.
63. D. Ferrari, G. Fink, *Macromol. Mater. Eng.* **2005**, *290*, 1125–1136.
64. M. Stork, A. Herrmann, T. Nemnich, M. Klapper, K. Müllen, *Angew. Chem. Int. Ed.* **2000**, *39*, 4367–4369.
65. V. F. Tisse, R. M. Briquel, T. F. L. McKenna, *Macromol. Symp.* **2009**, *285*, 45–51.
66. V. F. Tisse, F. Prades, R. Briquel, C. Boisson, T. F. L. McKenna, *Macromol. Chem. Phys.* **2010**, *211*, 91–102.
67. E. Tioni, J. P. Broyer, V. Monteil, T. McKenna, *Ind. Eng. Chem. Res.* **2012**, *51*, 14673–14684.
68. T. Taniike, T. Funako, M. Terano, *J. Catal.* **2014**, *311*, 33–40.
69. M. A. Bashir, V. Monteil, C. Boisson, T. F. L. McKenna, *AIChE J.* **2017**, *63*, 4476–4490.
70. M. A. Bashir, T. F. L. McKenna, in *Polym. React. Eng. Dispersed Syst. Vol. I* (Ed.: W. Pauer), Springer International Publishing, Cham, **2018**, 19–63.
71. D. Tran, C. S. Sowah, K. Y. Choi, *Macromolecules* **2022**, *55*, 2444–2455.
72. M. E. Z. Velthoen, J. D. Meeldijk, F. Meirer, B. M. Weckhuysen, *Chem. Eur. J.* **2018**, *24*, 11944–11953.
73. A.-E. Nieuwelink, J. C. Vollenbroek, R. M. Tiggelaar, J. G. Bomer, A. van den Berg, M. Odijk, B. M. Weckhuysen, *Nat. Catal.* **2021**, *4*, 1070–1079.

Chapter 6

Monitoring the Temperature and
Activity of an Olefin Polymerization
Catalyst Using Luminescence
Thermometry



During olefin polymerization on supported polymerization catalysts, temperature fluctuations arise from the inherent exothermicity of the catalytic reaction, inter- and intraparticle heterogeneities, as well as catalyst bed heterogeneities. In this **Chapter**, the application of luminescence thermometry for remote temperature sensing during gas-phase ethylene polymerization is demonstrated. Core-shell NaYF_4 nanoparticles (NPs), doped with lanthanide ions such as Er^{3+} and Yb^{3+} (i.e., $\text{NaYF}_4:\text{Er}^{3+},\text{Yb}^{3+}/\text{NaYF}_4$), display highly efficient, temperature-dependent upconversion luminescence. By depositing these temperature sensors on a silica-supported zirconocene catalyst (i.e., $\text{Zr}/\text{MAO}/\text{SiO}_2$, with MAO = methylaluminoxane), the temperature of the olefin polymerization catalyst was monitored under reaction conditions. In general, the strongly exothermic behavior of the catalyst was found to be directly related to its kinetic profile. Luminescence thermometry thus yields insights into the activity of olefin polymerization catalysts at high temporal resolutions. Deviations between identical testing runs were observed, possibly indicating a significant influence of the catalyst bed composition and packing on mass and heat transfer. The experiments also lay the foundation for *in situ* temperature mapping experiments on individual catalyst particles. These will provide new insights into the degree of inter- and intraparticle heterogeneity at the onset of olefin polymerization at (sub-)micrometer resolutions.

6.1 Introduction

Olefin polymerization reactions on supported catalyst systems, such as Phillips, Ziegler-Natta and metallocene-based catalyst materials, are known to be highly exothermic. Ethylene polymerization, for instance, produces a reaction heat of 93.6 kJ per mol of reactant.^[1] In large-scale industrial olefin polymerization processes, it is vital to avoid excessive heat formation inside the reactor as it can lead to hotspot formation, catalyst degradation, reactor fouling and polymer melting, with the latter having severe implications for the product morphology, as well as heat and mass transfer.^[2,3] With temperature determining the reaction rate, as is defined by the Arrhenius equation,^[4] insufficient heat transfer inside and from a commercial reactor can lead to very high olefin polymerization rates and, eventually, to a thermal runaway of the reactor. This can have detrimental effects on both the product quality and the stability of the process.

In the field of olefin polymerization catalysis, various analytical techniques have been explored to study reaction temperatures. For example, Fink *et al.* employed reaction calorimetry to study the heat evolution during slurry-phase propylene polymerization.^[5] The group of McKenna, on the other hand, used thermocouples at the inlet and outlet of a fixed bed micro-reactor to monitor the gas-phase temperature during ethylene polymerization on a silica-supported zirconocene catalyst material. A reproducible temperature increase of ~ 25.5 K was observed (reaction conditions: 6 bar C₂H₄, 353 K, and 50 mg catalyst).^[3] Further investigations revealed a strong dependency of heat transfer on the ethylene flow rate^[6–8] and on the composition of the material in contact with the catalyst particles^[9]. While the above-mentioned ‘bulk’ temperature detection methods undoubtedly represent important contributions to this field, they do not possess the ability to directly measure the temperature of a catalyst particle’s surface. To the best of our knowledge, infrared (IR)-thermography experiments performed by Pater *et al.* are pioneering in this field. In their work, individual Ziegler-Natta catalyst particles were imaged, thereby revealing significant temperature increases of up to 20 K at the onset of propylene and ethylene co-polymerization (reaction conditions: 14 bar C₃H₆, 1 bar C₂H₄, and 338 K).^[10]

In this **Chapter**, we explore luminescence thermometry^[11,12] as an alternative analytical approach to monitor the surface temperature of supported olefin polymerization catalysts in a non-invasive manner. As previously demonstrated by our group, lanthanide-based luminescence thermometry is highly suitable for temperature detection during catalytic processes at high temporal resolutions.^[13,14] Lanthanides display narrow emission lines with minimal overlap due to 4f–4f transitions and can generate a high-energy photon via the absorption of two or more low-energy photons (i.e., upconversion).^[15] This effectively results in luminescence in the visible regime after excitation with IR light. The luminescence itself originates from the excitation of lanthanide ions into two thermally coupled energy levels and their subsequent radiative relaxation to an energetically lower energy level. With the population of the two states governed by Boltzmann statistics, the associated luminescence intensity ratio is temperature-dependent. The derivation of temperature is solely based on the luminescence intensity ratio and is independent of probe concentration, excitation power and system alignment.^[16]

Lanthanide ions (Ln^{3+}) can be incorporated into inorganic nanocrystals with low phonon energies (e.g., NaYF_4 and Y_2O_3) to obtain high-performance temperature sensors with sufficient thermal stability and chemical inertness over a wide temperature range.^[17–21] An undoped shell of inorganic host material (e.g., undoped NaYF_4) can also be added to form core-shell structures. This reduces the quenching of excited states at the nanocrystal surface (via energy transfer to high-energy vibrations of solvent and ligand molecules) and vastly improves the upconversion efficiency of the particles.^[22–24]

In this **Chapter**, the suitability of Er^{3+} - and Yb^{3+} -doped NaYF_4 core-shell nanoparticles (i.e., $\text{NaYF}_4:\text{Er}^{3+},\text{Yb}^{3+}/\text{NaYF}_4$) for temperature detection during gas-phase ethylene polymerization is discussed. For this purpose, a silica-supported zirconocene catalyst material (i.e., $\text{Zr}/\text{MAO}/\text{SiO}_2$) was used as a model system. This catalyst material has been studied in detail in **Chapters 2, 4 and 5**. By impregnating the catalyst with the core-shell nanoparticles, the temperature at the surface of the $\text{Zr}/\text{MAO}/\text{SiO}_2$ catalyst bed was successfully monitored during the early stages of polymerization at 1 bar ethylene pressure.

6.2 Experimental Methods

6.2.1 Catalyst Preparation

Information on the synthesis of the zirconocene-based catalyst material (i.e., $\text{Zr}/\text{MAO}/\text{SiO}_2$) can be found in **Chapter 2**. A batch of 35 nm-sized $\text{NaYF}_4:\text{Er}^{3+},\text{Yb}^{3+}/\text{NaYF}_4$ core-shell (NPs), doped with 2% Er^{3+} and 18% Yb^{3+} and dispersed in cyclohexane, was synthesized following an adaptation of the thermal decomposition procedure reported by Homann *et al.* (**Figure 6.1**).^[23,25] The NP size was determined using an FEI Tecnai 12 transmission electron microscope (TEM) operating at 120 keV.

6.2.2 Synthesis of the $\text{NaYF}_4:\text{Er}^{3+},\text{Yb}^{3+}/\text{NaYF}_4$ Core-Shell Nanoparticles

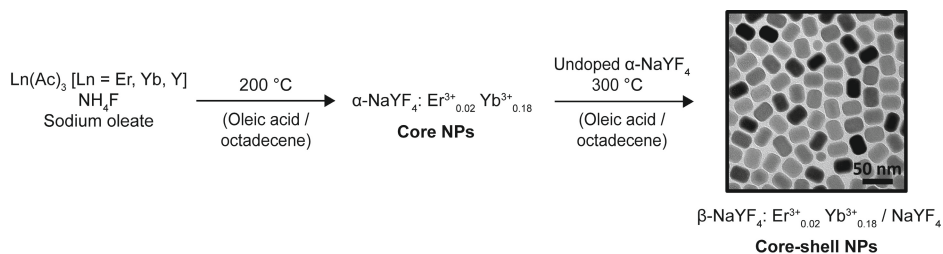


Figure 6.1 Schematic of the synthesis route reported by Homann *et al.* for monodisperse $\text{NaYF}_4:\text{Er}^{3+},\text{Yb}^{3+}/\text{NaYF}_4$ core-shell nanoparticles (NPs).^[23] The undoped NaYF_4 shell reduces the quenching of excited Ln^{3+} -states and thus significantly increases the nanoparticles' luminescence efficiency.^[22]

6.2.3 Deposition of the $\text{NaYF}_4:\text{Er}^{3+},\text{Yb}^{3+}/\text{NaYF}_4$ Core-Shell Nanoparticles

The $\text{NaYF}_4:\text{Er}^{3+},\text{Yb}^{3+}/\text{NaYF}_4$ core-shell NPs were deposited onto the Zr/MAO/SiO₂ catalyst via solution impregnation inside the glovebox. To make this possible, the catalyst was first suspended in dry pentane, followed by the addition of a dry cyclohexane dispersion of the core-shell NPs. The solvents were removed via evaporation. The distribution of the NPs was assessed via scanning electron microscopy-energy dispersive X-ray spectroscopy (SEM-EDX) with a FEI Helios NanoLab G3 UC scanning electron microscope. A weight loading of 1 wt% nanoparticles was adopted for all experiments.

6.2.4 Determination of the Catalyst Activity

The activity of the Zr/MAO/SiO₂ catalyst in the presence and absence of $\text{NaYF}_4:\text{Er}^{3+},\text{Yb}^{3+}/\text{NaYF}_4$ core-shell NPs was assessed *in situ* via diffuse reflectance infrared Fourier transform spectroscopy (DRIFTS), as previously described in **Chapter 4**. A Bruker Tensor 37 spectrometer, featuring a liquid nitrogen-cooled MCT (mercury cadmium telluride) detector, was employed to acquire spectra every 30 s in the range of 4000–900 cm⁻¹ at 4 cm⁻¹ spectral resolution and 16 s scan time. For all experiments, a Harrick Praying Mantis™ High Temperature Reaction Chamber was loaded inside a glovebox with a small amount of glass wool, a VICI Jour® stainless steel frit and approximately 12 mg of catalyst (or NP-treated catalyst). After loading, the reaction cell was transferred to the DRIFTS set-up and connected to the gas lines. The bypass of the cell was flushed with nitrogen for 10 min before pure ethylene (C₂H₄, 1 bar, 5 mL/min) was introduced. All ethylene polymerization reactions were performed at room temperature. The acquired data were processed using an in-house developed MATLAB™ code. First, a background subtraction was performed on all acquired spectra using a spectrum recorded of the catalyst under nitrogen atmosphere before the reaction. The spectral range was then reduced to 2800–3200 cm⁻¹. Principal component analysis (PCA) was subsequently applied to the spectra that were recorded in the presence of ethylene. To establish a fitting model for the whole time series, the first Eigenspectrum (first principal component) of each data set was fitted via a least squares linear combination (LSLC) fitting with 10 manually assigned pseudo-Voigt peaks (2851, 2890, 2920, 2958, 2968, 2988, 3011, 3019, 3077 and 3124 cm⁻¹; ± 2 cm⁻¹ for all values; 2800 cm⁻¹ and 3200 cm⁻¹ defined as boundaries for fitting; method according to Whiting *et al.*^[26]). The area of the peak fitted to the symmetric CH₂ stretching vibration band at 2851 cm⁻¹ was then evaluated as a function of time. The first time derivative of this time evolution yields the olefin polymerization rate. All reported activity plots correspond to the average of three individual testing runs.

6.2.5 Luminescence Thermometry

Luminescence thermometry measurements were performed with a 980 nm continuous wave laser (0.5 W), an Ocean Optics Vis-NIR combined light source and detection probe, a short-pass filter and an Ocean Optics QEPro CCD spectrometer for detection. The relevant emission peaks for thermometry originate from the ²H_{11/2}–⁴I_{15/2} (525 nm) and ⁴S_{3/2}–⁴I_{15/2} (541 nm) inter-

configurational f–f transitions of Er³⁺ after excitation of one or more Yb³⁺ ions (sensitizers) with 980 nm light and subsequent upconversion energy transfer (**Figure 6.2**).^[13,27]

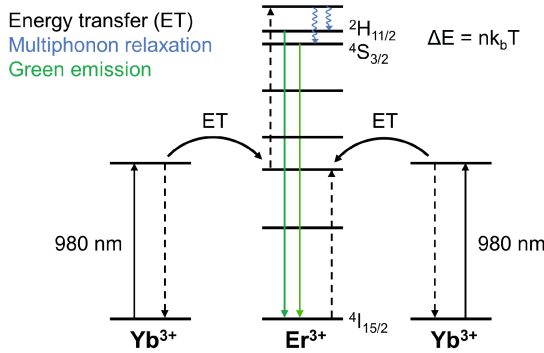


Figure 6.2 Simplified energy level diagram of the Er³⁺/Yb³⁺ couple featuring the transitions that contribute to the upconversion process upon excitation with 980 nm light. The ²H_{11/2} and ⁴S_{3/2} energy levels are thermally coupled (populations governed by Boltzmann statistics).

Due to the small energy difference ($\approx 700 \text{ cm}^{-1}$) between the ⁴S_{3/2} and ²H_{11/2} states, fast thermal equilibration is observed. The populations of these two thermally coupled, excited states are governed by a Boltzmann distribution, as described below (Equation 6.1):

$$\frac{N_2}{N_1} = e^{\left(\frac{-\Delta E}{k_b T}\right)} \tag{Eq. 6.1}$$

N_i corresponds to the population of an excited state i, ΔE represents the energy difference between two thermally coupled states, k_b is the Boltzmann constant and T is the temperature. As the emission intensity is proportional to the population of an emitting state, the luminescence intensity ratio I₂/I₁ of two states can be expressed as:

$$\frac{I_2}{I_1} = \frac{A_2 g_2}{A_1 g_1} \cdot e^{\left(\frac{-\Delta E}{k_b T}\right)} = c \cdot e^{\left(\frac{-\Delta E}{k_b T}\right)} \tag{Eq. 6.2}$$

where I_i represents the integrated luminescence intensity of a given excited state I and A_i corresponds to the spontaneous emission rate to the ground state with a degeneracy g_i. A temperature increase leads to a higher population of the high energy state (i.e., ²H_{11/2}, **Figure 6.2**), which is manifested in a stronger luminescence. This is also evident from Equation 6.1: The N₂/N₁ ratio increases with temperature. Equation 6.2 can then be rearranged to yield a linear correlation between the natural logarithm of the emission intensity ratio I₂/I₁ of the associated states and the reciprocal temperature:

$$\ln\left(\frac{I_2}{I_1}\right) = \ln c - \frac{\Delta E}{k_B T} \tag{Eq. 6.3}$$

6.2.5.1 Calibration and Data Analysis

The luminescence of the catalyst/NP system was calibrated with spectra that were collected at intervals of 10 K while heating the sample in a Linkam THMS600 microscope stage from 303 K (blue) to 473 K (red) in air (**Figure 6.3**). The data analysis was performed using an in-house developed code in Wolfram Mathematica. All acquired spectra were normalized to the maximum intensity of the ${}^4S_{3/2}-{}^4I_{15/2}$ emission peak. The normalized spectra were then evaluated by integrating each spectrum in the 510–530 nm (${}^4S_{3/2}-{}^4I_{15/2}$ emission peak, I_2) and 537–564 nm (${}^2H_{11/2}-{}^4I_{15/2}$ emission peak, I_1) ranges and plotting the obtained logarithmic intensity ratios $\ln(I_2/I_1)$ against the reciprocal temperature ($1/T$). A fit of the resulting plot yielded $\Delta E \approx 736 \text{ cm}^{-1}$, which stands in agreement with values from the literature.^[16,20] Unknown temperatures were subsequently determined by calculating the luminescence intensity ratio for a given spectrum and plugging this into Equation 6.4 to determine T:

$$T = \frac{\Delta E}{k_B \left(\ln c - \ln \left(\frac{I_2}{I_1} \right) \right)} \quad (\text{Eq. 6.4})$$

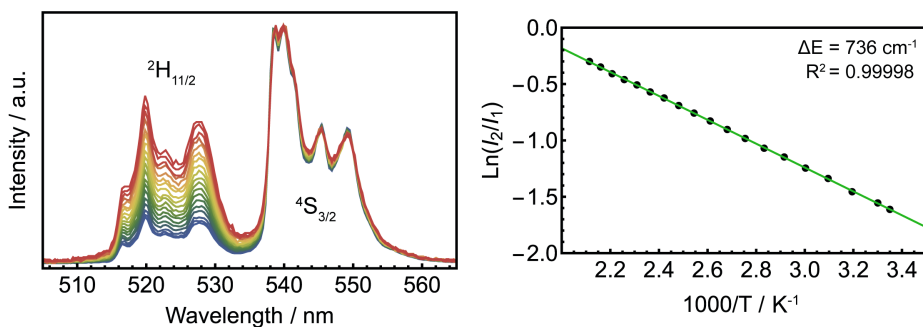


Figure 6.3 Luminescence spectra of $\text{NaYF}_4:\text{Er}^{3+}, \text{Yb}^{3+}/\text{NaYF}_4$ core-shell nanoparticles (NPs) collected between 303 K (blue) to 473 K (red) during excitation with 980 nm light (left). The emission spectra were normalized to the maximum intensity of the ${}^4S_{3/2}-{}^4I_{15/2}$ emission peak (537–560 nm). By plotting the logarithm of the corresponding luminescence intensity ratios I_2/I_1 , versus $1000/T$, a linear fit is obtained (right). This can be used to determine the unknown temperature of a catalyst bed from its corresponding luminescence intensity ratio when irradiated with 980 nm light.

6.2.5.2 *In Situ* Catalyst Characterization

Two different measurement cells were used for performing the *in situ* experiments: A custom-made stainless steel spectroscopy cell with an optical quartz window and a Harrick Praying Mantis™ High Temperature Reaction Chamber. For measurements with the custom cell, the NP-treated catalyst material was loaded on top of a polytetrafluoroethylene (PTFE) disc inside the custom reaction cell under inert conditions inside a glovebox. Due to the lower thermal conductivity of PTFE [0.26 W/(m·K), at 323 K]^[28] relative to high-density polyethylene (HDPE) [0.43 W/(m·K)]^[29], amorphous silica [1.38 W/(m·K)]^[9] and, most importantly, stainless steel [cell material, 13.8 W/(m·K)]^[9], the heat transfer via conduction is reduced. The Harrick cell was loaded following the procedure stated in Section 6.2.4. After taking the loaded

cell out of the glovebox, the fiber probe was placed approximately 1.5 cm above the quartz window of the cell, orthogonal to the sample surface. Prior to polymerization, the bypass of the cell was flushed with nitrogen for 10 min. Subsequently, pure ethylene (C_2H_4 , 5 mL/min) was introduced. All olefin polymerization reactions were performed 1 bar ethylene. Emission spectra were acquired using a 1 s integration time.

6.3 Results and Discussion

The aim of the series of experiments that is described in this **Chapter** was to explore luminescence thermometry as an analytical method for temperature detection and activity determination in olefin polymerization catalysis. To make this possible, the following three requirements had to be validated: i) A homogeneous distribution of the temperature sensors on the catalyst particles, ii) the chemical compatibility of the temperature sensors with sensitive olefin polymerization catalysts, and iii) correlations between the acquired temperature data and kinetic data that is derived from a complementary method.

6.3.1 Assessing the Distribution of the Temperature Sensors on the Catalyst

As mentioned above, the core-shell nanoparticles (NPs) were deposited on the $Zr/MAO/SiO_2$ catalyst material via solution impregnation. Loadings in the range of 1–5 wt% resulted in a high coverage and homogeneous distribution of the NPs on the surface of the catalyst particles, as is evident from scanning electron microscopy-energy dispersion X-ray (SEM-EDX) measurements (**Figures 6.4** and **6.5**). No significant agglomeration of the NPs was observed with the SEM-EDX method. A loading of 1 wt% was adopted for all temperature measurements to limit the chemical and physical influence of the NPs on the catalyst (i.e., stability and accessibility of the active sites).

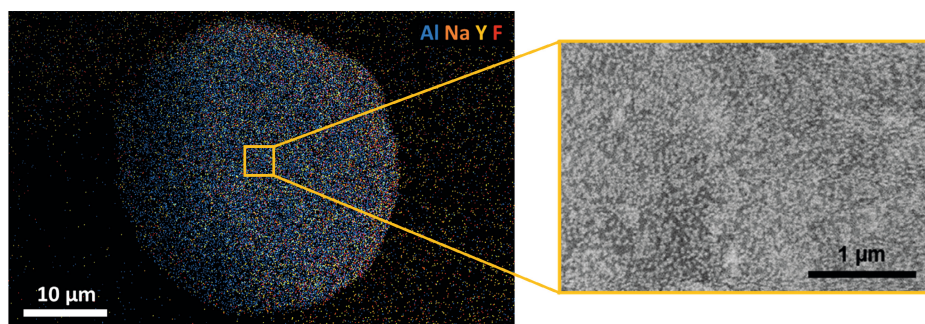


Figure 6.4 Energy-dispersive X-ray (EDX) map (left) and scanning electron microscopy (SEM) image (right) of a $Zr/MAO/SiO_2$ catalyst particle (with MAO = methylaluminoxane) that was treated with ~ 5 wt% $NaYF_4:Er^{3+},Yb^{3+}/NaYF_4$ core-shell nanoparticles (NPs). The sodium (Na), yttrium (Y) and fluorine (F) EDX maps, together with the SEM image, clearly indicate a homogeneous coverage of the catalyst particle's surface with nanoparticles. The aluminum (Al) map represents the distribution of the co-catalyst methylaluminoxane (MAO), which is homogeneously distributed over the entire catalyst particle.

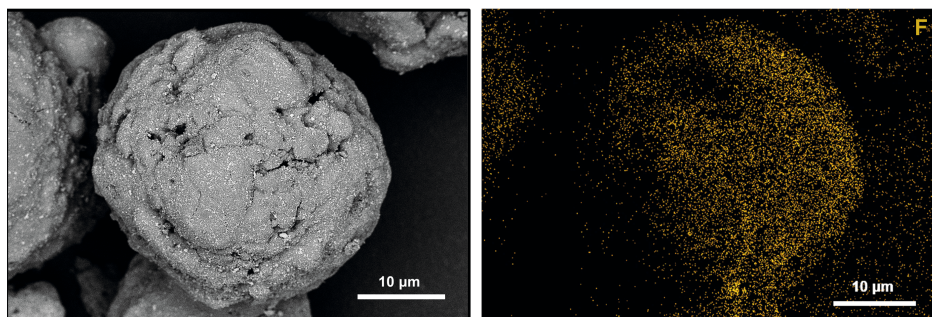


Figure 6.5 Scanning electron microscopy (SEM) image (left) and energy-dispersive X-ray (EDX) map (right) of a Zr/MAO/SiO₂ catalyst particle (with MAO = methylaluminoxane) that was treated with ~ 1 wt% NaYF₄:Er³⁺,Yb³⁺/NaYF₄ core-shell nanoparticles (NPs). The fluorine (F) EDX map points to a homogeneous coverage of the catalyst particle's surface. The left half of the particle features a lower F signal due to its sub-optimal orientation with respect to the EDX detector.

6.3.2 Investigating the Chemical Compatibility of the Catalyst and the Temperature Sensors

The activity of the Zr/MAO/SiO₂ catalyst material remained unaffected in the presence of the NaYF₄:Er³⁺,Yb³⁺/NaYF₄ core-shell nanoparticles at a loading of 1 wt%. This was demonstrated with diffuse reflectance infrared Fourier transform spectroscopy (DRIFTS, **Figure 6.6**), which can be used to monitor the formation of polyethylene at the catalyst bed surface (more details can be found in **Chapter 4**). The activity was determined as time derivative of the integrated $\nu_s(\text{C-H})$ band at approximately 2851 cm⁻¹ – a vibrational band that is representative for the presence and growth of polyethylene.

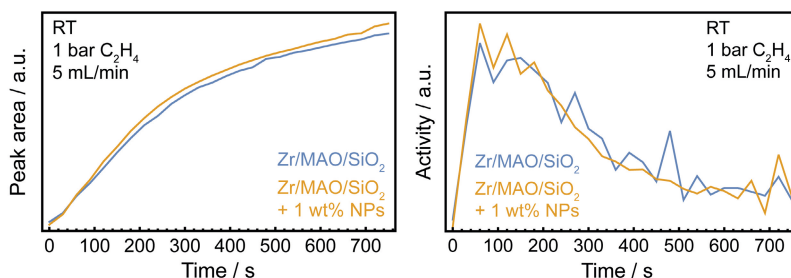


Figure 6.6 Activity data of the Zr/MAO/SiO₂ catalyst material (with MAO = methylaluminoxane) in the presence and absence of 1 wt% NaYF₄:Er³⁺,Yb³⁺/NaYF₄ core-shell nanoparticles (NPs) (measured in a Harrick cell, ~ 12 mg catalyst, room temperature, pressure of 1 bar C₂H₄, and a flow rate of 5 mL/min) as derived from *in situ* diffuse reflectance infrared Fourier transform spectroscopy (DRIFTS) experiments. Left: Symmetric C-H stretching vibration (2851 cm⁻¹) band areas plotted against time. Right: Catalyst activities (first time derivative of 2853 cm⁻¹ band area) plotted against time.

6.3.3 Assessing the Influence of the Reaction Cell on the Temperature Profile

After confirming the chemical compatibility of the sensitive metallocene-based catalyst material with the core-shell nanoparticles, temperature measurements were performed using two different reaction cells.

In a first set of experiments, a custom-made reaction cell was used (**Figure 6.7**). In this cell, the reactant gas flows over the catalyst powder. With conduction playing a significant role in the heat transfer of particle diameters of 10–50 μm diameter (we refer here to CFD calculations by McKenna *et al.* ^[30,31]), the catalyst powder was placed on top of a PTFE disc to minimize heat transfer to the steel reaction cell. Three runs, conducted with ~ 2 mg of dispersed Zr/MAO/SiO₂ catalyst at 1 bar C₂H₄ (5 mL/min) and room temperature, revealed a temperature rise of ~ 7 –9 K upon switching the feed gas from nitrogen to ethylene (**Figure 6.7**). The sharp initial increase is mainly attributable to olefin polymerization activity and to a lesser extent to the change in gas composition (~ 2 K increase due to the difference in the thermal conductivity of the gases). Following the increase at reaction onset, the temperature decreased gradually over time. This can be attributed to the onset of mass transfer limitations that are associated with the build-up of polyethylene, thus leading to a slower reaction rate (induction period). ^[10,32,33] The sample amount was subsequently increased to 10 mg, while also ensuring that the catalyst packing was more compact. Interestingly, this led to a significantly more pronounced temperature increase of ~ 51 K (**Figure 6.7**). In several experiments, starting temperatures in the range of ~ 304 – 312 K (i.e., higher than the temperature of the laboratory; ~ 293 K) were observed. These differences are attributed to laser heating, which is governed by the distance of the probe to the catalyst bed, as well as to the packing of the catalyst bed. Both affect the dissipation of heat from and within the catalyst powder (assuming comparable laser powers).

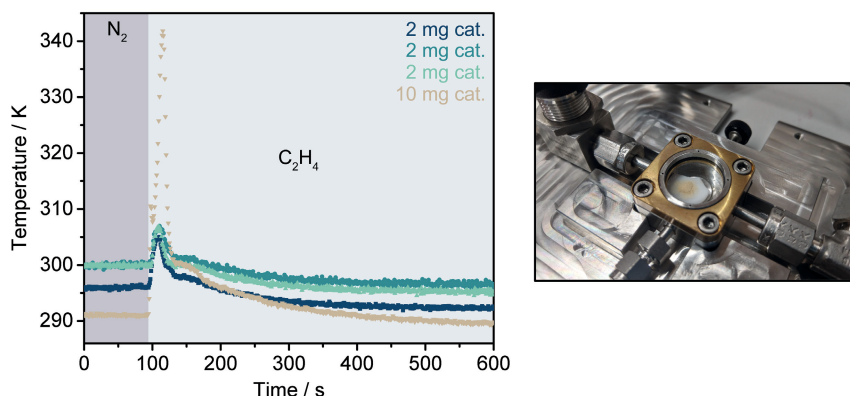


Figure 6.7 Temperature profiles recorded of the Zr/MAO/SiO₂ catalyst material (with MAO = methylaluminoxane) under study during gas-phase ethylene polymerization in a custom reaction cell. Experimental conditions: ~ 2 – 10 mg catalyst, room temperature, a pressure of 1 bar C₂H₄, and a flow rate of 5 mL/min.

To further study the influence of the reaction cell and sample packing on heat transfer, experiments were also performed with a Harrick reaction cell using ~ 12 mg of catalyst material. The catalyst powder was loaded on top of a stainless steel frit inside the cylinder of the cell. In contrast to the custom-made reaction cell, gas flows through the catalyst bed from top to bottom. As is evident in **Figure 6.8**, the obtained temperature profiles were markedly broader, thus either indicating higher heat generation (due to higher catalyst activity) or slower heat dissipation due to the cell design and sample packing.

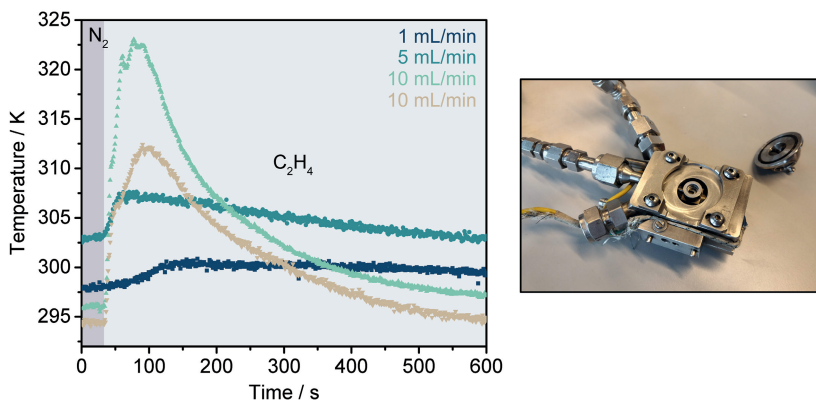


Figure 6.8 Temperature profiles recorded of the Zr/MAO/SiO₂ catalyst material (with MAO = methylaluminoxane) during gas-phase ethylene polymerization at different ethylene flow rates in a Harrick reaction cell. Experimental conditions: ~ 2 mg catalyst, compact packing, a pressure of 1 bar C₂H₄, and room temperature.

6.3.4 Determining the Influence of the Ethylene Flow Rate and Reaction Cell Set Temperature on the Temperature Profile

Different ethylene flow rates (i.e., 1 mL/min, 5 mL/min, and 10 mL/min at a pressure of 1 bar) were adopted to study the role of the reactant flow rate on the exothermicity of the olefin polymerization reaction. As can be observed in **Figure 6.8**, the temperature increase was larger at higher ethylene flow rates. While flow rates of 1 mL/min and 5 mL/min produced temperature spikes of ~ 2.5 K and ~ 4 K, respectively, a flow rate of 10 mL/min of ethylene resulted in substantially higher temperature increases of ~ 18 K and ~ 27 K. The higher flow rate of ethylene results in a higher local concentration of ethylene at the active sites, thereby increasing the rate and the exothermicity of the reaction. The narrowing of the temperature profiles at higher ethylene flows also suggests an earlier onset of mass transfer limitations, which lower the reaction rates. Interestingly, significant differences in exothermicity and reaction rate can be observed between individual testing runs at the onset of olefin polymerization, which has also been observed during gas-phase testing of the catalyst material (**Chapter 2**). The different starting temperatures of the catalyst beds may be explained by variations in their composition and packing (including possible effects of residual solvent from the impregnation procedure), resulting in differences in heat transfer and dissipation.

6.3.5 Determining the Influence of the Reaction Cell Set Temperature on the Temperature Profile

The temperature of the Harrick cell was varied to study the influence of the reaction temperature on heat formation and reactivity. At set temperatures of 323 K, 343 K and 363 K and an ethylene flow rate of 10 mL/min (1 bar), temperature increases of ~ 15 K, ~ 18 K and ~ 49 K were observed (**Figure 6.9**). It must be noted that the measurements at the set points of 343 K and 363 K were effectively performed at ~ 331 K and ~ 349 K. This may be associated with an insufficient equilibration period after reaching the desired set temperature, thus resulting in a lower temperature at the surface of the catalyst bed. Given that temperature rises of ~ 18 K and ~ 27 K were observed at room temperature (**Figures 6.8** and **6.9**), no clear trend in heat evolution was established as a function of temperature for the given data and experimental conditions. While the largest temperature increase was observed at the highest temperature (349 K), the catalyst bed packing is likely to have significantly influenced all runs, hence accounting for differences in exothermicity amongst similar (**Figure 6.9**) or identical (**Figure 6.8**) testing runs.

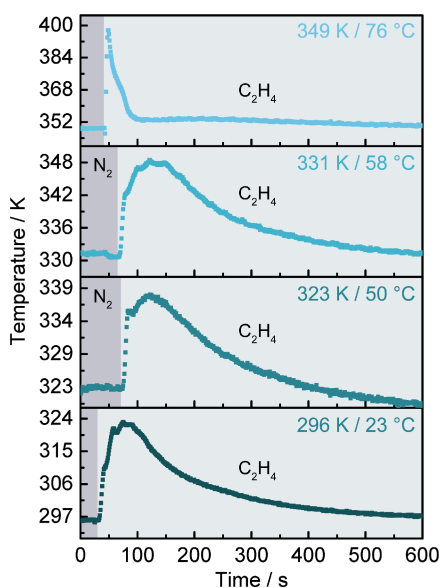


Figure 6.9 Temperature profiles recorded of the Zr/MAO/SiO₂ catalyst material (with MAO = methylaluminoxane) during gas-phase ethylene polymerization at different ethylene flow rates in a Harrick reaction cell. Experimental conditions: ~ 12 mg catalyst, compact packing, a pressure of 1 bar C₂H₄, a flow rate of 10 mL/min, and room temperature.

Interestingly, minor deviations in temperature can be observed in most runs within tens of seconds after the initial temperature increase. These fluctuations could be related to mass transfer limitations and the occurrence of first fragmentation events that subsequently release new active sites, thereby increasing the rate of the olefin polymerization reaction.

6.3.6 Correlating Luminescence Thermometry and Activity Data

The temperature profile of the catalyst material was compared to the kinetic data derived from the DRIFTS data. Both sets of data were acquired with the same cell under identical conditions (i.e., room temperature, a pressure of 1 bar C_2H_4 , and a flow rate of 5 mL/min). As can be noted in **Figure 6.10**, the temperature evolution of the polymerization reaction (i.e., an increase of ~ 8 K) is directly related to the catalyst's kinetics, as expected according to the Arrhenius equation. Both represent the pre-polymerization regime that is characteristic for supported olefin polymerization catalysts.^[32]

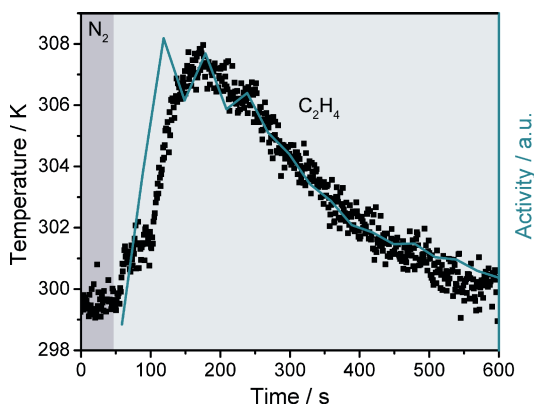


Figure 6.10 Temperature and activity plots for the nanoparticles (NPs)-treated Zr/MAO/SiO₂ catalyst material (with MAO = methylaluminoxane) during gas-phase ethylene polymerization (as measured in a Harrick reaction cell, ~ 12 mg catalyst, room temperature, a pressure of 1 bar C_2H_4 , and a flow rate of 5 mL/min; the activity curve was shifted along the x-axis to match the temperature curve). The temperature profile of the catalyst is directly related to its kinetic profile.

6.4 Conclusions

Lanthanide-doped NaYF₄ core-shell nanoparticles (NPs), displaying temperature-dependent luminescence, were homogeneously deposited on a silica-supported metallocene-based catalyst (i.e., a Zr/MAO/SiO₂ material) without inhibiting its polymerization activity. The green upconversion luminescence of the NPs was exploited to obtain well-defined temperature profiles, which yield kinetic information on the catalyst material. In contrast to more conventional techniques for temperature detection, luminescence thermometry allows for the direct yet non-invasive acquisition of a catalyst bed's surface temperature, even at minimal sample amounts. It is sensitive enough to study the effect of the reaction cell design and catalyst bed preparation on heat formation, transfer and dissipation. The high temporal resolution of the developed technique makes it well-suited for monitoring the activity of catalyst materials at the onset of olefin polymerization. The analysis can be performed online as it does not require significant post-processing of the acquired data.

The significant temperature spikes of up to 51 K that have been detected here under mild reaction conditions (e.g., 1 bar ethylene at 5–10 mL/min, 10–12 mg catalyst, room temperature) underline the need for efficient heat transfer during gas-phase olefin polymerization reactions. In the absence of a pre-polymerization procedure or under suboptimal operating conditions, a polymerization reaction at high pressures is likely to involve significant local temperature increases (i.e., hotspots) in the catalyst bed due to particle overheating, which could drastically affect the morphology of the formed polymer product.

In future research, the upconversion luminescence of $\text{Er}^{3+}/\text{Yb}^{3+}$ -doped NPs can be exploited for temperature mapping experiments at high spatial resolutions.^[16,34–36] By using suitable microscopy systems (e.g., confocal fluorescence microscope), temperature maps of individual catalyst particles can be acquired. This will help to explore the intra- and interparticle heterogeneity amongst catalyst particles, in terms of their activity, at the onset of olefin polymerization. Confocal microscopy may also be suitable to monitor the temperature below the catalyst surface. This will require the integration of temperature sensors into the supports of olefin polymerization catalysts. Silica-coated core-shell NPs (i.e., $\text{NaYF}_4:\text{Er}^{3+},\text{Yb}^{3+}/\text{NaYF}_4/\text{SiO}_2$) can be integrated into SiO_2 , $\text{Mg}(\text{OEt})_2$ or MgCl_2 supports to study industrial-grade polymerization catalysts, including Ziegler-Natta and Phillips-type catalyst systems.

Acknowledgments

Thomas van Swieten (Utrecht University, UU) is gratefully acknowledged for his assistance with the temperature measurements and providing the Wolfram Mathematica code for data analysis. Martijn Mekkering (UU) is thanked for the synthesis of the $\text{NaYF}_4:\text{Er}^{3+},\text{Yb}^{3+}/\text{NaYF}_4$ core-shell nanoparticles. Florian Meirer (UU) is recognized for his help with the analysis of the DRIFTS data. Sander Deelen (UU) is thanked for the design of the custom reaction cell. Robin Geitenbeek (UU) is acknowledged for his experimental advice.

References

1. D. Jeremic, *Polyethylene*, in *Ullmann's Encycl. Ind. Chem.*, **2014**, 1–42.
2. J. R. Severn, J. C. Chadwick, R. Duchateau, N. Friederichs, *Chem. Rev.* **2005**, *105*, 4073–4147.
3. E. Tioni, J. P. Broyer, R. Spitz, V. Monteil, T. F. L. McKenna, *Macromol. Symp.* **2009**, *285*, 58–63.
4. K. J. Laidler, *J. Chem. Educ.* **1984**, *61*, 494–498.
5. G. Fink, B. Tesche, F. Korber, S. Knoke, *Macromol. Symp.* **2001**, *173*, 77–87.
6. E. J. G. Eriksson, T. F. McKenna, *Ind. Eng. Chem. Res.* **2004**, *43*, 7251–7260.
7. B. Olalla, J. P. Broyer, T. F. L. McKenna, *Macromol. Symp.* **2008**, *271*, 1–7.
8. E. Tioni, R. Spitz, J. P. Broyer, V. Monteil, T. McKenna, *AIChE J.* **2012**, *58*, 256–267.
9. E. J. G. Eriksson, G. Weickert, T. F. McKenna, *Macromol. React. Eng.* **2010**, *4*, 95–108.
10. J. T. M. Pater, G. Weickert, W. P. M. van Swaaij, *AIChE J.* **2003**, *49*, 450–464.
11. D. Jaque, F. Vetrone, *Nanoscale* **2012**, *4*, 4301–4326.
12. C. D. S. Brites, S. Balabhadra, L. D. Carlos, *Adv. Opt. Mater.* **2019**, *7*, 1–30.
13. R. G. Geitenbeek, A. E. Nieuwelink, T. S. Jacobs, B. B. V. Salzmänn, J. Goetze, A. Meijerink, B. M. Weckhuysen, *ACS Catal.* **2018**, *8*, 2397–2401.
14. T. Hartman, R. G. Geitenbeek, G. T. Whiting, B. M. Weckhuysen, *Nat. Catal.* **2019**, *2*, 986–996.
15. F. Auzel, *Chem. Rev.* **2004**, *104*, 139–173.
16. T. P. van Swieten, T. van Omme, D. J. van Den Heuvel, S. J. W. Vonk, R. G. Spruit, F. Meirer, H. H. P. Garza, B. M. Weckhuysen, A. Meijerink, F. T. Rabouw, R. G. Geitenbeek, *ACS Appl. Nano Mater.* **2021**, *4*, 4208–4215.
17. P. Haro-González, I. R. Martín, L. L. Martín, S. F. León-Luis, C. Pérez-Rodríguez, V. Lavín, *Opt. Mater.* **2011**, *33*, 742–745.
18. D. Li, Y. Wang, X. Zhang, K. Yang, L. Liu, Y. Song, *Opt. Commun.* **2012**, *285*, 1925–1928.
19. X. Xu, Z. Wang, P. Lei, Y. Yu, S. Yao, S. Song, X. Liu, Y. Su, L. Dong, J. Feng, H. Zhang, *ACS Appl. Mater. Interfaces* **2015**, *7*, 20813–20819.
20. R. G. Geitenbeek, P. T. Prins, W. Albrecht, A. van Blaaderen, B. M. Weckhuysen, A. Meijerink, *J. Phys. Chem. C* **2017**, *121*, 3503–3510.
21. R. G. Geitenbeek, B. B. V. Salzmänn, A. E. Nieuwelink, A. Meijerink, B. M. Weckhuysen, *Chem. Eng. Sci.* **2019**, *198*, 235–240.
22. F. T. Rabouw, P. T. Prins, P. Villanueva-Delgado, M. Castelijns, R. G. Geitenbeek, A. Meijerink, *ACS Nano* **2018**, *12*, 4812–4823.
23. C. Homann, L. Krukewitt, F. Frenzel, B. Grauel, C. Würth, U. Resch-Genger, M. Haase, *Angew. Chem. Int. Ed.* **2018**, *57*, 8765–8769.
24. T. Rinkel, A. N. Raj, S. Dühren, M. Haase, *Angew. Chem. Int. Ed.* **2016**, *55*, 1164–1167.
25. M. J. Mekkering, *Towards in Situ Temperature Detection at the Single-Particle Level on Supported Olefin Polymerization Catalysts*, M.Sc. thesis, Utrecht University, **2019**.
26. G. T. Whiting, F. Meirer, D. Valencia, M. M. Mertens, A. J. Bons, B. M. Weiss, P. A. Stevens, E. de Smit, B. M. Weckhuysen, *Phys. Chem. Chem. Phys.* **2014**, *16*, 21531–21542.
27. N. Menyuk, K. Dwight, J. W. Pierce, *Appl. Phys. Lett.* **2003**, *21*, 159–161.
28. D. M. Price, M. Jarratt, *Thermochim. Acta* **2002**, *392–393*, 231–236.
29. J. Yu, B. Sundqvist, B. Tonpheng, O. Andersson, *Polymer* **2014**, *55*, 195–200.
30. T. F. McKenna, D. Cokljat, P. Wild, *Comput. Chem. Eng.* **1998**, *22*, S285–S292.
31. T. F. McKenna, D. Cokljat, R. Spitz, D. Schweich, *Catal. Today* **1999**, *48*, 101–108.
32. G. Fink, B. Steinmetz, J. Zechlin, C. Przybyla, B. Tesche, *Chem. Rev.* **2000**, *100*, 1377–1390.
33. J. Zechlin, B. Steinmetz, B. Tesche, G. Fink, *Macromol. Chem. Phys.* **2000**, *201*, 515–524.
34. E. Saidi, N. Babinet, L. Lalouat, J. Lesueur, L. Aigouy, S. Volz, J. Labéguerie-Egéa, M. Mortier, *Small* **2011**, *7*, 259–264.

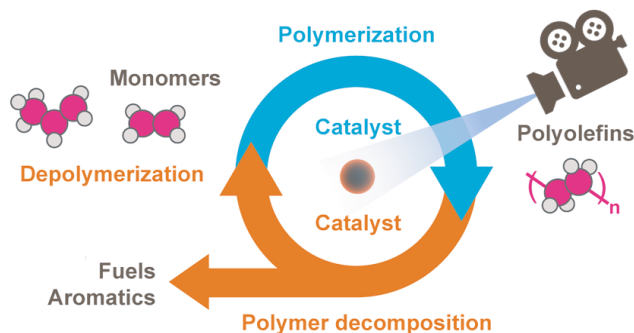
35. F. Vetrone, R. Naccache, A. Zamarrón, A. J. De La Fuente, F. Sanz-Rodríguez, L. M. Maestro, E. M. Rodríguez, D. Jaque, J. G. Sole, J. A. Capobianco, *ACS Nano* **2010**, *4*, 3254–3258.
36. X. Zhu, J. Li, X. Qiu, Y. Liu, W. Feng, F. Li, *Nat. Commun.* **2018**, *9*, 2176.

Chapter 7

Visualizing the Structure, Composition and Activity of Single Catalyst Particles for Olefin Polymerization and Polyolefin Decomposition

This **Chapter** is based on the following scientific article:

M. J. Werny, F. Meirer, and B. M. Weckhuysen. *Submitted for publication.*



The structural and morphological characterization of individual catalyst particles for olefin polymerization, as well as for the reverse process of polyolefin decomposition, can provide an improved understanding for how these catalyst materials operate under relevant reaction conditions. In this review, we discuss an emerging analytical toolbox of 2D and 3D chemical imaging techniques that is suitable for investigating the chemistry and reactivity of related catalyst systems. While synchrotron-based X-ray microscopy still provides unparalleled spatial resolutions in 2D and 3D, a number of laboratory-based techniques, most notably focused ion beam-scanning electron microscopy, confocal fluorescence microscopy, infrared photoinduced force microscopy and laboratory-based X-ray nano-computed tomography, have helped to significantly expand the arsenal of tools available to scientists in heterogeneous catalysis and polymer science. In terms of future research, the review outlines the role and impact of *in situ* and *operando* (spectro-)microscopy experiments, involving sophisticated reactors as well as online reactant and product analysis, to obtain real-time information on the formation, decomposition, and mobility of polymer phases within single catalyst particles. Furthermore, the potential of fluorescence microscopy, X-ray microscopy and optical microscopy is highlighted for the high-throughput characterization of olefin polymerization and polyolefin decomposition catalysts. By combining these chemical imaging techniques with, for example, chemical staining methodologies, selective probe molecules as well as particle sorting approaches, representative structure-activity relationships can be derived at the level of single catalyst particles.

7.1 Introduction

Over the past century, the polyolefin industry has grown steadily.^[1,2] In fact, polyolefin resins accounted for 45% of the total polymer production in 2017.^[3] Polyolefins are widely used in our day-to-day lives due to their advantageous physical, chemical, and mechanical properties. The insufficient recycling of these materials as well as their uncontrolled release into the environment,^[1] however, represent pressing problems and require immediate attention.

From a historical point of view, industrial olefin polymerization has its roots in the 1930s.^[4] It was in this period that ethylene was first polymerized to form low-density polyethylene (LDPE) via a high-temperature and high-pressure radical process. In the 1950s, two families of heterogeneous catalysts were discovered for olefin polymerization under milder conditions, i.e., the Phillips catalyst (e.g., $\text{CrO}_x/\text{SiO}_2$) and the Ziegler-Natta catalyst (e.g., $\text{TiCl}_4/\text{MgCl}_2$).^[4] Until this very day, the two catalyst systems contribute largely to the production of various grades of high-density polyethylene (HDPE), linear low-density polyethylene (LLDPE), as well as polypropylene (PP).^[5] Supported metallocene/MAO-based catalysts (with MAO = methylaluminoxane) were discovered in the 1980s and are well suited to producing specialty polymers with more complex microstructures and tacticities, such as isotactic PP (i-PP).^[6,7]

In contrast to the rather mature field of catalytic olefin polymerization, the field of catalytic polyolefin recycling has only gained momentum in recent years. Processes, such as catalytic pyrolysis (i.e., thermal cracking), hydrocracking and hydrogenolysis, offer viable pathways to convert plastic waste into chemical building blocks, thus ensuring the circularity of these polymer materials.^[8,9] The aim is to convert plastic waste into, for example, naphtha-like fractions for refining operations, fuels such as gasoline or diesel, and valuable monomers for the polyolefin industry (**Figure 7.1A**). By employing heterogeneous catalysts, such as zeolites, for the pyrolysis of polyolefins, such as PP, a mixture of alkanes and methyl-aromatics can be obtained at temperatures that are lower than those employed in non-catalytic pyrolysis.^[10] In fact, affordable solid catalysts, such as fluid catalytic cracking (FCC) and related equilibrium FCC cracking (ECAT) catalysts, have been reported to convert PP into aliphatic and aromatic compounds, alkenes and propylene in the absence of hydrogen.^[11] Supported metal nanoparticles (most commonly Pt, Ru, and Ni), metal oxides and zeolite catalysts, on the other hand, have shown promising performance in the hydrocracking and hydrogenolysis of HDPE, LDPE, and mixed plastic waste.^[12-18]

Mechanistically speaking, polyolefins, such as PE or PP, are formed via insertion of ethylene or propylene into a M-H or M-alkyl bond, followed by multiple insertions of monomers into the resulting M-alkyl bond.^[19-21] According to the principle of microkinetic reversibility, the olefin polymerization reaction can be reversed to yield olefinic monomers. This process of depolymerization, which essentially involves a β -alkyl elimination step, is thermodynamically unfavorable (i.e., endergonic, see potential energy diagram in **Figure 7.1B**).^[22,23] In fact, the activation energies for the thermal decomposition of PE and PP have been reported to lie in the range of ~ 140 – 300 kJ/mol.^[24] The hydrogenolysis of the olefin, however, results in the process of polymer chain scission becoming thermodynamically accessible (**Figure 7.1B**).

^[20,23,25,26] This was validated in 1988 by Dufaud and Basset, who reported on a supported

Ziegler-Natta-type zirconium hydride catalyst that not only formed PE, but also cleaved the same molecule in the presence of hydrogen at 150 °C.^[20]

Having explored this mechanistic correlation between olefin polymerization and depolymerization, it is also of interest to consider the physicochemical properties of the heterogeneous catalyst systems under reaction conditions. While significant mass transfer limitations arise during olefin polymerization due to a rapid build-up of polymer in the pores of the catalyst support,^[27,28] mass transfer is similarly limited when molten polymer enters the macropores of a heterogeneous catalyst particle during a polyolefin decomposition reaction. It is thus clearly evident that the spatial distribution of the polymer phase, and, in the case of polyolefin cracking, its mobility and decomposition, critically influence the reactivity of a catalyst particle. In order to make definitive conclusions about these dynamic processes, imaging techniques with high spatial and temporal resolutions are necessary. These can deliver information on the morphology of individual particles (**Figure 7.1C**) at the nanometer scale, thus helping to identify and define structure-activity relationships.

Single particle data can generally help to rationalize trends derived from bulk catalytic testing. Similarly important, however, is the identification of particles with atypical or unexpected reactivities, structures and compositions. Considering the large degrees of interparticle heterogeneity that are observed in pristine industrial catalysts,^[29–31] investigations into a representative number of individual particles at high spatial resolutions, preferably in 3D, are vital to fully understand their structural and chemical complexity. This becomes even more relevant when considering the lifetime of a catalyst inside a chemical reactor, where concentration and temperature gradients, and, in certain cases, dynamic reactor operations (e.g., fluidized bed reactors, stirred tank reactors, loop reactors, etc.) result in varying reaction conditions and residence times for individual catalyst particles. This affects their reactivity, composition and morphology.

In the past, various characterization techniques have been successfully used to visualize and understand the structural evolution of industrially relevant olefin polymerization catalysts. In this review, we provide an overview of these state-of-the-art analytical techniques and will highlight their potential for studying structural and compositional changes in olefin polymerization and the reverse process of catalytic plastic decomposition/cracking (**Table 7.1**). Both laboratory- and synchrotron-based techniques can deliver information on the structure, composition and reactivity of relevant heterogeneous catalysts at the single particle level. Such insights are vital for a better understanding of the catalysts, mass transport and reaction pathways, and can ultimately advance the design of novel catalyst materials.

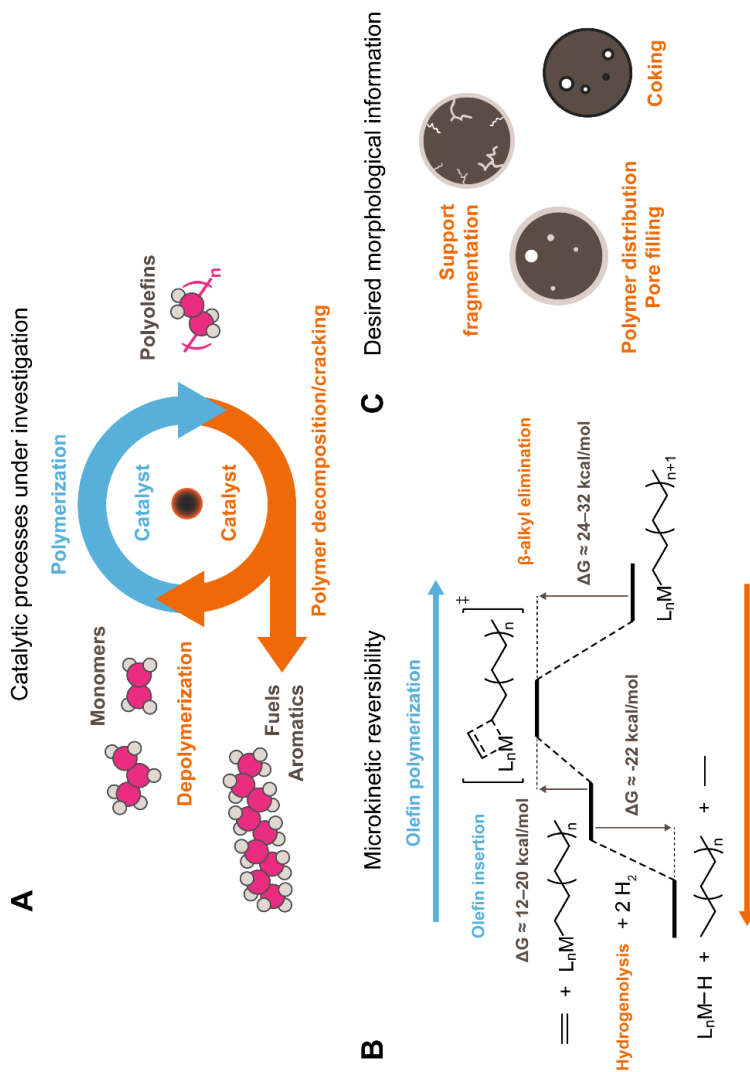


Figure 7.1 A: Catalyst-mediated circularity in the polyolefins value chain. Polyolefins can be decomposed or cracked in the presence of a catalyst to yield fuels and aromatics, or depolymerized catalytically to form the chemical building blocks (i.e., monomers) that they have been synthesized from. B: Potential energy diagram for the processes of olefin insertion (i.e., polymerization), β -alkyl elimination (i.e., depolymerization) and hydrogenolysis. Reproduced and adapted from reference [23]. Copyright © 2022 Wiley-VCH GmbH, published by John Wiley and Sons. C: Main insights that can be extracted with 2D and 3D chemical imaging techniques from heterogeneous catalysts employed in olefin polymerization and polymer decomposition/cracking reactions.

Table 7.1 Overview of 2D and 3D imaging techniques with sub-micron spatial resolutions that have been applied to olefin polymerization or polyolefin decomposition/cracking catalyst particles (including cross-sections thereof).

Characterization technique	Typical samples/ measurement regions	Advantages	Disadvantages
Scanning electron microscopy (SEM)	Individual or multiple catalyst particles/ particle cross-sections in 2D	Very high 2D spatial resolutions, laboratory-based technique, short measurement times, no image reconstruction algorithms required, element-specific imaging if combined with energy-dispersive X-ray spectroscopy (EDX)	Very time-intensive 3D imaging (slice and view), elaborate and destructive sample preparation required for imaging particle cross-sections (focused ion beam milling or microtoming), XRF data acquired with EDX is difficult to quantify and not representative of bulk materials
Scanning transmission electron microscopy (STEM)	Microtomed catalyst particle cross-section in 2D, typical measurement areas: $< 10^2 \mu\text{m}^2$	Very high 2D spatial resolutions, laboratory-based technique, short measurement times, no image reconstruction algorithms required, element-specific imaging if combined with energy-dispersive X-ray spectroscopy (EDX)	Non-representative of complex composite materials, elaborate and destructive sample preparation required for imaging particle cross-sections (microtoming), very time-intensive 3D imaging
Atomic force microscopy (AFM)	Individual catalyst particle/planar catalyst surface or particle cross-section, typical measurement areas: $< 10^2 \mu\text{m}^2$	Very high 2D spatial resolutions, laboratory-based technique, short-medium measurement times, topological information, no image reconstruction algorithms required	Only 2D imaging, small scan area, flat samples required, non-representative of complex composite materials, elaborate and destructive sample preparation required for imaging particle cross-sections (FIB/microtoming)
Infrared photoinduced force microscopy (IR PIFM)	Individual catalyst particle/planar catalyst surface or particle cross-section, typical measurement areas: $< 10^2 \mu\text{m}^2$	Very high 2D spatial resolutions, laboratory-based technique, short-medium measurement times, material identification via IR nano-spectroscopy, topological information via AFM, mechanical properties via phase imaging, no image reconstruction algorithms required	Only 2D imaging, small scan area, flat samples required, non-representative of complex composite materials, elaborate and destructive sample preparation required for imaging particle cross-sections (FIB/microtoming)

Table 7.1 Overview of 2D and 3D imaging techniques with sub-micron spatial resolutions that have been applied to olefin polymerization or polyolefin decomposition/cracking catalyst particles (including cross-sections thereof). (*continued*)

Characterization technique	Typical samples/ measurement regions	Advantages	Disadvantages
Raman microscopy	Individual particle/ particle cross-section in 2D	Short-medium measurement times, laboratory-based technique, relatively non-destructive, no image reconstruction algorithms required, 3D imaging via confocal Raman microscopy	Low-moderate spatial resolutions, beam damage possible
Confocal fluorescence microscopy (CFM)	Individual or multiple particles/particle cross-sections in 2D and 3D	High sample throughput (both in 2D/3D), short measurement times, laboratory-based technique, non-destructive, no image reconstruction algorithms required	Moderate spatial resolutions, scattering and absorption impede characterization of larger catalyst particles (i.e., only sub-volumes can be measured)
Single-molecule fluorescence (SMF) microscopy	Individual catalyst particle in 2D	Short-medium measurement times, laboratory-based technique, non-destructive, no image reconstruction algorithms required	Moderate spatial resolutions, limited to 2D, may require the use of fluorescent model compounds instead of actual reactants, elaborate data analysis
Scanning X-ray transmission microscopy (STXM)	Microtomed particle cross-section in 2D	Very high 2D spatial resolutions, element-specific imaging, relatively non-destructive	Only 2D imaging, small scan area, synchrotron-based technique, capital intensive, thin samples required (< 1 μm), elaborate data analysis
Nano-computed tomography (nanoCT)	Individual or multiple particles in 3D	High 3D spatial resolutions, relatively non-destructive, laboratory-based technique (more accessible than synchrotron-based X-ray microscopy)	Medium-long measurement times, low-medium sample throughput, capital intensive, elaborate image reconstruction and data analysis
Ptychographic X-ray computed tomography (PXCT)	Individual or multiple particles in 3D	Very high 3D spatial resolutions, yields quantitative data on electron density, relatively non-destructive	Long measurement times and low sample throughput with a single beam (not applicable for multibeam operation), synchrotron-based technique, capital intensive, elaborate image reconstruction and data analysis

Table 7.1 Overview of 2D and 3D imaging techniques with sub-micron spatial resolutions that have been applied to olefin polymerization or polyolefin decomposition/cracking catalyst particles (including cross-sections thereof). (*continued*)

Characterization technique	Typical samples/ measurement regions	Advantages	Disadvantages
X-ray fluorescence (XRF) tomography	Individual or multiple particles in 3D	Element-specific 3D imaging, relatively non-destructive, yields quantitative data	Long measurement times, low sample throughput, moderate spatial resolutions, synchrotron-based technique, capital intensive, elaborate image reconstruction and data analysis
Holotomography	Individual or multiple particles in 3D	High sample throughput, high 3D spatial resolutions, short measurement times, relatively non-destructive	Synchrotron-based technique, capital intensive, elaborate image reconstruction and data analysis

7.2 Assessing the Morphology and Activity of Supported Olefin Polymerization Catalyst Particles

Conventional polyolefins, such as PE and PP, are solid materials that are formed via polymerization of their respective monomers, i.e., ethylene, propylene and, depending on the PE grade, different co-monomers such as 1-butene, 1-hexene or 1-octene. As mentioned above, the production of HDPE, LLDPE and PP is dominated by various transition metal-based catalysts on inorganic supports, such as silica or magnesium chloride. Once these polymers are formed inside the pores of a given catalyst support, stress is generated. When this stress crosses a certain threshold, as is, amongst others, determined by the mechanical stability of the support material, the support begins to break apart. This physical disintegration of the catalyst support is referred to as fragmentation. The process of fragmentation plays a central role in the morphological development of olefin polymerization catalyst particles. Under ideal conditions, each spherical catalyst particle in the size range of 10–100 μm disintegrates uniformly during polymerization to form a 100–3000 μm sized polymer particle with the same shape as the initial catalyst support. The catalyst support remains highly dispersed in the formed polymer matrix. This is known as the replica effect.^[32] An incomplete fragmentation of the support can lead to residual support fragments in the formed polymer, often affecting its quality, and lower the total polymer yield. Uncontrolled or very rapid fragmentation, on the other hand, can result in the break-off of smaller support fragments, which continue to fragment and polymerize as separate entities. These so-called ‘fines’ are known to affect the physico-chemical properties of the polymer and can also cause reactor fouling.

Two mechanisms of catalyst particle fragmentation, namely, the layer-by-layer and the sectioning mechanism, have been widely reported in literature.^[33–36] It is the synergy of both mechanisms that ultimately guarantees uniform particle growth and a high dispersion of the catalyst in the formed polymer matrix.^[37,38] In the layer-by-layer mechanism, polymerization and fragmentation start at the surface of the catalyst particle or its constituent support granulates, resulting in their gradual disintegration from the surface towards their respective cores (**Figure 7.2A**). In the sectioning mechanism, the formation of large, extensive cracks results in the cleavage of the support granulates, or, in some cases, of the entire catalyst particle into multiple larger fragments (**Figures 7.2B** and **7.2C**). The fragmentation of the support is generally more uncontrolled and can lead to a fast exposure of active sites deep within the catalyst particle. The contribution of either mechanism is dictated by the properties of the catalyst support (i.e., surface area, porosity, pore size distribution, particle size and mechanical rigidity), the active sites (distribution, structure, activity and accessibility), the type of α -olefin monomer, the crystallinity of the formed polymer, the process conditions (i.e., temperature, pressure, reaction phase, stirring rate, catalyst bed fluidization, co-catalyst type, and concentration), as well as heat transfer and mass transfer, which are strongly related to the operating conditions.^[27,28,39] The large number of experimental variables creates significant complexity when attempting to identify factors that are largely responsible for a given catalyst particle morphology. In addition to this, the considerable speed of the fragmentation process under industrial conditions currently impedes any true *in situ* characterization of catalyst particles.

In the following sections, leading analytical techniques for the 2D and 3D assessment of olefin polymerization catalyst particle morphologies and activities will be discussed. The here discussed morphological investigations were predominantly performed *ex situ* on pristine and pre-polymerized catalyst samples.

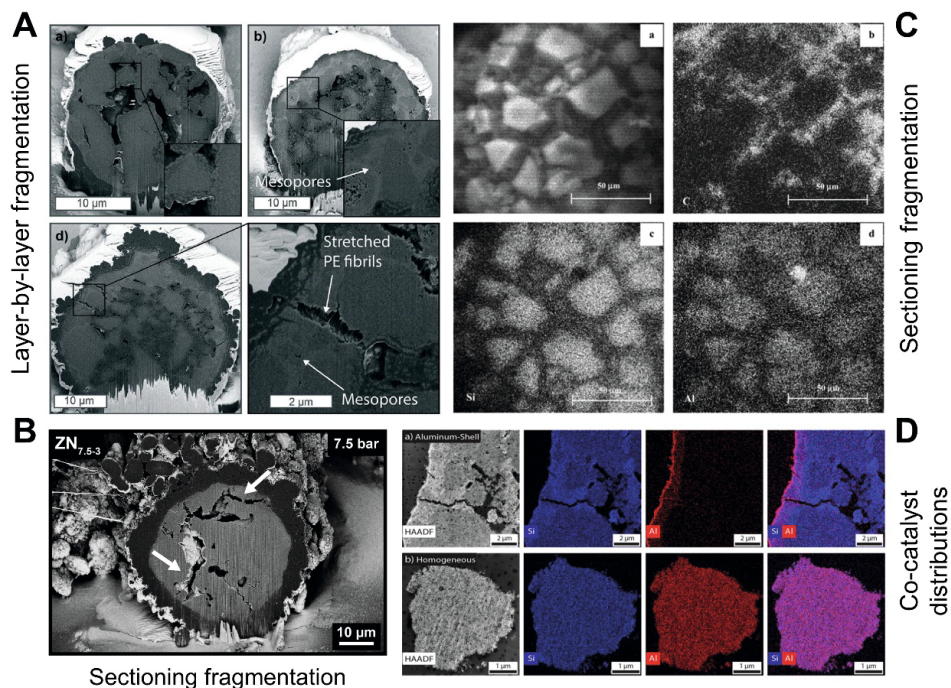


Figure 7.2 Examples of morphological and chemical information that can be extracted with different electron microscopy techniques. A: Focused ion beam-scanning electron microscopy (FIB-SEM) cross-sectional images of silica-supported metallocene-based catalyst particles pre-polymerized in gas-phase at 1 bar ethylene pressure and room temperature for different periods of time. Light gray domains correspond to the silica support, while the dark gray domains represent polyethylene (PE). A strong manifestation of the layer-by-layer fragmentation mechanism is evident, both at the particle surface and at the exposed surfaces of the supports' constituent granulates. Reproduced and adapted from reference [47] with permission from the Royal Society of Chemistry under the CC BY 3.0 license. The figure is an excerpt of the original. Copyright © 2022 Werny *et al.*, published by Wiley-VCH GmbH. C: Scanning electron microscopy (SEM) image (top left) and energy-dispersive X-ray spectroscopy (EDX) maps (C: top right, Si: bottom left, and Al: bottom right) of a silica-supported metallocene catalyst particle after polymerization with propylene (1 h, 50 °C, 4 bar propylene pressure). The outer sphere of the particle has fragmented following the sectioning fragmentation mechanism. Reprinted (adapted) with permission from reference [50]. Copyright © 2005, American Chemical Society. D: Scanning transmission electron microscopy-energy-dispersive X-ray spectroscopy (STEM-EDX) maps (Si: blue, Al: red) recorded of the microtomed cross-sections of two pristine silica-supported metallocene catalysts with Al/Zr molar ratios of 51 (top) and 132 (bottom). A distinct aluminum (Al) shell is observed in the sample with a lower Al loading, while the Al distribution is more homogeneous at higher loadings. Reproduced from reference [29] under the CC BY-NC-ND 4.0 license. Copyright © 2018 Velthoen *et al.*, published by Wiley-VCH Verlag GmbH & Co. KGaA.

7.2.1 Electron Microscopy

Scanning electron microscopy (SEM) is one of the most commonly used methods to assess the morphology of supported polymerization catalyst particles^[40–45] and can yield unparalleled 2D resolutions below 30 nm. It is generally used to determine both the external and internal morphology of individual particles. For the latter, the cross-sections of individual particles are accessed via microtoming or focused ion beam (FIB) cutting and are subsequently imaged. By adopting a horizontal FIB cutting approach^[38], complementary scanning probe techniques, such as infrared photoinduced force microscopy (IR PiFM, **Figure 7.3**) and atomic force microscopy-infrared spectroscopy (AFM-IR), as well as vibrational microscopy techniques, such as IR or Raman microscopy, can be used to verify the distribution of different phases (e.g., silica, polymer, pores), either spectroscopically or topographically.^[38,46] Together, these methods can help to assess the chemical composition, mechanical properties and crystallinities of nascent polymers at different reaction stages.^[38,46]

In recent studies, SEM has been used to image and investigate the early stages of pre-polymerization and fragmentation in silica-supported metallocenes, both at low and high ethylene pressures.^[38,47–49] Here, the particle cross-sections were imaged in backscattered electron (BSE) mode, thus yielding clear contrast between the polymer and the more electron denser silica fragments (**Figure 7.2A**). From a mechanistic point of view, the layer-by-layer mechanism was found to play a prominent role in the fragmentation of these catalyst systems. Contributions from the sectioning mechanism were only observed under more pronounced mass transfer limitations, often in domains of low macroporosity. A remarkably pronounced involvement of the sectioning mechanism was reported for a silica-supported Ziegler-Natta catalyst, which was investigated with FIB-SEM (**Figure 7.2B**) and nano-computed tomography (nanoCT). Extensive crack formation - associated with the fast kinetics of the Ziegler-Natta catalyst, a rapid formation of polyethylene and significant pressure build-up - led to the break-up of entire catalyst particle particles in the early stages of slurry-phase ethylene polymerization.^[48]

SEM instruments are usually equipped to perform energy-dispersive X-ray spectroscopy (EDX). This can be a useful complementary tool for determining the distribution of different catalyst components and reaction products (**Figure 7.2C**).^[50,51] Velthoen *et al.* used SEM-EDX, along with scanning transmission electron microscopy-energy-dispersive X-ray spectroscopy (STEM-EDX, **Figure 7.2D**), to visualize and quantify compositional heterogeneities in silica-supported metallocene samples with different co-catalyst (methylaluminoxane, MAO) loadings.^[29] The investigation of multiple particles helped to identify an optimal MAO loading at which the interparticle heterogeneity was sufficiently low. Tran *et al.* used a combination of FIB-SEM and energy-dispersive X-ray spectroscopy (EDX) to study the impact of the impregnation time and catalyst solution concentration on the radial distribution of a zirconocene complex in individual catalyst particle cross-sections, and the influence thereof on the catalyst particle morphology.^[52] High metallocene concentrations in the peripheral regions of the particle were postulated to cause more fines in the final polymer product.

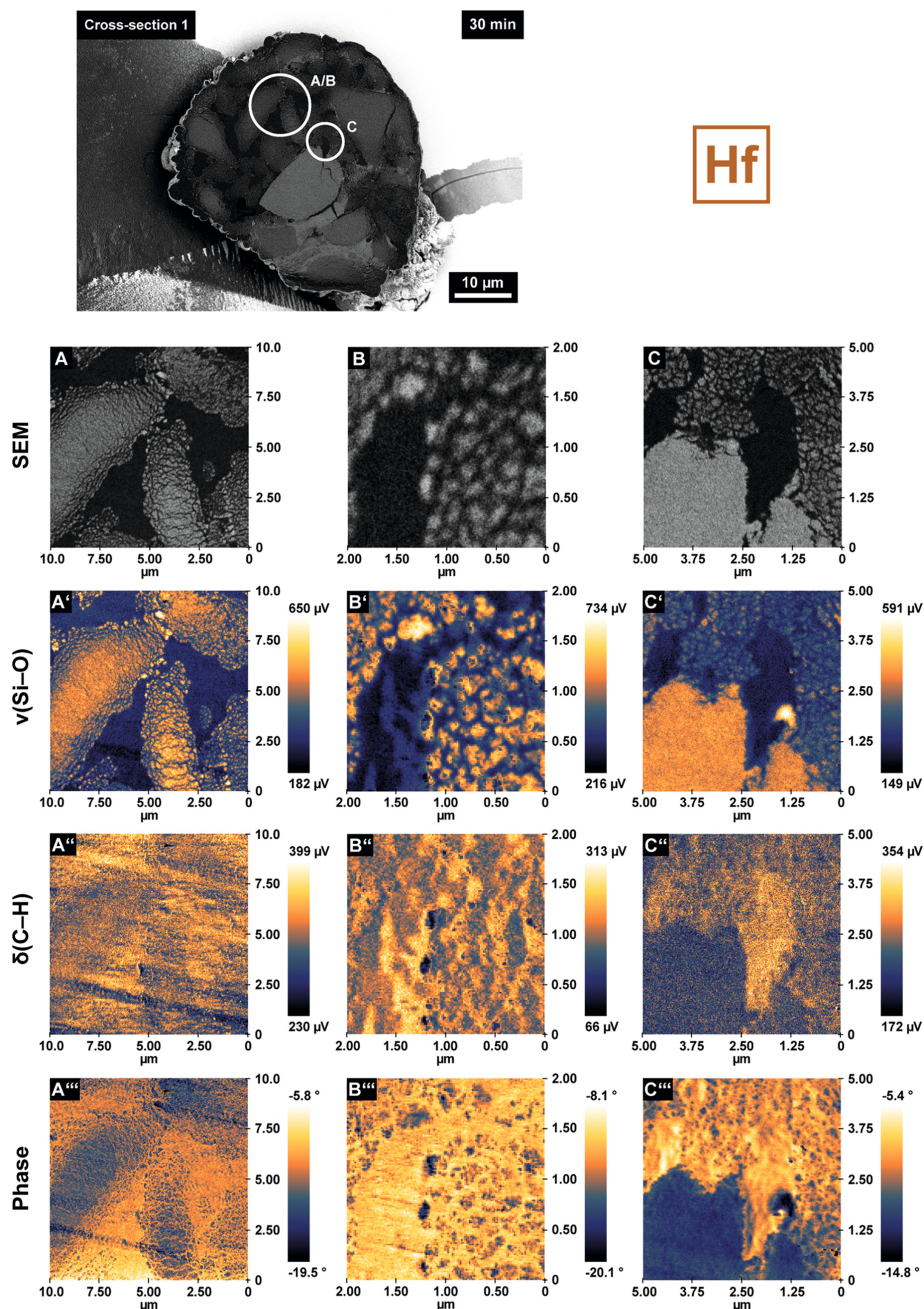


Figure 7.3 Scanning electron microscopy (SEM) and infrared photoinduced force microscopy (IR PiFM) data recorded on the horizontal cross-section of a silica-supported hafnocene (Hf = hafnocene/MAO/SiO₂ with MAO = methylaluminoxane) after ethylene pre-polymerization (30 min, room temperature, 1.6 bar ethylene pressure). With the help of IR PiFM, the distribution of different materials (e.g., silica, PE) in the composite particle can be verified spectroscopically [i.e., by recording IR maps at defined wavenumbers for v(Si-O) and δ(C-H)] as well as mechanically (i.e., via phase imaging). Reproduced and adapted from reference [38]. Copyright © 2021 Werny et al., published by American Chemical Society under the CC BY-NC-ND 4.0 license.

7.2.2 X-Ray Microscopy

X-ray microscopy is highly suitable for studying the structure and chemical composition of heterogeneous catalysts, often in 3D.^[53,54] By relying on absorption or phase imaging contrast, catalyst components and products with different electron densities can be distinguished. Techniques such as scanning transmission X-ray microscopy (STXM, 2D); transmission X-ray microscopy (TXM, 3D) and X-ray fluorescence tomography (XRF, 3D) can even be used to determine the spatial distribution and chemical state of specific elements. In contrast to SEM, which requires the physical removal of a particle sub-volume for cross-sectional imaging, X-ray microscopy is generally considered to be relatively non-destructive.

In the field of olefin polymerization catalysts, the first efforts to image individual catalyst particles with hard X-rays can be traced back to Conner and Jones in the early nineties.^[55–58] Since then, the resolution of synchrotron-based X-ray techniques has steadily improved, advancing from microns to nanometers. For example, 2D STXM has been used to image and correlate the speciation of polyethylene, chromium (Cr) and titanium (Ti) in microtomed cross-sections of Cr- and Cr/Ti-based Phillips catalysts at 50–100 nm spatial resolutions (*ex situ*; recorded at STXM end stations at the Canadian Light Source (CLS), Advanced Light Source (ALS) and Swiss Light Source (SLS), **Figure 7.4**).^[59,60] The technique has also recently been employed to study the orientation of polymer chains in low- and high-density regions of stretched polyethylene.^[61]

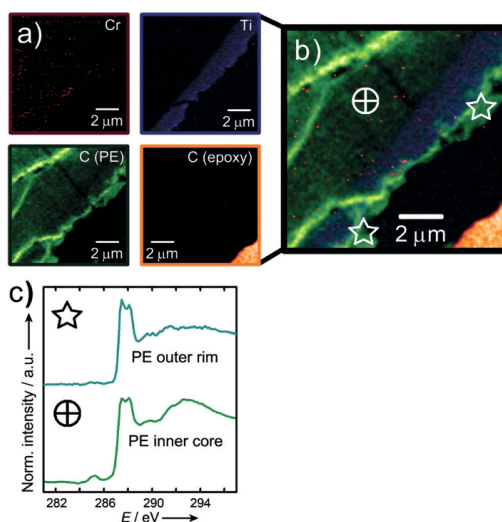


Figure 7.4 Elemental maps of a Phillips-type Cr/Ti/SiO₂ catalyst particle cross-section after ethylene pre-polymerization at 100 °C and 1 bar ethylene pressure (Cr: dark red, Ti: blue, C, C from polyethylene: green, C from the epoxy resin: orange) as recorded with soft X-ray spectromicroscopy (scanning transmission X-ray microscopy, STXM). C K-edge X-ray absorption spectroscopy (XAS) revealed different types of polyethylene in the interior and at the edge of the microtomed catalyst particle. The measurements were performed at the beamline 10ID-1 at the Canadian Light Source. Reproduced from reference [59]. Copyright © 2015 Cimil et al., published by Wiley-VCH Verlag GmbH & Co. KGaA.

In the field of 3D imaging, high spatial resolutions have been achieved with ptychographic X-ray computed tomography (PXCT), a phase contrast-based method that combines scanning X-ray microscopy with coherent diffraction imaging^[62]. Ptychography was combined with X-ray fluorescence (XRF) microscopy at the P06 beamline at PETRA III (Deutsches Elektronen-Synchrotron, DESY) to visualize the distribution of titanium sites within an individual 40 μm Ziegler-Natta catalyst particle that was pre-polymerized with propylene (**Figure 7.5**).^[37] A synergy between the sectioning and the layer-by-layer mechanism was reported. XRF microscopy yielded quantitative data on the distribution and concentration of Ti sites – an approach that is particularly advantageous when the phase contrast between the support and polymer is insufficient. In the future, XRF microscopy could potentially be applied to several other industrial polymerization catalyst systems, such as the Cr-based Phillips catalyst and Zr-based metallocenes, provided that the desired X-ray absorption edge falls within the energy range of a given imaging set-up and self-absorption effects remain limited.

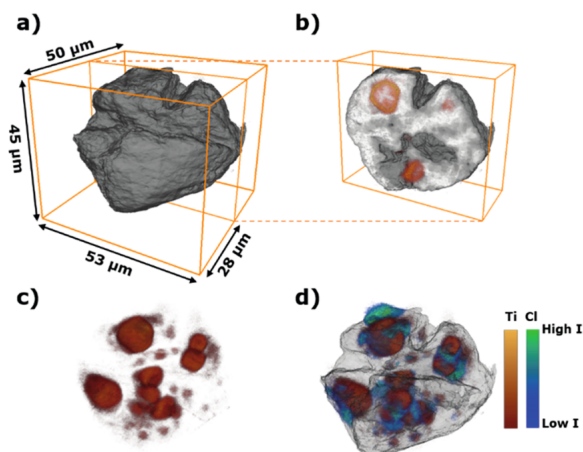


Figure 7.5 Reconstructed 3D volume of a propylene-polymerized Ziegler–Natta catalyst particle [electron density reconstruction: gray scale, Ti X-ray fluorescence (XRF) signal: red, Cl XRF signal: green]. The particle was characterized with hard X-ray ptychography and XRF at the P06 beamline, PETRA III, Deutsches Elektronen-Synchrotron (DESY). Reproduced from reference [37] under the CC-BY-NC-ND license. Copyright © 2020 American Chemical Society.

The PXCT set-up at beamline P06 was also used to characterize an ensemble of 434 ethylene pre-polymerized Ziegler catalyst particles over a time period of 22 h (theoretical median diameter after polymerization: $D_{50, \text{polymerized}} = 5.9 \mu\text{m}$, $120 \times 120 \times 20 \mu\text{m}^3$ field of view).^[63] A 3D spatial resolution of 74 nm was determined via Fourier shell correlation (FSC) analysis. The large number of characterized particles facilitated a statistical evaluation of the degree of support fragmentation via image segmentation and processing algorithms (**Figure 7.6**). Similar to the above-mentioned studies on silica-supported olefin polymerization catalysts, the analysis revealed contributions from both the layer-by-layer and sectioning mechanism, with the latter more heavily involved in particles displaying advanced fragmentation degrees.

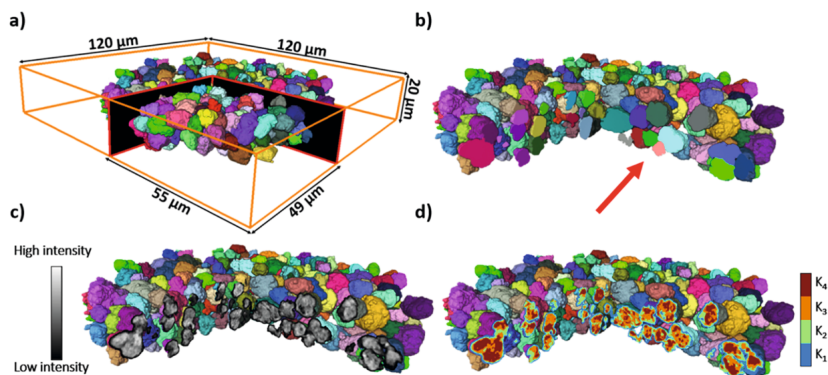


Figure 7.6 Reconstructed 3D volumes of 434 pre-polymerized Ziegler catalyst particles that were segmented with a k-means clustering algorithm to quantify their morphological heterogeneity. The particles were measured with hard X-ray ptychography at the P06 beamline, PETRA III, DESY. Reproduced from reference [63] under the CC BY-NC-ND 4.0 license. Copyright © 2021 Bossers *et al.*, published by American Chemical Society.

While ptychography clearly sets the benchmark in terms of spatial resolution, phase contrast-based full-field holotomography enables significantly higher sample throughput due to its shorter measurement times. Recent holotomography measurements at beamline ID16B at the European Synchrotron Radiation Facility (ESRF) of pre-polymerized metallocene-based catalyst particles, with diameters equal to or larger than 40 μm , only took 10–15 min per particle (**Figure 7.7A**). The samples were measured at four sample-to-detector distances. With the technique yielding clear contrast between low atomic number (Z) polyethylene and silica (**Figures 7.7A** and **7.7B**), it represents a promising alternative to ptychography, especially when larger sample sets or particles are under investigation. The GINIX holotomography set-up at the P10 beamline at PETRA III (DESY), was also used to investigate a silica-supported metallocene ($D_{50, \text{pristine}} = 25.0 \mu\text{m}$) at multiple reaction stages.^[31] A quantitative assessment of the particles' support and pore space architectures revealed large structural heterogeneity at five different reaction stages (**Figure 7.7B**). As structural parameters govern the degree of mass transport through the particles, they have a significant influence on the particles' morphological evolution upon polymerization.

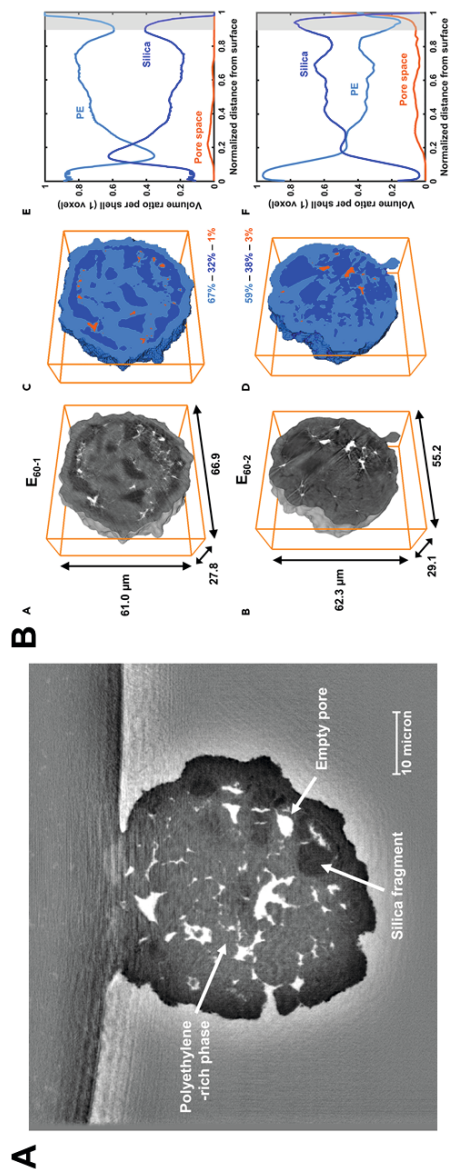


Figure 7.7 A: Reconstructed virtual cross-section of a zirconocene-based catalyst particle that was pre-polymerized in slurry-phase for 5 min at 10 bar ethylene and room temperature (unpublished data; light grey = polyethylene-rich phase, dark grey = silica-rich phase, white = macropore space). The particle was measured with hard X-ray holotomography at the ID16B beamline at the European Synchrotron Radiation Facility (ESRF) in less than 15 min. B: Reconstructed and segmented grayscale volumes of two hafnocene-based catalyst particles that were pre-polymerized in gas-phase for 60 min at 1.6 bar ethylene pressure and room temperature. The particles were measured with hard X-ray holotomography at the P10 beamline, PETRA III, DESY. Radial phase distribution analysis clearly demonstrated significant inter- and intraparticle heterogeneity amongst particles from the same batch. Reproduced and reprinted from reference [31], Copyright © 2021, with permission from Elsevier Inc.

Last but not least, laboratory-based computed tomography (CT), an absorption contrast-based technique, represents an accessible alternative to synchrotron-based methods for characterizing pristine and polymerized catalyst particles.^[28,48,64–66] Nano-computed tomography (nanoCT) has been reported to deliver sub-180 nm resolutions for different silica-supported olefin polymerization catalysts (**Figure 7.8**), as determined via Fourier shell correlation analysis (FSC).^[48] In general, laboratory-based CT instruments offer experimental and operational flexibility to researchers who do not have regular access to synchrotron facilities.

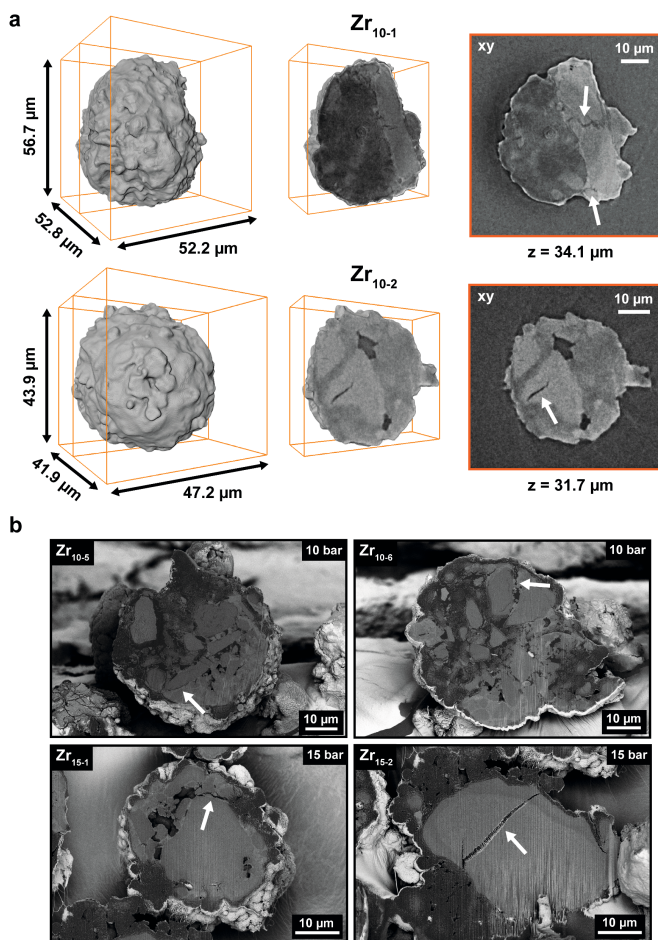


Figure 7.8 Reconstructed particles and virtual cross-sections of two zirconocene-based catalyst particles that were pre-polymerized in slurry-phase for 1 min at 10 bar ethylene pressure and room temperature. The propagation of extensive cracks (indicated by white arrows) was studied with laboratory-based (light grey = silica-rich phase, dark gray = polyethylene-rich phase, dark gray/black = macropore space). The data was acquired with laboratory-based nano computed tomography (nanoCT) to study the propagation of extensive cracks in the support (indicated by white arrows) was studied. Reproduced and adapted from reference [48] under the CC BY 4.0 license. The figure is an excerpt of the original. Copyright © 2022 Werny *et al.*, published by Wiley-VCH GmbH.

7.2.3 Optical Microscopy

Optical microscopy has been widely applied in the field of synthetic polymers^[67] and olefin polymerization, delivering information on the composition, formation and morphology of polymers, as well as on kinetics of polymerization reactions. For instance, Blum *et al.* have used fluorophore-tagged olefin monomers and microscopy to visualize ring-opening metathesis polymerization (ROMP) reactions *in situ*.^[68–70] The group was able to identify a preferential formation of fluorescent polymer on a homogeneous Grubbs catalyst in solution rather than on a heterogeneous Grubbs catalyst (**Figure 7.9A**).^[68] Chen *et al.* studied the ROMP of norbornene, also catalyzed by a Grubbs catalyst, using optical microscopy.^[71,72] By monitoring the height of a tethered magnetic particle, they were able to measure the extension of the growing polymer chain under reaction conditions (**Figure 7.9B**). Interestingly, the extension of the polymer chain was not continuous and linear due to conformational entanglements arising from newly incorporated monomers. In the field of industrially applied olefin polymerization catalyst systems, various groups have used optical video microscopy, together with appropriate reaction cells, to track the growth of individual catalyst particles during gas-phase polymerization reactions (**Figure 7.9C**).^[73–79] Pater *et al.* even studied the temperature evolutions of individual catalyst particles under reaction conditions using infrared imaging (**Figure 7.9D**).^[80] A more widely applicable approach was introduced by the group of Mülhaupt, who used video microscopy and focused beam reflectance measurement (FBRM) probes to monitor the growth of catalyst particles during slurry-phase polymerizations in a stirred reactor.^[81] In contrast to many of these efforts, which delivered information on particle growth and kinetics, the Müllen group employed laboratory-based confocal fluorescence microscopy (CFM), in combination with specific support staining procedures, to determine the internal morphology and composition of supported olefin polymerization catalysts (**Figures 7.9E and 7.9F**).^[82–85] In these studies, the distribution of the support in the polymer matrix was assessed non-invasively based on its fluorescence, thus yielding insights into the process of fragmentation. Müllen *et al.* also introduced the use of perylene-based dyes to differentiate between several silica-supported metallocenes, employed in the same polymerization run, using UV light.^[86] Certain silica-supported metallocenes are even known to exhibit autofluorescence and are thus suitable for a direct characterization via CFM. Our group recently combined CFM with advanced image processing to quantitatively assess support fragmentation in a large number of autofluorescent metallocene-based catalyst particles.^[87] This delivered representative insights into inter- and intraparticle heterogeneity during the early stages of ethylene polymerization at 10 bar ethylene pressure (**Figure 7.9G**).

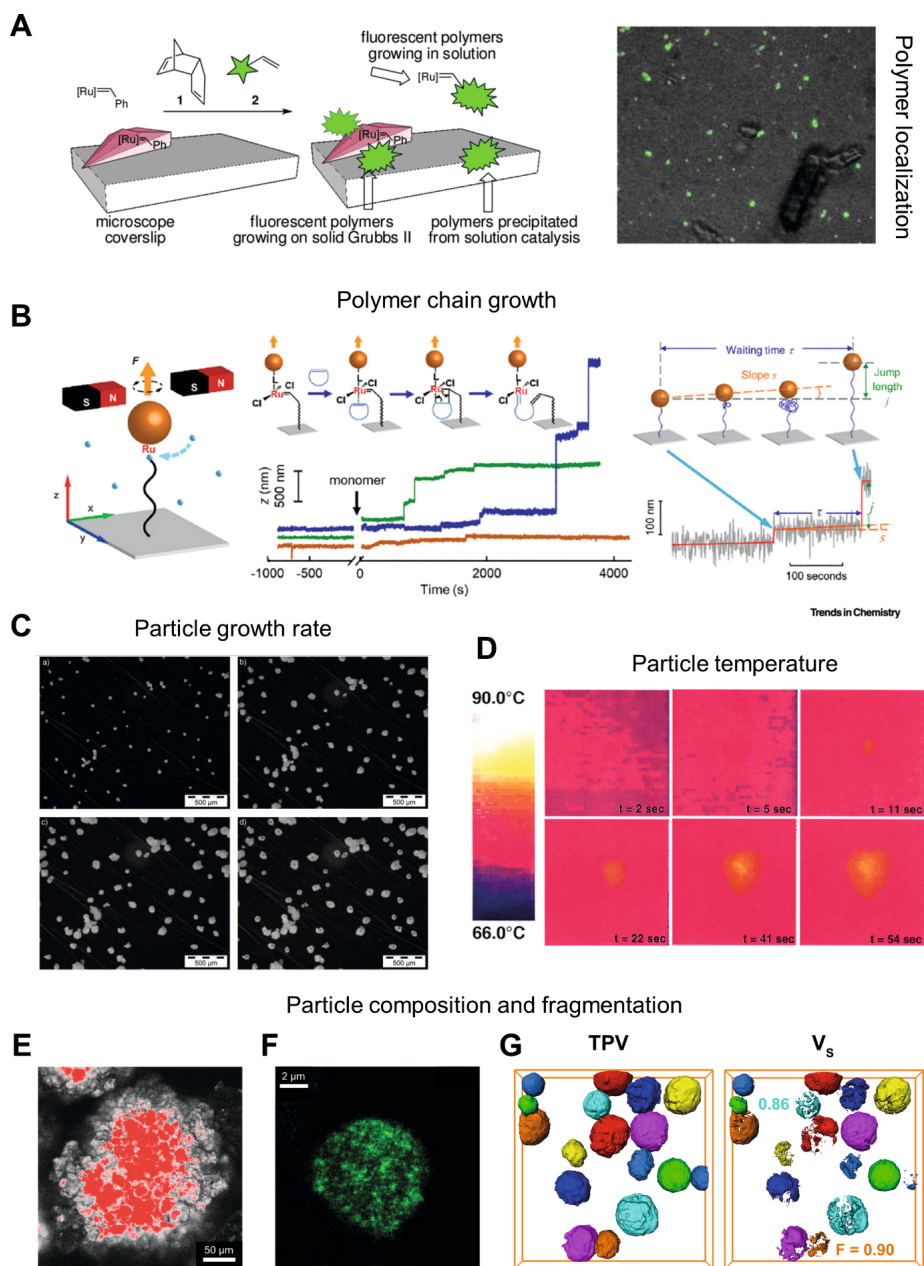


Figure 7.9 Chemical information that can be extracted from supported olefin polymerization catalysts with optical microscopy. A: Ruthenium-catalyzed polymerization of a fluorophore-tagged olefinic monomer. The resulting fluorescent polymer was localized with fluorescence microscopy. Reproduced and adapted from reference [68]. The figure is an excerpt of the original. Copyright © 2011, American Chemical Society. B: Real-time extension-versus-time trajectory for a growing polymer chain during a Grubbs catalyst-mediated ring opening metathesis polymerization. Reproduced and adapted from reference [72].

The figure is an excerpt of the original. Copyright © 2021 Elsevier Inc. All rights reserved. C: Optical images recorded of silica-supported metallocene catalyst particles during gas-phase ethylene polymerization at 10 bar ethylene pressure and 60 °C (reaction stages: 0 min, 60 min, 120 min and 180 min) that were used to assess their respective growth rates. Reproduced from reference [77]. Copyright © 2003 Wiley-VCH Verlag GmbH & Co. KGaA, Weinheim; published by John Wiley and Sons. D: Infrared images recorded of a Ziegler-Natta catalyst particle during olefin polymerization, yielding insights into the temperature of the particle. Reproduced from reference [80]. Copyright © 2003 American Institute of Chemical Engineers (AIChE), published by John Wiley and Sons. E: Confocal fluorescence microscopy (CFM) image of an ethylene polymerized metallocene/MAO/X-based catalyst (MAO = methylaluminoxane and X = perylene-stained silica support), revealing its internal morphology. Reproduced and adapted from reference [83]. The figure is an excerpt of the original. Copyright © 2005 WILEY-VCH Verlag GmbH & Co. KGaA, Weinheim, published by John Wiley and Sons. F: CFM image of an ethylene polymerized metallocene/MAO/Y-based catalyst, with Y = porous, rhodamine B-stained polyurethane support. Reproduced and adapted from reference [85]. The figure is an excerpt of the original. Copyright © 2013 Wiley Periodicals, Inc.; published by John Wiley and Sons. G: Reconstructed 3D CFM data of multiple autofluorescent zirconocene/MAO/SiO₂ particles after ethylene pre-polymerization (with TPV = total particle volume; V_s = Volume of silica-dominant domains; fragmentation parameter F = (1-V_s)/TPV). The figure is an excerpt of the original. Reproduced and reprinted from reference [87] under the CC BY 4.0 license. Copyright © 2022 Werny *et al.*, published by American Chemical Society. In E–G, the support has been impregnated with a fluorophore, while the formed polymer is not fluorescent.

7.2.4 Other Techniques

Scanning probe techniques such as atomic force microscopy (AFM)^[88–90], atomic force microscope-infrared spectroscopy (AFM-IR)^[91–93], and infrared photoinduced force microscopy (IR PiFM)^[38,94–96] represent powerful tools to assess the topology and morphology of polymer materials at high spatial resolutions down to a few nanometers. In a study by Ruddick *et al.*, phase-imaging AFM was used to study the fragmentation of a Phillips catalyst at different stages of ethylene polymerization.^[97] Larger support fragments were detected at the surface of the polymerized catalyst. The authors postulated that these larger fragments, owing to their smaller surface areas, were less active in comparison to smaller fragments and thus pushed to the surface of the catalyst during polymerization. In a more recent study, IR PiFM was used to image cross-sections of an ethylene pre-polymerized hafnocene catalyst particle at sub-20 nm resolution.^[38] IR maps were recorded at characteristic wavenumbers for the Si–O stretching vibration of silica (SiO₂) and the symmetric C–H bending vibration of the methylene (CH₂) group (**Figure 7.3**). A clear spectroscopic differentiation between the silica support and formed polyethylene was thus obtained, thereby helping to identify fragmentation pathways and visualize crack formation. The two phases were also clearly distinguishable in the phase imaging mode, which is suitable for assessing mechanical material properties. Further studies could employ quantitative nanomechanical mapping (QNM) and nano indentation testing to quantify mechanical material properties, such as elasticity, via the Young's modulus.^[98] Besides the above-mentioned techniques, Raman microscopy can also be used to monitor the formation and distribution of polymer (**Figure 7.12A**).^[46] While the technique's resolution is lower, it has the benefit of being able to capture larger sample areas in comparatively short measurement times.

7.3 Determining the Distribution of Polymer and Related Decomposition Products in Polyolefin Cracking Catalysts

During catalytic pyrolysis, hydrocracking and hydrogenolysis, polyolefins, such as PP and PE, are converted to a mixture of aliphatic, aromatic and olefinic hydrocarbons. As the reaction is conducted at elevated temperatures, the polymers melt to form viscous fluids that may infiltrate the pore space of catalyst particles. Thermal pre-cracking of the polymer chains to shorter chains is hypothesized to occur, which increases the accessibility of shorter chains and intermediate cracking products to the particle interior for further reactions.^[11] A similar effect may be achieved with other (thermo-)chemical (e.g., non-catalytic pyrolysis, solvolysis, dissolution/precipitation, etc.^[8]) and mechanochemical methods (e.g., ball milling^[99-101]) that reduce the average polymer chain length. In general, as the polymer decomposition reaction proceeds, a more extensive dissociation of the polymer chains takes place. Furthermore, subsequent aromatization of the formed intermediates results in the formation of different coke species. Both the degree of polymer intrusion into the pores of a given catalyst body and the distribution of coke species can be visualized with different high-resolution imaging techniques.

7.3.1 Electron Microscopy

Focused ion beam-scanning electron microscopy (FIB-SEM) represents an accessible characterization tool to obtain data on polymer localization and mobility. The technique is suitable for assessing the degree of polymer intrusion and pore utilization in macroporous catalyst particles that have been contacted with polyolefins at elevated temperatures. This can yield insights into the roles of a polymer's viscosity and a catalyst's pore space accessibility on the performance of a given catalyst. Further studies could utilize a combinatorial SEM-EDX-CFM (EDX = energy dispersive X-ray spectroscopy, CFM = confocal fluorescence microscopy) approach to determine the chemical composition of different phases with distinct reactivities (e.g., coking or specific interactions with probe molecules) in a catalyst particle cross-section, thereby helping to identify structure-performance relationships.

7.3.2 X-Ray Microscopy

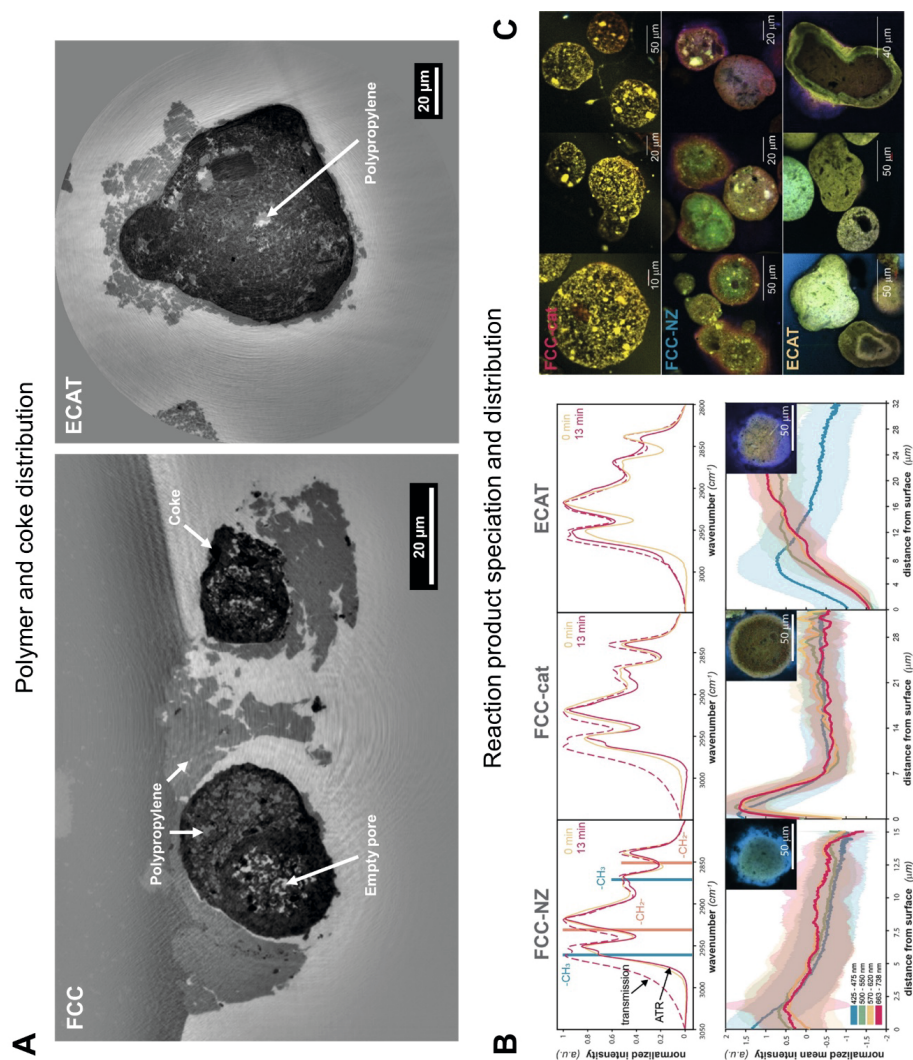
X-ray microscopy can provide information on the degree of polymer intrusion into the pores of a given catalyst particle in 3D. Recent hard X-ray holotomography measurements on FCC particles and equilibrium FCC catalyst (ECAT) particles, used for a limited amount of time in the catalytic pyrolysis of low molecular weight PP, revealed differences in the degree of polymer intrusion (**Figure 7.10A**). These are mostly likely associated with the particle architecture and the degree of porosity in the outer layers of the catalyst particles. In fact, the studied ECAT particles, in contrast to most of the FCC particles, were found to possess an internal pore structure that was more accessible for PP. Furthermore, coke deposits were clearly detectable in the particles (**Figure 7.10A**). This stands in agreement with previous experiments by Vesely *et al.*, who first demonstrated the suitability of holotomography for detecting and

quantifying coke in FCC catalyst particles.^[102] In the future, both the distribution and volume of coke can be quantified by scanning reacted polyolefin cracking catalyst particles before and after calcination (i.e., via differential contrast tomography, as reported by Vesely *et al.*^[102]). The tomographies can then be used to simulate the diffusion of reaction intermediates and products through the macropore space of the catalyst particle, both in the presence and absence of polymer, as well as coke. Experiments by Weber *et al.* on Ni/Al₂O₃ catalysts demonstrated that coke deposits can also be localized with hard X-ray ptychography (PXCT) at high spatial resolutions (sub-100 nm).^[103] With the resolution of imaging set-ups steadily improving, it may soon be possible to image the process of pore filling in the mesopore regime (i.e., 2–50 nm). The spatial distribution of certain catalyst components, in relation to, for example, formed coke species, could also be probed with transmission X-ray microscopy (TXM), X-ray fluorescence tomography (XRF) and X-ray diffraction (XRD) tomography.^[102,104–108]

7.3.3 Optical Microscopy

While electron and X-ray microscopy provide unparalleled spatial resolutions in 2D and 3D, confocal fluorescence microscopy (CFM) can provide complementary information on the formation and distribution of fluorescent reaction products, such as aromatics and coke, in multiple catalyst particles. Vollmer *et al.* used CFM to study the formation and localization of early-stage cracking products in fluid catalytic cracking particles (i.e., FCC/FCC-NZ, with NZ = No Zeolite), and equilibrium FCC catalyst (ECAT) particles, after a 13 min reaction with polypropylene (PP) at 250 °C (**Figure 7.10B**, bottom).^[11] In general, higher fluorescence intensities were observed in the outer rings of FCC and FCC-NZ catalyst particles, indicating that cracking and possibly aromatization were predominantly occurring at the particle surface and sub-surface regions. In the case of ECAT, on the other hand, the radial fluorescence intensity profile increased towards the center of the particles. This was linked to the presence of metal deposits (i.e., Fe, Ni, and V), which are expected to increase the pre-cracking activity of the catalyst matrix, thereby enhancing the transport of cracking products and reaction intermediates into the particle interiors, where they subsequently form aromatics. Attenuated total reflectance-infrared spectroscopy (ATR-IR) and transmission Fourier-transform infrared (FTIR) spectroscopy helped to further assess the degree of cracking in the bulk PP surrounding the catalyst particles and in the catalyst/PP composite, respectively (**Figure 7.10B**, top). While cracking products were only detected in higher concentrations inside or in close vicinity of the FCC and FCC-NZ catalyst phase, cracking products were also observed in the bulk PP surrounding the ECAT catalyst particles. The authors attributed this to reaction products that had diffused out through the plastic layer surrounding the ECAT catalyst material.

Figure 7.10 Information obtained on polyolefin cracking catalysts via high resolution X-ray and optical microscopy. A: Reconstructed virtual cross-sections of fluid catalytic cracking (FCC) and equilibrium cracking catalyst (ECAT) particles that have partially reacted with polypropylene (PP) at 250 °C (details about the samples and reaction conditions can be found in reference [11]). Differences in the degree of polymer intrusion between the particles as well as high local concentrations of coke (high electron density, dark gray) are clearly visible. The particles were measured with holotomography at beamline ID16B at the European Synchrotron Radiation Facility (ESRF, unpublished data). B: Confocal fluorescence microscopy (CFM) images and Fourier-transform infrared spectroscopy (FTIR) spectra of PP/catalyst mixtures after quenching the reaction at 250 °C. Radial intensity profiles, based on the measured CFM images, indicate differences in the distribution of fluorescent reaction products between FCC/FCC-NZ and ECAT (FCC-NZ = FCC catalyst, No Zeolite; and ECAT = equilibrium cracking catalyst). All samples were microtomed prior to characterization with CFM. Reproduced from reference [11] under the CC BY 4.0 license. Copyright © 2021 Vollmer *et al.*, published by Wiley-VCH GmbH. C: CFM images recorded of FCC, FCC-NZ and ECAT catalysts after a full reaction run with PP at ~450 °C. All samples were microtomed prior to characterization with CFM. High concentrations of fluorescent aromatics and coke species are visible as distinct yellow domains. Reproduced from reference [11] under the CC BY 4.0 license. The figure is an excerpt of the original. Copyright © 2021 Vollmer *et al.*, published by Wiley-VCH GmbH.



CFM measurements were also performed on all catalysts after a full reaction run with PP at ~ 450 °C. Well-defined bright spots, observed in FCC catalyst particles and allocated to high local aromatics and coke concentrations in zeolite domains, were not visible in the ECAT catalyst (**Figure 7.10C**). The authors postulated that the zeolite domains are less accessible in ECAT due to metal deposits. The domains may have also been deactivated via streaming in the regenerator of the FCC unit. Despite this, all catalysts formed significant amounts of aromatics, suggesting that zeolite is not necessary for the aromatization of PP. The bright features in FCC only appeared after a full reaction run, which further confirmed the hypothesis that pre-cracking in the catalyst matrix precedes aromatization in the zeolite domains. Future research efforts may be directed towards the rational design of highly porous catalysts that are potentially more suitable for the conversion of viscous polymers. By using CFM, particle accessibilities and activities can easily be determined for catalysts with different porosities and pore space architectures, based on the fluorescent coke species that are formed. Furthermore, pristine catalyst particles can be stained with fluorophores and (reactive) probe molecules to visualize their 3D structure, activity, as well as the distribution of different components and catalytically active phases.^[109–111] Fluorophore-tagged polymers could even be used to study polymer melting and intrusion into the pores of a given catalyst with CFM.

7.4 *In Situ* and *Operando* Characterization of Individual Catalyst Particles for Olefin Polymerization and Polyolefin Decomposition

In situ and *operando* (**Figure 7.11A**) X-ray microscopy at the nanometer length scale represents a powerful approach for obtaining more detailed insights into the behavior of heterogeneous catalysts under operating conditions.^[53,54,112,113] Generally speaking, this requires the implementation of sophisticated micro- and nanoreactor systems with low dead volumes, suitable windows or capillaries for high X-ray transmission (e.g., Si_3N_4 or quartz), as well as stable gas flows under high-temperature and high-pressure operating conditions.

In 2008, our group started using reactor set-ups with integrated MEMS (microelectromechanical systems) chips for performing 2D scanning transmission X-ray microscopy (STXM) on different types of Fischer-Tropsch catalysts (**Figure 7.11B**) under *in situ* and *operando* conditions (up to 4 bar and 500 °C).^[114–116] In general, the use of soft X-rays often requires the use of relatively thin samples (≤ 1 μm) in comparison to hard X-ray-based tomography experiments. More recently, Grunwaldt *et al.* reported on another reactor design featuring a MEMS chip for complementary X-ray nano-imaging and spectroscopy under reaction conditions (**Figure 7.11C**). Using this reactor, 3D X-ray ptychographic measurements can be performed at 1 bar pressure and at temperatures of up to 1100 °C, covering an angular range of $\pm 35^\circ$.^[117]

Capillary-based microreactors^[118,119] represent a promising alternative to reactors with integrated MEMS devices as they enable significantly higher angular ranges. The technical challenge here, however, remains in using heating equipment that is compatible with the sensitive beamline optics, both in terms of the released heat and spatial constraints. In 2012, our group started using capillary-based microreactor systems (capillary diameter = 100 μm)

with appropriate heating devices for *in situ* transmission X-ray microscopy (TXM) on catalyst particles at 1–30 bar and up to 600 °C.^[120–123] In a more recent design, the quartz or Kapton capillary is attached to a holder (Figure 7.11D, simplified schematic) with heat-resistant epoxy while the heating is provided by a nichrome wire in a cylindrical chamber. A water-cooled aluminum cage with X-ray windows prevents overheating of the optical components.

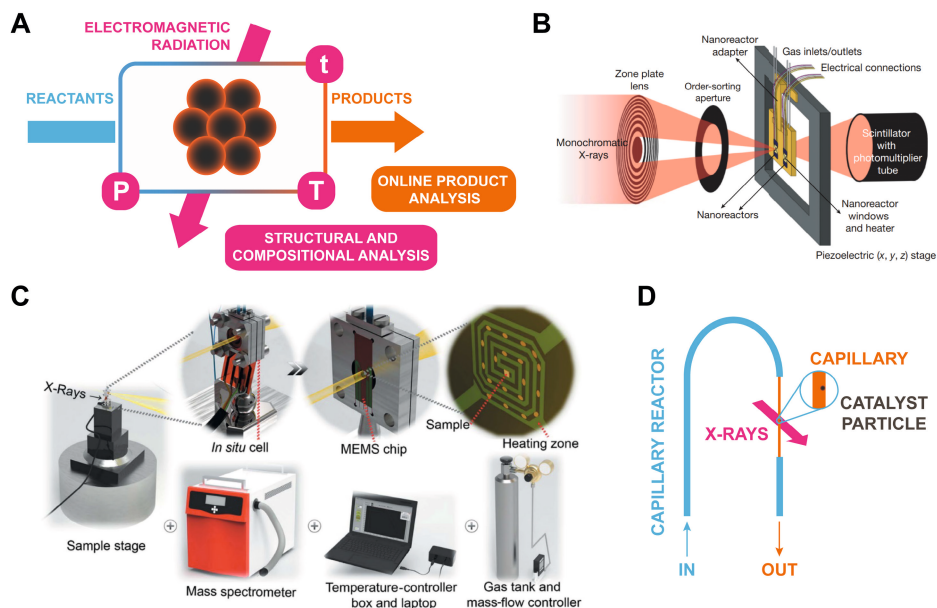


Figure 7.11 A: Schematic of the *operando* spectroscopy approach for characterizing catalysts in their working state. The structure and chemical composition of the catalyst is monitored directly under reaction conditions, while simultaneously assessing the formed reaction products (e.g., via gas chromatography or mass spectrometry). B: Scanning transmission X-ray microscopy (STXM) set-up first used by Weckhuysen *et al.* to study Fischer-Tropsch catalysts *in situ*. The measurements were performed at beamline 11.0.2 of the Advanced Light Source at the Lawrence Berkeley National Laboratory, USA. Reproduced and adapted from reference [114]. Copyright © 2008, Macmillan Publishers Limited. All rights reserved. C: Schematic of the reactor set-up used by Grunwaldt *et al.* for *in situ* 2D and 3D ptychography at the P06 nanoprobe beamline of PETRA III, Deutsches Elektronen-Synchrotron (DESY). Reproduced from reference [117] under the CC BY 4.0 license. Copyright © 2019 Fam *et al.*, published by International Union of Crystallography. D: Simplified illustration of the capillary-based microreactor employed by Weckhuysen *et al.* for *in situ* transmission X-ray microscopy (TXM) experiments at beamline 6-2c of the Stanford Synchrotron Radiation Lightsource (SSRL).

Over the last years, capillary-based reactor systems have become increasingly established and have been used to study different heterogeneous catalysts with various X-ray-based imaging techniques at length scales ranging from millimeters to nanometers.^[124–128] Future efforts must, however, be directed towards designing compact reactor systems (e.g., chip-based reactors as reported by Drake *et al.*^[129]) that have integrated heating and cooling elements, while also enabling high gas pressures and, hence, realistic reaction conditions. Reactors with low spatial requirements are advantageous as they will ensure a given reactor's compatibility

with multiple imaging set-ups and beamlines. Furthermore, the number of missing imaging angles should be minimized in future reactor designs (see design by Holler *et al.*^[130]) to limit reconstruction artefacts and guarantee the highest possible imaging resolution.

In the context of olefin polymerization catalysts, sophisticated reactors will provide the means for tracking the morphological evolution of individual catalyst particles *in situ*. The main challenge remains in maintaining the stability of the air- and moisture-sensitive catalyst particles that are loaded into the reactor inside an inert environment (e.g., glovebox). Due to the relatively fast polymerization rates, a pulsing approach with ethylene and an inert gas may have to be adopted. The previously mentioned holotomography set-up at ID16B (ESRF, **Figure 7.7A**) enables high temporal and spatial resolutions and would therefore be suitable for such *quasi in situ* measurements.^[131–133] With the flux and coherence of synchrotron radiation as well as the speed of microscopy set-ups and detectors steadily improving^[134–136], it may even become possible to monitor polymerization reactions live (i.e., true *in situ/operando* experiments without pulsing) at spatial resolutions of a few tens of nanometers. To maximize the temporal resolution, however, it could be beneficial to perform measurements at slightly lower spatial resolutions. The acquired data would provide valuable input for refining existing models that are used to simulate support fragmentation^[27,28,137].

Catalysts for polymer decomposition, on the other hand, can be loaded with a limited amount of polymer and subsequently imaged with X-ray nanotomography. Ideally, tomographies are collected before, during, and after the reaction, while monitoring both the reactants and the reaction products. This could provide insights into (i) the intrusion of polymer into the particle, (ii) polymer decomposition, and (iii) coke formation^[102].

By using suitable reaction cells (e.g., cells by Linkam Scientific, Harrick Scientific Products Inc.), confocal fluorescence microscopy (CFM) can also potentially be used to study heterogeneous polymerization and (hydro)cracking catalysts under working conditions. Provided the concentration of fluorophore is sufficiently high, structural and chemical changes to catalysts may be observed in real time. The decomposition of polymers on polymer decomposition catalysts may be imaged *in situ* or *operando* due to the high concentration of fluorescent coke species that are formed. Thus, by correlating changes in the fluorescence of the formed intermediates and products and the monitored composition of gas-phase products, new structure-activity correlations may be obtained.

7.5 High-Throughput Experimentation and Machine Learning to Assess Interparticle Heterogeneity in Olefin Polymerization and Polyolefin Decomposition Catalysts

Industrially applied catalysts, such as supported olefin polymerization catalysts^[29,31] and cracking catalyst (e.g., FCC/ECAT)^[30], are per definition heterogeneous in nature. The degree of heterogeneity and any associated chemical implications thereof are, however, poorly understood. Optical and X-ray (fluorescence) microscopy techniques can bridge the gap between single catalyst particle studies and bulk catalyst characterization approaches and help to elucidate relevant structure-performance relationships in a statistically relevant number of catalyst particles.

In the field of heterogeneous olefin polymerization catalysts, confocal fluorescence microscopy (CFM), in synergy with automated image segmentation (e.g., via machine learning) and data analysis, has the potential to become a high-throughput tool for determining the morphology of multiple catalyst particles after synthesis as well as after (pre)-polymerization (quality control). While the acquisition of 2D data provides a mean of comparing and screening different reaction stages and catalyst batches at high sample throughput (in the range of 10^2 – 10^3 particles per h), 3D imaging can be used to accurately assess the composition of multiple catalyst particle sub-volumes in a limited space of time (~ 2 h scan time for a $178 \mu\text{m} \times 178 \mu\text{m} \times 30 \mu\text{m}$ field of view^[87]). Material-specific staining procedures^[82,83,85], autofluorescent catalysts, fluorophore-tagged monomers^[69] and fluorescent probe molecules (e.g., fluorescent external/internal donors for Ziegler-Natta catalysts) will help to extend the methodology to a variety of supported olefin polymerization catalysts. In the field of X-ray microscopy, hard X-ray holotomography and ptychographic X-ray computed tomography are particularly well suited to measuring large sample sets of polymerization catalyst particles in 3D.^[31,63] Automated image reconstruction, segmentation^[138-141] and analysis can greatly improve the efficiency of the data analysis. This, in turn, will further increase the throughput of the techniques and will help to deliver statistically relevant chemical insights. Next-generation synchrotrons and instrumental advances will most likely make X-ray microscopy the method of choice for collecting high-resolved morphological data on a representative number of particles 3D. Finally, planar model olefin polymerization catalyst systems^[142-148], potentially in form of spherical caps or micro-islands^[46] (**Figure 7.12A**), could find application in high-throughput catalyst characterization and testing studies. By targeting a large number of islands with various micro-spectroscopic tools, correlations between the composition and structure of the employed catalyst material and the morphology, composition and crystallinity of the formed polymers can be investigated. Furthermore, islands of different chemical compositions could be screened in parallel under identical reaction conditions. This could also be realized with small wafers, featuring different catalyst and co-catalyst formulations, that are placed in the same reaction cell or chamber. By installing the required analytical instruments inside for example, a glovebox, samples could even be characterized at multiple reaction stages.

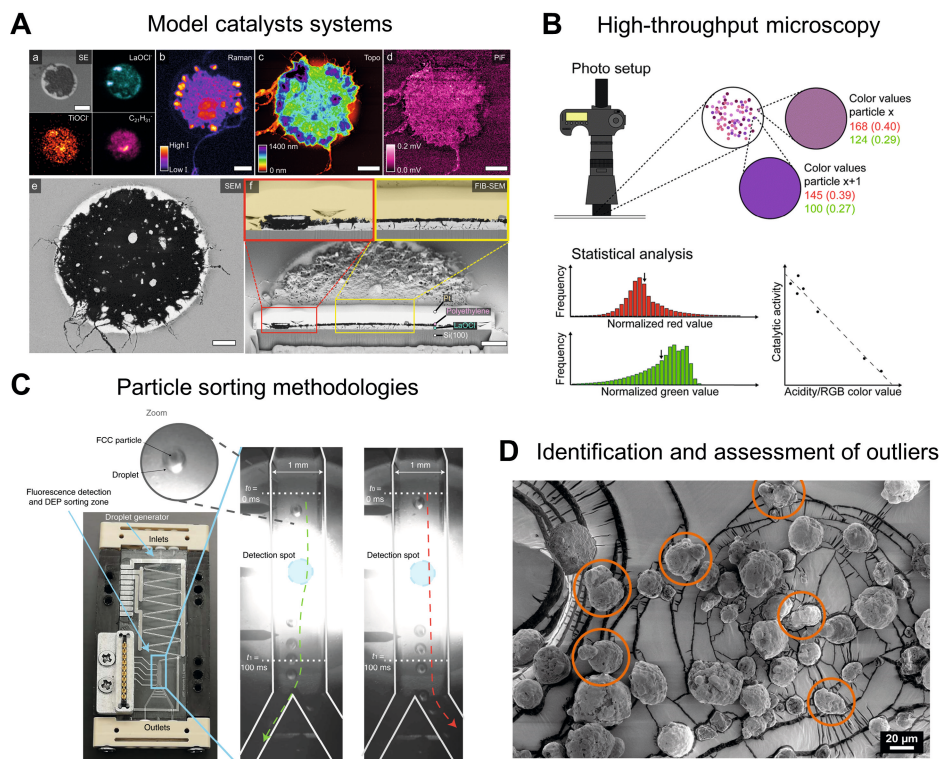


Figure 7.12 Synthetic and analytical approaches that can be exploited to obtain representative insights into the chemical behavior of heterogeneous catalyst materials, either at the level of one particle or multiple particles. **A:** Development of model catalyst systems that enable high-throughput characterization with 2D (spectro-)microscopy techniques. Reproduced from reference [46] under the CC BY 4.0 license. Copyright © 2022 Bossers *et al.*, published by Springer Nature. **B:** Implementation of high-throughput microscopy techniques and automated data analysis to characterize large sample sets. Reproduced from reference [110] with permission from the Royal Society of Chemistry under the CC BY 3.0 license. **C:** Sorting approaches to divide single catalyst particles according to their composition, structure and reactivity. Reproduced and adapted from reference [111]. Copyright © 2021, Nieuwelink *et al.*, under exclusive license to Springer Nature Limited. **D:** Systematic studies to identify and assess individual catalyst particles with irregular morphologies (i.e., agglomerates formed during spray drying of the catalyst support, strongly elongated or irregularly shaped particles) or compositions under reaction conditions (unpublished SEM data).

In the field of cracking catalysts, high-throughput approaches have already been implemented. Kerssens *et al.* were able to optically differentiate between FCC particles containing either zeolite Y or ZSM-5 in a mixed catalyst batch of 25000 catalyst particles after a chemical staining reaction with 4-fluorostyrene.^[110] Furthermore, by using 4-methoxystyrene as a fluorescent probe molecule, they were able to assess the acidity (considered as representative for the catalytic activity) and micropore volume of the catalyst particles (**Figure 7.12B**). A similar approach could be applied to FCC catalysts after different stages of polyolefin decomposition to study their accessibilities and acidity as a function of time. Nieuwelink *et al.* have studied interparticle heterogeneities in density-separated fractions of a ECAT catalyst by overlaying

Fe and Ni X-ray fluorescence (XRF) maps with CFM images recorded after reaction with different probe molecules.^[30] The degree of deactivation was linked to the Ni content of a given particle. Both studies could be implemented in a similar fashion for catalysts employed in polyolefin decomposition to study properties such as accessibility and acidity at the level of individual particles.

While certain structure-activity relationships have been established, the precise influence of particles with irregular structures and deviating chemical compositions is not well understood. Dielectrophoretic (**Figure 7.12C**) and magnetophoretic particle sorting approaches,^[111,149] in interplay with suitable optical microscopy (e.g. fluorescence microscopy) and machine learning algorithms, could be used to separate catalysts according to different criteria. For instance, olefin polymerization catalyst and fluid catalytic cracking particles could be sorted according to their initial morphology, chemical composition (e.g., metallocene and co-catalyst loading in the case of olefin polymerization catalysts, metal contaminants in the case of ECAT) or activity (e.g., acidity based on reactions with probe molecules in the case of FCC/ECAT^[110]). This would ultimately yield more uniform catalyst batches with narrower spreads in activity. Investigating the reactivity and morphology of outliers (**Figure 7.12D**) could potentially advance our understanding of their exact role in catalytic reactions. As a consequence, new insights into the structural, compositional, and chemical requirements for catalytic reactions will be gained.

7.6 Summary and Outlook

Synchrotron- and laboratory-based chemical imaging techniques have emerged as useful tools for assessing the evolution of supported olefin polymerization catalysts in 2D and 3D. Electron, fluorescence and X-ray microscopy in particular provide representative chemical and morphological information at the nanoscale. The growing analytical toolbox discussed in this review can be employed in a similar fashion to obtain new physicochemical insights into the process of polyolefin decomposition or cracking. By visualizing the decomposition and mobility of commodity polymers, such as polypropylene and polyethylene, in individual catalyst particles, an improved mechanistic understanding for the processes of catalytic pyrolysis, hydrocracking and hydrogenolysis can be obtained. Despite *in situ* and *operando* microscopy and tomography studies still being in their infancy within this field of research, they hold great promise for assessing structure-composition-performance relationships in single catalyst particles. Furthermore, spatial insights into catalyst activity may be obtained by employing luminescent nanocrystals that function as local temperature sensors,^[150,151] while the local pressure build-up during polymerization could be tracked with the help of novel pressure sensors.^[152] Temperature maps^[153] and potentially pressure maps can thus be acquired under reaction conditions by using conventional microscope systems with suitable excitation sources. In the field of X-ray microscopy, multibeam X-ray ptychography, once fully developed, will significantly increase the available field of view and reduce scanning times, opening up new avenues for the characterization of polymerization and depolymerization catalysts at high sample throughput and unparalleled spatial resolutions.^[154–156]

In general, technological advancements will gradually improve the sensitivity and speed of many of the here discussed characterization methods. This will allow for polymerization and cracking catalysts to be studied in greater detail, possibly under reaction conditions. The acquired insights will guide the design of improved catalyst systems, which will play an important role in making our society more sustainable and circular.

Acknowledgments

Julie Villanova (ESRF), Victor Vanpeene (ESRF), Luca Carnevale (University of Twente), Rafael Mayorga-González (Utrecht University, UU) and Caroline Versluis (UU) are acknowledged for their experimental support at beamline ID16B (ESRF). Ina Vollmer (UU) and Michael Jenks (UU) are thanked for providing the FCC and ECAT particles for the holotomography measurements at ID16B.

References

1. R. Geyer, J. R. Jambeck, K. L. Law, *Sci. Adv.* **2017**, *3*, e1700782.
2. W. Kaminsky, *Macromol. Chem. Phys.* **2008**, *209*, 459–466.
3. R. Geyer, in *Plast. Waste Recycl.*, Elsevier, **2020**, 13–32.
4. D. W. Sauter, M. Taoufik, C. Boisson, *Polymers* **2017**, *9*, 1–13.
5. J. Qiao, M. Guo, L. Wang, D. Liu, X. Zhang, L. Yu, W. Song, Y. Liu, *Polym. Chem.* **2011**, *2*, 1611–1623.
6. V. Busico, R. Cipullo, *Prog. Polym. Sci.* **2001**, *26*, 443–533.
7. W. Kaminsky, *J. Polym. Sci. Part A Polym. Chem.* **2004**, *42*, 3911–3921.
8. I. Vollmer, M. J. F. Jenks, M. C. P. Roelands, R. J. White, T. van Harmelen, P. de Wild, G. P. van der Laan, F. Meirer, J. T. F. Keurentjes, B. M. Weckhuysen, *Angew. Chem. Int. Ed.* **2020**, *59*, 15402–15423.
9. A. J. Martín, C. Mondelli, S. D. Jaydev, J. Pérez-Ramírez, *Chem* **2021**, *7*, 1487–1533.
10. W. Zhao, S. Hasegawa, J. Fujita, F. Yoshii, T. Sasaki, K. Makuuchi, J. Sun, S. I. Nishimoto, *Polym. Degrad. Stab.* **1996**, *53*, 129–135.
11. I. Vollmer, M. J. F. Jenks, R. Mayorga González, F. Meirer, B. M. Weckhuysen, *Angew. Chem. Int. Ed.* **2021**, *60*, 16101–16108.
12. D. Munir, Abdullah, F. Piepenbreier, M. R. Usman, *Powder Technol.* **2017**, *316*, 542–550.
13. G. Celik, R. M. Kennedy, R. A. Hackler, M. Ferrandon, A. Tennakoon, S. Patnaik, A. M. Lapointe, S. C. Ammal, A. Heyden, F. A. Perras, M. Pruski, S. L. Scott, K. R. Poeppelmeier, A. D. Sadow, D. Massimiliano, *ACS Cent. Sci.* **2019**, *5*, 1795–1803.
14. A. Tennakoon, X. Wu, A. L. Paterson, S. Patnaik, Y. Pei, A. M. LaPointe, S. C. Ammal, R. A. Hackler, A. Heyden, I. I. Slowing, G. W. Coates, D. Massimiliano, B. Peters, W. Huang, A. D. Sadow, F. A. Perras, *Nat. Catal.* **2020**, *3*, 893–901.
15. F. Zhang, M. Zeng, R. D. Yappert, J. Sun, Y. H. Lee, A. M. LaPointe, B. Peters, M. M. Abu-Omar, S. L. Scott, *Science* **2020**, *370*, 437–441.
16. S. Liu, P. A. Kots, B. C. Vance, A. Danielson, D. G. Vlachos, *Sci. Adv.* **2021**, *7*, 8283–8304.
17. C. Wang, T. Xie, P. A. Kots, B. C. Vance, K. Yu, P. Kumar, J. Fu, S. Liu, G. Tsilomelekis, E. A. Stach, W. Zheng, D. G. Vlachos, *JACS Au* **2021**, *1*, 1422–1434.
18. C. Jia, S. Xie, W. Zhang, N. N. Intan, J. Sampath, J. Pfaendtner, H. Lin, *Chem Catalysis* **2021**, *1*, 437–455.
19. P. Cossee, *J. Catal.* **1964**, *3*, 80–88.
20. V. Dufaud, J. M. Basset, *Angew. Chem. Int. Ed.* **1998**, *37*, 806–810.
21. W. Kaminsky, A. Laban, *Appl. Catal. A Gen.* **2001**, *222*, 47–61.
22. G. W. Coates, Y. D. Y. L. Getzler, *Nat. Rev. Mater.* **2020**, *5*, 501–516.
23. F. D. Cannavacciuolo, R. Yadav, A. Esper, A. Vittoria, G. Antinucci, F. Zaccaria, R. Cipullo, P. H. M. Budzelaar, V. Busico, G. P. Goryunov, D. V. Uborsky, A. Z. Voskoboinikov, K. Searles, C. Ehm, A. S. Veige, *Angew. Chem. Int. Ed.* **2022**, *61*, e202202258.
24. R. Miranda, J. Yang, C. Roy, C. Vasile, *Polym. Degrad. Stab.* **2001**, *72*, 469–491.
25. J. Corker, F. Lefebvre, C. Lécuyer, V. Dufaud, F. Quignard, A. Choplin, J. Evans, J. M. Basset, *Science* **1996**, *271*, 966–969.
26. W. Kaminsky, F. Hartmann, *Angew. Chem. Int. Ed.* **2000**, *39*, 331–333.
27. T. F. L. McKenna, A. Di Martino, G. Weickert, J. B. P. Soares, *Macromol. React. Eng.* **2010**, *4*, 40–64.
28. A. Alizadeh, T. F. L. McKenna, *Macromol. React. Eng.* **2018**, *12*, 1700027.
29. M. E. Z. Velthoen, J. D. Meeldijk, F. Meirer, B. M. Weckhuysen, *Chem. Eur. J.* **2018**, *24*, 11944–11953.
30. A. E. Nieuwelink, M. E. Z. Velthoen, Y. C. M. Nederstigt, K. L. Jagtenberg, F. Meirer, B. M. Weckhuysen, *Chem. Eur. J.* **2020**, *26*, 8546–8554.
31. M. J. Werny, R. Valadian, L. M. Lohse, A.-L. Robisch, S. Zanoni, C. Hendriksen, B. M. Weckhuysen, F. Meirer, *Chem Catalysis* **2021**, *1*, 1413–1426.
32. J. R. Severn, J. C. Chadwick, R. Duchateau, N. Friederichs, *Chem. Rev.* **2005**, *105*, 4073–4147.
33. G. Fink, B. Steinmetz, J. Zechlin, C. Przybyla, B. Tesche, *Chem. Rev.* **2000**, *100*, 1377–1390.

34. G. Fink, B. Tesche, F. Korber, S. Knoke, *Macromol. Symp.* **2001**, 173, 77–87.
35. B. Horáčková, Z. Grof, J. Kosek, *Chem. Eng. Sci.* **2007**, 62, 5264–5270.
36. F. Machado, E. L. Lima, J. C. Pinto, T. F. McKenna, *Polym. Eng. Sci.* **2010**, 51, 302–310.
37. K. W. Bossers, R. Valadian, S. Zaroni, R. Smeets, N. Friederichs, J. Garrevoet, F. Meirer, B. M. Weckhuysen, *J. Am. Chem. Soc.* **2020**, 142, 3691–3695.
38. M. J. Werny, J. Zarupski, I. C. ten Have, A. Piovano, C. Hendriksen, N. H. Friederichs, F. Meirer, E. Groppo, B. M. Weckhuysen, *JACS Au* **2021**, 1, 1996–2008.
39. M. Ahsan Bashir, T. F. L. McKenna, *Polym. React. Eng. Dispersed Syst. Vol. 1*, Springer International Publishing, **2018**, 19–63.
40. P. Kittilsen, T. F. McKenna, H. Svendsen, H. A. Jakobsen, S. B. Fredriksen, *Chem. Eng. Sci.* **2001**, 56, 4015–4028.
41. J. T. M. Pater, G. Weickert, J. Loos, W. P. M. van Swaaij, *Chem. Eng. Sci.* **2001**, 56, 4107–4120.
42. J. M. Zhou, N. H. Li, N. Y. Bu, D. T. Lynch, S. E. Wanke, *J. Appl. Polym. Sci.* **2003**, 90, 1319–1330.
43. S. Knoke, F. Korber, G. Fink, B. Tesche, *Macromol. Chem. Phys.* **2003**, 204, 607–617.
44. H. Hammawa, S. E. Wanke, *Polym. Int.* **2006**, 55, 426–434.
45. X. Zheng, J. Loos, *Macromol. Symp.* **2006**, 236, 249–258.
46. K. W. Bossers, L. D. B. Mandemaker, N. Nikolopoulos, Y. Liu, M. Rohnke, P. de Peinder, B. J. P. Terlingen, F. Walther, J. M. Dorresteijn, T. Hartman, B. M. Weckhuysen, *Nat. Commun.* **2022**, 13, 4954.
47. S. Zaroni, N. Nikolopoulos, A. Welle, A. Vantomme, B. M. Weckhuysen, *Catal. Sci. Technol.* **2021**, 11, 5335–5348.
48. M. J. Werny, D. Müller, C. Hendriksen, R. Chan, N. H. Friederichs, C. Fella, F. Meirer, B. M. Weckhuysen, *ChemCatChem* **2023**, 14, e202200067.
49. S. Zaroni, N. Nikolopoulos, A. Welle, V. Cirriez, B. M. Weckhuysen, *ChemCatChem* **2023**, e202300222.
50. X. Zheng, M. Smit, J. C. Chadwick, J. Loos, *Macromolecules* **2005**, 38, 4673–4678.
51. H. L. Rönkkö, T. Korpela, H. Knuuttila, T. T. Pakkanen, P. Denifl, T. Leinonen, M. Kemell, M. Leskelä, *J. Mol. Catal. A Chem.* **2009**, 309, 40–49.
52. D. Tran, C. S. Sowah, K. Y. Choi, *Macromolecules* **2022**, 55, 2444–2455.
53. J. D. Grunwaldt, C. G. Schroer, *Chem. Soc. Rev.* **2010**, 39, 4741–4753.
54. F. Meirer, B. M. Weckhuysen, *Nat. Rev. Mater.* **2018**, 3, 324–340.
55. W. Curtis Conner, S. W. Webb, P. Spanne, K. W. Jones, *Macromolecules* **1990**, 23, 4742–4747.
56. K. W. Jones, P. Spanne, S. W. Webb, W. C. Conner, R. A. Beyerlein, W. J. Reagan, F. M. Dautzenberg, *Nucl. Inst. Methods Phys. Res. B* **1991**, 56–57, 427–432.
57. K. W. Jones, P. Spanne, W. B. Lindquist, W. C. Conner, M. Ferrero, *Nucl. Instruments Methods Phys. Res. Sect. B Beam Interact. with Mater. Atoms* **1992**, 68, 105–110.
58. M. A. Ferrero, R. Sommer, P. Spanne, K. W. Jones, W. C. Conner, *J. Polym. Sci. Part A Polym. Chem.* **1993**, 31, 2507–2512.
59. D. Cicmil, J. Meeuwissen, A. Vantomme, J. Wang, I. K. van Ravenhorst, H. E. van Der Bij, A. Muñoz-Murillo, B. M. Weckhuysen, *Angew. Chem. Int. Ed.* **2015**, 54, 13073–13079.
60. M. K. Jongkind, F. Meirer, K. W. Bossers, I. C. ten Have, H. Ohldag, B. Watts, T. van Kessel, N. Friederichs, B. M. Weckhuysen, *Chem. Eur. J.* **2021**, 27, 1688–1699.
61. M. Arakawa, M. Kishimoto, Y. Nakanishi, K. Mita, M. Takenaka, *Polym. J.* **2022**, 54, 243–248.
62. F. Pfeiffer, *Nat. Photonics* **2018**, 12, 9–17.
63. K. W. Bossers, R. Valadian, J. Garrevoet, S. van Malderen, R. Chan, N. Friederichs, J. Severn, A. Wilbers, S. Zaroni, M. K. Jongkind, B. M. Weckhuysen, F. Meirer, *JACS Au* **2021**, 1, 852–864.
64. L. Seda, A. Zubov, M. Bobak, J. Kosek, A. Kantzas, *Macromol. React. Eng.* **2008**, 2, 495–512.
65. J. B. P. Soares, T. F. L. McKenna, *Polyolefin Reaction Engineering*, Wiley-VCH, **2012**.
66. L. Meisterová, A. Zubov, K. Smolná, F. Štěpánek, J. Kosek, *Macromol. React. Eng.* **2013**, 7, 277–288.
67. H. Coceancigh, D. A. Higgins, T. Ito, *Anal. Chem.* **2019**, 91, 405–424.
68. N. M. Esfandiari, S. A. Blum, *J. Am. Chem. Soc.* **2011**, 133, 18145–18147.
69. T. Cordes, S. A. Blum, *Nat. Chem.* **2013**, 5, 993–999.

70. Q. T. Easter, S. A. Blum, *Angew. Chem. Int. Ed.* **2017**, *56*, 13772–13775.
71. C. Liu, K. Kubo, E. Wang, K. S. Han, F. Yang, G. Chen, F. A. Escobedo, G. W. Coates, P. Chen, *Science* **2017**, *358*, 352–355.
72. C. Liu, S. Baral, K. Gu, X. Mao, P. Chen, *Trends Chem.* **2021**, *3*, 318–331.
73. J. T. M. Pater, G. Weickert, W. P. M. van Swaij, *Chimia* **2001**, *55*, 231–233.
74. V. P. Oleshko, P. A. Crozier, R. D. Cantrell, A. D. Westwood, *Macromol. Rapid Commun.* **2001**, *22*, 34–40.
75. K. Zöllner, K. H. Reichert, *Chem. Eng. Sci.* **2001**, *56*, 4099–4106.
76. K. Zöllner, K. H. Reichert, *Chem. Eng. Technol.* **2002**, *25*, 707–710.
77. S. Knoke, D. Ferrari, B. Tesche, G. Fink, *Angew. Chem. Int. Ed.* **2003**, *42*, 5090–5093.
78. M. Abboud, K. Kallio, K. H. Reichert, *Chem. Eng. Technol.* **2004**, *27*, 694–698.
79. D. Ferrari, G. Fink, *Macromol. Mater. Eng.* **2005**, *290*, 1125–1136.
80. J. T. M. Pater, G. Weickert, W. P. M. van Swaij, *AIChE J.* **2003**, *49*, 450–464.
81. R. Xalter, R. Mülhaupt, *Macromol. React. Eng.* **2010**, *4*, 25–39.
82. Y. Jang, K. Bieber, C. Naundorf, N. Nenov, M. Klapper, K. Müllen, D. Ferrari, S. Knoke, G. Fink, *e-Polymers* **2005**.
83. Y. J. Jang, C. Naundorf, M. Klapper, K. Müllen, *Macromol. Chem. Phys.* **2005**, *206*, 2027–2037.
84. M. Klapper, D. Joe, S. Nietzel, J. W. Krumpfer, K. Müllen, *Chem. Mater.* **2014**, *26*, 802–819.
85. R. Dorresteijn, S. Nietzel, D. Joe, Y. Gerkmann, G. Fink, M. Klapper, K. Müllen, *J. Polym. Sci. Part A Polym. Chem.* **2014**, *52*, 450–459.
86. M. Stork, A. Herrmann, T. Nemnich, M. Klapper, K. Müllen, *Angew. Chem. Int. Ed.* **2000**, *39*, 4367–4369.
87. M. J. Werny, K. B. Siebers, N. H. Friederichs, C. Hendriksen, F. Meirer, B. M. Weckhuysen, *J. Am. Chem. Soc.* **2022**, *144*, 21287–21294.
88. J. J. Janimak, L. Markey, G. C. Stevens, *Polymer* **2001**, *42*, 4675–4685.
89. I. L. Hosier, R. G. Alamo, J. S. Lin, *Polymer* **2004**, *45*, 3441–3455.
90. R. Pellecchia, P. Shutov, J. Wang, M. Gahleitner, *Macromol. React. Eng.* **2020**, *14*, 2000022.
91. A. Dazzi, C. B. Prater, Q. Hu, D. B. Chase, J. F. Rabolt, C. Marcott, *Appl. Spectrosc.* **2012**, *66*, 1365–1384.
92. F. Tang, P. Bao, Z. Su, *Anal. Chem.* **2016**, *88*, 4926–4930.
93. P. Nguyen-Tri, P. Ghassemi, P. Carriere, S. Nanda, A. A. Assadi, D. D. Nguyen, *Polymers* **2020**, *12*, 1–28.
94. D. Nowak, W. Morrison, H. K. Wickramasinghe, J. Jahng, E. Potma, L. Wan, R. Ruiz, T. R. Albrecht, K. Schmidt, J. Frommer, D. P. Sanders, S. Park, *Sci. Adv.* **2016**, *2*, e1501571.
95. K. L. Gu, Y. Zhou, W. A. Morrison, K. Park, S. Park, Z. Bao, *ACS Nano* **2018**, *12*, 1473–1481.
96. C. Sun, F. Pan, H. Bin, J. Zhang, L. Xue, B. Qiu, Z. Wei, Z. G. Zhang, Y. Li, *Nat. Commun.* **2018**, *9*, 743.
97. V. J. Ruddick, J. P. S. Badyal, *J. Phys. Chem. B* **1997**, *101*, 1791–1793.
98. T. J. Young, M. A. Monclus, T. L. Burnett, W. R. Broughton, S. L. Ogin, P. A. Smith, *Meas. Sci. Technol.* **2011**, *22*, 125703.
99. F. Cavalieri, F. Padella, *Waste Manag.* **2002**, *22*, 913–916.
100. V. Štrukil, *ChemSusChem* **2021**, *14*, 330–338.
101. V. P. Balema, I. Z. Hlova, S. L. Carnahan, M. Seyedi, O. Dolotko, A. J. Rossini, I. Luzinov, *New J. Chem.* **2021**, *45*, 2935–2938.
102. M. Veselý, R. Valadian, L. Merten Lohse, M. Toepperwien, K. Spiers, J. Garrevoet, E. T. C. Vogt, T. Salditt, B. M. Weckhuysen, F. Meirer, *ChemCatChem* **2021**, *13*, 2494–2507.
103. S. Weber, D. Batey, S. Cipiccia, M. Stehle, K. L. Abel, R. Gläser, T. L. Sheppard, *Angew. Chem. Int. Ed.* **2021**, *60*, 21772–21777.
104. F. Meirer, S. Kalirai, D. Morris, S. Soparawalla, Y. Liu, G. Mesu, J. C. Andrews, B. M. Weckhuysen, *Sci. Adv.* **2015**, *1*, e1400199.
105. S. Kalirai, U. Boesenberg, G. Falkenberg, F. Meirer, B. M. Weckhuysen, *ChemCatChem* **2015**, *7*, 3674–3682.

106. J. Ihli, R. R. Jacob, M. Holler, M. Guizar-Sicairos, A. Diaz, J. C. Da Silva, D. Ferreira Sanchez, F. Krumeich, D. Grolimund, M. Taddei, W. C. Cheng, Y. Shu, A. Menzel, J. A. van Bokhoven, *Nat. Commun.* **2017**, *8*, 809.
107. J. Ihli, D. Ferreira Sanchez, R. R. Jacob, V. Cuartero, O. Mathon, F. Krumeich, C. Borca, T. Huthwelker, W. C. Cheng, Y. Y. Shu, S. Pascarelli, D. Grolimund, A. Menzel, J. A. van Bokhoven, *Angew. Chem. Int. Ed.* **2017**, *56*, 14031–14035.
108. M. Gambino, M. Veselý, M. Filez, R. Oord, D. Ferreira Sanchez, D. Grolimund, N. Nesterenko, D. Minoux, M. Maquet, F. Meirer, B. M. Weckhuysen, *Angew. Chem. Int. Ed.* **2020**, *59*, 3922–3927.
109. I. L. C. Buurmans, J. Ruiz-Martínez, W. V Knowles, D. van Der Beek, J. A. Bergwerff, E. T. C. Vogt, B. M. Weckhuysen, *Nat. Chem.* **2011**, *3*, 862–867.
110. M. M. Kerssens, A. Wilbers, J. Kramer, P. De Peinder, G. Mesu, B. J. Nelissen, E. T. C. Vogt, B. M. Weckhuysen, *Faraday Discuss.* **2016**, *188*, 69–79.
111. A.-E. Nieuwelink, J. C. Vollenbroek, R. M. Tiggelaar, J. G. Bommer, A. van den Berg, M. Odijk, B. M. Weckhuysen, *Nat. Catal.* **2021**, *4*, 1070–1079.
112. A. M. Beale, S. D. M. Jacques, B. M. Weckhuysen, *Chem. Soc. Rev.* **2010**, *39*, 4656–4672.
113. J. N. Weker, X. Huang, M. F. Toney, *Curr. Opin. Chem. Eng.* **2016**, *12*, 14–21.
114. E. De Smit, I. Swart, J. F. Creemer, G. H. Hoveling, M. K. Gilles, T. Tyliczszak, P. J. Kooyman, H. W. Zandbergen, C. Morin, B. M. Weckhuysen, F. M. F. de Groot, *Nature* **2008**, *456*, 222–225.
115. F. M. F. de Groot, E. de Smit, M. M. van Schooneveld, L. R. Aramburo, B. M. Weckhuysen, *ChemPhysChem* **2010**, *11*, 951–962.
116. I. K. van Ravenhorst, C. Vogt, H. Oosterbeek, K. W. Bossers, J. G. Moya-Cancino, A. P. van Bavel, A. M. J. van der Eerden, D. Vine, F. M. F. de Groot, F. Meirer, B. M. Weckhuysen, *Angew. Chem. Int. Ed.* **2018**, *57*, 11957–11962.
117. Y. Fam, T. L. Sheppard, J. Becher, D. Scherhauser, H. Lambach, S. Kulkarni, T. F. Keller, A. Wittstock, F. Wittwer, M. Seyrich, D. Brueckner, M. Kahnt, X. Yang, A. Schropp, A. Stierle, C. G. Schroer, J. D. Grunwaldt, *J. Synchrotron Radiat.* **2019**, *26*, 1769–1781.
118. S. W. T. Price, K. Geraki, K. Ignatyev, P. T. Witte, A. M. Beale, J. F. W. Mosselmans, *Angew. Chem. Int. Ed.* **2015**, *54*, 9886–9889.
119. T. L. Sheppard, S. W. T. Price, F. Benzi, S. Baier, M. Klumpp, R. Dittmeyer, W. Schwieger, J. D. Grunwaldt, *J. Am. Chem. Soc.* **2017**, *139*, 7855–7863.
120. I. D. Gonzalez-Jimenez, K. Cats, T. Davidian, M. Ruitenbeek, F. Meirer, Y. Liu, J. Nelson, J. C. Andrews, P. Pianetta, F. M. F. de Groot, B. M. Weckhuysen, *Angew. Chem. Int. Ed.* **2012**, *51*, 11986–11990.
121. K. H. Cats, I. D. Gonzalez-Jimenez, Y. Liu, J. Nelson, D. van Campen, F. Meirer, A. M. J. van Der Eerden, F. M. F. de Groot, J. C. Andrews, B. M. Weckhuysen, *Chem. Commun.* **2013**, *49*, 4622–4624.
122. K. H. Cats, J. C. Andrews, O. Stéphan, K. March, C. Karunakaran, F. Meirer, F. M. F. de Groot, B. M. Weckhuysen, *Catal. Sci. Technol.* **2016**, *6*, 4438–4449.
123. J. C. Andrews, B. M. Weckhuysen, *ChemPhysChem* **2013**, *14*, 3655–3666.
124. A. Vamvakeros, S. D. M. Jacques, V. Middelkoop, M. Di Michiel, C. K. Egan, I. Z. Ismagilov, G. B. M. Vaughan, F. Gallucci, M. van Sint Annaland, P. R. Shearing, R. J. Cernik, A. M. Beale, *Chem. Commun.* **2015**, *51*, 12752–12755.
125. S. W. T. Price, D. J. Martin, A. D. Parsons, W. A. Sławiński, A. Vamvakeros, S. J. Keylock, A. M. Beale, J. F. W. Mosselmans, *Sci. Adv.* **2017**, *3*, e1602838.
126. P. Senecal, S. D. M. Jacques, M. Di Michiel, S. A. J. Kimber, A. Vamvakeros, Y. Odarchenko, I. Lezcano-Gonzalez, J. Paterson, E. Ferguson, A. M. Beale, *ACS Catal.* **2017**, *7*, 2284–2293.
127. A. Vamvakeros, S. D. M. Jacques, M. Di Michiel, D. Matras, V. Middelkoop, I. Z. Ismagilov, E. V. Matus, V. V. Kuznetsov, J. Drnec, P. Senecal, A. M. Beale, *Nat. Commun.* **2018**, *9*, 4751.
128. D. Matras, A. Vamvakeros, S. D. M. Jacques, M. Di Michiel, V. Middelkoop, I. Z. Ismagilov, E. V. Matus, V. V. Kuznetsov, R. J. Cernik, A. M. Beale, *J. Mater. Chem. A* **2021**, *9*, 11331–11346.
129. I. J. Drake, T. C. N. Liu, M. Gilles, T. Tyliczszak, A. L. D. Kilcoyne, D. K. Shuh, R. A. Mathies, A. T. Bell, *Rev. Sci. Instrum.* **2004**, *75*, 3242–3247.
130. M. Holler, T. Aidukas, L. Heller, C. Appel, N. W. Phillips, E. Müller-Gubler, M. Guizar-Sicairos, J. Raabe, J. Ihli, S. Svensson, *J. Synchrotron Radiat.* **2022**, *29*, 1223–1231.

131. G. Martinez-Criado, J. Villanova, R. Tucoulou, D. Salomon, J. P. Suuronen, S. Laboure, C. Guilloud, V. Valls, R. Barrett, E. Gagliardini, Y. Dabin, R. Baker, S. Bohic, C. Cohen, J. Morse, *Synchrotron Radiat.* **2016**, *23*, 344–352.
132. J. Villanova, R. Kumar, R. Daudin, P. Lhuissier, D. Jauffres, C. L. Martin, R. Tucoulou, S. Laboure, G. Martinez-Criado, L. Salvo, *Microsc. Microanal.* **2018**, *24*, 450–451.
133. V. Vanpeene, J. Villanova, A. King, B. Lestriez, E. Maire, L. Roué, *Adv. Energy Mater.* **2019**, *9*, 1803947.
134. P. Raimondi, *Synchrotron Radiat. News* **2016**, *29*, 8–15.
135. R. Röhlberger, C. G. Schroer, R. Wanzenberg, S. Klumpp, W. Wurth, *Synchrotron Radiat. News* **2019**, *32*, 27–31.
136. A. Rack, *Synchrotron Radiat. News* **2020**, *33*, 20–28.
137. T. F. McKenna, J. B. P. Soares, *Chem. Eng. Sci.* **2001**, *56*, 3931–3949.
138. C. E. Cardenas, J. Yang, B. M. Anderson, L. E. Court, K. B. Brock, *Semin. Radiat. Oncol.* **2019**, *29*, 185–197.
139. J. J. Bailey, J. Chen, J. Hack, M. Perez-Page, S. M. Holmes, D. J. L. Brett, P. R. Shearing, *J. Power Sources* **2021**, *509*, 230347.
140. A. D. Shum, C. P. Liu, W. H. Lim, D. Y. Parkinson, I. V. Zenyuk, *Transp. Porous Media* **2022**, *144*, 715–737.
141. K. Tang, Q. Meyer, R. White, R. T. Armstrong, P. Mostaghimi, Y. Da Wang, S. Liu, C. Zhao, K. Regenauer-Lieb, P. K. M. Tung, *Comput. Chem. Eng.* **2022**, *161*, 107768.
142. P. C. Thüne, J. Loos, P. J. Lemstra, J. W. Niemantsverdriet, *J. Catal.* **1999**, *183*, 1–5.
143. S. H. Kim, G. A. Somorjai, *J. Phys. Chem. B* **2001**, *105*, 3922–3927.
144. P. C. Thüne, J. Loos, U. Weingarten, F. Müller, W. Kretschmer, W. Kaminsky, P. J. Lemstra, H. Niemantsverdriet, *Macromolecules* **2003**, *36*, 1440–1445.
145. A. Andoni, J. C. Chadwick, S. Milani, H. J. W. Niemantsverdriet, P. C. Thüne, *J. Catal.* **2007**, *247*, 129–136.
146. A. Andoni, J. C. Chadwick, H. J. W. Niemantsverdriet, P. C. Thüne, *Macromol. Symp.* **2007**, *260*, 140–146.
147. S. Y. Lee, S. K. Kim, T. M. Nguyen, J. S. Chung, S. B. Lee, K. Y. Choi, *Macromolecules* **2011**, *44*, 1385–1392.
148. S. Y. Lee, K. Y. Choi, *Macromol. React. Eng.* **2014**, *8*, 755–765.
149. M. Solsona, A. E. Nieuwelink, F. Meirer, L. Abelmann, M. Odijk, W. Olthuis, B. M. Weckhuysen, A. van den Berg, *Angew. Chem. - Int. Ed.* **2018**, *57*, 10589–10594.
150. R. G. Geitenbeek, A. E. Nieuwelink, T. S. Jacobs, B. B. V. Salzmann, J. Goetze, A. Meijerink, B. M. Weckhuysen, *ACS Catal.* **2018**, *8*, 2397–2401.
151. T. Hartman, R. G. Geitenbeek, G. T. Whiting, B. M. Weckhuysen, *Nat. Catal.* **2019**, *2*, 986–996.
152. T. Hartman, R. G. Geitenbeek, C. S. Wondergem, W. van Der Stam, B. M. Weckhuysen, *ACS Nano* **2020**, *14*, 3725–3735.
153. T. P. van Swieten, T. van Omme, D. J. van Den Heuvel, S. J. W. Vonk, R. G. Spruit, F. Meirer, H. H. P. Garza, B. M. Weckhuysen, A. Meijerink, F. T. Rabouw, R. G. Geitenbeek, *ACS Appl. Nano Mater.* **2021**, *4*, 4208–4215.
154. Y. Yao, Y. Jiang, J. A. Klug, M. Wojcik, E. R. Maxey, N. S. Sirica, C. Roehrig, Z. Cai, S. Vogt, B. Lai, J. Deng, *Sci. Reports* **2020**, *10*, 1–8.
155. F. Wittwer, M. Lyubomirskiy, F. Koch, M. Kahnt, M. Seyrich, J. Garrevoet, C. David, C. G. Schroer, *Appl. Phys. Lett.* **2021**, *118*, 171102.
156. M. Lyubomirskiy, F. Wittwer, M. Kahnt, F. Koch, A. Kubec, K. V. Falch, J. Garrevoet, M. Seyrich, C. David, C. G. Schroer, *Sci. Reports* **2022**, *12*, 1–9.

Chapter 8

Summary, Conclusions and Future Perspectives

8.1 Summary and Conclusions

The morphological development of a supported olefin polymerization catalyst has direct implications for its activity and the quality of the polymer product that is formed. Identifying the key factors that are responsible for the morphologies of individual catalyst particles represents a complex scientific undertaking due to the large number of experimental variables involved in the olefin polymerization process.

In this PhD thesis, a range of analytical tools, including various microscopic and spectroscopic methods, was employed to determine the structure, morphology and composition of individual olefin polymerization catalyst particles that were pre-polymerized with ethylene under well-defined reaction conditions. The combination of multiple techniques at different length scales allowed us to establish structure-composition-performance relationships in both silica-supported metallocene and Ziegler-Natta catalysts. In general, advanced electron, X-ray and fluorescence microscopy were employed to obtain nano-resolved morphological data of multiple catalyst particles in 2D and 3D. The kinetics and accessibilities of the catalysts' active sites, on the other hand, were assessed *in situ* with bulk spectroscopy techniques, such as diffuse reflectance infrared Fourier transform spectroscopy (DRIFTS), luminescence thermometry and probe molecule infrared spectroscopy, as well as catalytic performance testing. Leveraging this synergy between single particle and bulk characterization techniques proved to be instrumental for rationalizing the structural complexity of supported olefin polymerization catalysts during the dynamic processes of polymer formation and support fragmentation (**Figure 8.1**).

To bridge the gap between single particle characterization approaches and bulk analytical techniques, we have studied larger sample sets with synchrotron-based hard X-ray holography and laboratory-based confocal fluorescence microscopy (CFM). Both techniques facilitated a high sample throughput in comparison to other high resolution imaging techniques and, in combination with image processing, provided quantitative insights into inter- and intraparticle heterogeneities (**Figure 8.1**). We believe that these methodologies can provide representative morphological insights into existing and newly designed olefin polymerization catalysts operating under various pre-polymerization conditions.

A more detailed summary of the individual chapters constituting this PhD thesis, as well as the main insights from our research on supported olefin polymerization catalysts, are provided below:

In **Chapter 1**, a brief introduction into the fields of catalysis, spectroscopy and olefin polymerization catalysis was given. Different classes of established olefin polymerization catalysts were discussed and the role of a catalyst's morphology during olefin polymerization was reviewed. Furthermore, challenges associated with conducting morphological investigations on supported polymerization catalysts were outlined.

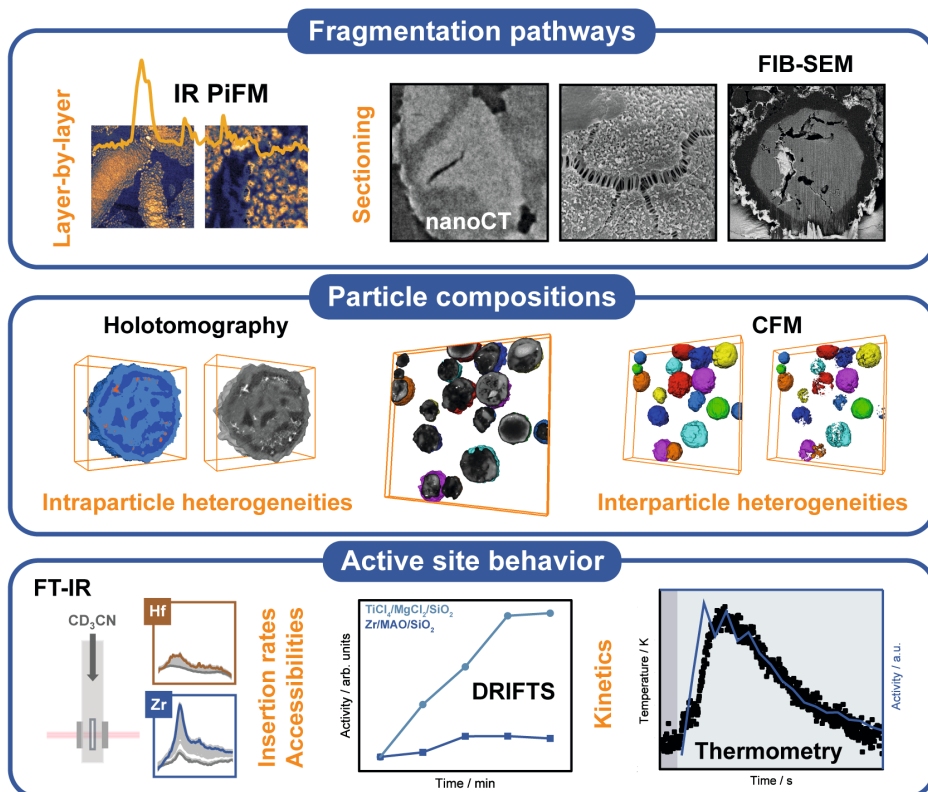


Figure 8.1 Schematic overview of the characterization techniques that were employed to investigate structure-composition-performance relationships in silica-supported olefin polymerization catalysts. The synergy of single particle, multi-particle and bulk characterization techniques was crucial for establishing clear correlations between the properties of interest.

In **Chapter 2**, two structurally analogous silica-supported hafnocene and zirconocene-based catalysts (i.e., X/MAO/SiO₂, X = metallocene complex, MAO = methylaluminoxane) were investigated at several different stages of gas-phase ethylene polymerization (i.e., the pristine catalyst and catalyst samples after 10 min, 30 min and 60 min of polymerization; reaction conditions: 1.6 bar, room temperature). A multi-scale microscopy and spectroscopy approach was used to establish correlations between the catalysts' respective morphologies and the properties of their active sites. The internal structures and morphologies of the catalyst particles were assessed with highly resolved focused ion beam-scanning electron microscopy (FIB-SEM) and infrared photoinduced force microscopy (IR PiFM). A layer-by-layer mechanism was identified as the dominant fragmentation pathway in the silica-supported hafnocene, which fragmented homogeneously. A more heterogeneous morphology, characterized by contributions from the sectioning mechanism, was, however, observed in the silica-supported zirconocene. This was attributed to significant differences in the catalysts' polymerization rates. The high polymerization rate of the zirconocene complex leads to a rapid accumulation of polymer, most notably at the particle surface, thereby limiting mass transfer and inhibiting

stress dissipation within the particle. To further rationalize these findings, time-resolved Fourier-transform infrared (FTIR) spectroscopy was performed with deuterated acetonitrile as a probe molecule at different concentrations. The experiments yielded insights into both the insertion behavior and the accessibilities of the catalysts' active sites. Not only were the active sites of the hafnocene-based catalyst intrinsically slower, but they were also less accessible due to the formation of stable heterodinuclear adducts with free trimethylaluminum (TMA, exists in equilibrium with MAO). In conclusion, our multi-scale approach yielded clear correlations between the properties of the active sites, mass transfer limitations and dominant fragmentation pathways in supported olefin polymerization catalyst particles.

In **Chapter 3**, the time series of hafnocene-based catalyst particles (i.e., Hf/MAO/SiO₂, see **Chapter 2**) was investigated in further detail. A total of 12 pristine and pre-polymerized catalyst particles, representing five stages of gas-phase ethylene polymerization (i.e., the pristine catalyst and catalyst samples after 1 min, 10 min, 30 min and 60 min of ethylene polymerization; reaction conditions: 1.6 bar, room temperature), were assessed in 3D using hard X-ray full-field holotomography. This delivered an improved understanding for the morphological evolution of the catalyst, which mainly follows a layer-by-layer fragmentation pathway. An in-depth quantitative characterization of the particles' porosities, pore networks (via pore network modelling) and 3D phase distributions revealed significant inter- and intraparticle heterogeneity during the early stages of gas-phase ethylene polymerization. Differences in catalyst particle morphology were attributed to the heterogeneous support and pore space architecture of the pristine catalyst particles, which result in varying degrees of mass transfer limitations. Decreases in macroporosity and pore space interconnectivity were observed with polymerization time and yield, thus underlining the importance of controlled catalyst support fragmentation in overcoming mass transfer limitations. From a methodological point of view, the experiments demonstrated two unique strengths of holotomography that are of particular interest for research on olefin polymerization catalyst systems: i) The ability to image and distinguish catalyst phases and products that are constituted by low atomic number elements, and ii) comparatively short measurement times, which facilitate high sample throughput and the acquisition of more representative data sets.

In **Chapter 4**, the structures of two different silica-supported polymerization catalysts, i.e., the above-mentioned silica-supported zirconocene (i.e., Zr/MAO/SiO₂) and a silica-supported Ziegler-Natta catalyst (i.e., TiCl₄/MgCl₂/SiO₂), were characterized after slurry-phase pre-polymerization at low and elevated ethylene pressures (7.5–10 bar ethylene pressure, room temperature). Laboratory-based techniques, such as nano computed tomography (nanoCT) and focused ion beam-scanning electron microscopy (FIB-SEM), were used to visualize the propagation of extensive cracks in 3D and 2D. Different factors regulating the occurrence of the sectioning fragmentation mechanism were thus identified. These include the kinetics of a catalyst (corroborated with *in situ* DRIFTS), the porosity of a catalyst's support, as well as the accessibility of a catalyst particle's internal volume at the onset of polymerization. Higher mass transfer resistance and insufficient stress dissipation were shown to amplify the involvement of the sectioning mechanism.

In **Chapter 5**, the autofluorescence of the zirconocene-based catalyst (i.e., Zr/MAO/SiO₂) was exploited to assess its morphology and composition with confocal fluorescence microscopy (CFM). The composition of the catalyst was studied at multiple different stages of slurry-phase ethylene polymerization (10 bar ethylene pressure, room temperature) at high sample throughput (2D: ≥ 135 particles per stage, 3D: 40 particles). A substantial degree of structural heterogeneity was observed before and during ethylene polymerization, as was previously reported for the structurally analogous silica-supported hafnocene-based catalyst (i.e., Hf/MAO/SiO₂) during gas-phase ethylene polymerization (**Chapters 2–4**). This heterogeneity is primarily attributed to the catalyst particles' diverse support structures and to inhomogeneities in the metallocene distribution. From a mechanistic point of view, the 2D and 3D screening revealed extensive contributions from a layer-by-layer fragmentation mechanism in synergy with a less pronounced sectioning mechanism. Furthermore, a certain degree of inactivity or dormancy, manifested in a lower degree of fragmentation, was observed in a significant fraction of particles at the onset of polymerization. This contributes to a broadening of the original particle size distribution over time. In combination with sophisticated staining procedures and fluorescent probe molecules, laboratory-based CFM is highly suitable for the morphological analysis of olefin polymerization catalysts and represents an accessible alternative to synchrotron-based experimentation. Due to its high sample throughput, it has the potential to be used a tool for quality control both in industry and academia.

In **Chapter 6**, *in situ* luminescence thermometry was applied for the first time to monitor the temperature of an olefin polymerization catalyst during gas-phase ethylene polymerization. NaYF₄:Er³⁺,Yb³⁺/NaYF₄ core-shell nanoparticles were employed as temperature sensors and were homogeneously dispersed on a silica-supported zirconocene-based catalyst (i.e., Zr/MAO/SiO₂) without any signs of immediate deactivation. The temperature profiles obtained for the catalyst at 1 bar ethylene pressure were shown to correlate with activity data that was acquired under identical reaction conditions via *in situ* DRIFTS. Thus, the temperature measurements yield kinetic information on the catalyst. Deviations in exothermicity were also observed between individual testing runs, pointing to a large influence of the catalyst bed composition and packing. The experiments lay the foundation for further studies, in which the temperature evolution of individual catalyst particles is mapped with scanning techniques such as CFM. This will yield insights into heterogeneities in temperature and activity at the catalyst particle surface at the onset of the olefin polymerization reaction.

In **Chapter 7**, a toolbox of analytical techniques, specifically employed for obtaining structural and chemical information on supported olefin polymerization catalyst particles, was presented. FIB-SEM, hard X-ray nanotomography, CFM and IR PiFM were highlighted as state-of-the-art methods for chemical imaging at the nanoscale. The techniques also hold great potential for determining the spatial distribution of carbon-based educts and products in heterogenous catalysts for polyolefin cracking and decomposition. Even greater insights could be delivered by *in situ* and *operando* microscopy and tomography experiments that establish clear links between the initial structure of a catalyst particle and its morphological evolution and activity during polymerization or polymer decomposition. At the same time, significant advances towards a more high-throughput assessment of supported olefin polymerization

and polyolefin decomposition catalysts are necessary to obtain more representative insights into catalyst particle morphology and reactivity.

All in all, our investigations revealed a simultaneous occurrence of two fragmentation pathways, i.e., the layer-by-layer mechanism and the sectioning mechanism, in silica-supported olefin polymerization catalysts during gas- and slurry-phase ethylene polymerization. The degree as to which a particular mechanism contributes to the fragmentation of a given catalyst was found to be strongly influenced by i) the kinetics and accessibility of the catalyst's active sites, and ii) the initial structure of the catalyst's support. Both are crucial in determining the rate of mass transfer and polymer formation during the olefin polymerization reaction. Furthermore, new methodological avenues for extracting more representative morphological data at nanometer spatial resolutions were established. X-ray (i.e., holotomography) and fluorescence microscopy (i.e., CFM), performed on large particle numbers, clearly demonstrated high degrees of inter- and intraparticle heterogeneity in silica-supported catalyst systems, which were quantified using advanced image segmentation and analysis.

8.2 Future Perspectives

Technological developments in the field of chemical imaging and spectroscopy will undoubtedly open up new opportunities to study supported olefin polymerization catalysts at improved spatio-temporal resolutions. However, there are several experimental variables that still require further investigation with our current technical means.

The experiments that this thesis is based on were primarily conducted at room temperature. With industrial olefin polymerization processes being conducted at elevated temperatures, further studies can be directed towards studying the influence of higher temperatures on the morphology of industrially-relevant catalyst systems. To obtain early-stage pre-polymerized samples at industrially relevant conditions (i.e., high pressures and temperatures), stopped-flow reactors, as employed by the groups of McKenna^[1-4], Terano^[5,6] and Taniike^[7], can be used. Further experimentation could also involve studying the morphological effect of co-monomers, such as 1-butene, 1-hexene or 1-octene, that are used to synthesize different grades of polyethylene, and hydrogen as a molecular weight control agent. Pre-polymerizations with propylene may also be of interest and can be performed for comparison with the same catalysts. In general, several of the above-mentioned research concepts are applicable to other supported polymerization catalysts, such as the silica-supported Phillips catalyst, as well as Mg(OEt)₂- and MgCl₂-supported Ziegler-Natta catalysts. The fragmentation of the catalysts' respective supports will vary due to differences in their mechanical stability, especially in the case of MgCl₂.^[8-12]

Another feasible research direction involves re-designing current industrial-grade olefin polymerization catalysts. In **Chapter 4**, the macroporosity of the silica support was discussed as an important factor that can regulate the degree of mass transfer resistance in a silica granulate or in a catalyst particle as a whole. By ensuring a more homogeneous distribution of larger macropores throughout the support, especially in larger support granulates, high degrees of local mass transfer resistance may be avoided, thus ensuring homogeneous support

fragmentation. Future research may involve re-designing polymerization-grade silica-supports in collaboration with industry and testing their performance in olefin polymerization. Any performance gains in terms of catalyst activity, morphology and product quality will have to outweigh the increase in costs that is potentially introduced by a new preparation method. Besides adapting the catalyst support, the distribution of other catalyst components, such as the metallocene and the co-catalyst (MAO), could be optimized. Our investigations with CFM (**Chapter 5**) revealed inhomogeneities in the distribution of the metallocene in a Zr/MAO/SiO₂ catalyst. By varying the preparation procedure and monitoring the effect thereof with CFM and high-throughput testing, more homogeneous metallocene distributions at the single particle level and, possibly, improved catalyst performance could be achieved. Similar approaches are required to assess the distribution and speciation of MAO in a representative number of particles at nanometer resolution. This could also help to minimize differences in activity and morphology between individual catalyst particles.

Finally, there are several approaches and methodologies that still require further optimization for implementation, yet have the potential to deliver impactful insights in the field of olefin polymerization catalysts (**Figure 8.2**). These are described in the following two sections that deal with *in situ* and *operando* as well as high-throughput experimentation.

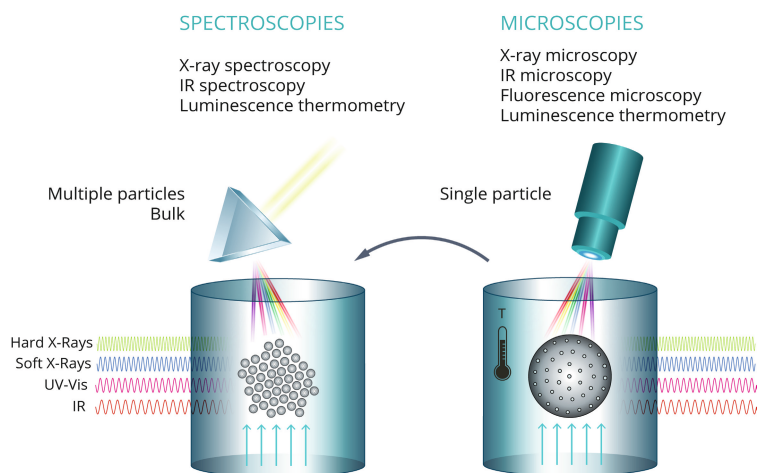


Figure 8.2 Schematic illustration of the spectroscopy and microscopy approaches that can be applied for *in situ* and *operando* single particle, multi-particle and bulk catalyst characterization.

8.2.1 *In Situ* and *Operando* Characterization of Individual Olefin Polymerization Catalyst Particles at the Nanoscale

As the spatial and temporal resolutions of microscopy and spectroscopy techniques gradually improve over time, it may become possible to study the genesis of active sites, early-stage polymer formation and support fragmentation in real time. Here, we report on analytical techniques and methods that could be suitable for extracting structural, morphological and chemical information from individual catalyst particles directly under reaction conditions.

8.2.1.1 *In Situ* Infrared Microscopy Experiments

The suitability of infrared photoinduced force microscopy (IR PiFM) for obtaining nano-resolved IR maps of the cross-section of an olefin polymerization catalyst was successfully demonstrated in **Chapter 2**. Inspired by this, a combination with probe molecules, such as carbon monoxide (CO) or d-acetonitrile (d-CD₃CN), for *in situ* imaging is proposed. Provided a suitable gas cell is developed for the IR PiFM system, spatially resolved maps of vibrational bands, attributable to formed acyl- or azaalkenylidene species^[13,14], can be acquired. This would help to visualize the insertion behavior and thus activity of the active sites at the catalyst surface at unparalleled spatial resolutions. In the case of CO as a probe molecule, Lewis acidic sites of different strength could be distinguished and mapped. Planar model systems (e.g., thin films or micro-islands) could be developed to facilitate easier data acquisition (spherical particles are difficult to image with tip-based scanning techniques). The pre-polymerization of suitable catalyst systems with ethylene or propylene could also be monitored spectroscopically with IR PiFM. Preferably, a catalyst with slow polymerization kinetics, in combination with a slowly inserting olefin monomer, is used. Alternatively, the cell is cooled to limit the rate of polymerization and thus the physical build-up of polymer at the catalyst surface. Both proposed experiments do not require any additional modifications to the IR PiFM instrument. The influence of the nascent polymer morphology and crystallinity on the evolution of the catalyst's surface morphology could also be investigated.

8.2.1.2 *In Situ* Fluorescence Microscopy Experiments

In **Chapter 5**, we demonstrated the potential of fluorescence microscopy for characterizing autofluorescent metallocene-based polymerization catalysts. By using dye-stained supports^[15–17], other types of olefin polymerization catalysts can be imaged *ex situ*. Widefield and confocal fluorescence microscopy could even be used to assess the distribution of fluorescent, chemosensitive probe molecules. These can help to selectively visualize different components of the catalyst material. The techniques can also be used to monitor the uptake of fluorescent dyes, thereby delivering information on the accessibilities of individual catalyst particles. In the past, fluorescence microscopy has also been employed to visualize the polymerization of fluorophore-tagged olefins *in situ*.^[18,19] This approach can be applied in a similar fashion to supported olefin polymerization catalysts to study the early stages of polymer formation on the catalyst surface. In the case of supported Ziegler-Natta catalysts, the coordination of fluorescent donor molecules to specific sites and crystal facets could also be investigated before and after pre-polymerization.

8.2.1.3 *In Situ* Temperature Mapping Experiments

As suggested in **Chapter 6**, *in situ* temperature mapping experiments can be performed with a confocal fluorescence microscope (CFM) that is equipped with a 980 nm laser (**Figure 8.3**).^[20] This will potentially reveal inhomogeneities in temperature and activity at the surface of individual catalyst particles at the onset of polymerization at a spatial resolution of up to approximately 1 μm. Furthermore, it may be possible to monitor the temperature of temperature sensors throughout a catalyst particle if the temperature sensors are integrated into the

framework of the catalyst support. By employing temperature sensors doped with different lanthanides, a range of lasers can be exploited for excitation (**Figure 8.4**). For instance, Raman microscopes equipped with more conventional lasers (e.g., 532 nm, 785 nm) could then be utilized for temperature mapping experiments.

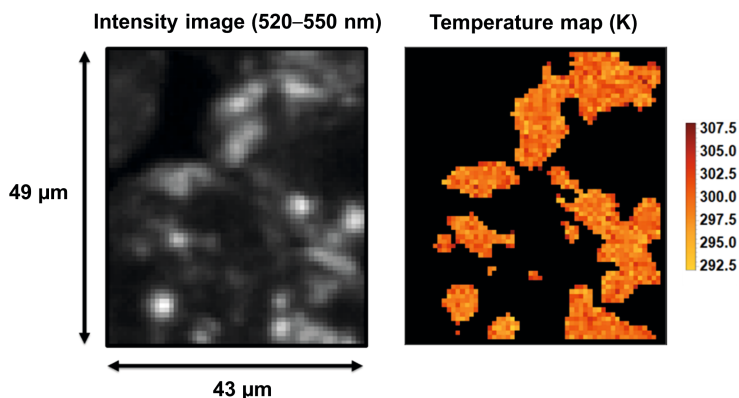


Figure 8.3 Integrated intensity (520–550 nm) and temperature maps recorded of a silica-supported zirconocene-based catalyst (i.e., $Zr/MAO/SiO_2$), treated with $NaYF_4:Er^{3+},Yb^{3+}/NaYF_4$ core-shell nanoparticles (5 wt%). The measurement was performed *ex situ* at room temperature using a 980 nm laser (0.5 W), an integration time of 100 ms and a field of view of $50 \mu m \times 50 \mu m$ (64×64 pixels). A threshold was set to exclude low intensity pixels from the temperature map.

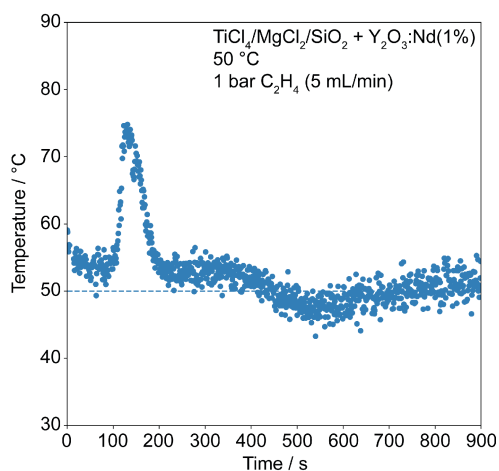


Figure 8.4 Temperature profile recorded of a silica-supported Ziegler-Natta catalyst (i.e., $TiCl_4/MgCl_2/SiO_2$), treated with $Y_2O_3:Nd(1\%)$ nanocrystals, during gas-phase ethylene polymerization at $50 \text{ }^\circ C$ (measured with a Harrick cell; $10 \text{ mL/min } C_2H_4$; 785 nm excitation, HORIBA Raman microscope; evaluation of spectra according to Kolesnikov *et al.*^[21]).

8.2.1.4 *In Situ* X-Ray Microscopy

As is evident from **Chapters 3** and **7**, full-field holotomography possesses a substantially faster acquisition speed compared to scanning techniques such as ptychographic X-ray computed tomography (PXCT) and X-ray fluorescence (XRF) tomography. Hence, it is the current method of choice for *in situ* nanotomography experiments, taking both the temporal and spatial resolution into consideration. The main challenge in executing such experiments, however, is the moisture and oxygen sensitivity of the involved catalyst materials. To counteract this, compact reactor cells, preferably featuring an integrated vertical capillary and localized heating elements, must be designed. The catalyst particles would then be transferred to this cell inside a glovebox under inert conditions. Due to the fast kinetics of the polymerization reaction on industrial catalyst systems, a pulsing approach would currently have to be adopted to conduct the experiment at the synchrotron beamline. Here, the pristine catalyst particle is first scanned under low inert gas flow. Then, the feed is switched to ethylene gas, thereby inducing the pre-polymerization of the particle. After the desired reaction period, the gas flow is switched back to the inert gas and a second tomography is acquired. This procedure would ideally be repeated multiple times to monitor the morphological evolution of the particle over several reaction stages. By coupling the set-up with a backpressure regulator, high ethylene pressures can be maintained. *In situ* tomography experiments as these would yield valuable data for directly assessing structure-activity relationships in individual olefin polymerization catalyst particles. Furthermore, the data could be used to refine existing models that are used to simulate support fragmentation^[22–24].

Inspired by the recent work of Arakawa *et al.*, in which scanning transmission X-ray microscopy (STXM) was used to study the chain orientation of polymer chains in the low- and high-density domains of stretched polyethylene,^[25] STXM could also be used to study polymer chain formation and orientation on olefin polymerization catalysts *in situ*. For this, planar model systems with limited thickness could be synthesized. Ideally, the systems would demonstrate a certain degree of fragmentation to investigate possible correlations between localized stress generation and polymer chain orientation in the formed polymer matrix.

8.2.2 High-Throughput Experimentation for Evaluating the Morphology and Reactivity of Multiple Olefin Polymerization Catalyst Particles

In **Chapters 3**, **5** and **7** of this PhD thesis, holotomography and confocal fluorescence microscopy (CFM) were introduced as high-throughput methods for the morphological screening of supported olefin polymerization catalysts. While confocal fluorescence microscopy, due to its large field of view, provides 3D data of multiple particle sub-volumes at sub-500 nm spatial resolutions within short measurement times (1–2 h), holotomography can be employed to acquire full 3D tomographies of individual particles at spatial resolutions in the range 100–200 nm within 10–15 min (ID16B, ESRF). Advances in machine learning will help to automate the segmentation and analysis of the collected tomography data sets.^[26–29] This, coupled with automated reconstruction algorithms, can radically transform data analysis in the field of 3D X-ray and fluorescence imaging. Both techniques can be used for quality control on pristine

and pre-polymerized catalyst samples, with laboratory-based confocal fluorescence microscopy representing a more accessible characterization technique. As previously mentioned, the implementation of sophisticated staining approaches (e.g., with dyes^[15,16] and chemosensitive probes) will further help to extend the CFM-based methodology to other supported polymerization catalyst materials to investigate their respective compositions at different stages of catalyst preparation and (pre-)polymerization. The implementation of high-throughput characterization techniques and machine learning algorithms could potentially provide sufficient data to simulate the fragmentation of realistic particle structures under model conditions.

Acknowledgments

Thomas van Swieten (Utrecht University, UU) and Martijn Mekkering (UU) are acknowledged for the temperature mapping experiment. Thimo Jacobs (UU) is thanked for his assistance with the thermometry experiment on the Ziegler-Natta catalyst.

References

1. F. M. Silva, J. P. Broyer, C. Novat, E. L. Lima, J. C. Pinto, T. F. McKenna, *Macromol. Rapid Commun.* **2005**, *26*, 1846–1853.
2. F. Machado, E. L. Lima, J. C. Pinto, T. F. McKenna, *Macromol. React. Eng.* **2009**, *3*, 47–57.
3. E. Tioni, J. P. Broyer, V. Monteil, T. McKenna, *Ind. Eng. Chem. Res.* **2012**, *51*, 14673–14684.
4. T. F. L. McKenna, E. Tioni, M. M. Ranieri, A. Alizadeh, C. Boisson, V. Monteil, *Can. J. Chem. Eng.* **2013**, *91*, 669–686.
5. T. Taniike, V. Q. Thang, N. T. Binh, Y. Hiraoka, T. Uozumi, M. Terano, *Macromol. Chem. Phys.* **2011**, *212*, 723–729.
6. T. Taniike, S. Sano, M. Ikeya, V. Q. Thang, M. Terano, *Macromol. React. Eng.* **2012**, *6*, 275–279.
7. A. Thakur, T. Wada, P. Chammingkwan, M. Terano, T. Taniike, *Polymers* **2019**, *11*, 1012.
8. V. W. Buls, T. L. Higgins, *J. Polym. Sci Part A-1 Polym. Chem.* **1970**, *8*, 1037–1053.
9. M. Kakugo, H. Sadatoshi, M. Yokoyama, K. Kojima, *Macromolecules* **1989**, *22*, 547–551.
10. J. T. M. Pater, G. Weickert, W. P. M. van Swaaij, *Chimia* **2001**, *55*, 231–233.
11. X. Zheng, J. Loos, *Macromol. Symp.* **2006**, *236*, 249–258.
12. F. Machado, E. L. Lima, J. C. Pinto, T. F. McKenna, *Polym. Eng. Sci.* **2010**, *51*, 302–310.
13. A. Piovano, J. Zarupski, E. Groppo, *J. Phys. Chem. Lett* **2020**, *11*, 5637.
14. M. J. Werny, J. Zarupski, I. C. ten Have, A. Piovano, C. Hendriksen, N. H. Friederichs, F. Meirer, E. Groppo, B. M. Weckhuysen, *JACS Au* **2021**, *1*, 1996–2008.
15. Y. J. Jang, C. Naundorf, M. Klapper, K. Müllen, *Macromol. Chem. Phys.* **2005**, *206*, 2027–2037.
16. R. Dorresteyn, S. Nietzel, D. Joe, Y. Gerkmann, G. Fink, M. Klapper, K. Müllen, *J. Polym. Sci. Part A Polym. Chem.* **2014**, *52*, 450–459.
17. K. B. Siebers, *Visualization and Quantification of Fragmentation in Olefin Polymerization Catalysts*, Utrecht Universitij, M.Sc. thesis, **2021**.
18. N. M. Esfandiari, S. A. Blum, *J. Am. Chem. Soc.* **2011**, *133*, 18145–18147.
19. T. Cordes, S. A. Blum, *Nat. Chem.* **2013**, *5*, 993–999.
20. T. P. van Swieten, T. van Omme, D. J. van Den Heuvel, S. J. W. Vonk, R. G. Spruit, F. Meirer, H. H. P. Garza, B. M. Weckhuysen, A. Meijerink, F. T. Rabouw, R. G. Geitenbeek, *ACS Appl. Nano Mater.* **2021**, *4*, 4208–4215.
21. I. E. Kolesnikov, A. A. Kalinichev, M. A. Kurochkin, D. V. Mamonova, E. Y. Kolesnikov, A. V. Kurochkin, E. Lähderanta, M. D. Mikhailov, *J. Lumin.* **2018**, *204*, 506–512.
22. T. F. McKenna, J. B. P. Soares, *Chem. Eng. Sci.* **2001**, *56*, 3931–3949.
23. T. F. L. McKenna, A. Di Martino, G. Weickert, J. B. P. Soares, *Macromol. React. Eng.* **2010**, *4*, 40–64.
24. A. Alizadeh, T. F. L. McKenna, *Macromol. React. Eng.* **2018**, *12*, 1700027.
25. M. Arakawa, M. Kishimoto, Y. Nakanishi, K. Mita, M. Takenaka, *Polym. J.* **2022**, *54*, 243–248.
26. C. E. Cardenas, J. Yang, B. M. Anderson, L. E. Court, K. B. Brock, *Semin. Radiat. Oncol.* **2019**, *29*, 185–197.
27. J. J. Bailey, J. Chen, J. Hack, M. Perez-Page, S. M. Holmes, D. J. L. Brett, P. R. Shearing, *J. Power Sources* **2021**, *509*, 230347.
28. A. D. Shum, C. P. Liu, W. Han Lim, D. Y. Parkinson, I. V. Zenyuk, *Transp. Porous Media* **2022**, <https://doi.org/10.1007/s11242-022-01833-0>.
29. K. Tang, Q. Meyer, R. White, R. T. Armstrong, P. Mostaghimi, Y. Da Wang, S. Liu, C. Zhao, K. Regenauer-Lieb, P. K. M. Tung, *Comput. Chem. Eng.* **2022**, *161*, 107768.

Appendices

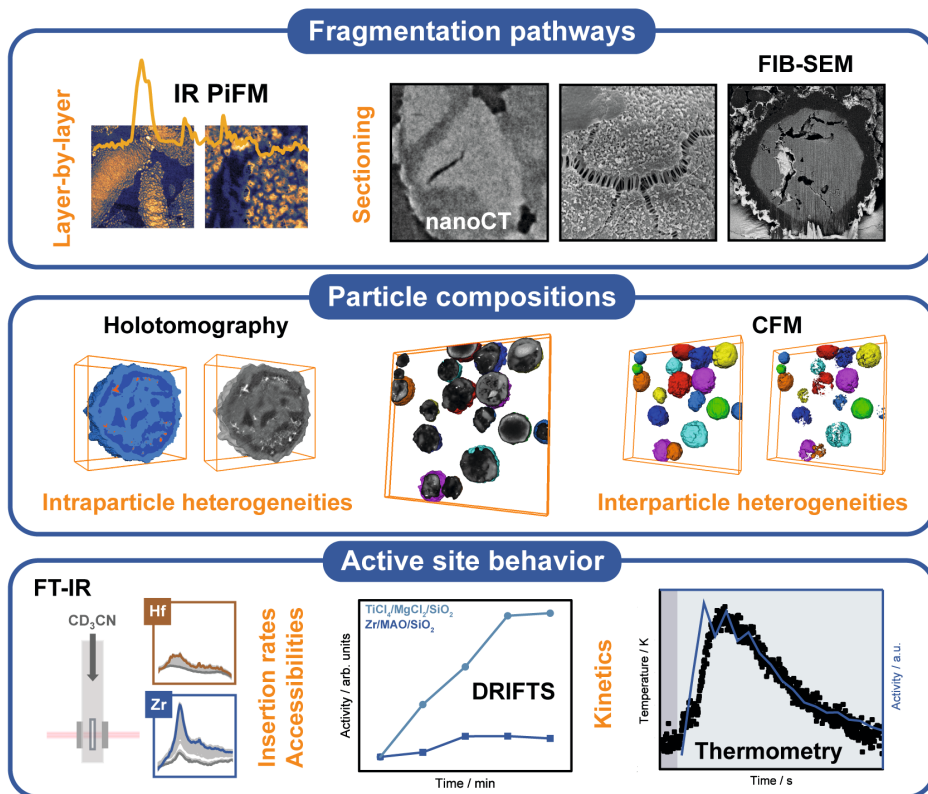
Appendix A: Nederlandse Samenvatting

De morfologische ontwikkeling van een katalysator op dragermateriaal voor de polymerisatie van olefinen heeft directe gevolgen voor de activiteit van de katalysator en de kwaliteit van het gevormde polymeerproduct. Bij het olefinopolymerisatieproces is een groot aantal experimentele variabelen betrokken. Daardoor is het identificeren van de factoren die verantwoordelijk zijn voor de morfologie van individuele katalysatordeeltjes is een complexe wetenschappelijke onderneming.

Om de structuur, morfologie, en samenstelling van individuele katalysatordeeltjes voor olefinopolymerisatie te bepalen, werden in dit proefschrift verschillende microscopische en spectroscopische methoden gebruikt. Vooraf aan de analyse, werden de katalysatordeeltjes al gepolymeriseerd met ethyleen onder gedefinieerde reactieomstandigheden. Door de combinatie van meerdere technieken op verschillende lengteschalen konden we structuur-samenstelling-prestatierelaties vaststellen in zowel metalloceen op silica dragermateriaal als Ziegler-Natta-katalysatoren. Over het algemeen werden geavanceerde elektronen-, röntgen- en fluorescentiemicroscopie gebruikt om morfologische gegevens op nanoschaal te verkrijgen van meerdere katalysatordeeltjes in 2D en 3D. De kinetiek en toegankelijkheid van de actieve sites van de katalysatoren werden daarentegen *in situ* beoordeeld met bulk-spectroscopietechnieken, zoals diffuse reflectie-infrarood Fourier-transformatiespectroscopie (DRIFTS), luminescentie-thermometrie en infraroodspectroscopie met sondemoleculen, evenals door het testen van katalytische prestaties. Het benutten van deze synergie tussen de karakteriseringstechnieken van individuele deeltjes en bulk bleek essentieel te zijn voor het rationaliseren van de structurele complexiteit van olefinopolymerisatiekatalysatoren op dragermateriaal tijdens de dynamische processen van polymeervorming en fragmentatie (**Figuur A1**).

Om de kloof tussen de karakterisering van individuele deeltjes en bulkanalysetechnieken te overbruggen, hebben we grotere monstersets bestudeerd met de volgende synchrotron methodes: harde röntgenholotomografie en laboratoriumgebaseerde confocale fluorescentiemicroscopie (CFM). Beide technieken faciliteerden een hogere monsterdoorvoer dan andere beeldvormingstechnieken met hoge resolutie. Daarnaast verschaften de synchrotron methodes, in combinatie met beeldverwerking, kwantitatieve inzichten in heterogeniteiten tussen de katalysatordeeltjes onderling en binnenin een individueel katalysatordeeltje (**Figuur A1**). We zijn van mening dat deze methodologieën representatieve morfologische inzichten kunnen bieden in bestaande en nieuw ontworpen katalysatoren voor olefinopolymerisatie onder verschillende polymerisatieomstandigheden.

In **Hoofdstuk 1** werd een korte introductie gegeven over katalyse, spectroscopie, en olefinopolymerisatie. Verschillende katalysatorcategorieën voor olefinopolymerisatie werden besproken en de rol van de katalysatorvorming tijdens olefinopolymerisatie werd besproken. Verder werden uitdagingen rondom het uitvoeren van morfologisch onderzoek naar polymerisatiekatalysatoren op dragermateriaal uigelijnd.



Figuur A1 Schematisch overzicht van de karakteriseringstechnieken die werden gebruikt om de relatie tussen structuur, samenstelling, en prestatie te onderzoeken in katalysatoren op silica dragermateriaal voor olefinepolymerisatie. De synergie van karakteriseringstechnieken tussen één deeltje, meerdere deeltjes, en bulk was cruciaal voor het vaststellen van duidelijke correlaties tussen de relevante eigenschappen.

In **Hoofdstuk 2** werden twee structureel analoge hafnoceen en zirkonoceen katalysatoren op silica dragermateriaal (d.w.z. X/MAO/SiO₂, X = metalloceencomplex, MAO = methylalumi-noxaan) onderzocht in verschillende stadia van gasfase ethyleenpolymerisatie. We keken naar de ongerepte katalysator en katalysatormonsters na 10 min, 30 min, en 60 min polymerisatie onder de volgende reactieomstandigheden: 1,6 bar druk en kamertemperatuur. Een multi-schaal microscopie en spectroscopie aanpak werd gebruikt om correlaties vast te stellen tussen de respectievelijke morfologieën van de katalysatoren en de eigenschappen van hun actieve sites. De interne structuren en morfologieën van de katalysatordeeltjes werden beoordeeld met gefocuste ionenbundel-scannende elektronenmicroscopie (FIB-SEM) en infrarood foto-geïnduceerde krachtmicroscopie (IR PiFM). Een laag-voor-laagmechanisme werd geïdentificeerd als de dominante fragmentatieroute in hafnoceen op silica dragermateriaal, dat homogeen fragmenteerde. Een heterogenere morfologie, gekenmerkt door bijdragen van het sectiemechanisme, werd echter waargenomen in zirkoonoceen op silica dragermateriaal. Dit werd toegeschreven aan significante verschillen in de polymerisatiesnelheden

van de katalysatoren. De hoge polymerisatiesnelheid van het zirkonoceencomplex leidt tot een snelle accumulatie van polymeer, met name aan het deeltjesoppervlak, waardoor de massaoverdracht wordt beperkt en de spanningsdissipatie in het deeltje wordt geremd. Om deze bevindingen verder te rationaliseren, werd tijdsgeresolveerde Fourier-transformatie infrarood (FT-IR) spectroscopie uitgevoerd met gedeutereerd acetonitril als een sondemolecuul in verschillende concentraties. De experimenten leverden inzicht op in zowel insertie van ethyleen ketens als de toegankelijkheid van de actieve sites van de katalysatoren. Niet alleen waren de actieve sites van de hafnoceen katalysator intrinsiek langzamer, ze waren ook minder toegankelijk vanwege de vorming van stabiele heterodinucleaire adducten met vrij trimethylaluminium (TMA, bestaat in evenwicht met MAO). Concluderend, onze multi-schaal aanpak leverde duidelijke correlaties op tussen de eigenschappen van de actieve sites, massaoverdrachtsbeperkingen, en dominante fragmentatieroutes in olefinepolymerisatiekatalysatordeeltjes op dragermateriaal.

In **Hoofdstuk 3** werd de tijdreeks van hafnoceen katalysatordeeltjes (d.w.z. Hf/MAO/SiO₂, zie **Hoofdstuk 2**) in meer detail onderzocht. Een totaal van 12 ongerepte en vooraf gepolymeriseerde katalysatordeeltjes werd onderzocht. Deze deeltjes vertegenwoordigen vijf stadia van ethyleenpolymerisatie in de gasfase: de ongerepte katalysator en katalysatormonsters na 1 min, 10 min, 30 min, en 60 min ethyleenpolymerisatie onder de reactieomstandigheden 1,6 bar druk en kamertemperatuur. De monsters werden in 3D beoordeeld met behulp van harde röntgenholotomografie. Dit leverde een beter begrip op van de morfologische evolutie van de hafnoceen katalysator, die voornamelijk laag-voor-laag fragmenteert. Een diepgaande kwantitatieve karakterisering van de porositeiten van de deeltjes, porienetwerken (via porienetwerkmodellering), en 3D-faseverdelingen onthulde significante heterogeniteit tussen en binnen de deeltjes tijdens de vroege stadia van gasfase ethyleenpolymerisatie. Onderlinge verschillen in de morfologie van katalysatordeeltjes werden toegeschreven aan het heterogene dragermateriaal en porie architectuur van de ongerepte katalysatordeeltjes, wat resulteert in verschillende mate van massaoverdrachtsbeperkingen. Afnames in macroporositeit en interconnectiviteit van de porieruimte werden waargenomen met polymerisatietijd en polymeer opbrengst. Dit benadrukt het belang van gecontroleerde fragmentatie van de katalysator drager bij het minimaliseren van massaoverdrachtsbeperkingen. Vanuit methodologisch oogpunt hebben de experimenten twee unieke sterke punten van holotomografie aangetoond die belangrijk zijn voor onderzoek naar olefinepolymerisatie katalysatorsystemen: i) het vermogen om katalysatorfasen en producten die worden gevormd door elementen met een laag atoomnummer, zoals koolstof en silica, af te beelden en te onderscheiden, en ii) relatief korte meettijden, die een hoge monsterdoorvoer en het verkrijgen van representatievere datasets mogelijk maken.

In **Hoofdstuk 4** werden de structuren van twee verschillende polymerisatiekatalysatoren op silica dragermateriaal, d.w.z. het bovengenoemde zirkonoceen op silica dragermateriaal (Zr/MAO/SiO₂) en een Ziegler-Natta-katalysator op silica dragermateriaal (TiCl₄/MgCl₂/SiO₂), gekarakteriseerd na polymerisatie in de slurryfase bij lage en verhoogde ethyleendrukken (7,5-10 bar ethyleendruk en kamertemperatuur). Analysetechnieken die in het laboratorium beschikbaar zijn, zoals nano-computertomografie (nanoCT) en gefocusseerde ionenbun-

del-scannende-elektronenmicroscopie (FIB-SEM), werden gebruikt om de ontwikkeling van uitgebreide scheuren in de katalysatordeeltjes in 3D en 2D te visualiseren. Verschillende factoren die het optreden van het sectiefragmentatiemechanisme reguleren, werden aldus geïdentificeerd. Deze omvatten de kinetiek van een katalysator (bevestigd met *in situ* DRIFTS), de porositeit van het dragermateriaal, en de toegankelijkheid van het interne volume van een katalysatordeeltje bij het begin van de polymerisatie. Hogere massaoverdrachtsbeperkingen en onvoldoende spanningsdissipatie bleken de betrokkenheid van het sectiemechanisme te versterken.

In **Hoofdstuk 5** werd de autofluorescentie van de zirkonoceen katalysator (d.w.z. Zr/MAO/SiO₂) gebruikt om de morfologie en samenstelling te bepalen met confocale fluorescentiemicroscopie (CFM). De samenstelling van de katalysator werd bestudeerd in meerdere verschillende stadia van ethyleenpolymerisatie in de slurryfase (10 bar ethyleendruk, kamertemperatuur) bij hoge monsterdoorvoer (2D: ≥ 135 deeltjes per stap, 3D: 40 deeltjes). Er werd een aanzienlijke mate van structurele heterogeniteit waargenomen voor en tijdens de ethyleenpolymerisatie, zoals eerder werd gerapporteerd voor de structureel analoge hafnoceen op silica dragermateriaal katalysator (d.w.z. Hf/MAO/SiO₂) tijdens de ethyleenpolymerisatie in de gasfase (**Hoofdstukken 2–4**). Deze heterogeniteit wordt voornamelijk toegeschreven aan de diverse dragermateriaal structuren en aan inhomogeniteiten in de metalloceenverdeling. Vanuit mechanistisch oogpunt onthulde de 2D- en 3D-screening uitgebreide bijdragen van een laag-voor-laag fragmentatiemechanisme in synergie met een minder uitgesproken sectiemechanisme. Verder werd een zekere mate van inactiviteit of slaapstand, die zich manifesteerde in een lagere mate van fragmentatie, waargenomen in een significante fractie van de deeltjes bij het begin van de polymerisatie. Dit draagt bij aan een verbreding van de oorspronkelijke deeltjesgrootteverdeling in de tijd. In combinatie met geavanceerde kleuringsprocedures en fluorescerende sondemoleculen, is de in het laboratorium beschikbare karakteriseringstechniek CFM zeer geschikt voor de morfologische analyse van olefinepolymerisatiekatalysatoren en vormt het een toegankelijk alternatief voor synchrotron experimenten. Vanwege de hoge monsterdoorvoer kan het worden gebruikt als hulpmiddel voor kwaliteitscontrole, zowel in de industrie als in de academische wereld.

In **Hoofdstuk 6** werd *in situ* luminescentiethermometrie toegepast om de temperatuur van een olefinepolymerisatie katalysator tijdens de polymerisatie van ethyleen in de gasfase te volgen. NaYF₄:Er³⁺,Yb³⁺/NaYF₄ kern-schil nanodeeltjes werden gebruikt als temperatuursensoren en werden homogeenverdeeld over een zirkonoceen katalysator op silica dragermateriaal (d.w.z. Zr/MAO/SiO₂) zonder enige tekenen van onmiddellijke deactivering. De temperatuurprofielen van de katalysator bij een ethyleendruk van 1 bar bleken te correleren met activiteitsgegevens die werden verkregen onder identieke reactieomstandigheden via *in situ* DRIFTS. Zo leveren de temperatuurmetingen kinetische informatie over de katalysator op. Afwijkingen in exothermiteit werden ook waargenomen tussen afzonderlijke testen, wat wijst op een grote invloed van de samenstelling en dichtheid van het katalysatorbed. De experimenten leggen de basis voor verder onderzoek, waarbij de temperatuurontwikkeling van individuele katalysatordeeltjes in kaart wordt gebracht met scantechnieken zoals CFM.

Dit zal inzicht geven in heterogeniteiten in temperatuur en activiteit aan het oppervlak van de katalysatordeeltjes tijdens het begin van de olefinepolymerisatiereactie.

In **Hoofdstuk 7** werd een gereedschapskist met analytische technieken gepresenteerd. Deze wordt specifiek gebruikt voor het verkrijgen van structurele en chemische informatie over olefinepolymerisatiekatalysatoren op dragermateriaal. FIB-SEM, harde röntgennanotomografie, IR PiFM en CFM werden benadrukt als state-of-the-art methoden voor chemische beeldvorming op nanoschaal. De technieken hebben ook potentie voor het bepalen van de ruimtelijke verdeling van koolstof educten en producten in heterogene katalysatoren voor het kraken en ontleden van polyolefinen. Nog grotere inzichten zouden kunnen worden verkregen met *in situ* en *operando* microscopie en tomografie-experimenten die duidelijke verbanden leggen tussen de initiële structuur van een katalysatordeeltje en zijn morfologische evolutie en activiteit tijdens polymerisatie of polymeerontleding. Tegelijkertijd zijn er aanzienlijke vorderingen nodig in de richting van een aanpak met hogere monsterdoorvoer van olefinepolymerisatie en polyolefine-ontledingskatalysatoren om representatievere informatie te verkrijgen over de morfologie en reactiviteit van katalysatordeeltjes.

Al in al onthulden onze onderzoeken een gelijktijdig optreden van twee fragmentatieroutes: het laag-voor-laagmechanisme en het sectiemechanisme in olefinepolymerisatiekatalysatoren op silica dragermateriaal tijdens de gas- en slurryfase ethyleenpolymerisatie. De mate waarin een bepaald mechanisme bijdraagt aan de fragmentatie van een bepaalde katalysator bleek sterk te worden beïnvloed door i) de kinetiek en toegankelijkheid van de actieve sites van de katalysator, en ii) de initiële structuur van het dragermateriaal. Beide zijn cruciaal bij het bepalen van de snelheid van massaoverdracht en polymeervorming tijdens de olefinepolymerisatiereactie. Bovendien werden nieuwe methodologische manieren ontwikkeld voor het extraheren van representatievere morfologische gegevens met nanometerresolutie. Röntgenstraling (d.w.z. holotomografie) en fluorescentiemicroscopie (d.w.z. CFM) uitgevoerd met grote deeltjesaantallen toonden duidelijk een hoge mate van inter- en intradeeltjesheterogeniteit in katalysatorsystemen op silica dragermateriaal, die werden gekwantificeerd met behulp van geavanceerde beeldsegmentatie en analyse.

Appendix B: List of Abbreviations and Symbols

A_s	Total area of pure silica domains and silica-dominant mixed phase domains
A_p	Total area of polymer-dominant mixed phase domains and macropore space
AFM-IR	Atomic Force Microscopy-Infrared spectroscopy
ATR-IR	Attenuated Total Reflectance-Infrared spectroscopy
BET	Brunauer-Emmett-Teller
BSE	Backscattered Electrons
CAGR	Compound Annual Growth Rate
CD_3CN	Deuterated acetonitrile
CFM	Confocal Fluorescence Microscopy
CY	Catalyst Yield
C_2H_4	Ethylene
d	diameter
DESY	Deutsches Elektronen-Synchrotron
DNA	Deoxyribonucleic Acid
DPI	Dutch Polymer Institute
DRIFTS	Diffuse Reflectance Infrared Fourier Transform Spectroscopy
E_A	Activation Energy
EDX	Energy Dispersive X-ray spectroscopy
EPS	Expanded Polystyrene
ESRF	European Synchrotron Radiation Facility
eV	electron Volt
F	Fragmentation parameter
FBP	Filtered Back Projection
FCC	Fluid Catalytic Cracking
FIB	Focused Ion Beam
FOV	Field Of View
FSC	Fourier Shell Correlation
FT	Fourier-Transform
g	gram
g_{PE}/g_{cat}	gram polyethylene per gram catalyst
h	hour
HDPE	High-Density Polyethylene
ICI	Imperial Chemical Industries
i-PP	isotactic Polypropylene
IR	Infrared
K	Kelvin
KB	Kirkpatrick-Baez
L	Liter
LDPE	Low-Density Polyethylene
LLDPE	Linear Low-Density Polyethylene
M	Metal
MAO	Methylaluminoxane
MEMS	Microelectromechanical Systems
min	minute

mm	millimeter
MWD	Molecular Weight Distribution
n	number
nm	nanometer
nanoCT	nano Computed Tomography
NP	Nanoparticle
PCA	Principal Component Analysis
PCC	Pearson's Correlation Coefficient
PE	Polyethylene
PET	Polyethylene Terephthalate
PiFM	Photo-induced Force Microscopy
PP	Polypropylene
PS	Polystyrene
PSD	Particle Size Distribution
PUR	Polyurethane
PVC	Polyvinylchloride
PXCT	Ptychographic X-ray Computed Tomography
R_i	Replication factor
RNA	Ribonucleic Acid
ROMP	Ring-Opening Metathesis Polymerization
rpm	revolutions per minute
s	second
SD	Standard Deviation
SE	Secondary Electron
SEM	Scanning Electron Microscopy
STEM	Scanning Transmission Electron Microscopy
STXM	Scanning Transmission X-ray Microscopy
t	ton
TEA	Triethylaluminum
TEM	Transmission Electron Microscopy
TiBA	Triisobutylaluminum
TPA	Total Particle Area
TPV	Total Particle Volume
TXM	Transmission X-Ray Microscopy
UV-VIS	Ultraviolet-Visible
V_s	Total volume of pure silica domains and silica-dominant mixed phase domains
V_p	Total volume of polymer-dominant mixed phase domains and macropore space
wt%	Weight percentage
XRF	X-Ray Fluorescence
2D	two-dimensional
3D	three-dimensional
°C	Degree Celsius
ΔG^0	Gibbs free energy
μL	microliter
μm	micrometer

Appendix C: List of Publications and Presentations

C1. List of Publications

This PhD thesis is based on the following scientific articles:

Correlating the Morphological Evolution of Individual Catalyst Particles to the Kinetic Behavior of Metallocene-Based Ethylene Polymerization Catalysts; M. J. Werny*, J. Zarupski*, I. C. ten Have, A. Piovano, C. Hendriksen, N. H. Friederichs, F. Meirer, E. Groppo, and B. M. Weckhuysen, *JACS Au* **2021**, 1, 1996–2008.

*Both authors contributed equally to this work.

X-ray Nanotomography Uncovers Morphological Heterogeneity in a Polymerization Catalyst at Multiple Reaction Stages; M. J. Werny*, R. Valadian*, L. M. Lohse, A.-L. Robisch, S. Zaroni, C. Hendriksen, B. M. Weckhuysen, and F. Meirer, *Chem Catalysis* **2021**, 1, 1413–1426.

*Both authors contributed equally to this work.

Elucidating the Sectioning Fragmentation Mechanism in Silica-Supported Olefin Polymerization Catalysts with Laboratory-Based X-Ray and Electron Microscopy; M. J. Werny, D. Müller, C. Hendriksen, R. Chan, N. H. Friederichs, C. Fella, F. Meirer, and B. M. Weckhuysen, *ChemCatChem* **2022**, 14, e202200067. Cover Feature.

Advancing the Compositional Analysis of Olefin Polymerization Catalysts with High-Throughput Fluorescence Microscopy; M. J. Werny, K. B. Siebers, N. H. Friederichs, C. Hendriksen, F. Meirer, and B. M. Weckhuysen, *J. Am. Chem. Soc.* **2022**, 144, 21287–21294.

Visualizing the Structure, Composition and Activity of Single Catalyst Particles for Olefin Polymerization and Polyolefin Decomposition; M. J. Werny, F. Meirer, and B. M. Weckhuysen. *Submitted for publication.*

Other publications:

Regulating Thermosensitive Behaviour in Three Polymorphs; M. J. Werny, and J. J. Vittal, *IUCrj* **2017**, 4, 202–203.

Fluctuating Storage of the Active Phase in a Mn-Na₂WO₄/SiO₂ Catalyst for the Oxidative Coupling of Methane; M. J. Werny, Y. Wang, F. Girgsdies, R. Schlögl, and A. Trunschke, *Angew. Chem. Int. Ed.* **2020**, 59, 14921–14926.

Silica-Magnesium-Titanium Ziegler-Natta Catalysts. Part II. Properties of the Active Sites and Fragmentation Behaviour; J. Zarupski, A. Piovano, M. J. Werny, A. Martini, L. Braglia, P. Torelli, C. Hendriksen, N. H. Friederichs, F. Meirer, B. M. Weckhuysen, and E. Groppo, *J. Catal.* **2023**, 423, 10–18.

Transport Limitations in Polyolefin Cracking at the Single Catalyst Particle Level; S. Rejman, I. Vollmer, M. J. Werny, E. T. C. Vogt, F. Meirer, and B. M. Weckhuysen, *Chem. Sci.* **2023**. Accepted for publication.

Fluorescent-Probe Characterization for Pore-Space Mapping with Single-Particle Tracking; R. M. González*, J. J. E. Maris*, M. Wagner, Y. Ganjkanlou, J. G. Bomer, M. J. Werny, F. T. Rabouw, B. M. Weckhuysen, M. Odijk and F. Meirer. Submitted for publication.

*Both authors contributed equally to this work.

C2. List of Oral and Poster Presentations at Conferences

Oral Presentations:

Multi-scale Investigation of Silica-Supported Ethylene Polymerization Catalysts during the Early Stages of the Reaction; M. J. Werny, J. Zarupski, A. Piovano, F. Meirer, E. Groppo, and B. M. Weckhuysen, October **2020**, Dutch Polymer Institute Annual Conference, Eindhoven, The Netherlands.

Assessing Correlations between the Fragmentation Behavior and the Kinetics of Silica-Supported Ethylene Polymerization Catalysts; M. J. Werny, J. Zarupski, I. C. ten Have, A. Piovano, C. Hendriksen, N. H. Friederichs, F. Meirer, E. Groppo, and B. M. Weckhuysen, May **2022**, The 27th North American Catalysis Society Meeting, New York, USA.

Correlating the Fragmentation Behavior and the Kinetics of Silica-Supported Metallocene-Based Polymerization Catalysts, M. J. Werny, J. Zarupski, I. C. ten Have, A. Piovano, C. Hendriksen, N. H. Friederichs, F. Meirer, E. Groppo, and B. M. Weckhuysen, June **2022**, The 19th International Symposium on Relations between Homogeneous and Heterogeneous Catalysis, Oslo, Norway.

Poster Presentations:

Multi-scale Investigation of Silica-Supported Ethylene Polymerization Catalysts During the Early Stages of the Reaction (MULTIPOL), M. J. Werny, F. Meirer and B. M. Weckhuysen, October **2018**, Shell Technology Center, Amsterdam, The Netherlands.

Study on the Activation of a Silica-Supported Ziegler-Natta Catalyst Using Single Particle UV-VIS Micro-Spectroscopy, M. J. Werny, F. Meirer and B. M. Weckhuysen, Dutch Polymer Institute Annual Conference, November **2018**, Eindhoven, The Netherlands.

Local Temperature Detection in Olefin Polymerization Catalysts Using Lanthanide-Doped NaYF₄ Nanoparticles, M. J. Werny, T. P. van Swieten, M. J. Mekkering, D. van den Heuvel, R. Geitenbeek, F. Meirer, A. Meijerink and B. M. Weckhuysen, 5th BlueSky Conference on Catalytic Olefin Polymerization, June **2019**, Sorrento, Italy.

Assessing Early-Stage Fragmentation in Olefin Polymerization Catalysts, M. J. Werny, N. Friederichs, R. Valadian, F. Meirer and B. M. Weckhuysen, Dutch Polymer Institute Annual Conference, November **2019**, Eindhoven, The Netherlands.

In Situ Temperature Detection in Olefin Polymerization Catalysts Using Lanthanide-Doped NaYF_4 Nanoparticles, M. J. Werny, T. P. van Swieten, R. Geitenbeek, A. Meijerink, F. Meirer and B. M. Weckhuysen, The Netherlands' Catalysis and Chemistry Conference XXI, March **2020**, Noordwijkerhout, The Netherlands.

Acknowledgments

And suddenly, 4 years at the Inorganic Chemistry and Catalysis (ICC) Group have come to an end. What a rollercoaster ride it has been! Thankfully, it has led to some interesting insights in the field of heterogeneous catalysis, many great friendships, countless lessons learned, and the PhD thesis you are reading right now! All of this would not have been possible without the support and contributions of a large number of people.

First and foremost, I have to thank my promoter and supervisor, **Prof. Bert M. Weckhuyesen**. Thank you for giving me the chance to join and experience a diverse research group that tackles critical research questions for the chemical industry and society at large. Our research is arguably more important now than ever before. Thanks for teaching me how to approach scientific questions with patience, structure, and attention to detail, as well as motivating me to dig deep for additional scientific insights. After four years, I am now much more aware of just how much work you do behind the scenes – thank you!

Secondly, I would like to thank my co-promotor and supervisor, **Dr. Florian Meirer**. I really appreciate your enthusiasm for science and your ability to think outside the box. It has definitely had a positive influence on the way I go about solving problems. Thank you for all the brainstorming sessions on polymerization catalysis, X-ray tomography and beam trips that we had in your office or online! Also, thank you for all your help with the analysis of more complex data – your ideas and methods really make a difference in our group!

Thirdly, I would like to express my gratitude towards **Dr. Annette Trunschke** and her team at Fritz-Haber-Institute in Berlin! You guided me through my first research project on heterogeneous catalysts and *operando* spectroscopy and inspired me to pursue a PhD in the very same field. Thank you!

In terms of projects and experimental work, I have to thank my collaborators at the Università degli Studi di Torino: **Prof. Elena Groppo**, **Dr. Jelena Zarupski** and **Dr. Alessandro Piovano**. It was a pleasure working with you on the DPI-funded MULTIPOL project, both on a professional and personal level! I wish you all the best and am curious to see what you can still learn about silica-supported olefin polymerization catalysts!

Talking about catalysts – many of the olefin polymerization catalysts that were investigated in this PhD thesis came from another team of competent and helpful individuals at SABIC: **Nic Friederichs**, **Dr. Coen Hendriksen**, **Robert Chan** and **Sander Janssen** – I have to thank all of you for your invaluable advice on olefin polymerization catalysis, and furthermore, for all the experimental support. Thank you for accommodating all our requests over the years!

Many of the rather challenging X-ray tomography experiments would have not been possible without the support of some very talented scientists! **Prof. Tim Salditt**, **Leon Lohse**, **Dr. Anna-Lena Robisch** (all Georg-August-Universität Göttingen) and **Dr. Roozbeh Valadian** (Utrecht University), thank you for your support during and after the beamtime at P10 (DESY). It was fantastic to see the results that holotomography yielded for olefin polymerization catalysts. **Dr. Dominik Müller** (Universität Würzburg) and **Dr. Christian Fella** (Fraunhofer IIS Würzburg), thanks for measuring all our samples with your department's lab-based nanoCT set-up – the results and the resolution were impressive! And finally, **Dr. Julie Villanova** and

Dr. Victor Vanpeene (European Synchrotron Radiation Facility, ESRF) – thank you for supporting us during our beamtime at ID16B. I am really excited about the acquisition speed of your set-up and am hoping that someone can use this to study olefin polymerization and depolymerization catalysts *in situ* one day!

Special thanks must go to the people who joined the beam trips at DESY, ESRF and Elettra: **Luca, Rafael, Roozbeh, Silvia, Sebastian, Caroline** (all Utrecht University), **Alessandro, Matteo, Alessia** (all Università degli Studi di Torino) and **Alexander** (ETH Zürich). A big thank you to you all! Also to you, **Ramon, Ad, Jochem, Oscar, Pascal, Fouad, Herrick** and **Joris** (all Utrecht University) – thank you so much for helping us with beam trip preparations, even when you had plenty of other work to do!

Dr. Thomas van Swieten, Dave van den Heuvel, Dr. Gerhard Blab and **Prof. Andries Meijerink** (all Utrecht University), I would like to thank you for sharing your knowledge on luminescence thermometry, collaborating on experiments, and modifying one of the CFMs at ICC for temperature mapping!

My appreciation also goes to you, **Chris Schneijdenberg, Eric Hellebrand** and **Hans Meeldijk** (all Utrecht University), for your assistance with the electron microscopes and sample preparation.

Sander Deelen (Utrecht University), thanks for making some fantastic spectroscopy cells and reactors! They certainly were put to good use.

Dymph Serree (Utrecht University), it was a pleasure working with you! Thank you for helping me with countless administrative and organizational tasks.

During my time at Utrecht University, I also had the pleasure of supervising two master students, **Martijn Mekkering** and **Kirsten Siebers**. Thank you Martijn and Kirsten for performing your research diligently. I wish you all the best with your respective PhDs!

Finally, I would like to acknowledge the **Dutch Polymer Institute (DPI)** for funding, as well as its industrial and academic community for teaching me the importance of considering the industrial relevance of my research!

On a more personal level, I would like to thank all the people I have met at ICC over the years (the list is long), be it technician, BSc student, PostDoc, secretary, PhD, HR or MSc student! Thanks for the good times and thank you for your support and help! I would especially like to thank you, **Francesco, Michael, Rafael, Joris, Laura, Florian, Kordula, Tessa, Ramon, Charlotte, Katinka, Donglong, Valerio, Thimo, Luca, Kirsten** and **Abi**, for keeping things fun at and outside of work!

Last but definitely not least, the biggest thanks to my family - **Penny, Hans, Louisa**, and **Sophia** - and to **Iris**. I would not be where I am without you!

Curriculum Vitae



Maximilian (Max) James Werny was born on August 2nd, 1994, in Hilden, Germany. After obtaining his Abitur in Bavaria, Germany, Max enrolled in an undergraduate degree (B.Sc.) in chemistry at the Technische Universität München (TUM) in 2012. During his Bachelor thesis, he conducted research on the 'Rare Earth Metal-mediated Group Transfer Polymerization of Novel Diaminovinylphosphonates' for the reversible capture and release of CO₂ under Prof. Bernhard Rieger. In 2015, Max continued with a graduate degree (M.Sc.) in chemistry at TUM, with a focus on inorganic chemistry and catalysis. In 2016, he joined the Department of Inorganic Chemistry, led by Prof. Robert Schlögl, at the Fritz-Haber-Institute of the Max-Planck-Gesellschaft, Berlin as a visiting researcher. Under the guidance of Dr. Annette Trunschke, Max characterized a Mn-Na₂WO₄/SiO₂ catalyst with *operando* spectroscopy, resulting in a publication on the 'Fluctuating Storage of the Active Phase in a Mn-Na₂WO₄/SiO₂ Catalyst for the Oxidative Coupling of Methane'.

During his time as an undergraduate and graduate student, Max worked in several chemical companies (i.e., BASF SE, Alantum Europe GmbH, BASF Construction Solutions GmbH, Vinnolit GmbH & Co. KG, and Wacker Chemie AG) on a part-time basis or as an intern, gaining experience in laboratory-, production- and business-related operations. In 2017, he also participated in the program TUMexchange, which allowed him to spend six months of his graduate degree at the National University of Singapore (NUS).

From 2018 to 2022, Max performed his doctoral research in the group of Prof. Bert M. Weckhuysen at Utrecht University. Here, he investigated the structures and reactivities of industrial-grade silica-supported olefin polymerization catalysts with advanced micro-spectroscopic techniques. The project was sponsored by the Dutch Polymer Institute (DPI) and involved close collaborations with groups from Torino (Italy), Göttingen (Germany) and Würzburg (Germany), as well as beamline scientists at DESY (Germany), Elettra (Italy) and ESRF (France). The most important insights from his research have been summarized in this PhD thesis, published in several peer-reviewed journals, and presented at both national and international conferences. Outside of work, Maximilian actively engages himself with strength training, CrossFit, road cycling and, when possible, diving and hiking. He is also an avid traveler and loves to spend time with his family and friends.

